Development of thermally regulated homogeneous assays and droplet-based microfluidic tools for probing secretion dynamics from pancreatic and adipose tissues

by

Juan Hu

A dissertation submitted to the Graduate Faculty of
Auburn University
in partial fulfillment of the
requirements for the Degree of
Doctor of Philosophy

Auburn, Alabama
August 4, 2018

Keywords: Immunoassay, Microfluidics, Obesity, Diabetes, Murine tissue

Approved by

Christopher J. Easley, Chair, Knowles Associate Professor of Chemistry and Biochemistry
Steven O. Mansoorabadi, Assistant Professor of Chemistry and Biochemistry
Douglas C. Goodwin, Associate Professor of Chemistry and Biochemistry
Robert L. Judd, Boshell Professor of Pharmacology

Abstract

Cells can transmit signals and adapt to microenvironment variations rapidly with dynamic processes, such as biomolecule secretion for signal delivery. Dynamic, oscillatory secretion is expected to exist in many cell types, but only a few selected tissues have been well investigated. This gap in information is likely due to the shortage of simple bioassays and compatible fluidic tools to directly sample and detect these secretions at high temporal resolution. To address this need, we have developed an integrated microfluidic droplet system. Using on-chip valving, droplets with consistent volume could be generated without the need to connect to macroscopic plumbing such as syringe pumps for droplet formation or cell perfusion. Homogeneous immunoassays and enzyme-coupled assays were also developed and optimized for on-chip, in-droplet readout and applied within the system to study dynamic secretions of proteins (insulin, asprosin) and small molecules (glycerol) from both primary tissues and cell spheroids at high temporal resolution (<4 s).

Chapter 1 introduces the research background. The prevalence of diabetes and obesity, functional tissues (pancreatic and adipose tissue) and related bioactive molecules are discussed. Another major part of introduction reviews the detection of bioactive molecules, including microfluidic tools and bioassays. Microfluidics is a powerful tool to integrate multiple techniques such as cell/tissue culture, secretion sampling, and detection on a small scale device, with rapid developments in the area in recent years. Bioassays are geared toward biomolecule quantification, where both high sensitivity and specificity are ideal. Particularly for integrating onto microfluidics, however, assays with simple workflow are much more suitable. Ultimately, simple assays, such as the homogeneous immunoassays discussed herein, can recognize their targets in complicated matrices and transfer this recognition into an easily detectable signal such as direct fluorescence.

In Chapter 2 and Chapter 3, homogeneous assays based on thermofluorimetric analysis (TFA) were developed for protein and small molecule quantification. TFA translates target levels quantitatively into multiplexable DNA melting transitions, allowing discrimination of the signal from the background, simultaneously. Chapter 2 discussed about TFA methods based on pairs of probes like antibody-oligo conjugated probes or aptamer pairs. Chapter 3 extends the TFA concept to study the binding of a single aptamer to protein targets, which can be used to quantify the targets or applied to monitor the progress of aptamer screening.

Based on previous and continuing work in Prof. Easley's lab, a microfluidic droplet system interfaced with enzymatic assays was developed and summarized in Chapter 4. The system was successfully adapted and utilized to detect the glycerol release from adipose tissue and encapsulated adipocytes. Interestingly, unique information was revealed about the dynamic function of adipose tissue, that glycerol release from the tissue was observed in a pulsatile pattern, distinctly different from adipocyte cell spheroids.

In Chapter 5, we began to explore the dynamic secretion of newly-discovered adipokine, asprosin. TFA assays for human and mouse asprosin were developed, and the isothermal format of the mouse asprosin assay was integrated into the microfluidic droplet system for high temporal resolution sampling and detection of asprosin. The results show that asprosin secretion was responsive to glucose and insulin reductions within a few minutes, and dynamic secretion behavior was also detected with asprosin. As a newly-discovered hormone, the secretion mechanisms and dynamics of asprosin release from adipose tissue are currently unknown, and these results represent the first report of dynamic asprosin secretion to our knowledge.

This dissertation concludes with Chapter 6, where we summarize the work and discuss the fact that further assay developments, combined with our novel microfluidic droplet-based sampling, should enable additional unique studies to be conducted on dynamic biological processes such as hormone or small-molecule secretion.

Acknowledgments

The past five years during my Ph.D. study has been like a journey. I have learned a lot in the Department of Chemistry and Biochemistry under the help of many people.

Firstly, I want to give sincere thanks to my advisor, Dr. Christopher J. Easley. Without his mentoring and support, I would not have been able to find the direction in this journey and reach my destination at the end. Dr. Easley continually encouraged me to study without stopping and to be confident without doubting myself.

Secondly, I want to express my appreciation to my committee members: Dr. Douglas C. Goodwin, Dr. Steven O. Mansoorabadi, and Dr. Robert L. Judd. Additionally, I should thank Dr. Philippe R. Gaillard for serving as my university reader. Thank you very much for spending your precious time on my committee. Your profound knowledge and rigorous academic attitude are my learning models. Many thanks also go to Dr. Bradley L. Merner, Dr. Konrad Patkowski, Dr. Curtis Shannon, Dr. Nedret Billor, Dr. Guanqun (Vivian) Cao, and Dr. Xiaoyu (Sophie) Li. I learned immensely from your courses. I also want to thank Timothy Knox, manager of Biological Research Facility, for helping mouse order and housing.

I am also very grateful to my amazing lab mates, Dr. Joonyul Kim, Dr. Jessica C. Brooks, Dr. Adriana Avila Flores, Dr. Xiangpeng Li, Dr. Jean Negou, Dr. Subramaniam Somasundaram, and Mark Holtan. You are so awesome and collaborative, and you have made me enjoy every day in the lab. I really appreciate Dr. Xiangpeng Li's continuous help since the first day I arrived in Auburn and over the next five years. Special thanks should also be given to my lovely friend Katarena Ford. Without you, I would have lost a lot of fun over these five years! You are my truest friend. Thanks and best of luck also to the other members in Dr. Easley's laboratory.

I want to give my thanks to everyone in the Auburn Karate Club. Shannon and Stephen are such good teachers and friends. I will never forget the days when we trained together and traveled for training camps and tests. I will find a new dojo and keep training in the future. Also thanks should be given to other friends in the club: Robert, Stephanie, Jessica and Ruo.

Finally, I would like to express my extreme gratitude to my parents and brother for your unwavering support.

Table of Contents

List of Figures

Chapter 1

Introduction

This work focuses on the development of bioassays and microfluidic tools to study the dynamic secretion of biomolecules from pancreatic and adipose tissue. As the introduction, this chapter begins with an overview of the disease states under study and the tissues involved, and it closes with a short review about microfluidics and bioanalytical assays used for biomolecule quantification.

1.1 Diabetes Mellitus

1.1.1 Diabetes and its epidemiology

Glucose is one major type of energy for our bodies. Glucose homeostasis is extremely important for health and the abnormality of glucose metabolism will usually result in diabetes. There are two major types of diabetes: type 1 diabetes mellitus (T1DM) and type 2 diabetes mellitus (T2DM). T1DM is an autoimmune disease, characterized by insufficient insulin production. The cause of T1DM is unknown but it is considered that the genetic and environmental factors are involved. T2DM is the chronic metabolic dysregulation, including carbohydrate, lipid and protein metabolism disorders to result in long-term hyperglycemia and insulin resistance. 90% of diabetic cases are T2DM. According to the estimation of International Diabetes Federation, 382 million adults in the world were type 2 diabetic in 2013, and the population will increase to 592 million in 2035 [1] (**figure 1.1**).

The persistent diabetic status will cause cardiovascular disease, vision loss, and the failure of nervous system, kidneys and other systems. T2DM is considered as a result of hormone dysregulation in obesity and shortage of exercise, but it is also related to aging, genetic factors, and gene-environment interconnection.

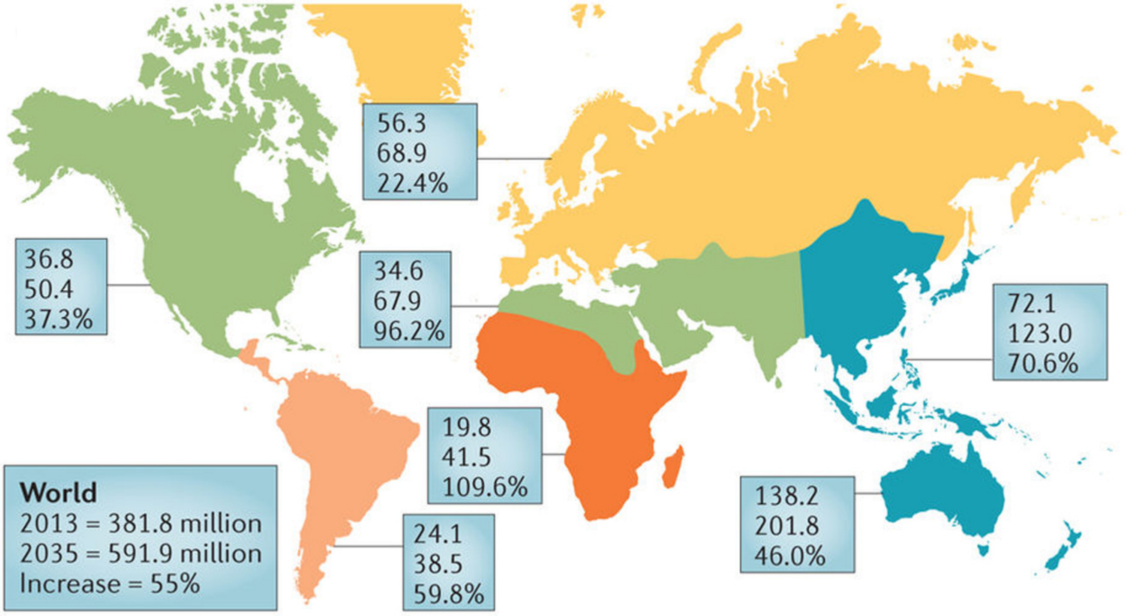

Figure 1.1: Global T2DM prevalence in 2013 and an extrapolated estimation for 2035 [2].The figure is reprinted with permission from ref [2] ©2015 Springer Nature.

1.1.2 Insulin secretion

The pancreas is a key organ in the digestive and endocrine system (**figure 1.2**). As a part of the digestive system, it can produce and release digestive enzymes for nutrients digestion and absorption. At the same time, as an endocrine organ, it can secrete several extremely essential hormones, containing insulin, glucagon, somatostatin, and pancreatic peptides. The islets of Langerhans are the important endocrine component of pancreatic tissue. In total, around 1 million of islets exist in a human pancreas, and these "microorgans" are composed of five different types of cells: α, β, δ, ϵ and pancreatic polypeptide-producing cells (PP cells). Different species have distinct percentages of the five types of cells in each islet. In humans, α-cells, making up of $\sim$30% of islet, produce glucagon to raise the glucose concentration in blood and to stimulate lipolysis in adipose tissue [3]; β-cells, accounting for $\sim$60% of islet, produce insulin to reduce the glucose concentration [3]; δ-cells, $<$10% of islet, generate somatostatin after food intake to inhibit the release of insulin and glucagon; PP-cells,$\sim$1% of islet, generate pancreatic polypeptide, which is enhanced in fasting and exercise, or when blood sugar levels are lower; and ϵ-cells, $<$1% of islet, produce ghrelin (growth hormone-releasing peptide) to regulate appetite and stimulate the lipogenesis. These hormones usually have both endocrine

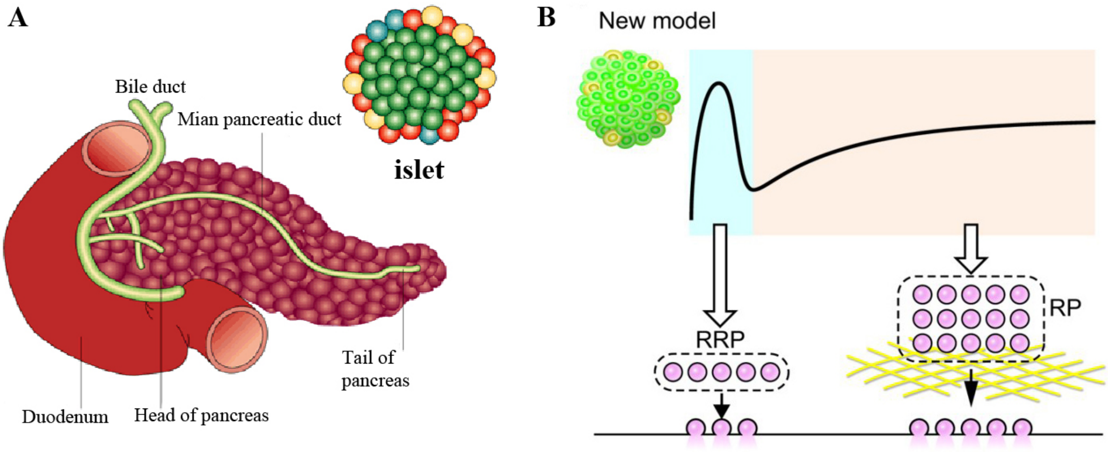

Figure 1.2: (A) Pancreas and pancreatic islets. Islets are composed of five major types of cells [8].(B)Biphasic secretion of insulin. The first phase is the docking and releasing of readily releasable pool (RRP), and the second phase is from the reserved pool [9].Figure A and B are reprinted with permission from ref [8] ©2015 Springer Nature, ref [9] ©2011 American Society for Clinical Investigation.

and paracrine functions. Besides being transported by the circulation system to and functioning on other organs, they also regulate hormone secretion from the other cells in islets. Thus, the cells in islets are connected and work together to secrete hormones correctly and much of the cell-to-cell communication occurs through gap junctions. For example, the whole-islet oscillations in insulin secretion are related to intercellular calcium oscillation waves are a result of coordination of β-cells through connexin-36 gap junctions [4]. The islets from connexin-36 knockout mouse model were shown to have reduced electrical coupling and slow and out-of-phase calcium waves [5, 6]. In addition, the β-cells–and perhaps the other cells– are under the regulation of neurotransmitters from the terminals of the nervous system [7].

Insulin secretion from β-cells of pancreatic islets occurs in a dynamic pattern, co-regulated by a variety of factors. Glucose-stimulated insulin secretion (GSIS) is the major mechanism of insulin secretion. One typical feature of GSIS is its biphasic pattern, as shown in **figure 1.2B**.

When food intake brings up the blood sugar concentration, the increased glucose is sensed by β-cells by Glut2 (glucose transporter 2) and transported into β-cells. The glucose is phosphorylated by glucokinase, which is the limiting step of glycolysis, and the concentration of glucokinase in the cell is another sensor of glucose level. Subsequently, glycolysis produces

ATP to increase the ATP/ADP ratio, which closes the ATP-dependent potassium (K_{ATP}) channel, resulting in the depolarization of the cell membrane to open the voltage-dependent Ca^{2+} channels (VDCCs) and allow the influx of Ca^{2+}, and high concentrations of Ca^{2+} can trigger SNARE protein-dependent docking and fusion of insulin-contained vesicles to the cell membrane to boost insulin exocytosis [10]. This is called the first phase of insulin secretion, the triggering step of GSIS (**figure 1.3**). Secreted insulin will be transported to muscle, liver, adipose tissue and brain, and they will coordinate to decrease the glucose level to normal concentration. The first phase of insulin secretion is usually around 10 minutes with a sharp concentration change just after the glucose level is elevated [11].

In the wake of the first phase, insulin secretion will enter the second phase, where insulin secretion keeps in a sustained and high level (**figure 1.2A**). The second phase can last up to 2 hours [11].

Due to difficulties in precisely sampling from small numbers of cells, bioanalytical methodology has been generally limited to investigating these insulin secretion dynamics at temporal resolutions on the order of minutes or hours. As discussed further in this dissertation, microfluidic systems have recently been developed that permit high-resolution secretion sampling, and some of these have even revealed tight coupling between intracellular Ca^{2+} and insulin oscillations.

1.1.3 The incretin effect

Insulin secretion is also regulated by other nutrients besides glucose and by factors like arginine and incretins. Incretins can potentiate the postprandial insulin secretion and the term “incretin effect” is used to describe that oral glucose administration can stimulate much more insulin secretion than intravenous injection. There are two known incretins: glucagon-like peptide-1 (GLP-1) and gastric inhibitory polypeptide (GIP). GLP-1 is released from the L cells and GIP from K cells of the intestine in the gastrointestinal system. Their release is stimulated by nutrient ingestion, and both can bind to their receptors expressed on the surface of β-cells in pancreatic islets. Their receptors are stimulatory G-protein coupled receptors (GPCRs), can activate adenylyl cyclase after binding with GLP-1 or GIP to transfer ATP to cAMP (cyclic

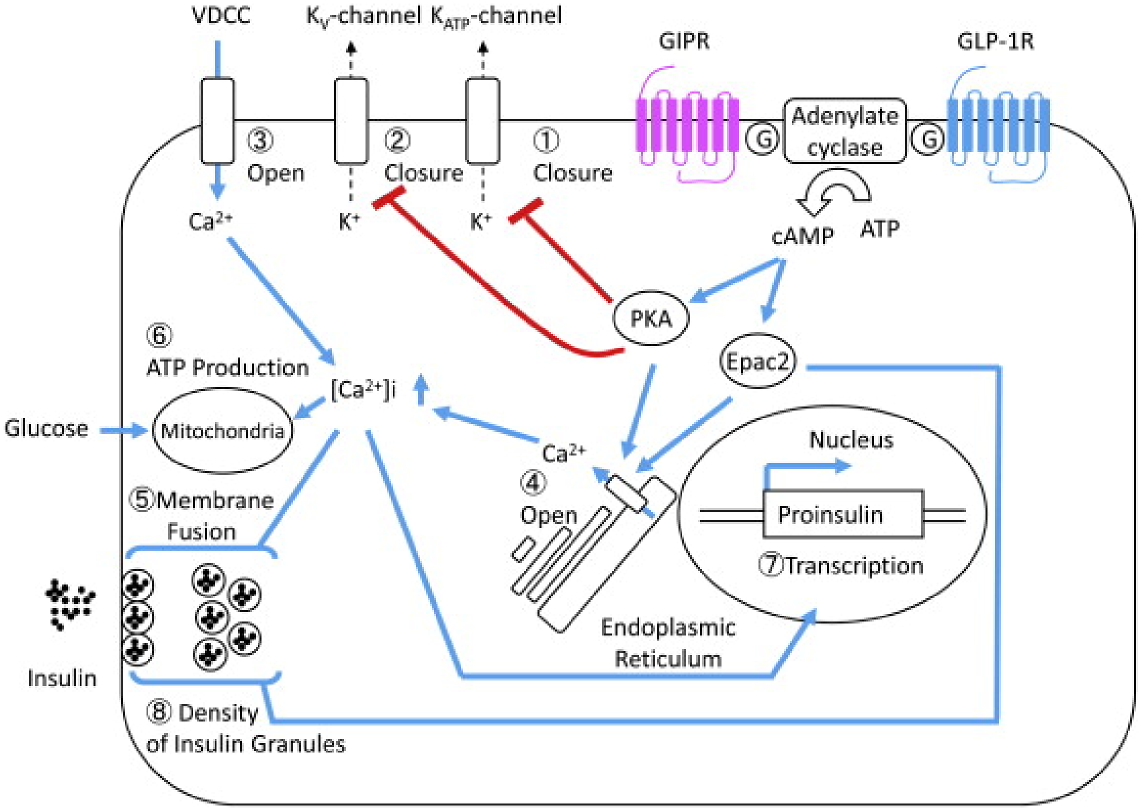

Figure 1.3: Molecular pathway of insulin secretion stimulated by glucose and incretins: GIP and GLP-1.The figure is reprinted with permission from ref [12] ©2011 Elsevier Ltd.

adenosine monophosphate). cAMP can activate protein kinase A (PKA) and Epac2 (exchange proteins activated by cAMP) to regulate the release and recharge of the calcium ion pool for insulin vesicles release and insulin granule production (**figure 1.3**) [11, 12]. Interestingly, the insulin secretion stimulation driven by these two incretins is glucose dependent. In the absence of a raised glucose level, the incretins will not elevate the insulin release, which is likely a protective effect to avoid hypoglycemia, the side effect of most of anti-diabetic medicines. GIP and GLP-1 not only regulate 50% of total insulin secretion but also stimulate β-cells proliferation by increasing the proliferation-related transcription factor PDX-1 (pancreatic duodenal homeobox-1 protein) [13, 14]. Therefore, the development of many anti-diabetic medicines now is based on analogs of the two incretins such as Exenatide (an analog of GLP-1) or inhibitors of dipeptidylpeptidase (DPP4) like Sitagliptin and Saxagliptin. DPP4 is an enzyme that deactivates GLP-1 and GIP, so its inhibition can allow incretins to stimulate more insulin secretion.

Very few studies have investigated the temporal dynamics of insulin secretion while varying the levels of incretin-type stimulations on islets or downstream tissues. As such, little is known about the changes that occur in islets over very short time scales after incretin signaling. In this work, we introduce several hormone and second messenger assays that are compatible with high resolution microfluidic sampling. These systems are well-poised to improve our understanding of incretin effect dynamics.

1.1.4 Insulin resistance

Insulin resistance is the impairment of insulin sensitivity of liver, muscle and adipose tissues, which is thought to result from overcompensated glucose metabolism in these tissues. The basal glucose concentration in the blood will be higher for the patients with insulin resistance; glucose uptake stimulated by insulin in muscle and adipose tissue reduces and the glucose production in the liver is out of control, resulting in the chronic hyperglycemia. In the early stages, islets will try to secrete more insulin to keep the glucose metabolism under regulation, but with the situation becoming worse, the overworked islets will start losing mass and eventually will not be able to secrete sufficient insulin to balance the glucose level.In other words, the eventual result is diabetes.

Notably, obesity related issues such as excessive fat accumulation in adipose tissue, fatty liver and infiltrating inflammatory cells in adipose tissue can all affect the metabolites and cytokines release from these tissues, and all of these effects have been related to the development of insulin resistance [15]. Overall, multiple organs and tissues contribute to the glucose homeostasis, and their disorders are all somehow related to the hyperglycemia and insulin resistance (**figure 1.4**) [2]. Under current technologies, the rapid and simultaneous quantification of a series of hormones and metabolites to decipher the complicated molecular interaction networks is still a difficulty.

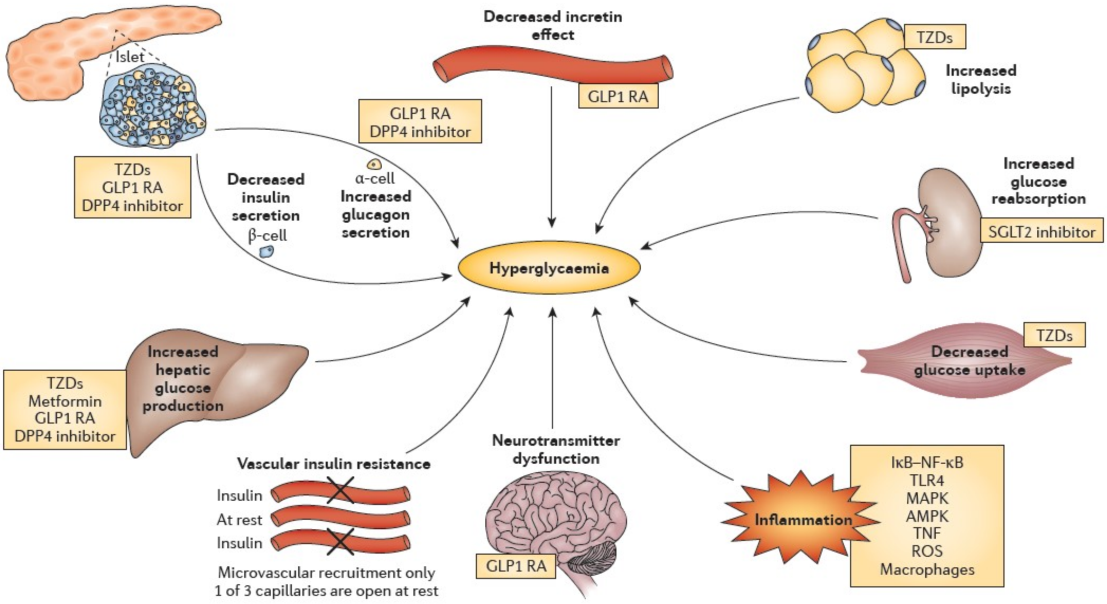

Figure 1.4: T2DM is characterized by chronic hyperglycemia, which is related to changes of cytokine production and resultant insulin resistance in pancreas, liver, intestine, adipose tissue, kidney, muscle, brain, and vascular system, along with infiltrating of immune cells [2]. TZDs = thiazolidinediones; NF-κB = nucleat factor kappa-light-chain-enhancer of activated B cells; TLR4 = Toll-like receptor 4; MAPK = mitogen-activated protein kinase; AMPK = 5' adenosine monophosphate-activated protein kinase;. TNF = tumor necrosis factor alpha; ROS = reactive oxygen species including peroxides, superoxide, singlet oxygen and hydroxyl radical. The figure is reprinted with permission from ref [2] ©2015, Springer Nature.

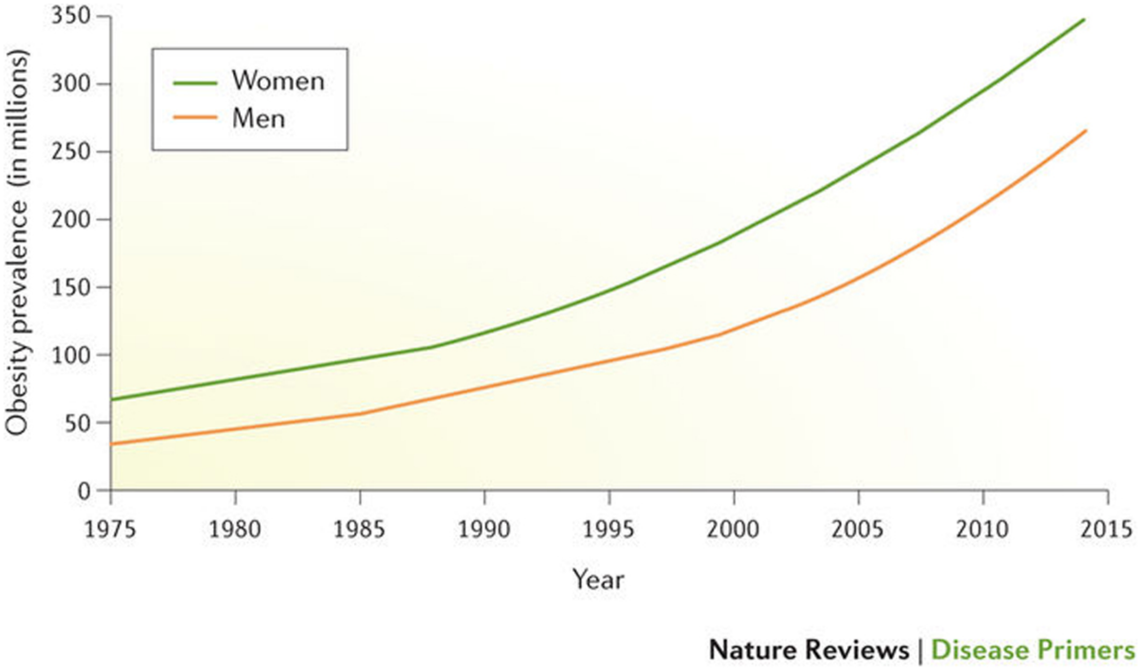

Figure 1.5: Obesity prevalence globally from 1975 to 2015.The figure is reprinted with permission from ref [16] ©2017 Springer Nature.

1.2 Obesity

1.2.1 Obesity and epidemiology

Like diabetes, obesity is also a 21st century epidemic (**figure 1.5**). This disorder is defined by excessive accumulation of adipose tissues and is usually associated with chronic and systematic inflammation.The WHO defines an obese patient as having a body mass index (BMI) greater than or equal to 30 kg/m^2 [16]. In 2016, 650 million adults were obese, and obese and overweight adults approach 40% ($\geq$ 2.1 billion) of the world population and 66% in US. It is estimated that by 2030 57.8% of the global adults will be overweight or obese if the obesity prevalence continues [17]. Studies show that 5% of global death is related to obesity and 2.8% of the world's GDP–about $2.0 trillion–is impacted by obesity [17]. The state of obesity increases the risks for many diseases such as type II diabetes [18], cardiovascular diseases, some types of cancer like breast cancer [19, 20], Alzheimers disease, and diseases related to mental health [21].

1.2.2 Adipose tissue: components and functions

Types of adipose tissue and Cell types in adipose tissue

For a given human's body weight, adipose tissue can account for anywhere 5 to 50% [22] of the total weight. For healthy adults, fat tissue is ~20% of whole body weight for males and 30% for females. Adipose tissue had been thought just as an energy reservoir, hormonally inert. But with the discovery of adipokines such as leptin [23] and adiponectin secreted by adipose tissue, the tissue was revaluated as a complicated, bioactive organ with metabolic and endocrine functions [24].

It is commonly considered that there are two major types of adipose tissue: white adipose tissue (WAT) and brown adipose tissue (BAT) (**figure 1.6**). WAT and BAT are different in function and anatomy [25]. The major responsibility of WAT is to be the storage of energy with large unilocular lipid droplet in cells, while BAT is mainly for heat production by non-shivering thermogenesis, consisting of small multi-locular lipid droplets and more mitochondria. Compared to large amount of WAT, BAT exists in less depots in adult, although there are much higher proportions in newborn babies. Recently, a new type of adipose tissue is described, the beige/ brite adipose tissue (**figure 1.6**), where adipocytes are generated from the browning (or beiging) of white adipocytes. Cold challenge or chemical stimulation can induce the beiging process, and WAT beiging is even considered as a potential therapeutic strategy in obesity and diabetes since the brown-like beige adipose tissues tend to burn fats to heat energy instead of storing them [26].

Adipose tissues also play different roles depending on their location. According to the anatomical position of fat in human body, fat tissues can be classified as visceral adipose tissue (VAT) or subcutaneous adipose tissue (SAT). The VAT depots include omental, mesenteric, gonadal, perirenal, epicardial, and retroperitoneal [27]. The distribution of VAT and SAT varies from species to species and person to person [28, 29] . The increase of visceral adipose tissue, especially omental and mesenteric VAT, is tightly related to the increased risk of cardiovascular diseases and T2DM. Conversely, the accumulation of SAT, especially in the hip and thigh (gluteofemoral fat), is protective from the obesity-related diseases [27, 29].

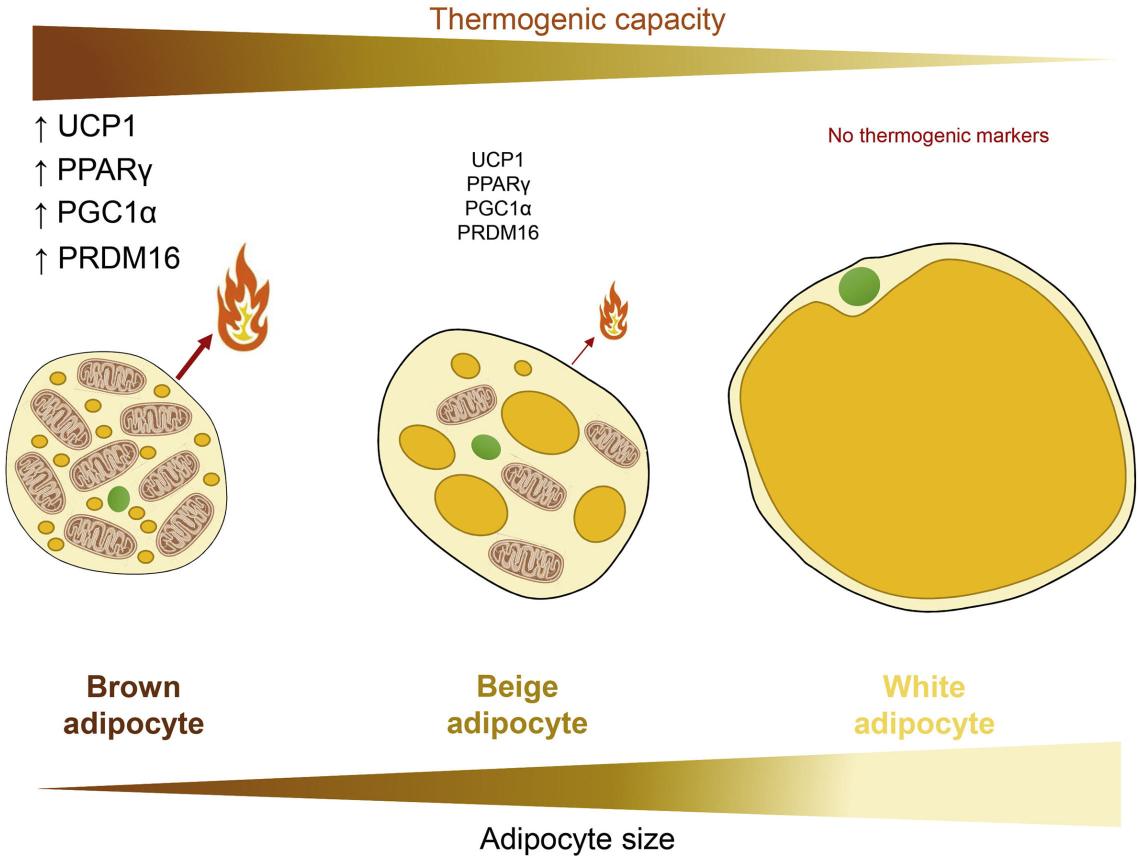

Figure 1.6: Three types of adipose tissues [25].UCP1 (uncoupling protein 1 in the mitochondria, also called thermogenin), PPAR$_\gamma$ (peroxisome proliferator-activated receptor gamma, a nuclear receptor, related to insulin sensitivity in adipose tissue), PGC1-α (peroxisome proliferator-activated receptor gamma coactivator 1-alpha, interacting with PPAR-γ and other transcription factors to regulate the mitochondria function), and PRDM16 (PR domain containing 16) are the thermogenesis-related factors.The figure is reprinted with permission from ref [25] ©2017 Elsevier Ireland Ltd.

Each adipose tissue also shows cell composition complexity. The tissue usually consists of adipocytes, preadipocytes, fibroblasts, T-cells, macrophages, stromovascular cells, endothelial cells, lymphocytes, nerve fibers and extracellular matrix [30]. Perhaps as a result of the relatively recent understanding of adipose tissue's complexity, few studies to date have carefully evaluated the dynamic function of the tissue.

Lipid metabolism and its regulations

One major function of adipose tissue is the regulation of lipid metabolism. WAT is the major organ to store energy in the form of triacylglycerols (TAG, known as triglyceride also). Fatty acids (FA), those taken up from the hydrolysis of TAG absorbed by intestine cells from food, are transported to adipose tissue and into the adipocytes, then re-esterified to form TAGs with glycerol 3-phosphate synthesized in glucose metabolism. FA can also arrive from *de novo* lipogenesis, usually happening in liver [31]. During fasting status where energy is in demand, the stored TAG will go through lipolysis and is hydrolyzed into diacylglycerol (DAG) and NEFA by adipose triglyceride lipase (ATGL). DAG can be further cleaved by hormone-sensitive lipase to monoacylglycerol (MAG) and NEFA. MAG is eventually decomposed into NEFA and glycerol under catalyzed by monoacylglycerol lipase (MGL). The NEFA can be used to produce energy by β-oxidization and the glycerol can be reused or transformed to glucose via gluconeogenesis in liver [32].

The lipolysis process is under the regulation of insulin, glucagon, epinephrine, norepinephrine (NE), and natriuretic peptides. It's well-known that a high concentration of circulating insulin responding to high concentration of blood sugar will inhibit lipolysis in adipocytes by downregulating the ATGL mRNA, while during fasting status the glucagon can stimulate the lipolysis of adipocytes. According to the hormone functions, the newly discovered hunger hormone, asprosin, should also be able to raise the lipolysis rate [33].

As shown by the signaling pathways in **figure 1.7**, lipolysis can be controlled through activation of $\beta_{1/2}$- adrenergic receptors (β- AR), which are G_sPCR (stimulatory G-protein coupled receptor), which signals through adenylyl cyclase (AC) to increase the cyclic-adenosine

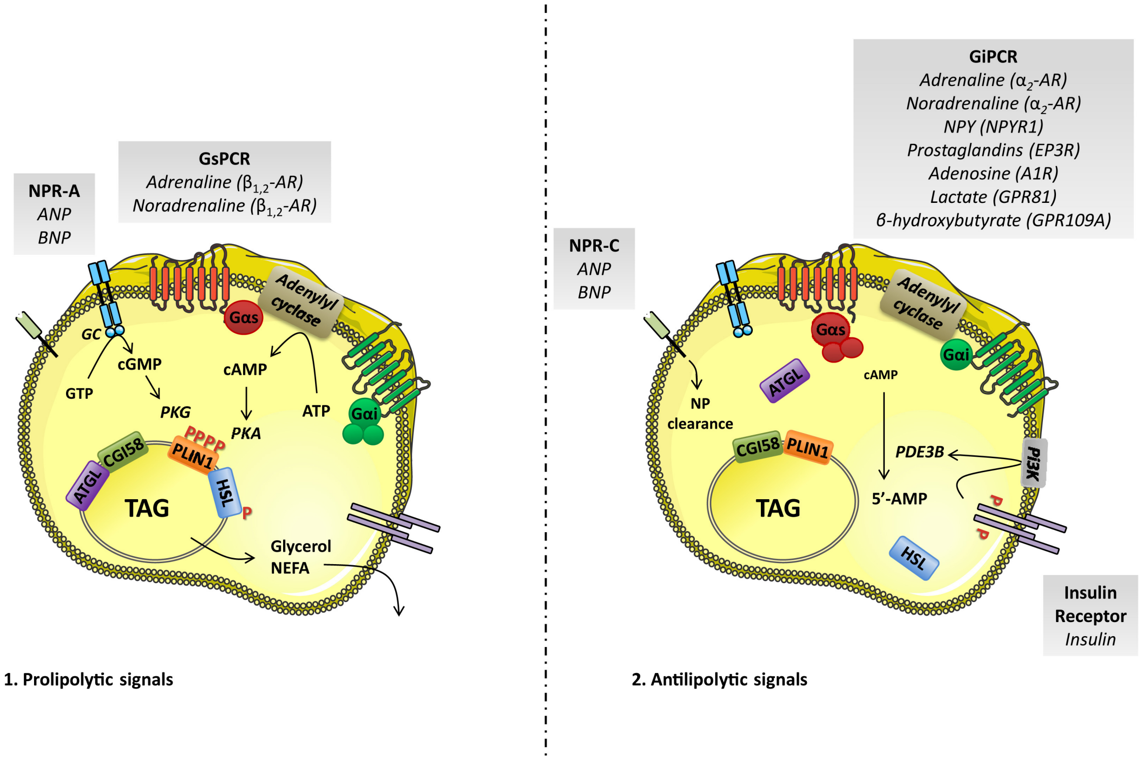

Figure 1.7: The prolipolytic and antilipolytic signaling in adipocytes [32] NPY1 (neuropeptide Y) can stimulate feeding. The figure is reprinted with permission from ref [32] ©2016 Elsevier.

monophosphate (cAMP) [34]. Downstream effects include protein kinase A (PKA), Hormone-sensitive Lipase (HSL) and perilipin (PLIN1). Isoproterenol (a derivative of epinephrine) and forskolin (agonist of AC) are able to enhance the intracellular cAMP amount to stimulate lipolysis. Interestingly, the regulation of catecholamines on lipolysis is age-related in some fat depots [28], which may indicate the age-related obesity.

Conversely, the activation of α_2- adrenergic receptors (α_2- AR), which are G_iPCR (inhibitory G-protein coupled receptor) will function oppositely to inhibit lipolysis after activated (**figure 1.7A**) [32].

Other regulator of lipolysis are natriuretic peptides (NP), ethanol [35], and compounds such as caffeine [36].

1.2.3 Adipokines and endocrine function of adipose tissue

From the previous section, we know that adipose tissue accounts for ~10% of insulin-stimulated glucose uptake, where glucose is metabolized for energy or transferred to TG as energy storage. Another critical role of adipose tissue is its endocrine function. Glucose and lipids metabolism in adipose tissue for energy balance are regulated by multiple organs and tissues, and they can sense energy level and coordinate with each other by release of hormones or metabolites [37] (**figure 1.8**). Adipose tissue is the largest endocrine organ and secretes a series of bioactive cytokines related to the regulation of energy homeostasis and the inflammatory system.

Here, we focus mainly on hormone secretion in white adipose tissue (WAT), from which more cytokines (adipokines) are produced compared to brown adipose tissue (BAT). Leptin was the first identified adipokine. It is considered as a satiety hormone that reduces food intake by targeting on the hypothalamus and it has a lipolytic effect to raise the energy expenditure in WAT [38]. Both of VAT and SAT can secrete leptin and SAT shows higher level of leptin mRNA in women. The circulated concentration of leptin is also proportional to the body fat weight. Adiponectin is another important and abundant adipokine. Produced only in adipocyte, it is considered as insulin sensitizer and its amount is reduced in visceral obesity. Adiponectin can also regulate inflammatory/anti-inflammatory processes [39]. The lymphocytes and stromal cells present in adipose tissue also produce and secrete resistin, which can reduce food intake. Sex steroids can also be secreted from adipose tissue, but their functions are not yet elucidated [38]. TNF_{α} (tumor necrosis factor-α) and IL-6 (interleukin-6) are synthesized and secreted from the macrophages and T-cells in adipose tissue to inhibit adipogenesis, and the increase of TNF is correlated to high BMI and associated with insulin resistance [18]. Many other proteins are also produced and secreted by adipose tissue, such as chemerin, omentin, vaspin, vistatin, DPP4, and others[40]. Many of these cytokines have not been characterized well, and new ones remain to be uncovered. Notably, their characterization and discovery would greatly benefit from simple, rapid, and low-cost but efficient quantitative assays-a subject of Chapter 2 and 5 of this work.

Because many cytokines are produced in adipose tissue, and they participate in crosstalk with other organs, malfunction of WAT will result in obesity and obesity-related diseases like T2DM, cardiovascular disease, and other metabolic diseases [41], and the development of these diseases is related to the insulin resistance of adipose tissue. Furthermore, the alteration of

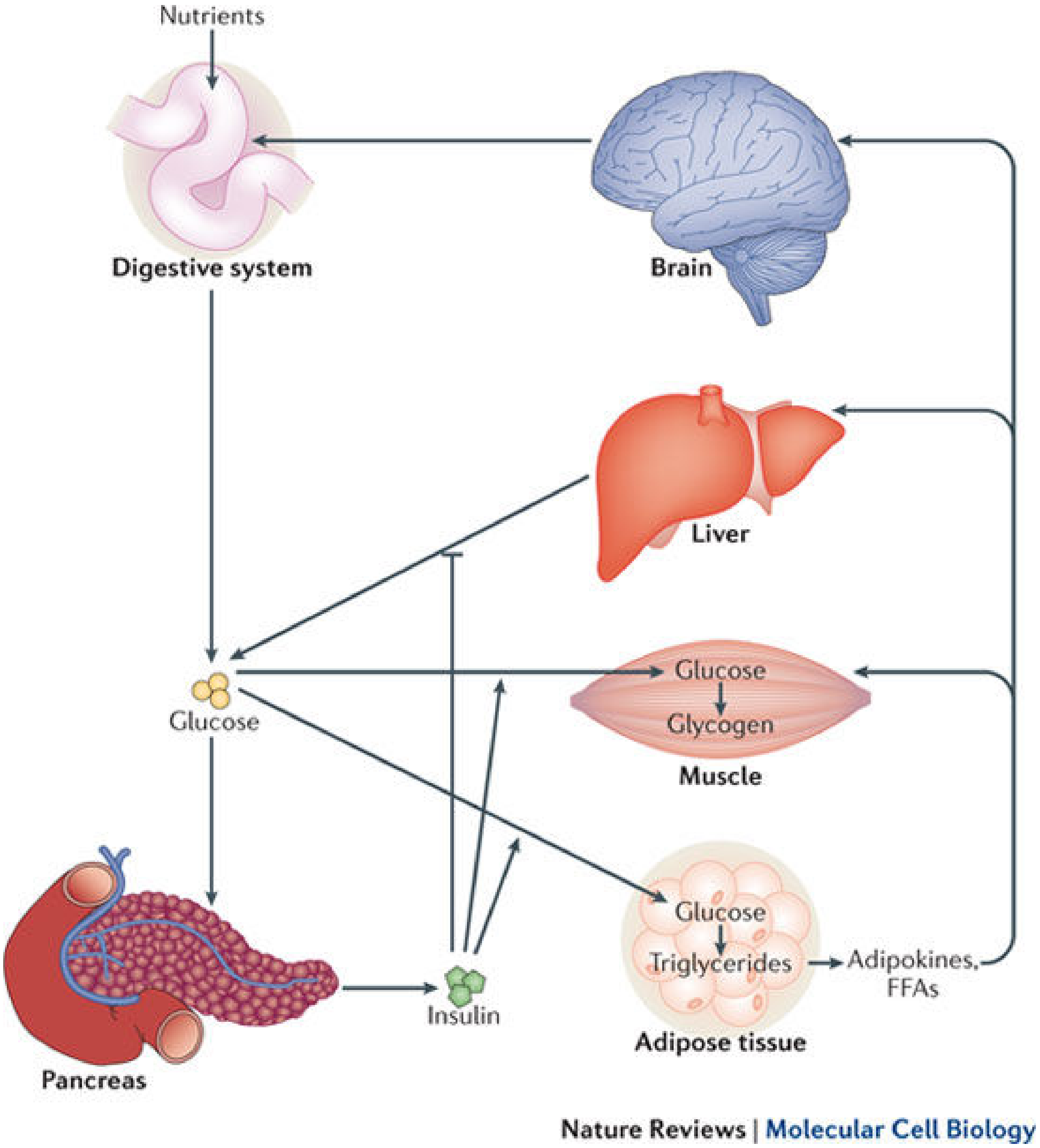

Figure 1.8: Regulation of energy homeostasis in multi organs and tissues.The figure is reprinted with permission from ref [37] ©2017 Springer Nature.

lipolysis can result in higher basal concentrations of glycerol and FFA in blood, which is associated with insulin resistance; it can attenuate the response of adipose tissue to stimulated hormone such as catecholamines owing to the decreased lipolytic G_s, increased antilipolytic α_2 adrenoceptors and lower level of HSL [42]. Increased leptin and TNF_α will also raise basal lipolysis in obesity; hyperleptinemia is highly correlated to the insulin resistance. These already significant correlations between obesity and insulin resistance need further investigation, thus method development in the area remains an important goal of bioanalytical chemists.

1.2.4 Connections in adipose tissue

Cytokines are secreted from adipose tissue in dynamic patterns, and further evidence of these effects are shown in Chapter 4 using our microfluidic systems. This type of dynamic secretion is likely due to cell-to-cell communication because cells are naturally connected to each other and function in a high-level coordination in multicellular organisms. Here, I highlight two types of important connections in WAT, gap junctions and nerve-cell innervation.

Gap junction

Cell junctions are essential parts for intercellular connection in tissues, giving the only channels for the direct contact of cytoplasmic matrices [43]. Gap junction intercellular communication (GJIC) (**figure 1.9A**) is one type of cell junction. Gap junctions are channels of 1.4-1.6 nm in diameter on the cell membrane, which are composed of two connexons (**figure 1.9B**), and they allow low molecule-weight ($<$ 1000 Da) molecules to exchange between cells including the ions (e.g. Ca^{2+}), metabolites (e.g. ATP, glucose), and second messengers (e.g. cAMP) [44]. Known for some time for existing in brain, liver, cardiac, and skeletal muscle tissues [44, 45], gap junctions are mainly responsible for the buffering and transferring of cellular signaling between cells to synchronize the electrical and metabolic activities of cells in the intact tissue [46]. The abnormal function of gap junctions and mutation of gap junction genes are related to heart diseases, hearing impairment [47, 48], and other pathological states.

Multiple publications have proved that gap junctions exist in brown and white adipose tissues, consisting of paired connexin 43 proteins and functioning for intercellular communication to synchronize the cellular events for energy balance and the inflammatory response [49, 50, 46, 51].

The synchronized cellular activities by GJIC will accelerate and amplify the response of adipocytes stimulated by hormones from other organs or tissues to regulate the lipid metabolism, adipokine secretion and immune response as an endocrine organ. In example, gap junctions (Cx43) are shown to be required to propagate the sympathetic nervous signals in beiging of WAT in cold challenging [26]. However, the direct responsibilities of gap junctions in adipokines secretion remain to be further understood. In Chapter 5, we use novel techniques to show evidence–similar to the removal of gap junctions in pancreatic β-cells where cells lost calcium oscillation [52]–that the gap junctions also play a vital role in the dynamic secretion of adipokines from WAT.

Nerve-cell innervation

Energy homeostasis involves the regulation of food intake, energy expenditure and a variety of metabolic processes. The central neuronal system (CNS) is another important part of the physiological system that helps conserve the metabolic homeostasis and energy balance for the whole body. Adipose tissues have been known to be innervated by terminals of the sympathetic nervous system (SNS) [53, 54], and it was commonly considered that brown adipose tissue is more innervated than white adipose tissue (WAT) and that the innervation of WAT is more due to the blood vessels through the tissues [55]. But with more investigations on the lipolysis and beiging of WAT, it was revealed that the fat pads of WAT are well connected by a network of sympathetic arborizations. A recent article has reported $>90\%$ adipocytes (**figure 1.10A**) in the inguinal WAT (iWAT) are apposed closely to the sympathetic fibers, which can be activated by cold exposure for WAT beiging regulated through β-adrenergic receptor [56]. Not just the browning of WAT is under the regulation of SNS, as the lipolytic effect of leptin on the WAT is also related to the neuro-adipose junction. In this study, the optogenetic activation of sympathetic nerves in iWAT was used to mimic the lipolytic effect of leptin by increase of

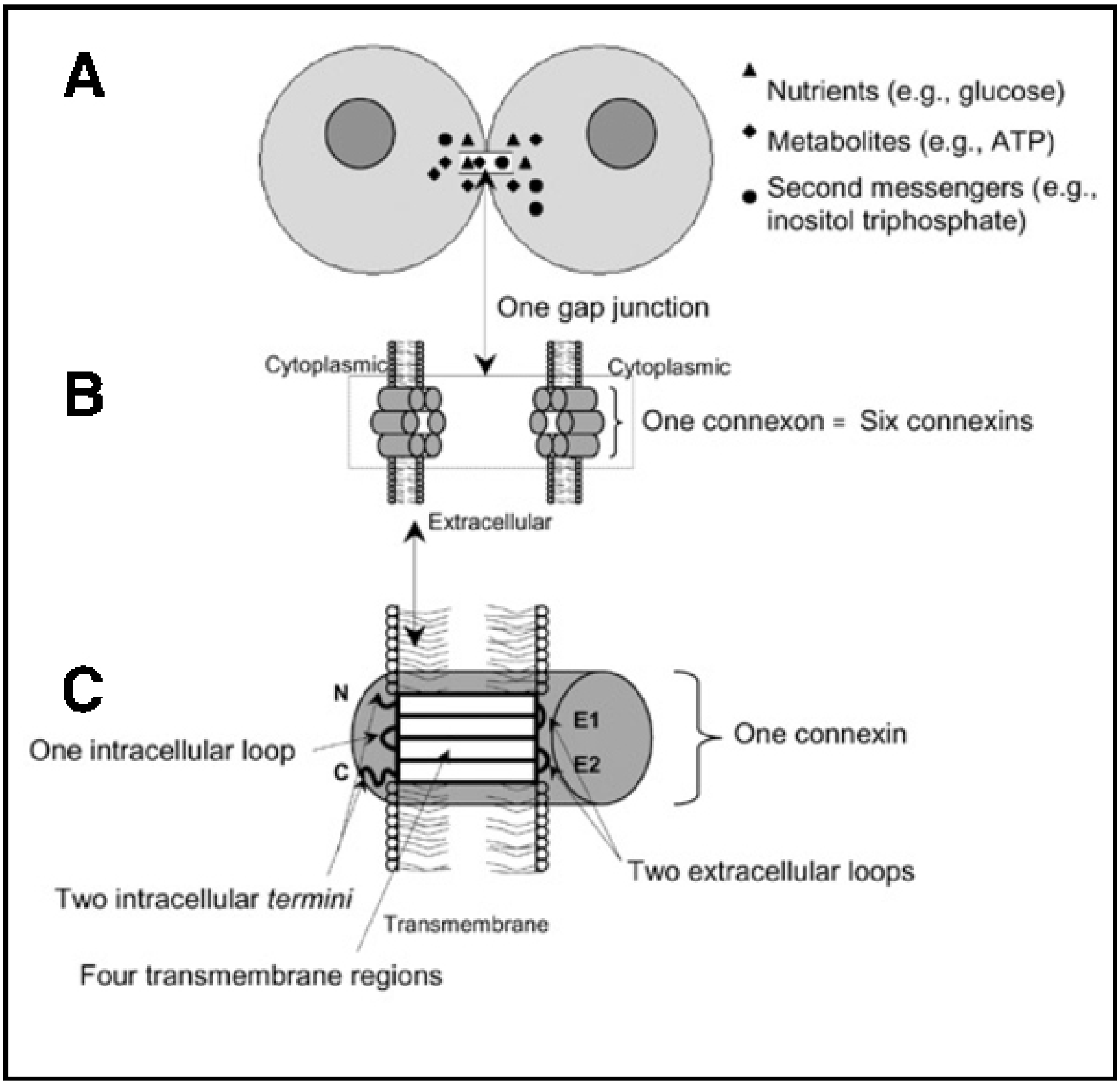

Figure 1.9: (A) Gap junction intercellular communication (GJIC); (B) A pair of connexons form a GJIC channel, and each connexon contains six subunits named as connexin; (C) The structure of a transmembrane protein, connexin.The figure is reprinted with permission from ref [43] ⓒ2008 Future Science.

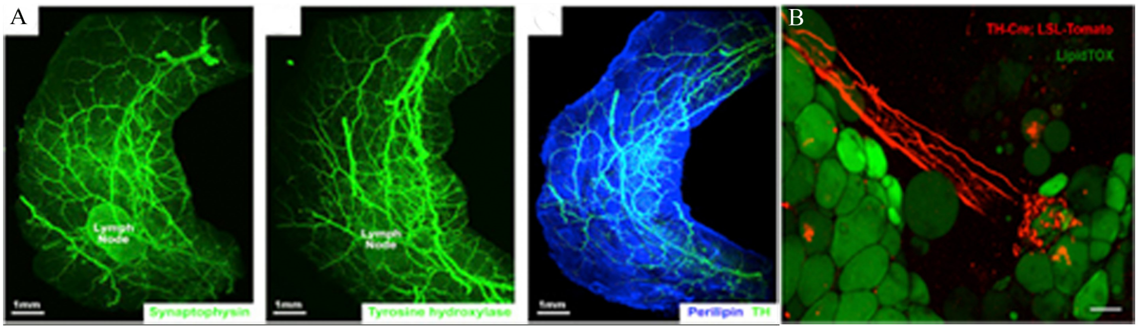

Figure 1.10: (A) The sympathetic innervation of inguinal WAT. Synaptophysin is a pan-neuronal marker and tyrosine hydroxylase is the marker of sympathetic neuron [56]. (B) The connection of neuron and adipocytes in iWAT fat pad in the anesthetized mouse [57].Figure A and B are reprinted with permission from ref [56] ©2017 Elsevier Inc, ref [57] ©2015 Elsevier Inc

norepinephrine and signaling through the β-adrenergic receptor (**figure 1.10B**) [57]. Furthermore, the electrical stimulation of the hapothalamus can trigger increased FFAs and glycerol [58]. Overall, the sympathetic system has been found to have profound effects in lipolysis and anabolic pathways (**figure 1.11**). The WAT is also innervated by the parasympathetic nervous system (PNS) [59, 60]. The parasympathetic stimuli inputs are related to insulin sensitivity of fat tissue and to the endocrine function of the tissues through the secretion of leptin and adiponectin [59].

Connected by the sympathetic and parasympathetic nervous systems, the brain, adipose tissues, pancreas, muscle and digestive system form interconnected loops that regulate the appetite and metabolic activities of adipose tissues (**figure 1.12**)[16]. The innervation of adipose tissues is also considered to play a role in the difference of lipid metabolism and immobilization in different types of adipose tissues [54]. In deciphering studies herein that focus on dynamic WAT function (Chapters 4 and 5), it will be important to understand these SNS and PNS connections to WAT *in vivo*.

1.3 Dynamic study of biomolecule secretion

From what I have discussed so far, it should be clear that the regulation of metabolism and hormone secretion in pancreatic and adipose tissues is a complex network. It is important to study these tissues with higher precision techniques to have better insight about what causes

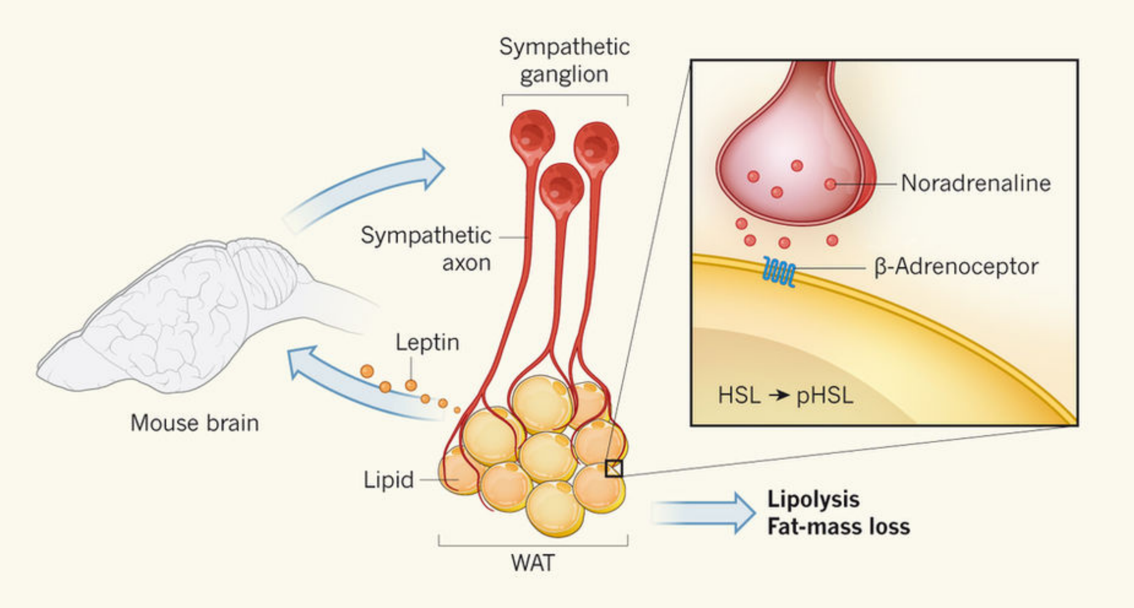

Figure 1.11: Lipolytic effect of leptin to promote the fat loss though the sympathetic nervous system. The secreted catecholamine from the nerve terminal can activate β-adrenergic receptor to enhance the lipolysis in adipocytes.The figure is reprinted with permission from ref [61] ©2015 Springer Nature.

diabetes and obesity and how to keep or bring back our bodies in energy homeostasis and balance of endocrine system to prevent or cure the diseases. For understanding the tissue function more thoroughly, the metabolites, secreted proteins and related signaling molecules from the tissues should be quantified under regular condition and simulated status and at high temporal resolution if possible. A variety of conventional assays are available for the detection and quantification of proteins and small molecules, which I will discuss it in a later section. However, intercellular metabolism and extracellular hormone secretion are not simple to keep correlated in the same pattern and at consistent rate–they secrete dynamically. As mentioned earlier, a typical example is the calcium wave and synchronization of insulin secretion from coupled β-cells in pancreatic islets [4]. Even with well-developed systems for imaging and sampling from islets, it is still very difficult to assemble an experimental system that can simultaneously measure intercellular Ca^{2+} and insulin secretion.

Biological systems consist of many dynamic molecular machineries and can deal with the signals and give responses at a high speed. **Figure 1.13** shows how fast various biological response in cells can be processed, such as microsecond-to-millisecond cell signaling or second-to-minute scale protein synthesis. Therefore, to study the active functions of cells and

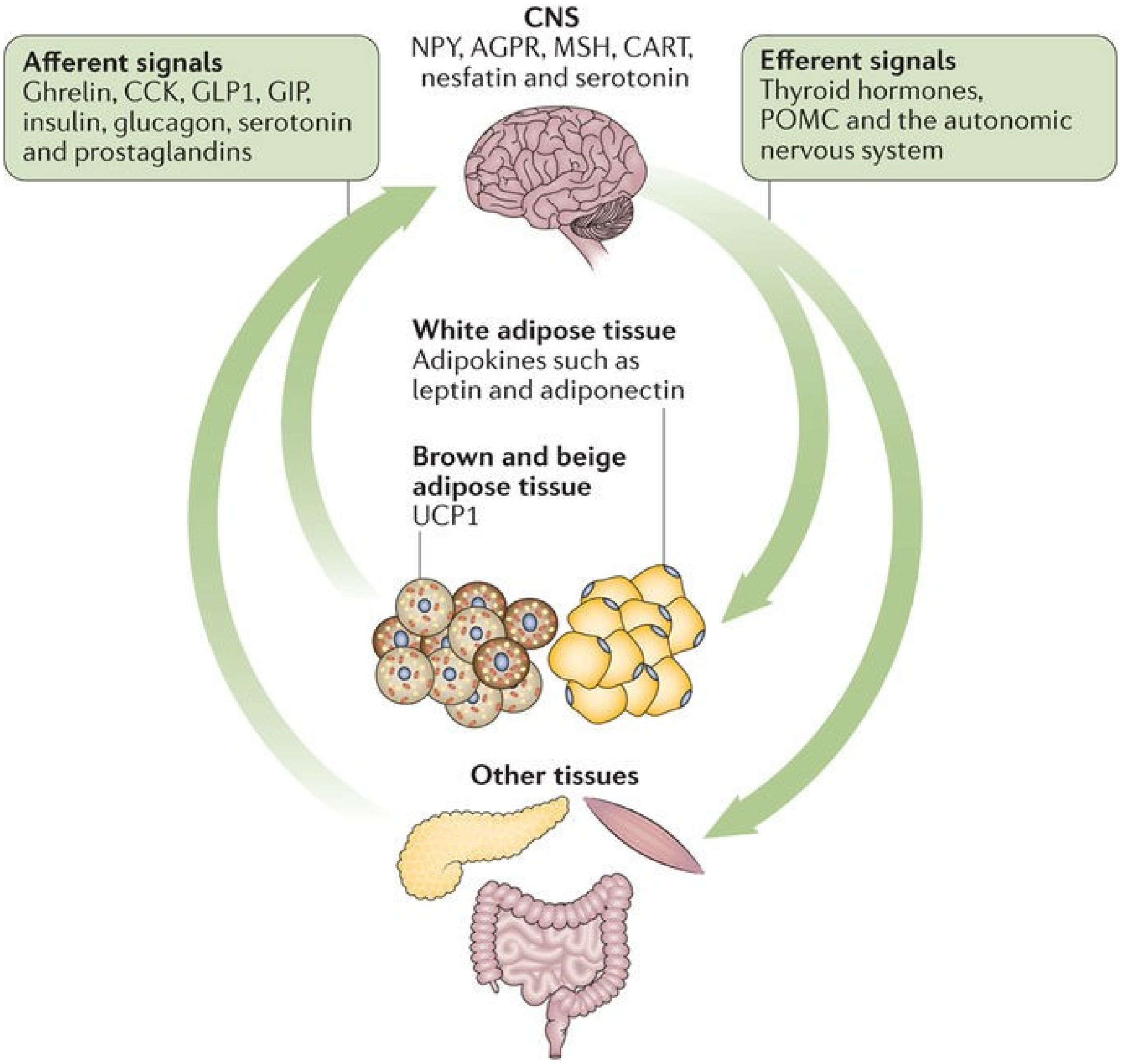

Nature Reviews | Disease Primers

Figure 1.12: The appetite control system. The terminals of SNS and PNS in adipose tissue can sense the energy level and secrete the adipokines, such as leptin and adiponectin from WAT and UCP1 (uncoupling protein 1) from BAT, to function on the brain to produce neurotransmitters and peptides to trigger the food intake (neuropeptide Y (NPY) and agouti-related peptide (AGRP)) curb the appetite (melanocyte-stimulating hormone (MSH) and amphetamine-regulated transcript protein (CART).The figure is reprinted with permission from ref [16] ©2017 Springer Nature.

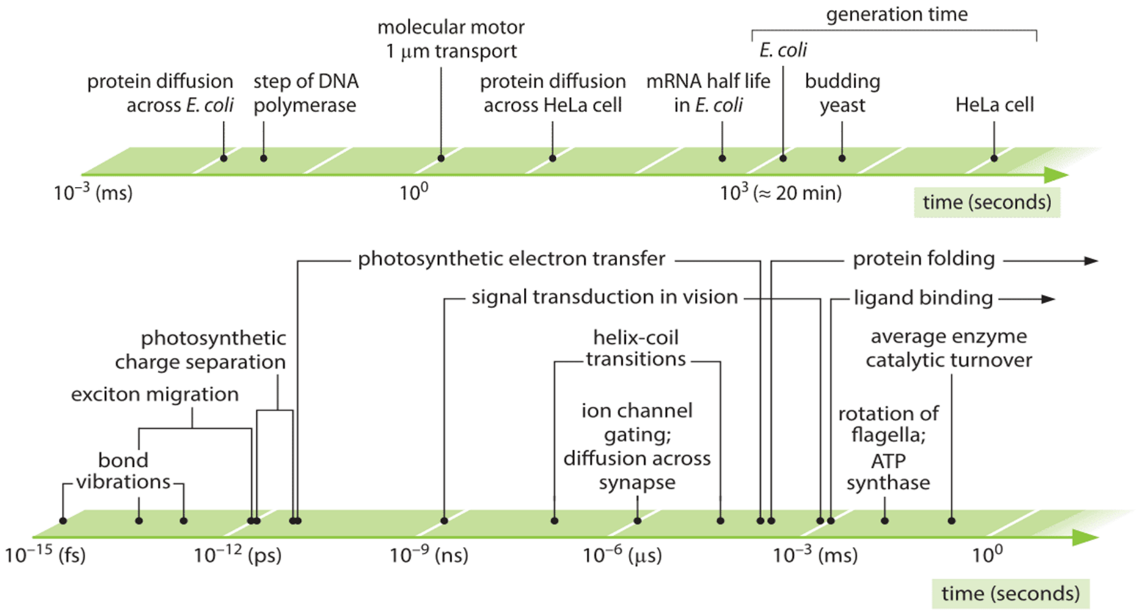

Figure 1.13: Timescales of biological processes.The figure is reprinted with permission from ref [63] ©2015 Tylor and Francis.

tissue, a tool or technique with high temporal resolution is required to control and monitor the sampling in real time. The development of microfluidic technologies effectively shined a light on reforming the investigative methods of cell biology [62]. Due to its accurate and precise control of time and solution volume and its good compatibility with various assays and microscopy, it is an ideal tool for dynamic studies of biomolecules secretion from pancreatic and adipose tissue. In the sections that follow, several relevant microfluidic concepts are introduced.

1.4 Microfluidics

Microfluidics is defined as “the science and technology of systems that process or manipulate small (10^{-9} to 10^{-18} liters) amounts of fluids, using channels with dimensions of tens to hundreds of micrometers” (quote from Prof. George Whiteside) [64]. The development of microfluidics has been motivated by the small consumption of reagents and samples, low cost, rapid analysis with high sensitivity and high resolution, and the most important characteristic–small size but with highly integrated devices, i.e. lab-on-a-chip system (**figure 1.14A-B**) [64].

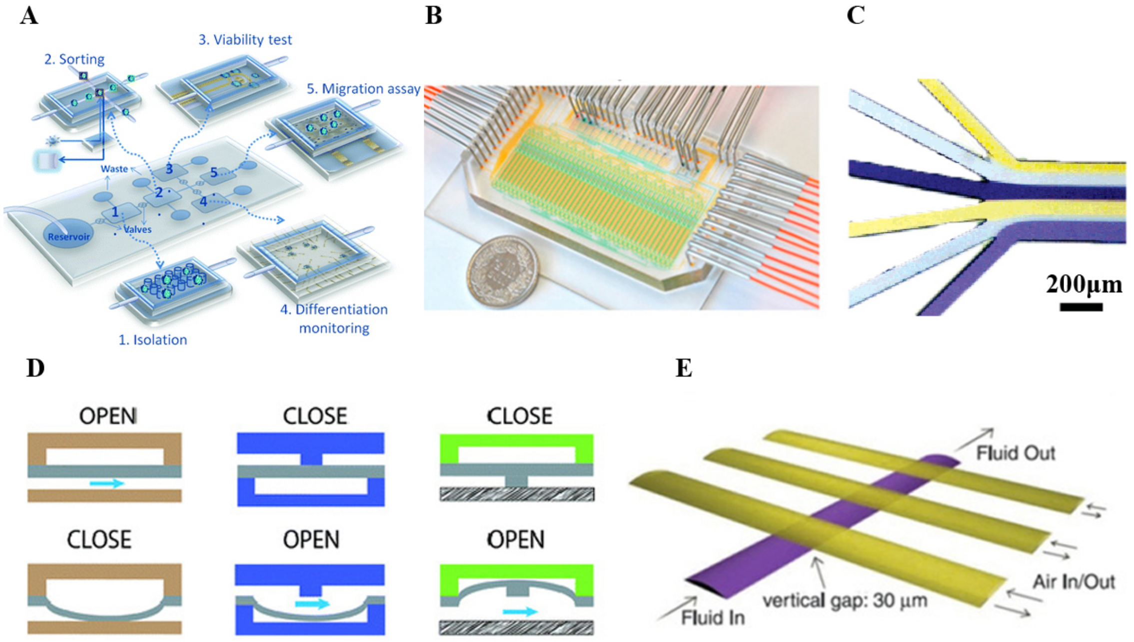

Figure 1.14: (A) Lab-on-a-chip: a microfluid chip with multiple modules to deal with cell isolation, sorting, viability test, differentiation, and migration monitoring [65]; (B) Microfluidic chip with multi-layers PDMS for studying the immune response of single cells [66]; (C) Laminar (non-turbulent) flow in microfluidic channels [67]; (D) Pneumatic microvalves for microfluidic chip to control fluid flow [68]; (E) Micropumping with three microvalves used to direct fluid flow by sequentially switching in a peristaltic pattern [69].Figure A,B,C and D are reprinted from ref[65] ©2013 Royal Society of Chemistry, ref [66] ©2016 Elsevier, ref [67] ©2005 American Chemical Society, ref [68] ©2016 Royal Society of Chemistry, ref [69] ©2016 MDPI.

1.4.1 Materials and components for microfluidics

PDMS (polydimethylsiloxane) is an elastomer widely used to manufacture microfluidic chips due to its easy fabrication, optical transparency, gas permeability, thermal stability and biocompatibility. The surface of PDMS can also be treated to be hydrophilic or hydrophobic for different application purposes. The flexibility of PDMS makes it able to be fabricated into microvalves and micropumps used for switching on/off of fluid flowing or driving flowing within the microchannels [69], **figure 1.14D-E**. Besides PDMS, other materials can also be used, like glass, paper, and thermoplastics. The fabrication of glass microchips is more complicated than PDMS, although PDMS is swelled or dissolved in most of organic organic solvents while [70, 71] glass can tolerate these solvents. Paper is considered as the ideal material for point-of-care microfluidics, such as in lateral flow microfluidics, owing to its low cost [70, 71].

1.4.2 Continuous microfluidics

According to the mode of fluids flowing within the microchannel, microfluidics can be generally classified as continuous flow microfluidics or droplet-based microfluidics.

One distinct feature of microfluidics is that the fluid flowing in micrometer dimension channels is laminar, i.e. non-turbulent, due to the small Reynolds number ($Re = \rho \mathrm{uL}/\mu$; where ρ is fluid density, u is velocity, μ is fluid viscosity, L is length).In these devices, *Re* is much less than 100 and usually less than 10, meaning that viscous forces within the fluid are much stronger than inertial forces. In continuous-flow systems, laminar flow patterns are readily observed as fluids flow in parallel in the same channel without mixing (**figure 1.14C**). Laminar flow can be used to deliver fluids to a specific area of the channel at high spatial resolution. This unique control was applied in gap junction studies since the fluid's pattern determined that a dye could be selectively transported to cells only in the middle of the channel, so the diffusion of dye to the cells close to the sides of channel occurred only through cell-to-cell communication [46].

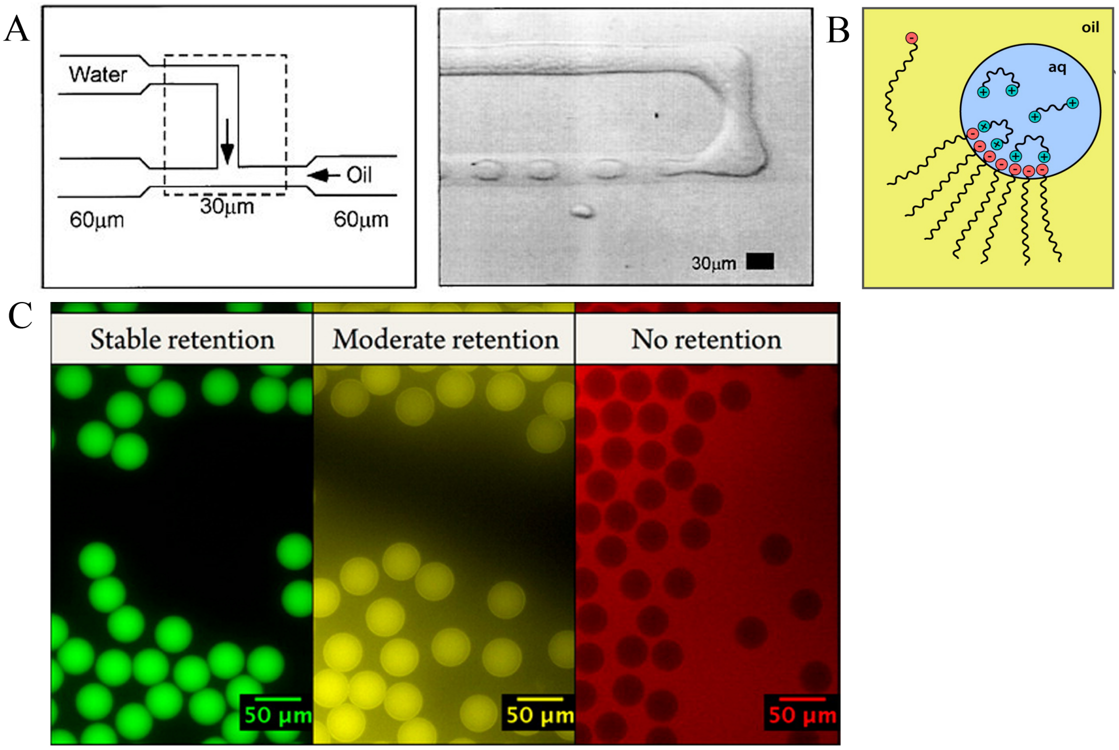

Figure 1.15: (A) The first microfluidic device for droplet formation [72]; (B) Water-in-oil droplets [75]; (C) The leaking of fluorogenic molecules from droplets into the oil phase [76]]. Figure A, B and C are reprinted from ref [72] ©2013 Royal Society of Chemistry, ref [75] ©2016 American Chemical Society, ref [76] ©2015 American Physical Society.

1.4.3 Droplet-based microfluidics

In the context of this work, microfluidic droplets refer effectively to highly controlled water-in-oil emulsion. These droplets, are small volumes of aqueous solution in oil (picoliters to nanoliters) that can be produced in a microfluidic chip by flowing aqueous liquids into another immiscible continuous medium such as oil (**figure1.15 A**) [72]. Different from emulsions in conventional tubes, droplets formed in microfluidic devices are highly uniform in size (between 10-200 μm) because of the precise control of solution volume in microfluidics [73]. Compared to continuous flow systems, droplet-based microfluidics can reach the goals of miniaturization of reactions as well as parallelization at same time since the tiny size of droplets can be formed very fast, at rates up to 8.4 MHz [74]. Droplet microfluidics has allowed breakthroughs in high-throughput screening with less usage of reagents and much lower cost. More technique details in droplet microfluidics will be presented below.

Droplet formation

Continuous phase and surfactant Water-in-oil droplet-based microfluidics can compartmentalize tiny amount of components and materials inside for reaction (**figure1.15 B**). Since each drop should be considered a separate container for its reaction, leaking of components will reduce the sensitivity of detection and perhaps give a false reading. It is therefore essential to produce stable droplets and avoid crosstalk between droplets and between droplets and the continuous phase (**figure 1.15 C**). At the same time, taking the application of droplets into consideration, the microenvironment in droplets needs to be biocompatible if it is for the capture and detection of biomolecules and/or biochemical reaction. In a word, it is highly important to choose the continuous phase along with another critical component for droplet formation, the surfactant.

Mineral oil and other hydrocarbon oils have been used as the continuous oil phase to form droplets in emulsions, but they are generally incompatible with PDMS because they can since they cause swelling of the PDMS devices; these oils can also cause unwanted extraction of organic reagents and some biological reagents from the aqueous phase into the oil. Several perfluorocarbon (PFCs) oils is proved to be biocompatible, more thermally and chemically stable, and having higher respiratory-gas solubility because the strong carbon-fluorine bond makes it hydrophobic and lipophobic. PFCs such as HFE7500 and FC-40 are widely exploited as carrier oils in droplet-based microfluidics today [77] to minimize the cross-contamination between droplets. **Figure 1.16 A** shows the chemical structure of HFE7500.

The surfactant is another very important component in droplet formation. Thermodynamically, droplets are prone to fuse each other and smaller ones tending toward becoming larger because two immiscible phases tend to generate an interface with the minimum of energy by coalescence (the aging of emulsion) and Ostwald ripening (small particles tend to dissolve into larger one in inhomogeneous solutions). To reduce the surface tension between droplets and the continuous carrier oil,a surfactant is used, which will increase the energy barrier for coalescence of two droplets and increase droplets stability. Since perfluorocarbon oil is chosen as the carrier oil, fluorosurfactants with perfluorocarbon tails will easily dissolve and stabilize well in

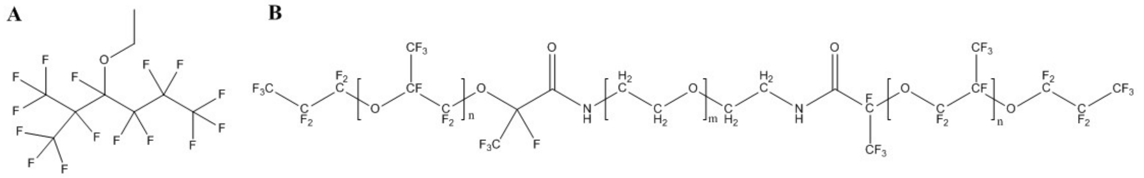

Figure 1.16: : (A) 3M$^{\text{TM}}$ Novec$^{\text{TM}}$ HEF7500 for carrier fluid; (B) PFPE-PEG- PFPE triblock-copolymer for surfactant [78].

the continuous phase. On the other hand, to keep the advantages of microfluidics for bioanalytical science, biocompatible surfactants are necessary. For this purpose, a non-ionic surfactant with polyethylene glycol (PEG) as a head group and perfluorinated polyethers (PFPE) as the tail was synthesized by Professor Weitzs group (**figure 1.16B**) [78], and is now commercially available (as Pico-Surf$^{\text{TM}}$) due to its superiority in the field. The non-ionic head points toward inside of water-in-oil droplet, which will form an inert interface to charged biomolecules like proteins, DNA and RNA to avoid non-specific adsorption of these molecules on the interface. Therefore, many biological assays and biochemical reactions can now be carried out in droplet microfluidic systems. In droplet formation, triblock surfactants with mediate molecular weight will diffuse faster, which will be a better choice for droplet generation at high rate. But for the droplet reinjection into channel, the large-molecule surfactants will help stabilize the droplets under shear stress of flowing [78].

Fluorocarbon oils and PFPE surfactants are carefully chosen to solve the issues of the droplet stability, but there is still one more issue that needs solving, namingly the leaking problem of hydrophobic organic molecules between droplets. These molecules may barely dissolve in fluorinated oil, but the surfactants can help increase these molecules' solubility [79, 80]. Since the higher retention of hydrophilic molecules in water-in-oil droplet, the fluorophores for assays can be modified to be more hydrophilic to increase the retention, for example, fluorescein (FAM) attached with peptide, the glycosylated coumarin or oligonucleotides attached to enzyme [74]. This problem can also be solved by using biopolymers as additive such as carboxymethyl cellulose (CMC), BSA (bovine serum albumin), sucrose and dextran [81]. Prof. Hollfelders group has reported that with the increase of surfactant amount, the partition of 3-*O*-methylfluorescein into oil phase was raised after 7 h incubation. But if 5% BSA was added into the aqueous solution with 0.75% (w/w) surfactant Abil EM 90, the retention of the fluorescein, from the hydrolysis of fluorescein diphosphate (FDP) by enzyme expressed by E. coli cells, can be conserved even after 20h incubation in droplets [79]. Later, Prof. Baret group has proven that BSA can increase the solubility of biomolecules in oil phase to reduce the crosstalk in thermodynamic way instead of the kinetic barrier formation in the interface [82].

Passive control and active control for droplet generation There are three types of microdevices commonly used for passive droplet generation. T-junction, also called cross-flow, was introduced by the Quake group [72] and is widely used due to its simplicity and capability of forming highly monodisperse droplets at a rate up to 7.4 kHz with less than 2% coefficient of variation (CV) [83, 84]. The T-junction has been modified to other formats by changing the angle of two channels between the dispersed and continuous phase (**figure 1.17A. ii-iv**) or adding more channels for different aqueous solutions (v, vi, vii.-K-junction and viii.-V-junction) [85]. Another commonly exploited format is flow-focusing (**figure 1.17C**). Hydrodynamic focusing is applied in the simple cross channels to chop the aqueous jet into droplets at a high speed of tens of kHz (**figure 1.17C**). The third type of geometry is co-flow, where the two immiscible fluids encounter in parallel streams (**figure 1.17B**). The droplet generation rate for co-flow chip can be close to flow-focusing. Fewer examples are available for active control of droplet formation. The Niu group has reported forming droplets by a miniature peristaltic pump (**figure 1.17D**) [86]. The Zeng group has used normally closed valves to actively control droplet formation parameters on-chip [87], and Prof. Easley's lab has used the Quake-style, normally closed-valves on-chip as controls to produce the droplets [88], which will be further discussed in Chapter4.

Droplet manipulation: merging, storage, detection, sorting Since droplets are usually generated in a large amount at a very high speed, methods to sort and categorize them in microchannels should be developed to utilize them as micro-containers for biochemical and biological reactions. To deal with the extremely large number of droplets, integrated and automatic methods are needed to manipulate them. The manipulation of droplets usually includes mixing, merging, splitting, on-chip and off-chip incubation, storage, reinjection, droplet detection, and sorting (**figure 1.18**). While traveling through the microchannel, a convective vortex

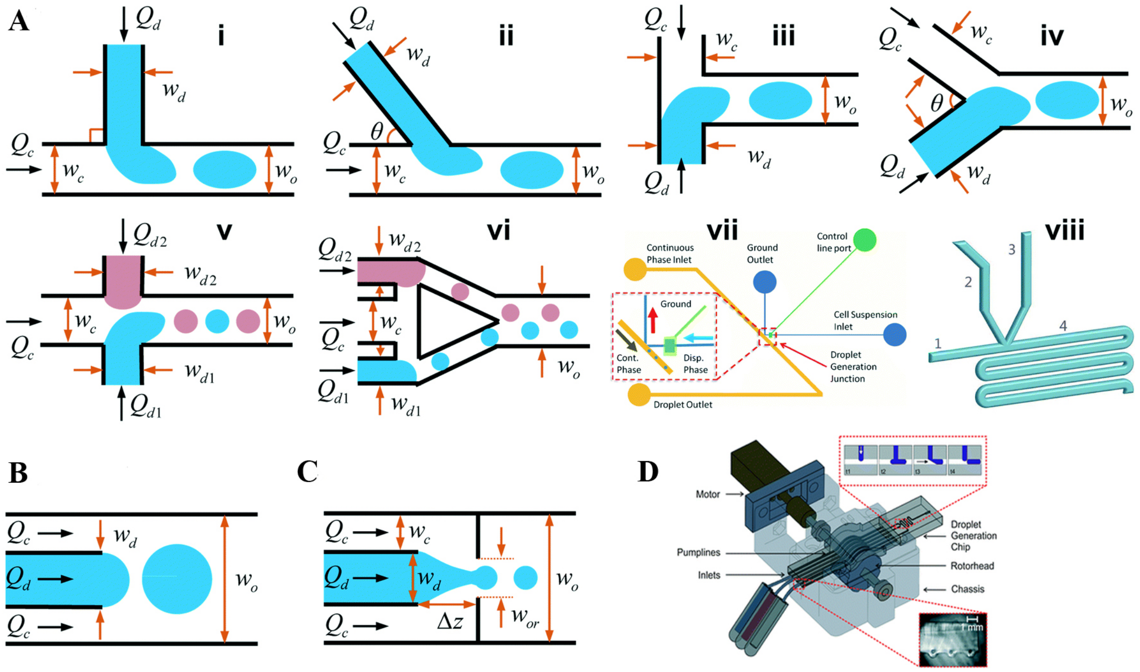

Figure 1.17: Droplet formation by different channel geometries. (A) T-junction channel. (B) Co-flow channel. (C) Flow-focusing channel [85]. (D) Peristaltic pumping for droplet formation [86].Figure A, B and C are reprinted with permission from ref [85] ©2016 Royal Society of Chemistry. Figure D is reprinted with permission from ref [86] ©2017 Royal Society of Chemistry.

will be produced in the droplet, which brings the effective mixing of the components in the droplets. A short zigzag channel will make the mixing more efficient because the droplets will be stretched and folded repeatedly (**figure 1.18b**) [89]. Droplet merging or fusing is commonly introduced by electric fields (**figure 1.18c**). The Abate group has reported the use of salt water electrode to generate high enough electric field on chip for droplet merging [90] and the method is widely used now. The electrocoalescence of droplets is due to the destabilization of the oil film in the interface between two water-in-oil droplets [91]. A similar dielectrophoretic force can also be used in droplet sorting (**figure 1.18g**), where the droplets are deflected by electric field and guided into the specific channel [92]. Droplet sorting can also be operated under the control of surface acoustic wave (SAW) or magnetic field, and pneumatic valves [93]. The methods of fluorescence -activated dielectrophoresis [94, 92] and size-based sorting based on hydrodynamics [95] have been applied for droplet detection and sorting.

Long channels are generally good enough for short-term incubation (**figure 1.18d**). For long incubation, the droplet emulsion cream needed to be produced to store more droplets (**figure 1.18e**). The Paegel group has reported a microchip designs to dissipate the continuous oil to pack droplets to form the emulsion creamer [96]. For longer and larger amount of storage, standard laboratory tubes are a better choice (**figure 1.18j**). Other operations like reinjection are shown in the figure (**figure 1.18h** and **i**). These technologies provide researchers more flexibility to establish an integrated and automatic device for a variety of different applications.Indeed, our work reported in later chapters leverages on-chip valve-based control, droplet formation at T-junctions, zigzag mixers, on-chip incubation, and optical detection.

Applications of droplet-based microlfuidics

Droplets are being applied more and more in biotechnology. The small vessels with pico- to nano-liter volume are ideal microreactors for single cells, genes, and molecules. The automatic and high-speed formation and sorting also drive the droplet applications inyo high-throughput screening [91].

Leveraging encapsulation in droplets Droplets can encapsulate many types of molecules and materials inside. The microfluidic system is able to control the microenvironment in the compartments to mimic the cell function; for example, a synthetic cell was generated via bottom-to-up sequential assemble [98]. Such custom vessels should be ideal for creating *in-vitro* models of cell [73]. On the other hand, microfluidic droplets are excellent reactors for small-size and high-throughput tests because of their small volume (0.5 pL -tens of nL) and large-amount production [97]. Furthermore, rapid mixing by chaotic advection and no dispersion when they travel through the network of channels. Many types of biological and biochemical reaction can be miniaturized in droplets (**figure 1.19**). Droplet-based microfluidic systems can control reaction time tightly, even being used to study enzyme kinetics at the low millisecond time scale[89, 99]. Biological DNA assays based on the FRET and biotin-streptavidin binding have also been exploited within picoliter droplets [100]. Another attractive application of droplets is compartmentalization of single DNA or RNA molecule followed by a PCR amplification reaction, thereby allowing single copies of DNA or RNA to be detected in the droplets [101]. Both of prokaryotic and eukaryotic cells can be encapsulated and grow in the droplets. Due to the small size, large amounts of each individual droplet can be controlled to trap single cell or bacteria for later analysis.

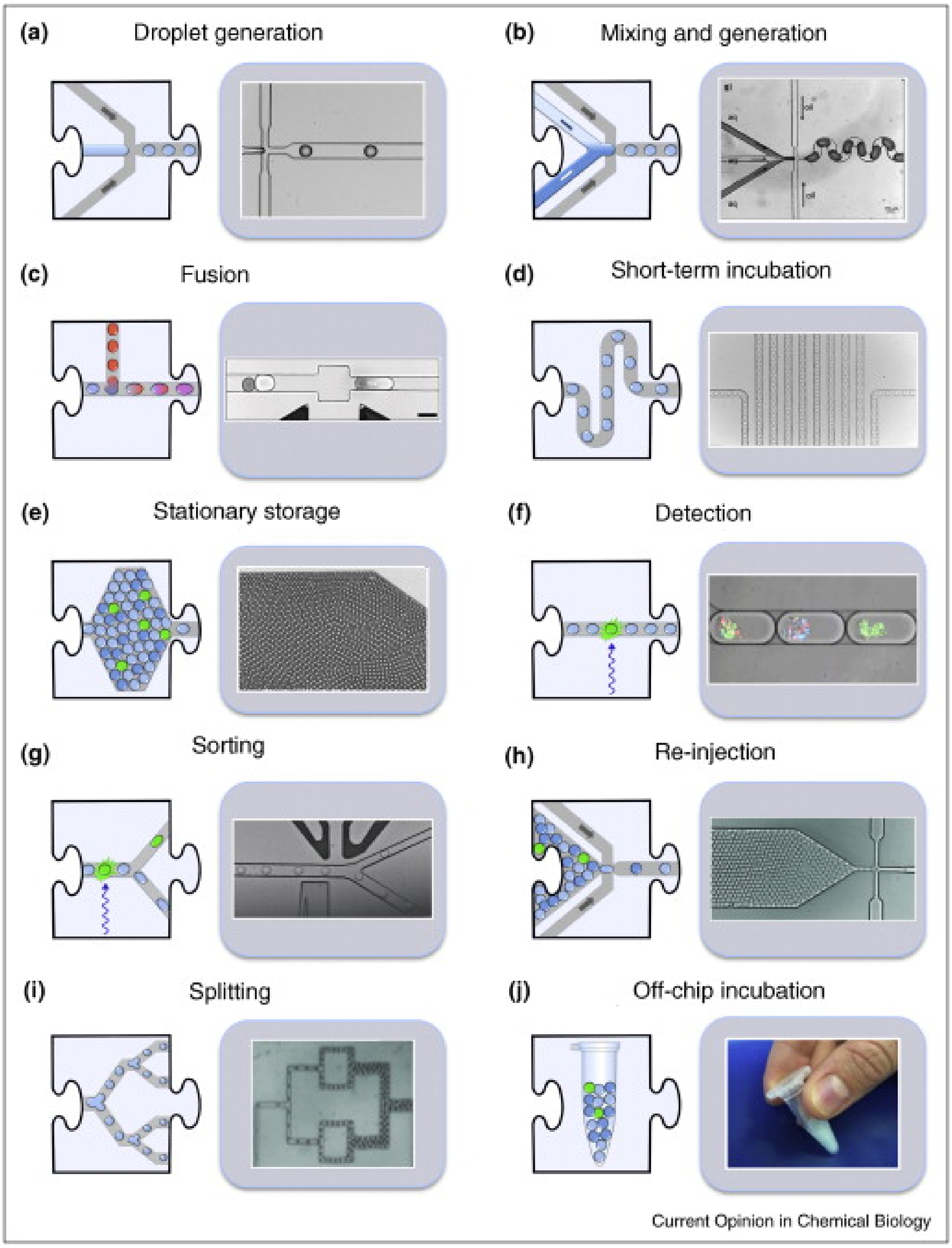

Figure 1.18: Droplet manipulation.The figure is reprinted with permission from ref [97] ©2017 Elsevier Ltd.

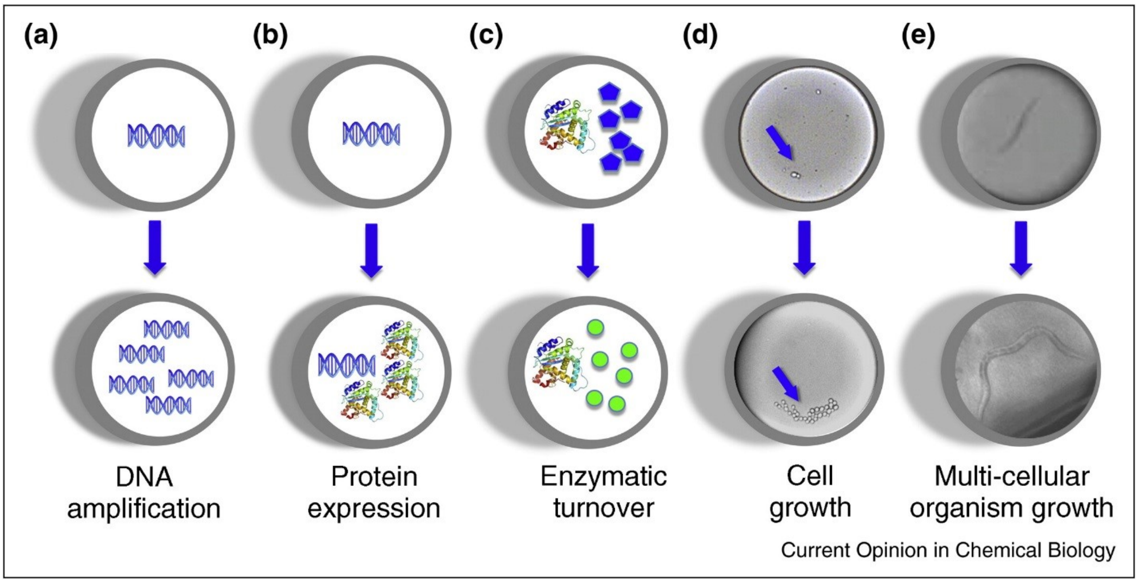

Figure 1.19: Biological reactions in the droplets.The figure is reprinted with permission from ref [97] ©2017 Elsevier Ltd.

With its unique benefits, droplet microfluidics is now a powerful tool for drug screening [102], enzyme mutant screening [103], vaccine candidate screening by single-virus assays [104] and from hybridoma cells [105, 106], and bacteria or yeast variant screening [107].

Single cell analysis Traditional bioanalysis for cell biology operates in bulk measurements of many cells, exhibiting large variation in phenotype and obscuring cell heterogeneity, which is essential to tissue function. In recent years, one of the most attractive application of droplet-based microfluidics is single cell manipulation. For example, single bacterial cell trapped in picoliter droplet were grown for antibiotic resistance test [108]. The fastest development, however, is happened in the genomic, transcriptomic and epigenomic analyses of single cells in droplets. Combining the single-cell droplet techniques, barcode methods and NGS, the Weitz lab developed a droplet barcoding chip, named inDrop (indexing droplets), to study the heterogeneity of cell population in their transcriptomics (**figure 1.20A**) [109]. Their group and others also reported another similar technique, called Drop-seq, to study the transcriptional profile of cells from tissues using microparticles instead of hydrogel to deliver primers for library preparation [110] (**figure 1.20B**). Later, these single-cell RNA sequencing techniques have been successfully applied to study the CRISPR-mediated perturbation in single cells [111, 112].

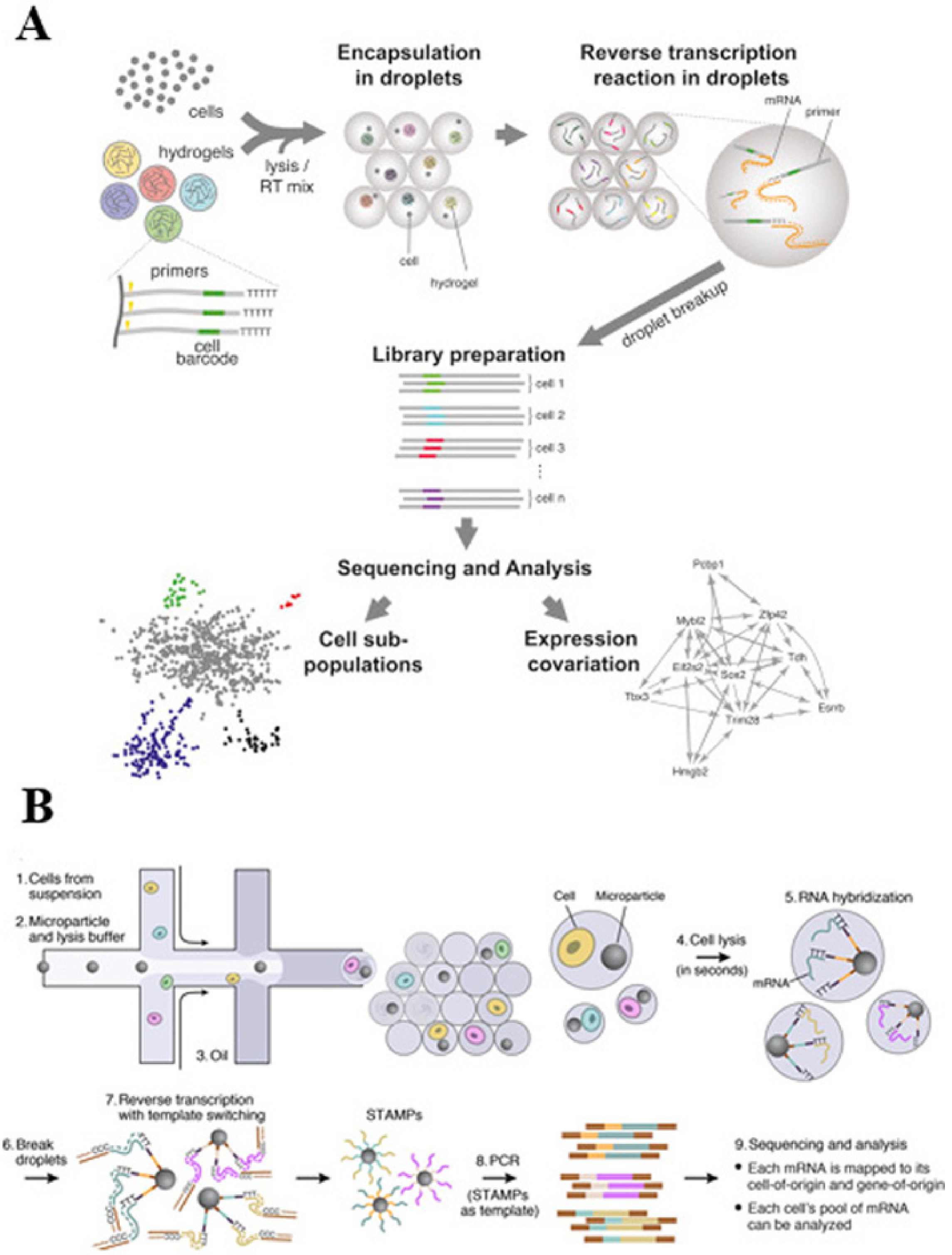

Figure 1.20: Single cell analysis in droplets.(A) inDrop for single-cell transcriptomic analysis; (B) Drop-seq for mRNA sequencing to study cell population.Figure A and B are reprinted with permission from ref [109] ©2015 Elsevier Ltd, and ref [110] ©2015 Elsevier Ltd.

Until now, droplet microfluidics has shown its strengths in digital analysis ("yes" or "no" answers), for simplified detection at high speed. But droplets should also be able to be applied in analog analyses after calibration of on-chip assay, and better sensitivity and precision of the assay should be achieved since the precise control of solution volume and hundreds or thousands or more of reactions can be repeated by only using a tiny amount of reagents. Statistically, the large sample number can help to reduce the standard error of measurements to enhance the precision of assay, and our group has developed novel analytical modes using droplets phase-locked to the detection methods [113, 114, 115]. Therefore, droplets can become a potentially powerful tool for biomolecules quantification and dynamic studies of their secretion. However, to achieve this goal, we need to choose existing assays or develop suitable assays for biomolecule detection that are compatible with microfluidic volume scales (nanoliter range). If possible, a homogeneous assay format (mix-and-read) is a good choice for assay miniaturization due to its simple workflow and the potential for direct optical readout. Below, in the final main section of the chapter, I discuss homogeneous assays in more detail and focus on the assays relevant to our research.

1.5 Homogeneous immunoassays

1.5.1 Heterogeneous versus homogeneous immunoassays

In disease diagnostics and development of therapeutic methods, cytokine and metabolite detection and quantification with high sensitivity and specificity are keys. The changes of cytokines functions are not only biomarkers of many diseases, but also the guidance for treatment efficacy. Bioanalytical assay development toward proteins and other bioactive molecules can facilitate the advancement of diseases diagnostics and therapeutics.

According to the workflow, assays can be classified into two main types–heterogeneous or homogeneous (**figure 1.21A**). In immunoassays, the enzyme-linked immunosorbent assay (ELISA) is the gold standard of protein detection, which is a typical heterogeneous immunoassay. Traditional sandwich-ELISA is proceeded in microtiter plates (usually in 96-well plate), where primary antibodies are immobilized on the bottom of each well and can capture target molecules after incubation with the sample, followed by washing step that remove the nonbinding agents, and finally an added secondary antibody is conjugated with enzymes to catalyze a reaction to produce many chromophores for optical detection. The reactions in ELISA are sequential and a washing step is always needed after each reagent is added, which makes ELISA time-consuming. The limit of detection (LOD) of ELISA can be about sub-picomolar, but the cost of the assay is high and the 96-well plate setting limits the operational flexibility. To reduce the volume of assay solution and increase the sensitivity further, digital ELISA was developed and commercialized (**figure 1.21B**). Digital ELISA integrates a microwell array with bead-based ELISA to detect single protein, and the absolute target molecule number can be calculated based on the digital output because the excessive amount of beads are applied to capture the targets in the sample and the beads are loaded into microwells and each well will contain only one bead to ensure one-bead-one-molecule and one-well-one-bead [116]. Digital ELISA has limit of detection down to zeptomolar range[117], but similarly, the instrument and assay kit costs make it more suitable for routine, high-volume diagnostics in clinics instead of biological research laboratories. Furthermore, these assays are less appropriate in microfluidics due to the need for miniaturization of every step in the multi-step assay procedure.

Homogeneous immunoassays are assays following a mix-and-read workflow without washing steps. Examples, including the amplified luminescent proximity homogeneous immunoassay (ALPHA) (**figure 1.21C**), homogeneous time-resolved fluorescence (HTRF) (**figure 1.21D**), Luminex® xMAP® technology (**figure 1.21E**) and DNA-based homogeneous immunoassays such as molecular pincer assay, proximity ligation assay (PLA) (**figure 1.21F**) and proximity extension assay (PEA). DNA-based homogeneous assays will be discussed in more detail in the next section. ALPHA is an assay based on the singlet oxygen channeling from photosensitizer molecule to the proximal molecule which can react with singlet oxygen to produce chemiluminescent signal [118, 119]. The two molecules, conjugated on the probes, become close enough to allow the reaction to happen by binding the probes to the target. HTRF is also based on the proximity effect after binding to target, but time-resolved fluorophores are used instead of singlet oxygen. **Figure 1.21 D** displays that the assay can be competitive or non-competitive. In non-competitive assay format, probe pair are chosen to recognize the target to bring the donor and acceptor in proximity, while the competitive methodology utilizes the labeled target which give FRET signal and lose the signal after the labeled target is replaced by regular target molecule. xMAP is the assay where magnetic beads or polystyrene beads with fluorogenic molecule inside are used to immobilize the capture antibody for target recognition and detection antibody bound to target to get the donor and acceptor close enough for FRET. ALPHA, HTRF and Luminex® xMAP® assays are characteristic of simple mix-and-read manipulation but the assays are time consuming (> 2, 3, 6 hours, respectively) and the cost of these assays is still high because special labelling or beads are required.

1.5.2 Proximity effect and DNA-based homogeneous immunoassay

Binding of two probes to one target drives the distance between the two probes to become shorter. If the probes are labeled, these labels are brought into proximity and can exhibit enhanced reactivity toward each other. This is called the “proximity effect”, since the kinetics of such reactions are determined by the distance between reactant molecules. It is known that the intramolecular reactions can be much faster than intermolecular reactions by as much as 200,000 fold, which is the mechanism of some type of catalysts for many organic reactions. The proximity effect is also the foundation of the DNA-based homogeneous assays used in our work.The target molecule in these homogeneous immunoassays is functioning essentially as the “catalyst” to hold the two ”reactants” (labels on probes) close together to increase the rate of their interaction.

In DNA-based proximity assays, each affinity probe (antibody or aptamer) is conjugated with an extra DNA oligonucleotide. The ends of the two oligos on a pair of probes are designed to be complementary and able to form a weakly bound DNA duplex. When a pair of probes are assembled on one target molecule, the tails of DNA will become close together, and the rate of hybridization will be enhanced. By this way, the protein quantification is translated into DNA hybridization. A advantage of this assay format are that the DNA duplex stability can be under good control by adjusting the number of base pairs in the duplex, and DNA hybridization is able to be read out in many formats and even amplified by the polymerase chain reaction (PCR). The proximity effect for DNA-based assays is well explained by Prof. Chris Le, in

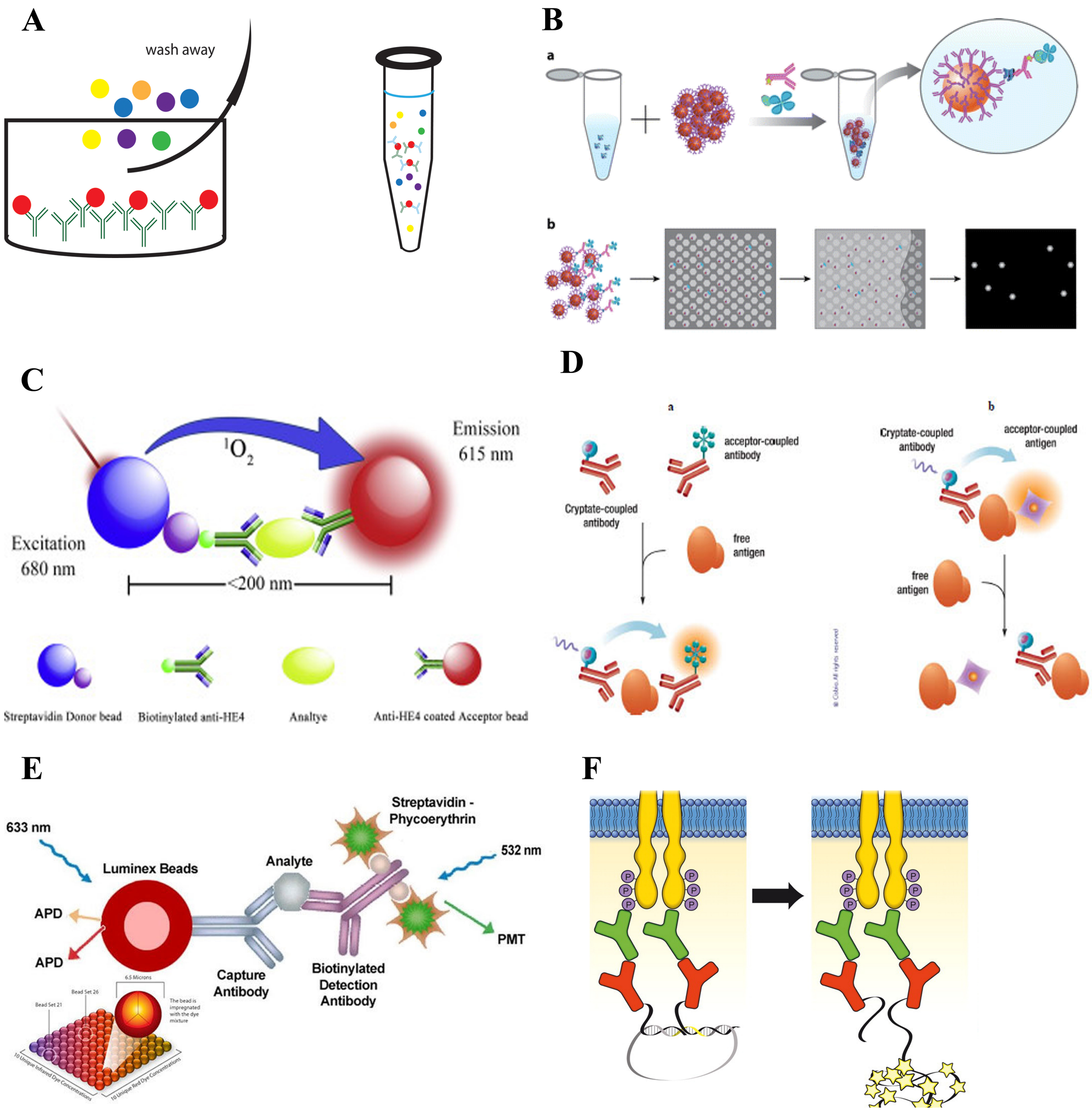

Figure 1.21: Immunoassay types.(A) heterogeneous immunoassay and homogeneous immunoassay; (B) digital ELISA [117]; (C) ALPHA based on singlet oxygen transfer [120]; (D) HTRF signal on (antibody pair recognition) and signal off assay (competitive assay) [121]; (E) Luminex® xMAP®, Luminex beads can be screened by fluorescence-activated cell sorting (FACS)[122]; (F) *In situ* proximity ligation assay for phosphorylated protein detection [123].Figure B, C, D, E and F are reprinted with permission from ref [117] ©2017 Annual Reviews, ref [120] ©2016 Elsevier B.V., ref [121] ©2016 Bentham Science Publishers, ref [122] ©2018 Springer Nature, and ref [123] ©2015 American Society for Biochemistry and Molecular Biology.

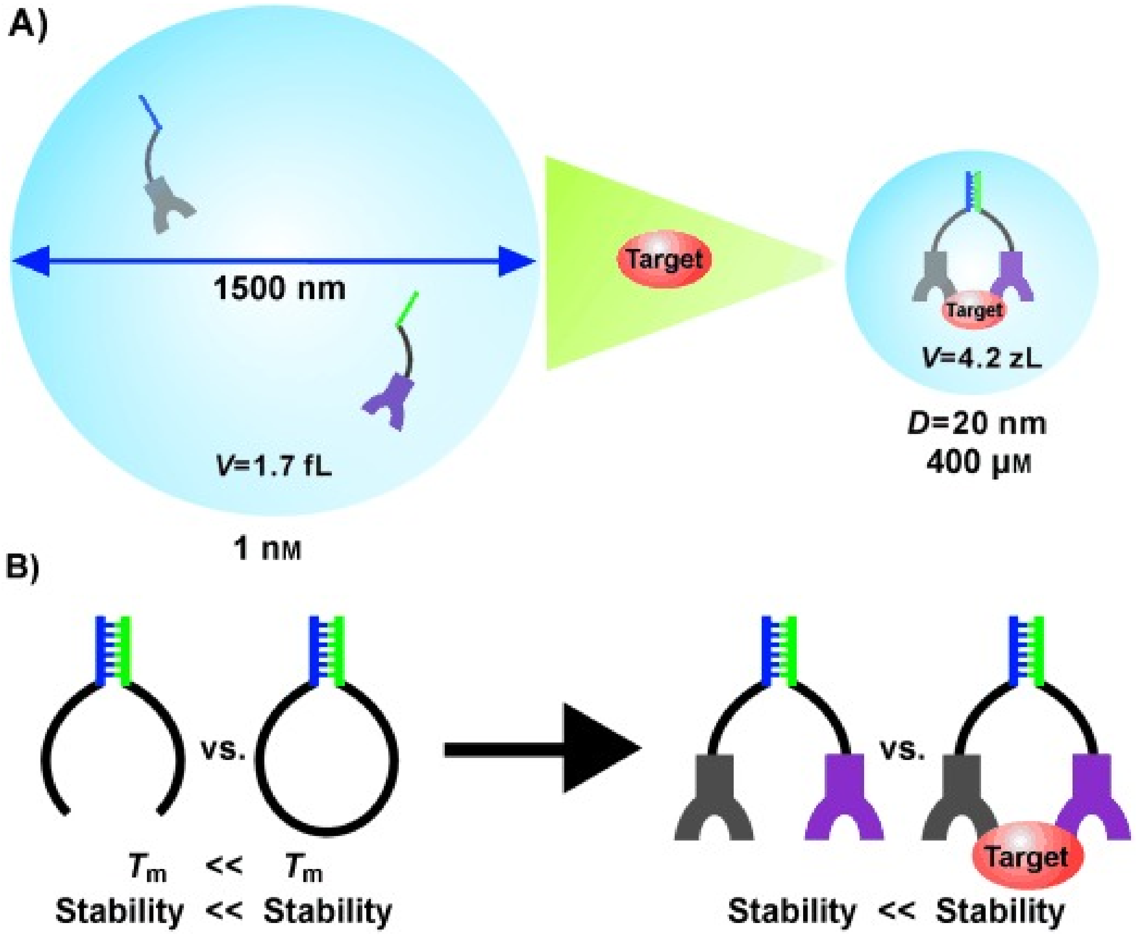

Figure 1.22: Immunoassay types.(A) Proximity effect: binding of the two probes to target can increase the tailed DNA local concentration from 1nM to 400 μM. (B) After the target-dependent complex is formed, the tailed DNA duplex become more stable than the complex without the target binding, which is similar to that the DNA duplex in hairpin structure possesses higher stability than the hybridization of two strands of DNA with same number of base pair [124].The figure is reprinted with permission from ref [124] ©2013 John Wiley and Sons.

figure1.22.As noted earlier, DNA-based proximity assays are well-suited for integration into microfluidic systems [114], since integrating a mix-and-read workflow on-chip is significantly simpler than designing chips for a multistep workflow.

Based on the methods for readout, there are three main types of DNA-driven proximity assays. The molecular pincer assay developed by the Heyduk lab utilizes optical readout for protein quantification, where the DNA assembly brings the donor and acceptor labels into close proximity to allow FRET (**figure 1.23A**). The electrochemical proximity assay (ECPA), invented by the Easley and Shannon group at Auburn University, employs the electrochemical signal as direct readout to quantify as low as femtomolar target concentration (**figure 1.23B**).

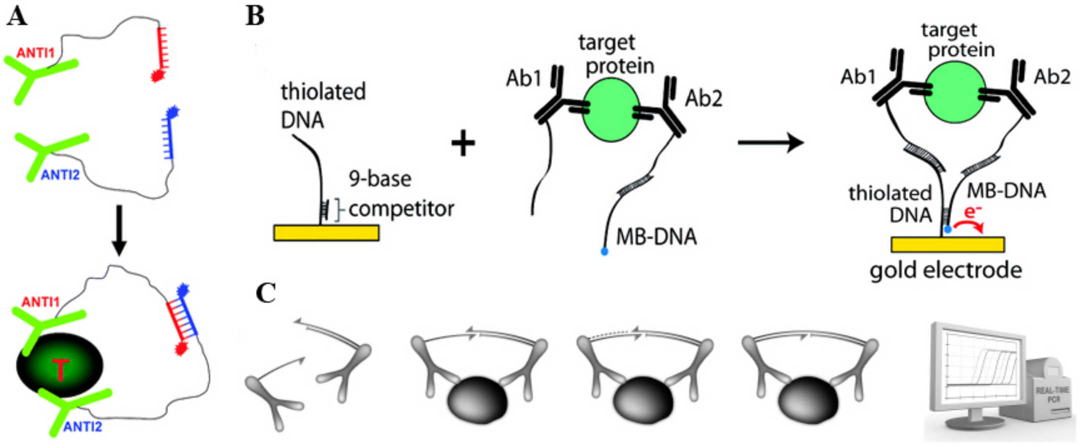

Figure 1.23: DNA-based proximity assys.(A) Molecular pincer assay based on the fluorescence resonance energy transfer [127]; (B) Electrochemical proximity assay (ECPA) based on the electrochemical readout [128, 129]; (C) Proximity extension assay (PEA) by qPCR (quantitative PCR) measurement [130].Figure A, B, and C are reprinted with permission from ref [127] ©2008 American Chemical Society, ref [128] ©2012 American Chemical Society, and ref [130] ©2011 Oxford University Press.

Another type of DAN driven assay is proximity ligation assay (PLA) [125] and proximity extension assay (**figure 1.23C**). Both assays were developed by make use of quantitative PCR to amplify the DNA and increase the detection sensitivity. Due to the amplified signal, PLA can detect zeptomoles of targets and can be multiplexed based on different DNA sequences for readout[126].

1.5.3 Affinity ligands and aptamer SELEX

One critical component in homogeneous immunoassays is the affinity probe pair. Until now, most of the assays are based on the antibody-oligo conjugated products. Antibodies can recognize and bind to antigens with high affinity and specificity, and the methodology of antibody production is well-developed and commercialized. The antibody, especially the monoclonal antibody holds very important functions in biological research and disease diagnosis, and therapy. However, the antibody production is carried out *in vivo* and requires immortalized hybridoma cell lines, which keeps the antibody production at high cost.

Another important type of affinity ligand is the aptamer. Aptamer is single-stranded of DNA or RNA probe, screened from library pools with 10^{12}-10^{13} diversities, that binds to target selectively as an antibody. Compared to antibodies, aptamer screening is proceeded in vitro by systematic evolution of ligands by exponential enrichment (SELEX) [131, 132]. Since it is generated in tubes, targets of aptamer can be immunogenic or non-immunogenic and it should be able to bind to any type of molecule. After selection, aptamers are usually produced by chemical synthesis, so the variation between batches is small and fluorophores or other modified functional groups are easily labeled onto the aptamer. Particularly for proximity assays, the cost of aptamer generation and labeling is much lower than labeled antibodies, since antibody-oilgo bioconjugation reactions are tedious and exhibit low yield. Another advantage of aptamers is that their structure changing can be induced by target, which makes it possible to enrich aptamer for unknown targets for biomarker discovery. However, because the natural structure of aptamers is less diverse and the SELEX methods of paired aptamers is unmet, the number of aptamer pairs is limited, and fewer aptamers are currently applied in biological research. If these limitations are overcome, aptamers will become more ideal affinity probes than antibodies, especially for DNA-driven, proximity based homogeneous assays.

1.5.4 Challenges with homogeneous immunoassays

Homogeneous immunoassays, especially fluorescence-based, enable simple mix-and-read workflow, low cost, and rapid readout. However, without the washing step and amplification of signal, the application of homogeneous assay can be limited by low signal-to-noise (S/N) ratio, especially in complicated biological matrices like cell lysates, serum, or plasma. One main reason for this is that the strong autofluorescence in the samples will interfere the fluorescence readout. To solve this problem conventionally, the sample should be diluted by tens to hundreds of times to eliminate the interference. However, the concentration of target molecules is also reduced largely at the same time, and will normally be out of the assay detection range. Another limitation is the low abundance of most protein targets, around or below the picomolar range in biological samples. Without amplification, targets with such low concentration will be undetectable in large-volumes of assay solution. Therefore, to make the homogenous immunoassay feasible in most of biological researches, we need overcome the drawback of low S/N ratio. To effectively eliminate the background, it must be discriminate form signal,and novel methods to do will be discussed more in the Chapter 2. To address the issue of low concentration of targets, one option is to decrease the assay's solution volume, as done with digital ELISA. In my dissertation work, microfluidics was used to enhance assay performance by increasing signal (limited dilution), and lock-in detection methods on-chip [113, 114, 115] permitted reduced noise. As discussed in the chapters that follow, we applied both droplet microfluidics and homogeneous immunoassays to investigate biomolecules secretion dynamics from pancreatic and adipose tissues. As predicted, doing so has enabled unique observations concerning the dynamics of adipose tissue function involving hormone secretion and lipolysis.

Chapter 2

DNA-driven homogeneous immunoassay based on proximity-induced fluorescence resonance energy transfer (FRET)

This chapter is recovered from publications: Joonyul Kim, Juan Hu, Andresa B.Bezerra, Mark D. Holtan, Jessica C. Brooks, and Christopher J. Easley. Protein quantification using controlled DNA melting transitions in bivalent probe assemblies. *Anal. Chem.* 2015, 87, 9576-9579; Juan Hu and Christopher J. Easley. Homogeneous assays of second messenger signaling and hormone secreting using thermofluorimetric methods that minimize calibration burden. *Anal. Chem.* 2017, 89 (16), 8517-8523.

2.1 Introduction

As mentioned in Chapter1, compared to heterogeneous assays, homogeneous protein assay is an archetypal assay platform which gives both simplicity and scalability on an assay. Since a common ambition of bioanalytical scientists is to simplify workflows by limiting user interaction and providing rapid sample-to-answer time, homogeneous assay formats have become increasingly desirable. However, these formats often suffer from the inability to discriminate target-dependent signal from target-independent background. Additionally, one common type of noise in the assay is the autofluorescence of complex matrices such as serum. To avoid the autofluorescence in biological samples, a used output is either a time-resolved fluorescence [133] or a chemiluminescence [118], which both require complex optics and special reagents, which increases costs and reduces the probability of use in the average research laboratory. One promising approach is to modify recently developed DNA-driven protein [128, 129, 125, 127, 134, 135, 130, 136, 124] and small-molecule assays [137, 138] toward readout on a single instrument.

In this chapter, it is shown that antibody-oligonucleotide [135] or aptamer [135, 136] probes can be interrogated by thermofluorimetric analysis (TFA) to permit facile discrimination of signal and background in DNA hybridization driven assays. Signal complexes consisting of probe-bound protein targets can be analytically separated from background complexes (probes only, no target) using DNA melting analysis. Thereby, protein quantities can be effectively translated into DNA melting transitions due to the thermodynamic stability imparted by target binding. In addition, other noises like autofluorescence will not change with temperature and can be automatically excluded. As a result, this differential approach permits rejection of background fluorescence interferences in matrices such as human serum or cell lysates.

Thermofluorimetric analysis (TFA) is further explored that by using a standard qPCR instrument TFA can be adapted to analyze two types of molecules of high importance to cell signaling studies: hormones and second-messengers. Previously developed DNA-driven assays for cyclic adenosine monophosphate (cAMP)[138] and insulin [127, 134] are shown to exhibit improved performance when adapted to our TFA readout methodology [135, 136]. Both cAMP and insulin can be quantified from single pancreatic islets under various treatments and in a temporally resolved manner. Furthermore, an unexpected benefit of TFA was discovered. Presumably due to the direct-readout mechanism (non-amplified) and the corrective differential analysis, signal magnitudesand thus calibration curveswere highly repeatable over a period as long as 7 months. Overall, this approach simplifies quantitative readout of proteins and small molecules to a single instrument that can also be used for DNA and RNA analyses, it provides a homogeneous mix-and-read workflow, and it minimizes calibration burden in cell signaling studies.

2.2 Experimental design

2.2.1 Reagents and Instrument

Bridge-It® Cyclic AMP (cAMP) all in one Assay Kits and Human Insulin FRET-PINCER Assay Kits were purchased from Mediomics, LLC (St. Louis, MO). Rat / Mouse Insulin ELISA kits (EZRMI-13K), Human Insulin solution, and bovine serum albumin (BSA) were all obtained from Millipore Sigma. Heat inactivated HyClone^{TM} Fetal Bovine Serum (FBS) was from Gel Healthcare Life Sciences. The human insulin concentration was confirmed by protein absorbance at 280 nm (A_{280}) using a NanoDrop 1000 spectrophotometer (Thermo Fisher). Hanks' Balanced Salt Solution (HBSS) was purchased from Lonza. D-glucose, HEPES (4-2-hydroxyethyl-1-piperazineethanesulfonicacid), penicillin-streptomycin, NaCl, $CaCl_2 \cdot 2H_2O$, KCl, and $MgCl_2 \cdot 6H_2O$ were purchased from Sigma-Aldrich (St. Louis, Missouri). Roswell Park Memorial Institute (RMPI) 1640, 1X with L-glutamine/ without glucose is from the Corning cellgro (MT-10043CV). Collagenase P was from Roche. Glucose-responsive insulinotropic peptide (GIP) was obtained from Bachem Americas (Torrance, CA). Forskolin ($>$95.0%, HPLC) was purchased from TCI America. The real-time quantitative PCR (qPCR) instrument used in all experiments was a Bio-Rad CFX96. Binding buffer is 50 mM Tris-HCl, pH 7.5, 100 mM NaCl, 1 mM $MgCl_2$ with 1% BSA. The sequences of thrombin aptamers are as below. Thr1_BHQ1:5'CAG TCC GTG GTA GGG CAG GTT GGG GTG ACT TTT ACT TTC TGC ACG ACA CTT TGG AAC AGC /3IABkFQ/; Thr2_TAMRA: /55-TAMK/ AAT AAC GTC AGA ATC GTA CTC GGG TGT GAC TAC TGG TTG GTG AGG TTG GGT AGT CAC AAA; connector: C7-12 - CGT TAT TGC TGT TCC AAA G; C8-12- ACG TTA TTG CTG TTC CAA AG; C9-12- GAC GTT ATT GCT GTT CCA AAG. Insulin antibodies (clones 3A6 and 8E2; Fitzgerald Industries). The sequences of insulin TFA are as below. AbA_BHQ2: /5AmMC6//iSp18/TCG TGG AAC TAT CTA GCG GTG TAC GTG AGT GGG CAT GTA GCA AGA GG/3BHQ_2/; AbB_TYE665: /5TYE665/GTC ATC ATT CGA ATC GTA CTG CAA TCG GGT ATT AGG CTA /iSp18//3AmMC6T/; connector: C'7-10: T GAT GAC CCT CTT GCT A; C'8-10: AT GAT GAC CCT CTT GCT A; C'10-10: G AAT GAT GAC CCT CTT GCT A. All DNA sequences used are purchased from IDT. Antibody-oligonucleotide conjugates were prepared as described in previous publications from Prof. Easley's lab[128, 129] by covalent attachment of AbA_BHQ1 to insulin antibody 3A6 (probe: 3A6_BHQ1) and AbB_TYE665 to insulin antibody 8E2 (probe: 8E2_ TYE665), respectively. Conjugation and purification were accomplished using the Antibody-Oligonucleotide All-In-One Conjugation

Kit (Solulink), according to the manufacturers instructions. The final conjugate concentrations were determined via the BCA protein assay.

2.2.2 TFA of thrombin assay and TFA of insulin assay 1

The concentration of each TFA component in total 20 μL of assay buffer is as below; 50 nM of a pair of thrombin aptamers and 70 nM of DNA connector for thrombin TFA and 6.3 nM of a pair of insulin antibody-oligonucleotide conjugates and 18.9 nM of DNA connector for insulin TFA. 5 μL of sample was used in both TFAs. The assay mixture was preincubated at 4 ^{o}C for 10 min before starting thermal scanning. Fluorescence, either TAMRA for thrombin TFA or TYE665 for insulin TFA 1, was measured at the end of 15 sec waiting time after reaching to the targeted temperature. The range of temperature scanned was from 4 ^{o}C to 65 ^{o}C with 0.5 ^{o}C interval. Isothermal proximity assay (IPA) was performed at 22 ^{o}C with same reaction mixture used in TFA.

2.2.3 TFA of insulin assay 2

To prepare assay probe solutions with the dual antibody-oligo probes, Pincer A and B stock solutions were diluted 25-fold and mixed using buffer C in the PINCER assay kit (Mediomics, LLC). Ten different concentrations of insulin used for the standard curve were made from the stock insulin solution by dilution in BMHH buffer with 0.1% BSA, containing 10 mM HEPES, 125 mM sodium chloride, 5.7 mM potassium chloride, 2.5 mM calcium chloride, and 1.2 mM magnesium chloride. 10 μL assay probe solution and 10 μL insulin standard were mixed and incubated at room temperature for 30 min, then loaded into the qPCR instrument. In cell assays, 4-5 islets were incubated in 40 μL of various treatment solutions for 1 h, and supernatants were collected. Aliquots of these samples were diluted 1-4 fold with buffer to a total of 10 μL then mixed with 10 μL assay probe solution and loaded into the instrument. Using the qPCR instrument for TFA, the mixtures were incubated at 4 ^{o}C for 10 min and then scanned thermally from 4 ^{o}C to 50 ^{o}C with a 0.5 ^{o}C increment and a 10-s delay before each fluorescence emission measurement. The FAM channel (λ_{ex} = 470 $\pm$ 20 nm, λ_{em} = 522 $\pm$ 8 nm) was chosen for fluorescence excitation and emission quantification for each solution during thermal scanning. The FRET donor and acceptor in this assay was FAM (a fluorescein derivative) and Cy5, respectively, although Cy5 was used merely as a FAM emission quencher within this work.

2.2.4 TFA of cAMP assay

To prepare assay probe solutions, the all in one assay solution and the 10x lysis buffer from the assay kit were warmed at 37 °C for 30 min then mixed together. Ten different concentrations of cAMP used for the standard curve were made from the stock cAMP solution using 1x KRB-IBMX buffer. 10 μL of assay solution and 10 μL cAMP standard solution were mixed and incubated at room temperature for 45 min, then loaded into the qPCR instrument. Cell sampling for cAMP assays were carried out on single islets as described below. For TFA readout, the solutions were incubated at 4 °C for 10 min and then scanned thermally from 4 °C to 94 °C with 0.5 °C temperature increment and a 10-s delay before each fluorescence emission measurement using the FAM channel, as noted above. The FRET donor and quencher in this assay was FAM and DABCYL, respectively.

2.2.5 Tissue extraction

Pancreatic tissues were extracted and islets were isolated as described previously [139, 140] from live C57BL/6J male mice. After extraction, islets were transferred and cultured in islet medium (RPMI 1640 with 10% heat inactivated FBS, 10 μg/mL penicillin-streptomycin and 11 mM glucose) at 37 °C under humidified 5% CO_2 overnight before using.

2.2.6 Single islet assays

For a given single-islet experiment, cultured islets were picked up and starved in the 3 mM glucose solution at 37 °C under humidified 5% CO_2 for 1 h and then equilibrated in KRB-IBMX buffer for 15 min at room temperature. Later, a single islet was taken out and placed in an 8 μL solution with different treatments at 37 °C for 30 min. 5 μL of the supernatants were collected for insulin secretion quantification by insulin TFA as detailed above. The remaining islet was lysed in a total of 20 μL lysis/assay buffer, and two 10 μL aliquots were analyzed by cAMP TFA as described above. For the dynamic, time-resolved studies, 21 different sets of single islets (all in different tubes with 8 μL of solution) were treated for different time periods (from 0 to 60 min, 3-min increment) in duplicate or triplicate; sample collection and cell lysis methods were the same as above.

2.2.7 Statistical analysis methods

The Student's unpaired *t* test with heterogeneous variance was used to process data for islet experiments. The Deming regression method was used for the correlation plot between the TFA assay and ELISA for insulin.

2.3 Results and discussion

2.3.1 Proof of concept by thrombin TFA assay

In DNA-based homogeneous assay, target-dependent probe proximity is assessed by quantifying the oligomeric tails of paired probes at equilibrium. Few approaches to optimize S/B ratio (signal to background ratio) have been reported [125, 141, 127], but none of these was systematic enough to understand the pairing of two probes by proximity effect. In this study, we aimed to develop a systematic analytical tool to separate a true signal (i.e. target-driven proximity of two probes) from total output in free solution. The inspiration was from that an enthalpy-driven DNA hybridization, readout in most DNA-based homogeneous assays, is sensitive upon temperature change. This thermodynamic characteristic allows resolving thermal stability of two complexes simply by temperature scanning; (1) background complex: probe pairs-DNA connector complex and (2) signal complex: target-probe pairs-DNA connector complex (**figure 2.1A**). We assume that association of probes to a target protein is relatively more entropy-driven event, so that it remains stable upon temperature change below 40 °C. As a proof-of-concept, we selected a pair of thrombin DNA aptamers [142, 143] in which their oligomeric tails were labeled with Blackhole Quencher 1 (BHQ1) and TAMRA fluorophore, respectively (Thr1_BHQ1 and Thr2_TAMRA) (**figure 2.1A**). The oligomeric tail of Thr1_BHQ1 is hybridized to a DNA connector with 12-bp long, not to be dissociated through entire range of temperature scanned.

The length of Thr2_TAMRA oligomeric tail to be hybridized is 9-bp long, designed to be dissociated during temperature scanning ($T_m < 30$ °C, T_m: melting temperature). We expected that local maxima of the dF/dT (the first derivative of fluorescence intensity with respect to the temperature) trace at two distinct temperatures should permit assignment and separation of the two major populations, background and signal complex. Also, it is expected to have an optimal temperature between two temperatures which allows the amount of signal complex maximized with zero background. Fluorescence quenching, the consequence of probe proximity, reached the maximum at low temperature, resulting in the lowest TAMRA fluorescence at the beginning of thermal scanning (**figure 2.1B**). The fluorescence increased in a temperature-dependent manner until 50 °C as a result of the dissociation of Thr2_TAMRA from DNA connector. The plateau at 50 °C suggests that 9-bp in Thr2_TAMRA with DNA connector was completely melted away. 20 nM thrombin in assay mixture yielded two phases of a melting curve which T_m is 27 °C and 43 °C, respectively, supporting that two different populations of DNA duplexes, which are from background complex and signal complex, are successfully separated upon their own thermal stability. We called this method thermofluorimetric analysis assay.

To estimate thermal stability of signal complex, the designed T_m of probe-DNA connector duplex should not be higher than T_m of probe-target complexes, which limits the maximal number of base-pairing in the DNA duplex. The minimum number of base-pairing is also limited for detectable fluorescence change induced by probe proximity. For systematic understanding of TFA with the length of DNA connector, we generated the novel thrombin thermofluorimetric map by linearly varying temperature from 5 to 55 °C (**figure 2.1C**). The target concentration was increased stepwise from 0 to 70 nM with 5 nM interval. The lengths of DNA connector to be hybridized to one probe (Thr2_TAMRA) were varied while keeping the length of DNA connector to the other probe constant (12-bp long with Thr1_BHQ1). Two different outputs (F: fluorescence and dF/dT: the first derivative of F) were mapped on two-dimensional space constructed by temperature and target concentration (**figure 2.1C**). In all three connector systems of both TFAs, fluorescence (F) was negatively correlated with target concentration in ranging of permissive temperature (at top panel in **figure 2.1C**), supporting the map is a tool to optimize DNA-based isothermal proximity assay (IPA). For instances, C8-12 connector allows thrombin assay having the highest sensitivity at an ambient temperature. Meanwhile, C7-12 and C9-12 connector direct the same assay to be optimized at below and above an ambient temperature, respectively. The dF/dT profile (at second panel) visualizes thermal stability of both background and signal complex, by showing two bright spots in the map. Compared to C9-12 connector system in thrombin TFA, C8-12 connector yields further separation of two spots, indicating larger difference in thermal stability between background complex and signal complex. It suggests that C8-12 connector provides the widest range of temperature which permits the highest S/B ratio in IPA. Same heat map for insulin TFA is created and is shown in **figure 2.1C**.

While isothermal versions of the same assay are nonresponsive in serum due to autofluorescence interferences (**figure 2.1F**), TFA is capable of analytically separating signal melt transitions from slowly varying autofluorescence background. Control over DNA connector sequences also allows multiplexed protein detection; insulin and thrombin were simultaneously quantified in serum with LODs of 0.81 and 1.88 nM (**figure 2.1D**), without compromising performance from the respective singleplex assay. The assay is functional in even more complex human plasma samples, where near complete recovery of sensitivity is possible using a red fluorescent tag (**figure 2.1E**). In previous insulin TFA with the probes (antibody-oligo conjugated by Solulink) didnt show the background peak (**figure 2.1C**), it may be due to the purity and multivalency of probes. In probes preparation, multiple oligonucleotides can be conjugated to one antibody and the simple column purification in the conjugation kit is not able to separate the antibodies with different number of oligos, which cause multivalency and unpurity of probes to influence the assay performance. Therefore, we changed the insulin TFA probes in later experiments from Solulink conjugated ones to the commercial available probes, purchased from Mediomics.

2.3.2 TFA exploration—a single instrument for second messengers and hormones

After proved the concept of TFA, we tried to apply the assay to more types of targets. Studies on the biology of cell signaling often necessitate confirmation of mechanistic pathways that signal through second messengers and lead to a cellular outcome such as hormone secretion. With current methodology, these studies typically require a combination of multi-step

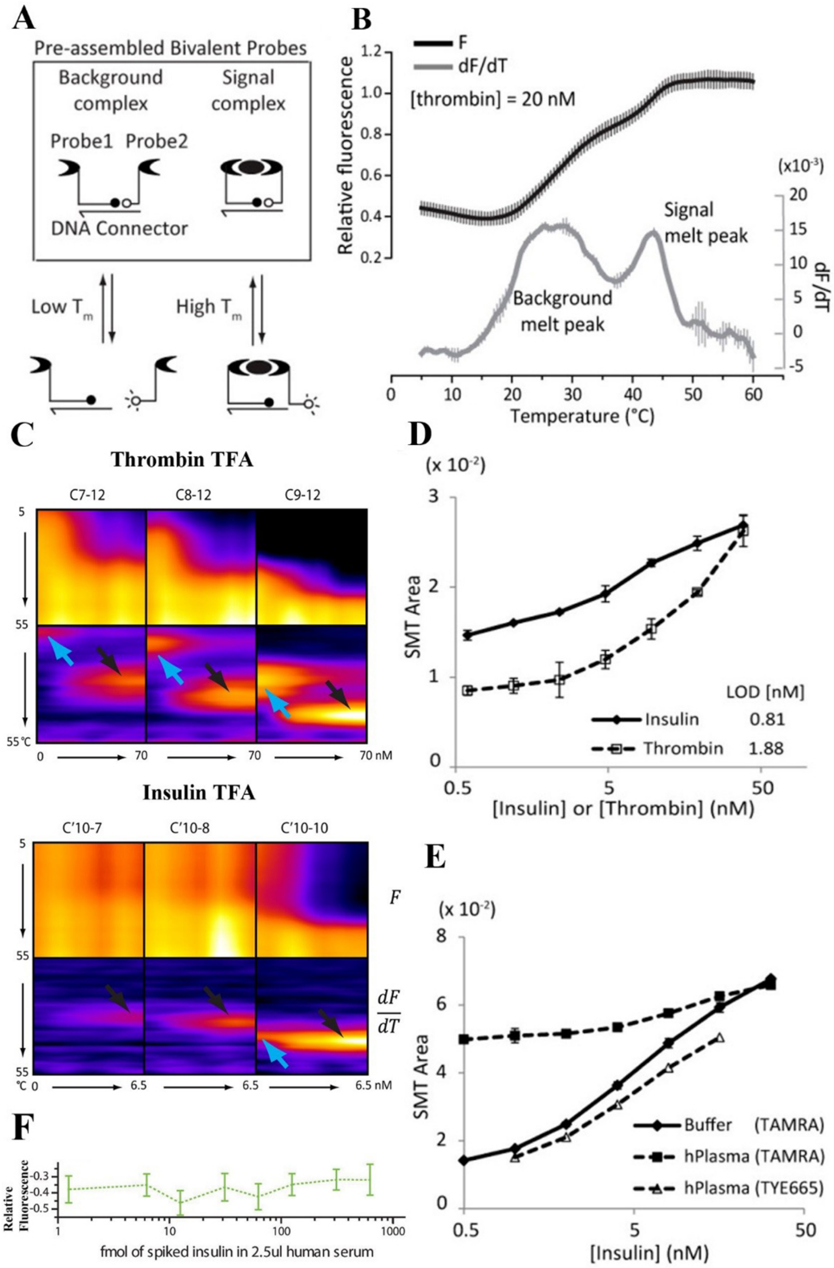

Figure 2.1: Thermofluorimetric analysis assay (TFA). (A) Schematic of TFA. (B) Fluorescence and dF/dT in the presence of 20 nM thrombin. (C) Two-dimensional TFA heat maps for thrombin and insulin in three different assay connector lengths (C7-12, C8-12, and C9-12 for thrombin; C'7-10, C'8-10 and C'10-10 for insulin), with protein concentration on the x-axis and temperature on the y-axis. Background melt peaks and signal melt peaks in each condition are highlighted with blue and black arrows in TFA dF/dT maps. Blue arrows = background melting transitions; black arrows = signal melting transitions. (D) Duplex TFA for insulin and thrombin quantification in 10-fold diluted human serum. (E) Duplex Insulin TFA in 10-fold diluted human plasma (filtered); longer wavelength fluorescence emission (TYE665) was shown to reduce autofluorescence effects as well. SMT area is the are under the curve of the deconvoluted signal melt transition peak. (F) Insulin IPA by spiking insulin into 2.5 μL human serum. These figures are reprinted with permission from ref [135] ©2015 American Chemical Society.

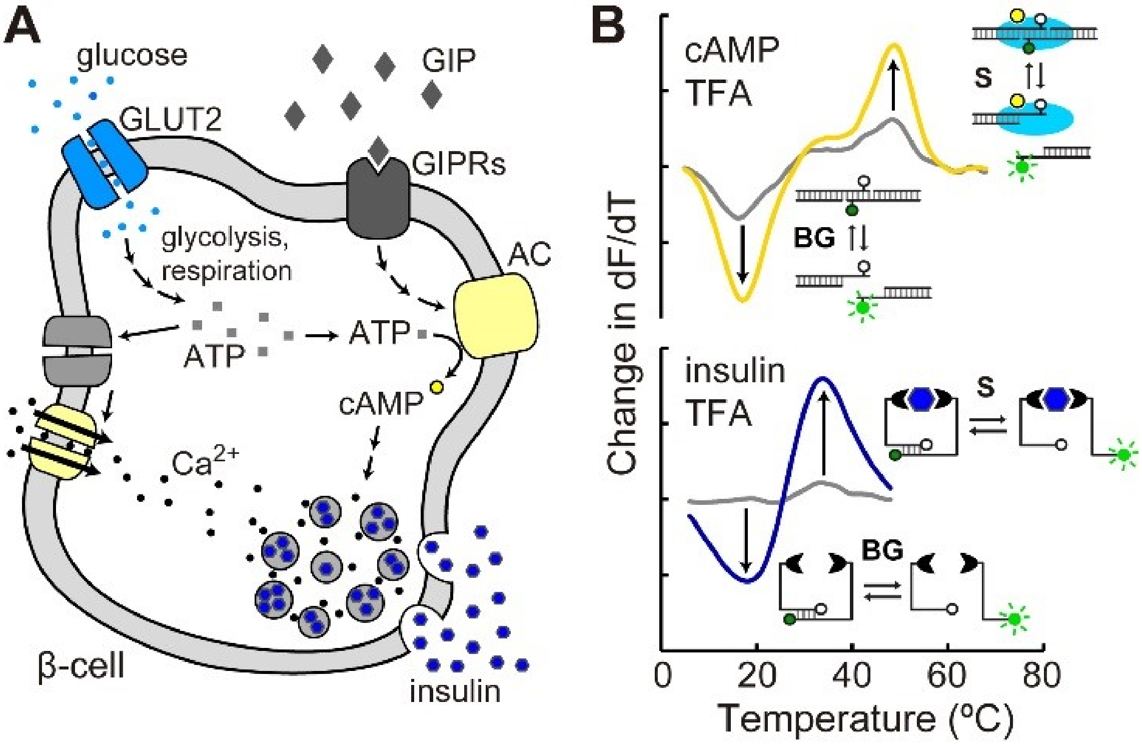

Figure 2.2: Thermofluorimetric analysis (TFA) for homogeneous, mix-and-read, bioanalysis of second messengers and secreted hormones with a standard qPCR instrument. (A) Schematic of pancreatic -cell signalling that is interrogated by TFA in this work. (B) Differential thermal analysis of fluorescence signals can be used to quantify either intracellular cAMP or secreted insulin using DNA-driven assay formats. Changes in signal (S) and background (BG) melting transitions are shown alongside schematics of both assay formats. These figures are reprinted with permission from ref [144] ©2017 American Chemical Society.

techniques with customized instruments, resulting in prolonged analytical workflow and a need for additional expertise. As depicted in **figure 2.2**, our approach permits quantification of intracellular signals and secreted hormones from the same cells by leveraging thermofluorimetric analysis (TFA) with a standard qPCR instrument.

In this session, we chose to interrogate insulin secretion pathways in pancreatic islets to demonstrate the benefits of TFA. Insulin TFA is re-investigated by commercial accessible probes. As mentioned in the first chapter, insulin is well known as a dominant endocrine hormone which is secreted by β-cells within pancreatic islets. The hormone serves as a signal to various other tissues such as muscle, adipose, liver, and brain [15, 145], and it is the key hormone that encounters disrupted signaling in obesity, diabetes, and metabolic syndrome [146]. Glucose stimulates insulin secretion in a cascade through glucose transporters

(GLUT2), glycolysis and respiration, depolarization of the cell membrane (K^+ and Ca^{2+} channels), and exocytosis (**figure 2.2A**). As mentioned in introduction, the "incretin effect" is a more recently discovered phenomenon defined by the significantly larger amount of insulin secreted after oral glucose input compared to intravenous glucose challenge. Gut-secreted glucose-responsive insulinotropic peptide (GIP) was discovered as one of the incretin hormones [147, 148, 149, 12, 150], and it is a potent stimulant of insulin release in the hyperglycemic state. GIP signals through its receptor and increases cyclic AMP (cAMP), which affects various pathways in β-cell depolarization to amplify both the first and second phases of insulin secretion [9] (**figure 2.2A**). To study GIP related signaling in β-cells or pancreatic islets, cAMP and insulin assays are obligatory. As depicted in **figure 2.2B**, we have developed homogeneous, mix-and-read TFA protocols using two DNA-driven assays, allowing insulin and cAMP levels to be quantified with a single instrument. Fluorescence emission readout during thermal scanning allows differential thermal analysis (dF/dT) to be applied. We have proved that this approach allows separation of signal and background (two peaks for each trace in **figure 2.2B**) and effectively negate matrix-based interferences [135, 136].

2.3.3 TFA of DNA-assembling assays for insulin and cAMP

The insulin assay used here was originally designed for isothermal fluorescence readout. Antibody-oligonucleotide probes (**figure 2.2B**, bottom) provide a fluorescence resonance energy transfer (FRET) response in proportion to insulin [127, 134], driven by a target-dependent entropic stabilization often referred to as the proximity effect [128, 129, 135, 124, 141]. FRET occurs from a fluorophore labeled oligo to either a quencher molecule or a FRET pair on the other oligo. We hypothesized that adaptation of our TFA methodology [135, 136] to these probes would improve consistency and limit of detection while helping negate potential background interferences in cell perfusates.

Differential thermal analysis with these probes in the presence of varied insulin concentrations is shown in **figure 2.3A**. Details of data collection and analysis are shown in **figure 2.4** in a stepwise fashion. These results show melting transitions that represent analytical separation of background (peak at $\sim$20 °C) and signal (peak at $\sim$33 °C). The melting peaks represent

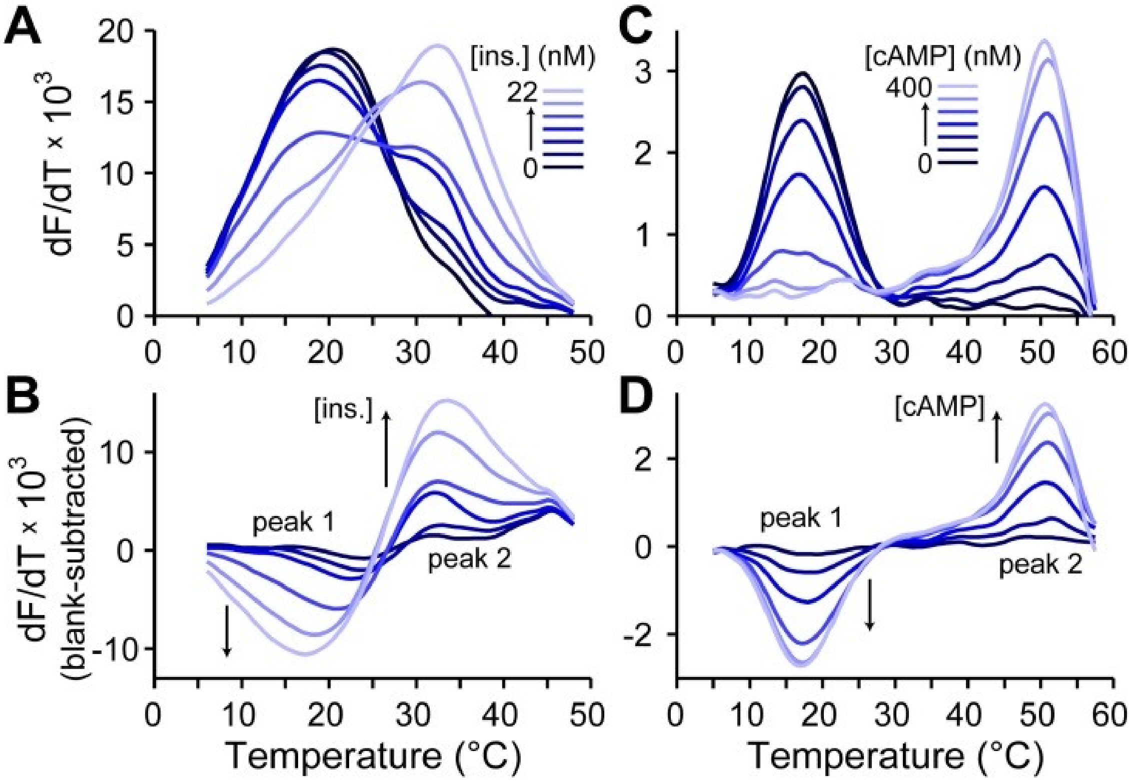

Figure 2.3: Representative data from insulin and cAMP TFA. (A) dF/dT curves with antibody-oligo probes show melting transitions that shift and change intensity in proportion to insulin levels. (B) Blank-subtracted dF/dT curves show clear insulin-dependent changes and allow removal of background interferences. (C) dF/dT curves with DNA-binding protein and oligo probes exhibit melting transitions that are cAMP dependent. (D) Similar, blank-subtracted curves for cAMP quantification. These figures are reprinted with permission from ref [144] ©2017 American Chemical Society.

fluorescence de-quenching transitions as the antibody-oligos dissociate, and this peak shift to a higher temperature when insulin provides increased thermodynamic stability to the complex. As insulin concentration was increased, the background peak decreased as the signal peak emerged and grew larger. Interestingly, the quality of this separation was comparable to the previou results using thrombin aptamer pairs yet was significantly improved compared to the in-house synthesized antibody-oligos (insulin TFA1 in 2.1) [135]. This enhancement could be a result of either the improved purification of the probes as we estimated or the simplification of the proximity assembly in this version of the assay, which does not require connector oligos. Leveraging the blank (zero insulin) subtraction method approach presented in the prior work of Prof. Easley's lab [136], the insulin-dependent portions of the TFA curves could then be easily visualized (**figure 2.3B**) and applied for the quantitative analysis presented below.

The cAMP assay used in this work was originally designed for isothermal fluorescence readout as well. In this case, cAMP serves as a ligand which stabilizes a DNA-binding protein toward associating with its recognition sequence [137, 138]. The recognition sequence of DNA is thus thermodynamically stabilized by the presence of cAMP, and a FRET pair can be used for readout. Again, we hypothesized that adaptation of our TFA methodology [135, 136] to these probes would result in the concomitant improvements in performance.

Differential thermal analysis with these probes in the presence of varied cAMP concentrations is shown in **figure 2.3C**. Data collection and analysis is detailed in **figure 2.4**. This assay showed nicely separated melting transitions. Background peaks were observed at ~17 °C and signal peaks at ~51 °C, representing the best separation (ΔT = 34 °C) achieved thus far with our TFA protocols. This separation quality is due to the high affinity of DNA-binding protein to its target DNA in the presence of the cAMP ligand [151] (~0.1 nM). Increases in cAMP concentration thus resulted in decreased background peak heights and increased signal peak heights, which is more easily visualized using the blank subtraction approach (**figure 2.3D**). To our knowledge, these data represent the first application of TFA to a DNA hybridization driven small molecule assay. Blank-subtracted data as shown in **figures 2.3B** and **2.3D** allowed removal of matrix effects [136] and was used for the subsequent calibrations and quantitative analysis of insulin and cAMP during cell signaling.

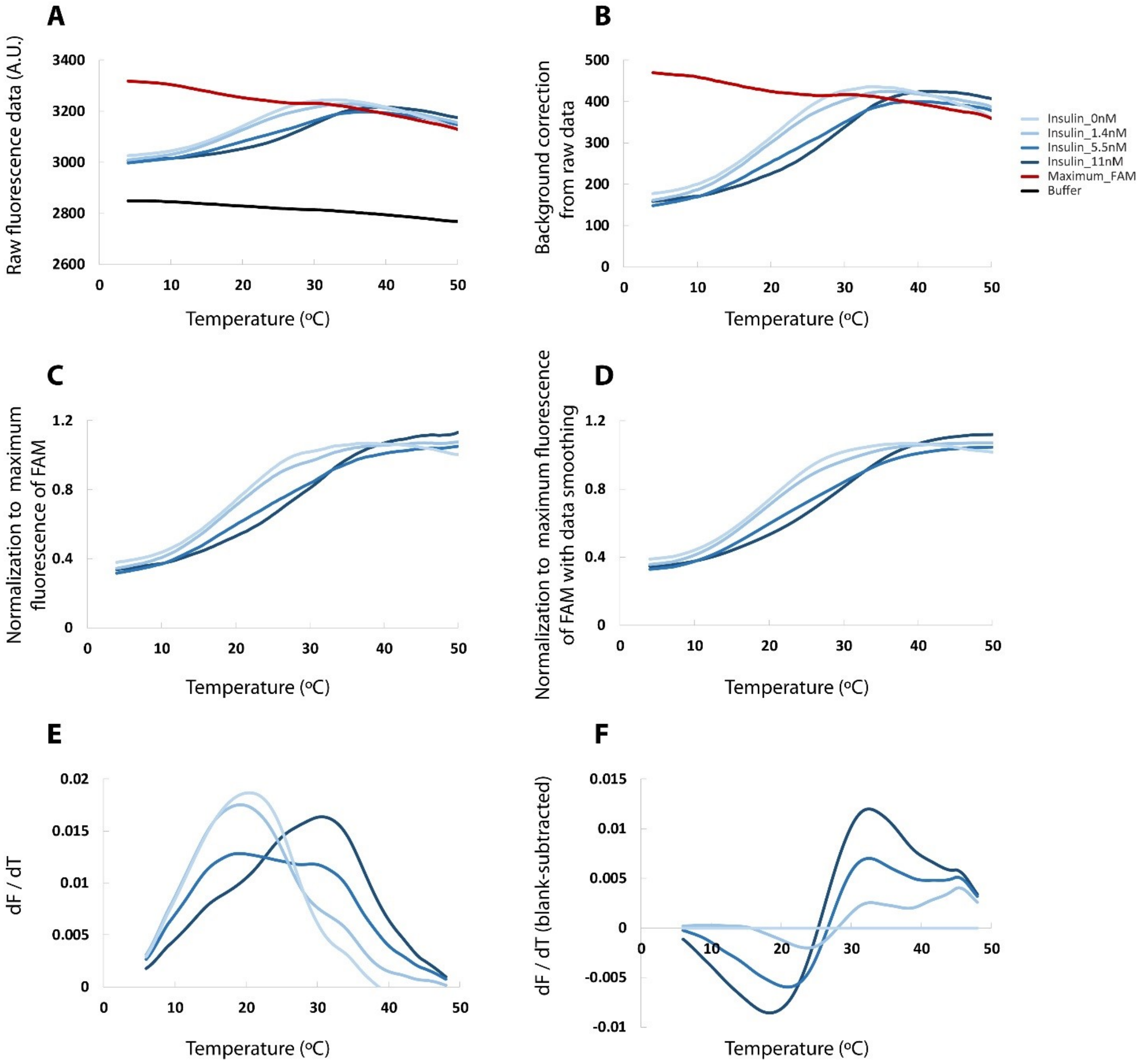

Figure 2.4: Data analysis for insulin TFA. (A) The raw fluorescence data measured by qPCR in FAM channel. (B) Background correction by subtracting the fluorescence measured from buffers in the assay. (C) Normalization of data in (B) to the maximum of fluorescence from the fluorophore (FAM) to correct the influence of temperature on fluorescence. (D) Data smoothing by 13-window data average. (E) The 1st derivative of fluorescence data in (D) by 9-window Savitzky-Golay filter. (F) dF/ dT data were subtracted by blank to separate the two peaks.These figures are reprinted with permission from ref [144] ©2017 American Chemical Society.

2.3.4 Highly repeatable standard curves for insulin and cAMP

Blank-subtracted data such as that shown in **figures 2.3B** and **2.3D** were used to generate TFA-derived standard curves for both insulin (**figure 2.5**) and cAMP (**figure 2.6**). This method allowed robust confirmation of the target-dependent response and the mechanism of binding. For instance, the insulin calibration curve shown in **figure 2.5A** could be generated by calculating the difference between the blank-subtracted dF/dT values of Peak 2 and Peak 1 (from **figure 2.3B**). The data can also be used to confirm that the total amount of probes remains constant (target-bound and unbound) by plotting the sum of Peak 2 and Peak 1 intensities in **figure 2.5B**. The fact that this sum is statistically equal to zero and is unchanged by analyte concentration proves that the analyte (insulin) is simply shifting the probes from a lower stability state (background peak, Peak 1) to a higher stability state (signal peak, Peak 2) but not altering the total number of probes.

Interestingly, the blank-subtraction method imparted unexpected consistency to the assay response. The three calibration curves shown in **figure 2.5A** were collected over a period of 7 months, yet the response (Peak 2 − Peak 1) was essentially equivalent. Even when combining all data over 7 months into a three-parameter Hill equation (Eq.2.1, below) for a nonlinear least-squares fitting, the data was highly correlated ($R^2 = 0.989$), with well-defined calibration parameters (a = 0.7391± 0.0671; b = 1.1142 ± 0.0965; c = 8.71 ± 1.69). The Hill equation was used due to the lack of an adequate analytical model for this assay, and the b value above 1.0 suggests a mild degree of cooperativity in binding of the antibody-oligo probes with target proteins. The 3σ limit of detection (LOD) was calculated to be 0.82 nM using the linear portion of this curve at lower concentrations, and the dynamic range extends to 22 nM under these conditions.

$$y = \frac{ax^b}{(c^b + x^b)} \tag{2.1}$$

Similar trends were observed using the blank-subtracted data from the cAMP TFA experiments. Peak difference data (**figure 2.6A**) was responsive to cAMP levels, while peak sum data (**figure 2.6B**) remained near zero and constant. Although the peak sum data did seem to deviate slightly from zero at a few points, the overall response was not correlated. Likewise,

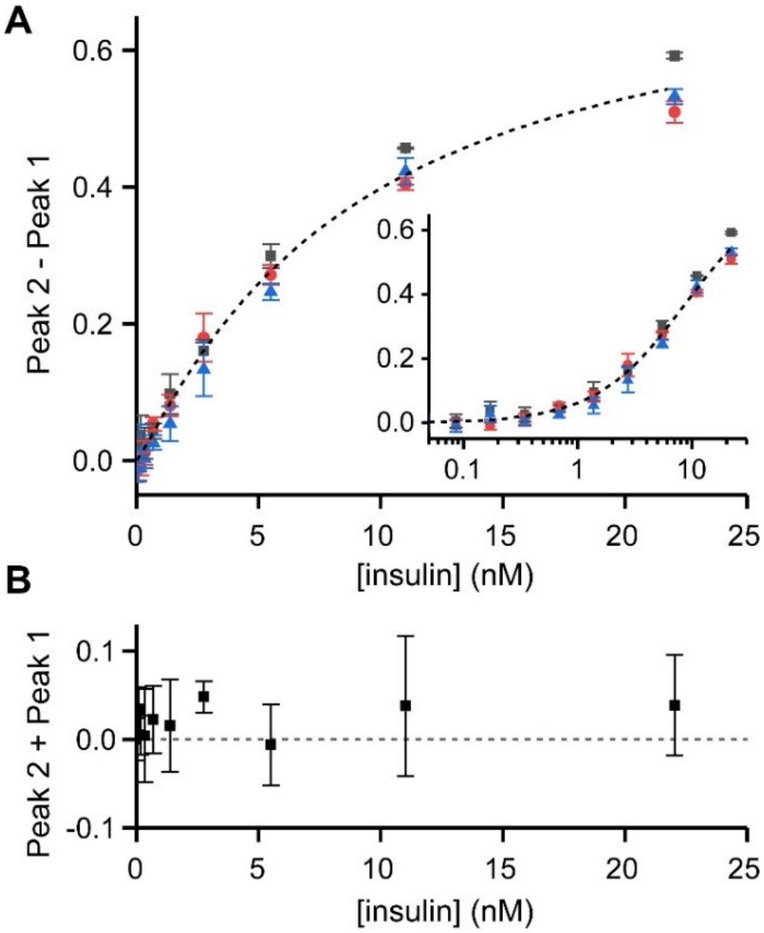

Figure 2.5: Repeatable insulin TFA calibrations for minimized calibration burden. (A) Over a 7-month period, insulin TFA assays were highly reproducible (R^2 = 0.989 for Hill equation fitting, dashed curve). Inset is a log-scale plot of the same data. (B) TFA peak sums were statistically equal to zero and unchanged by analyte concentration, confirming that insulin simply shifts the probes from the unquenched state to the quenched state without altering the total number of probes.These figures are reprinted with permission from ref [144] ©2017 American Chemical Society.

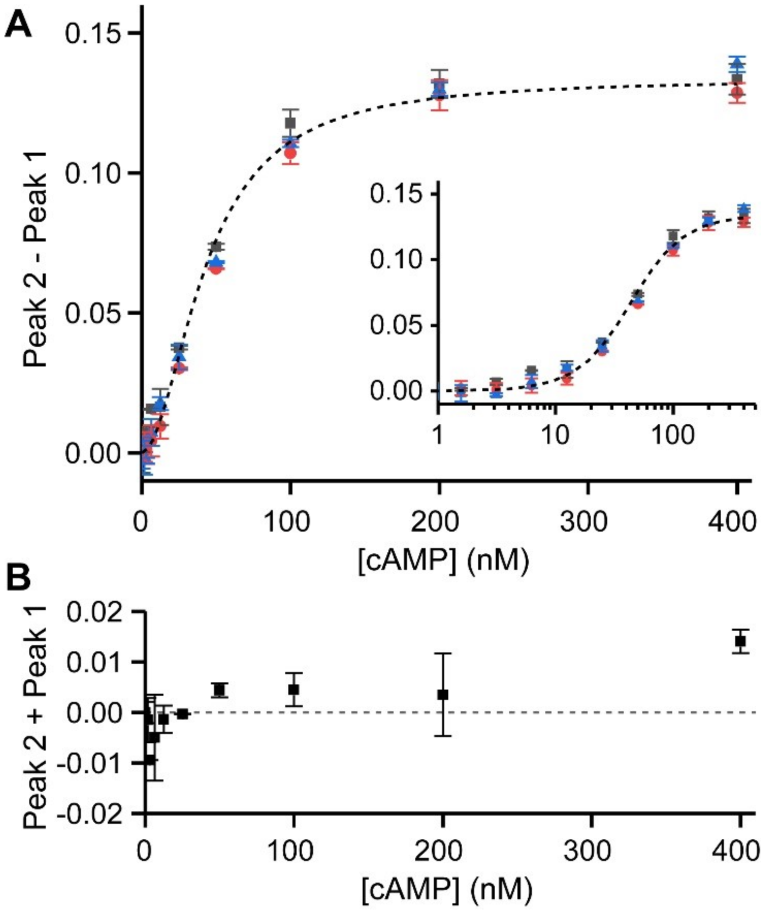

Figure 2.6: Repeatable cAMP TFA calibrations also minimized calibration burden. (A) Over a 4-month period, cAMP TFA assays were highly reproducible (R^2 = 0.988 for Hill equation fitting, dashed curve). Inset is a log-scale plot of the same data. (B) TFA peak sums were statistically equal to zero and unchanged by analyte concentration, as before with insulin (**figure 2.5B**).These figures are reprinted with permission from ref [144] ©2017 American Chemical Society.

the three calibrations shown in **figure 2.6A** were collected over a period of 4 months, and the response was essentially equivalent. The combination of all data gave a nicely correlated (R^2 = 0.988) response when fit to Eq.2.1, with well-defined parameters (a = 0.1337 ± 0.0029; b = 1.9022 ± 0.1379; c = 43.1945 ± 2.0399). The b value near 2.0 suggests significant cooperativity in binding, which is to be expected in this multi-component assay format. The 3σ limit of detection (LOD) was calculated to be 10.8 nM using the linear portion of the curve at lower concentrations, and the dynamic range extends to 200 nM.

In general, this high level of repeatability for both insulin and cAMP TFA adds to the practical value of the homogeneous, mix-and-read methodology. In our laboratory, this benefit allowed us to minimize the burden of calibrations during cell signaling studies. It was not necessary to carry out full range, multi-point calibrations on a day-to-day basis. In practice, we would run one or two standards (blank and high concentration) for quality control with each set of samples, then run a more thorough, 10-point system calibration (as shown in **figures 2.5** or **2.6**) every few weeks. Indeed, in validation experiments comparing insulin TFA with insulin ELISA on cell secretion samples, the methods were highly correlated despite having run samples for several months on a single TFA calibration curve (Deming regression, **figures 2.7**).

2.3.5 Insulin secretion quantification from islets with TFA

These simplified workflows, the minimized calibration requirements, and the low-volume sample compatibility permitted a number of biological experiments to be performed, even on single pancreatic islets. Following a variety of treatments on groups of 4-5 islets, supernatant was collected for insulin secretion quantification by TFA. As shown in **figure 2.8A**, islets responded to increases in glucose (3 mM to 11 mM) by secreting more insulin, as expected. 100 M diazoxide, a potassium channel activator that repolarizes the β-cells, decreased insulin secretion even at high glucose. Finally, 25 mM KCl effectively depolarized the cells further, promoting additional insulin secretion at high glucose. The incretin effect was also evaluated with single-islet experiments using GIP treatments. As shown in **figure 2.8B-C**, the glucose dependence of GIP-amplified insulin secretion was confirmed with single islets. More than

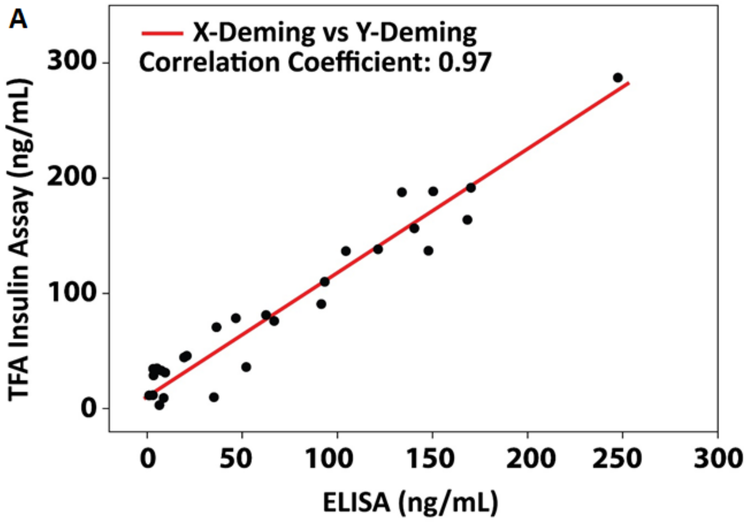

B

	Coefficient	Std. Error	95% Conf-L	95% Conf-U
Intercept	10.3725	5.219	-0.3553	21.1003
Slope	1.0758	0.0548	0.9631	1.1884

Figure 2.7: Correlation plot between insulin ELISA and insulin TFA using Deming regression. (A) The Deming regression was carried out using secretion samples of primary islets reported in the main text. The assays were well-correlated as expected, with a coefficient of 0.97. (B) Regression curve coefficients are tabulated along with standard error and 95% confidence limit statistics. The 95% confidence interval of the slope encompassed the ideal of 1.0, and the 95% confidence interval of the y-intercept encompassed the ideal of zero. These results indicate good correlation between the two methods (TFA and ELISA).These figures are reprinted with permission from ref [144] ©2017 American Chemical Society.

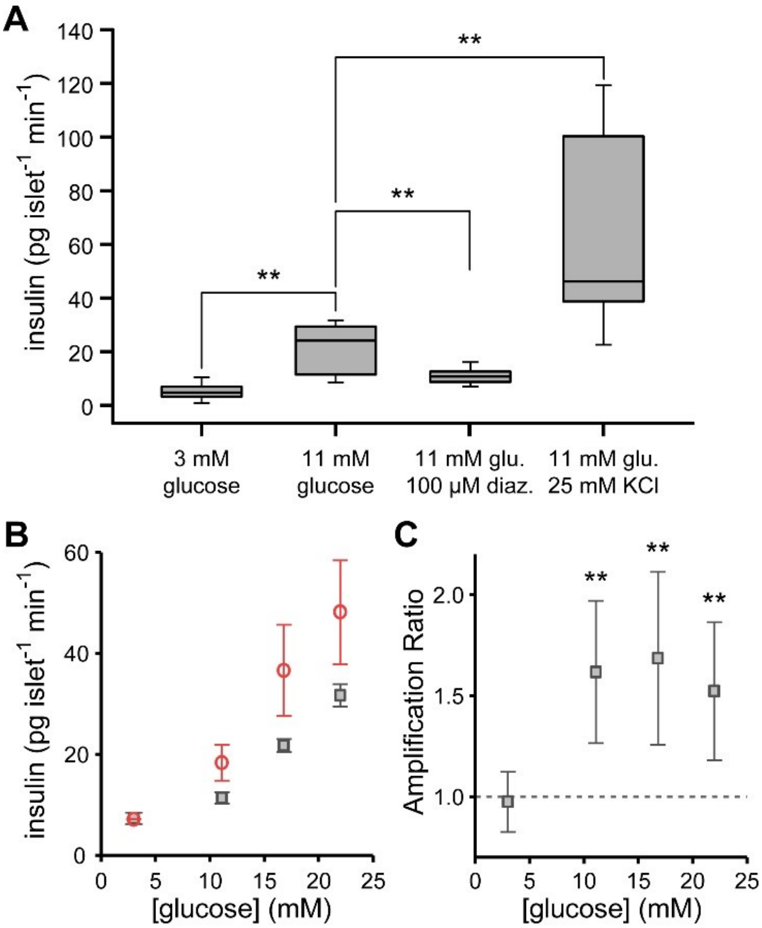

Figure 2.8: Biological validation of insulin TFA with antibody-oligo probes for assays on single pancreatic islets. (A) Single islets under various treatments were successfully assayed by TFA, with expected responses recorded. (B) GIP-dependent amplification of insulin secretion was also observed to be glucose-dependent, with (C) amplification ratios that showed at least 50% amplification at stimulatory glucose concentrations but no amplification at low glucose. ∗∗ denotes $p<0.01$ by student's *t*-test.These figures are reprinted with permission from ref [144] ©2017 American Chemical Society.

50% increases in insulin secretion were observed at all stimulatory glucose concentrations in the presence of 250 nM GIP, but there was no amplification observed at low glucose (3 mM), in agreement with previous studies on the incretin effect [147, 148, 149, 12, 150]. The simple, mix-and-read insulin TFA protocols were thus validated with single islets undergoing treatments that modulate exocytosis by acting upon glucose transporters, potassium and calcium channels, and G-protein-coupled receptors.

2.3.6 Insulin and cAMP assays on single islets with TFA

Both GIP and glucagon-like peptide-1 (GLP-1) are important incretin hormones synthesized and secreted by the gastrointestinal cells following meal ingestion. The principal function of GIP and GLP-1 in pancreatic -cells is to elevate glucose-induced insulin secretion [150, 149], as validated with our method in **figure 2.8B-C**. Akin to GLP-1, the incretin effect of GIP is through the incretin/cAMP pathway [147, 152]. As depicted in **figure 2.2A**, GIP binds to the GIP receptor (GIPR), a G protein-coupled receptor which further activates adenylyl cyclase (AC) to stimulate the formation of cAMP from ATP. cAMP activates various downstream pathways, and its combined effects with glycolysis results in a GIP-potentiated insulin secretion that only functions at high glucose levels [153, 154]. Glucose alone is insufficient at raising cAMP, as GIP alone is insufficient in amplifying insulin secretion, but these treatments together result in amplified insulin secretion.

Consequently, the glucose-dependent, GIP-amplified insulin secretion pathways in -cells of pancreatic islets are ideal for validation of our TFA methodology capable of measuring both insulin and cAMP with a single qPCR instrument. In each experiment, a single islet was stimulated, supernatant was sampled for insulin TFA, then the islet was lysed, and intracellular contents were sampled for cAMP TFA. Forskolin was chosen as a pharmacological cAMP-raising reagent on pancreatic islets, since it boosts intracellular cAMP through adenylyl cyclase (AC) [155] and has been shown to have a significant effect on enhancing cAMP levels in islets [156]. Forskolin can thus be used as a GIP mimicking reagent. The cAMP TFA results shown in **figure 2.9A** provide clear affirmation of these effects in single islets. Forskolin at both 1 μM and 10 μM strongly stimulated cAMP production within islets at both low (3.0 mM) and high (16.8 mM) glucose levels. GIP, however, only significantly increased cAMP at high glucose levels.

The insulin TFA results shown in **figure 2.9B** show the glucose-dependent nature of GIP-potentiated secretion. No significant increases in single-islet insulin secretion were observed at low glucose, using either forskolin or GIP. However, at high glucose levels, insulin secretion

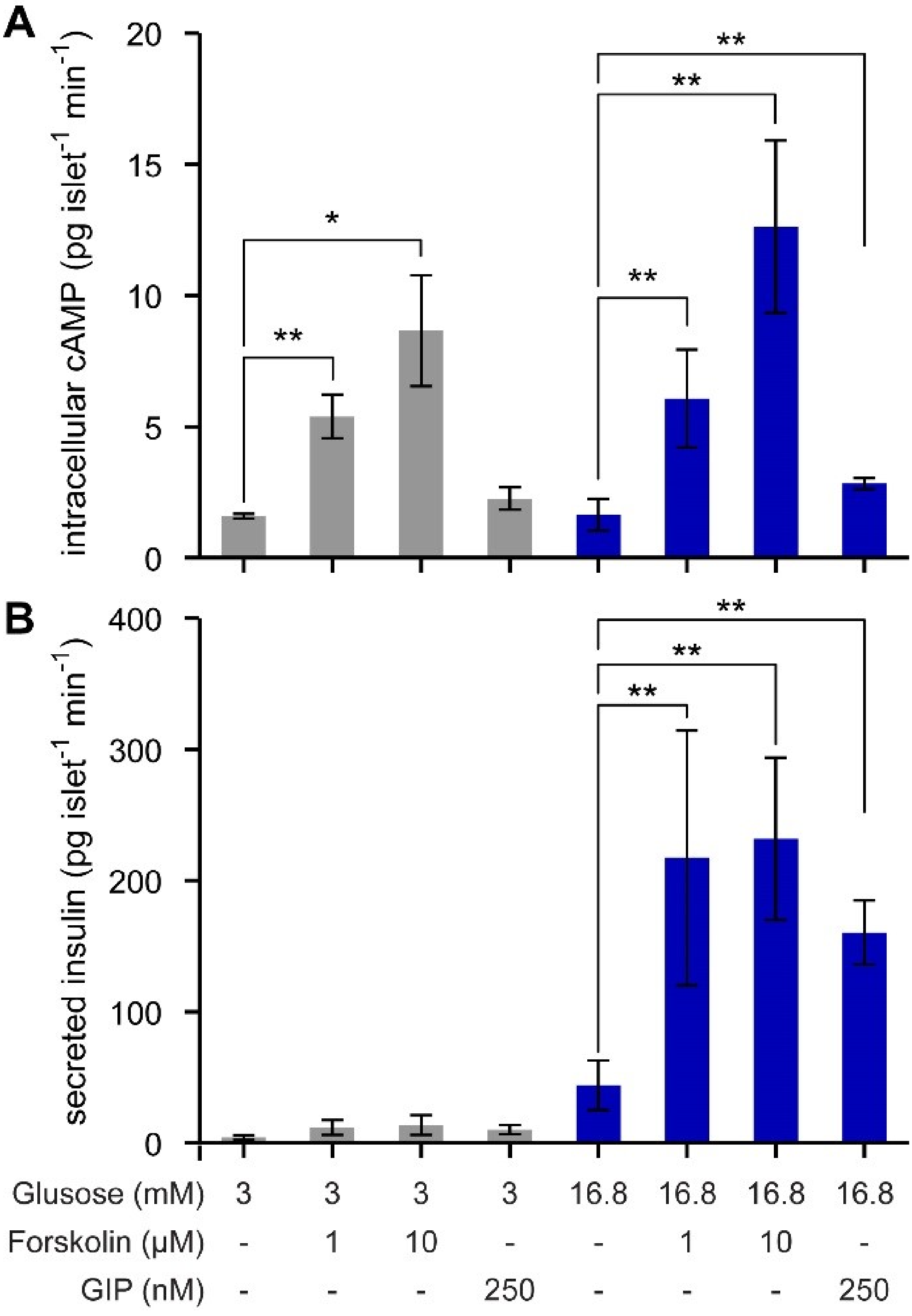

Figure 2.9: Quantitative analysis of cell signalling in single islets using TFA for both insulin and cAMP. (A) At low and high glucose levels, forskolin strongly stimulated cAMP at both 1 μM and 10 μM. GIP only significantly increased cAMP at high glucose levels. (B) The glucose-dependence of GIP-potentiated insulin secretion was validated, since the amplification only occurred at high glucose for either forskolin or GIP treatments. $**$ denotes p<0.01 by student's *t*-test.These figures are reprinted with permission from ref [144] ©2017 American Chemical Society.

was strongly amplified by both forskolin and GIP treatments. These results validated the permissive role of cAMP in amplifying insulin secretion [153]. Before the amplification pathway is initiated, the glucose-triggered pathway must first be activated.

The results in **figure 2.9** further validated the TFA protocols for cell signaling studies with a single instrument and simple workflows. Since TFA can eliminate most of the background interference from sample matrices, complicated and time-costing cAMP extraction steps from the lysis solution were not needed, and insulin quantification could be carried out on supernatants with little interference.

2.3.7 Temporally resolved insulin and cAMP assays on single islets

The non-amplified, direct-readout nature of TFA allows small volumes to be assayed, as low as 100 picoliters in our lab prior work [135]. This benefit permitted time-resolved studies of both insulin secretion and intracellular cAMP levels every 3 minutes, even on the same single islets (**figure 2.10**). Insulin secretion was observed to increase in a biphasic manner after changing glucose from 3.0 to 16.8 mM, while cAMP levels were undetectable in single islets at this temporal resolution. However, upon addition of 10 μM forskolin, both cAMP and insulin were detectable at 3-min resolution from single islets using TFA. To our knowledge, this is the first representation of both insulin and cAMP quantification from single islets at high temporal resolution, a feat enabled by the simplicity of TFA workflows and instrumentation.

2.3.8 Miniaturization of TFA on microfluidic system

As mentioned again and again previously, mix-and-read operation is a characteristic of homogenous assay, which enables the assay miniaturizable. A temperature-controlled microfluidic chip is built where an assay mixture is confined as low as 235 pL (**figure 2.11**). Simply by reducing an assay volume, the detection limit of thrombin TFA rivals to PLA detection limit without any signal amplification. Assay time is less than 3 min. The signature dF/dT background and signal peaks shown in 235 pL assay mixture (**figure 2.11D**) proved that assay volume could be reduced more than eighty-five thousand times. The standard curve of thrombin, insulin and cAMP TFA assays were obtained and single-islet cAMP accumulation under

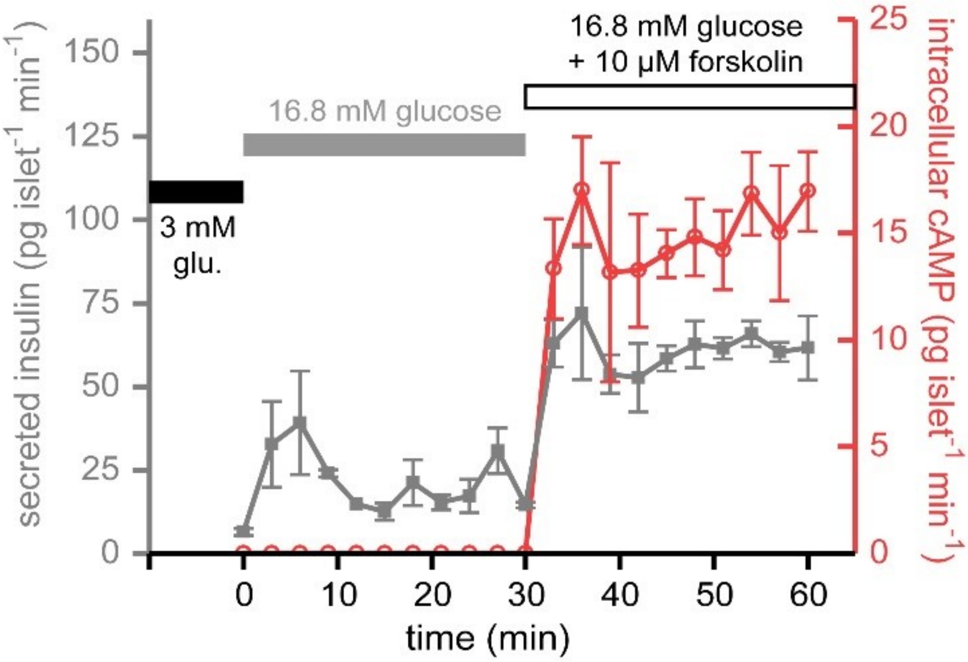

Figure 2.10: Single-islet insulin and cAMP levels could be assayed with TFA at 3-min temporal resolution. These results were enabled by the simple workflow, low volume requirement, and direct readout nature of TFA with a standard qPCR instrument.The figures is reprinted with permission from ref [144] ©2017 American Chemical Society.

the stimulation of 16.8 mM glucose with 250 nM GIP was done in the microfluidic system (**figure 2.12**). The corresponding insulin secretion from each islet was quantified by insulin TFA assay in tube. Compared the **figure 2.12A** with **2.12B**, the amount of insulin secretion is following the trend of cAMP accumulation amount. The 7-channel microfluidic system is only the preliminary proof of miniaturized TFA by microfluidics. For further research, the simplified temperature controlling system (e.g. two-temperature zones) and detection system (e.g. optical fibers) are the direction of improved miniaturized TFA.

2.4 Conclusions

We showed that TFA can efficiently separate the signal form background in DNA-based homogeneous assays. It was a standalone assay as well as gave an insight on developing and optimizing DNA based IPA. As an assay platform, TFA has unprecedented advantages. First, TFA is the only tool to measure analytes in complex biological matrix among other direct assays using a simple fluorescence optic, which is feasibly the most economical. Also, it is robust and highly reproducible because the value (dF/dT) is internally normalized. Secondly, it is truly one-step mix-and-read assay taking less than 40 min. Although LODs are certainly lower using amplified assays with more complex workflows (e.g. ELISA), the sub-nanomolar

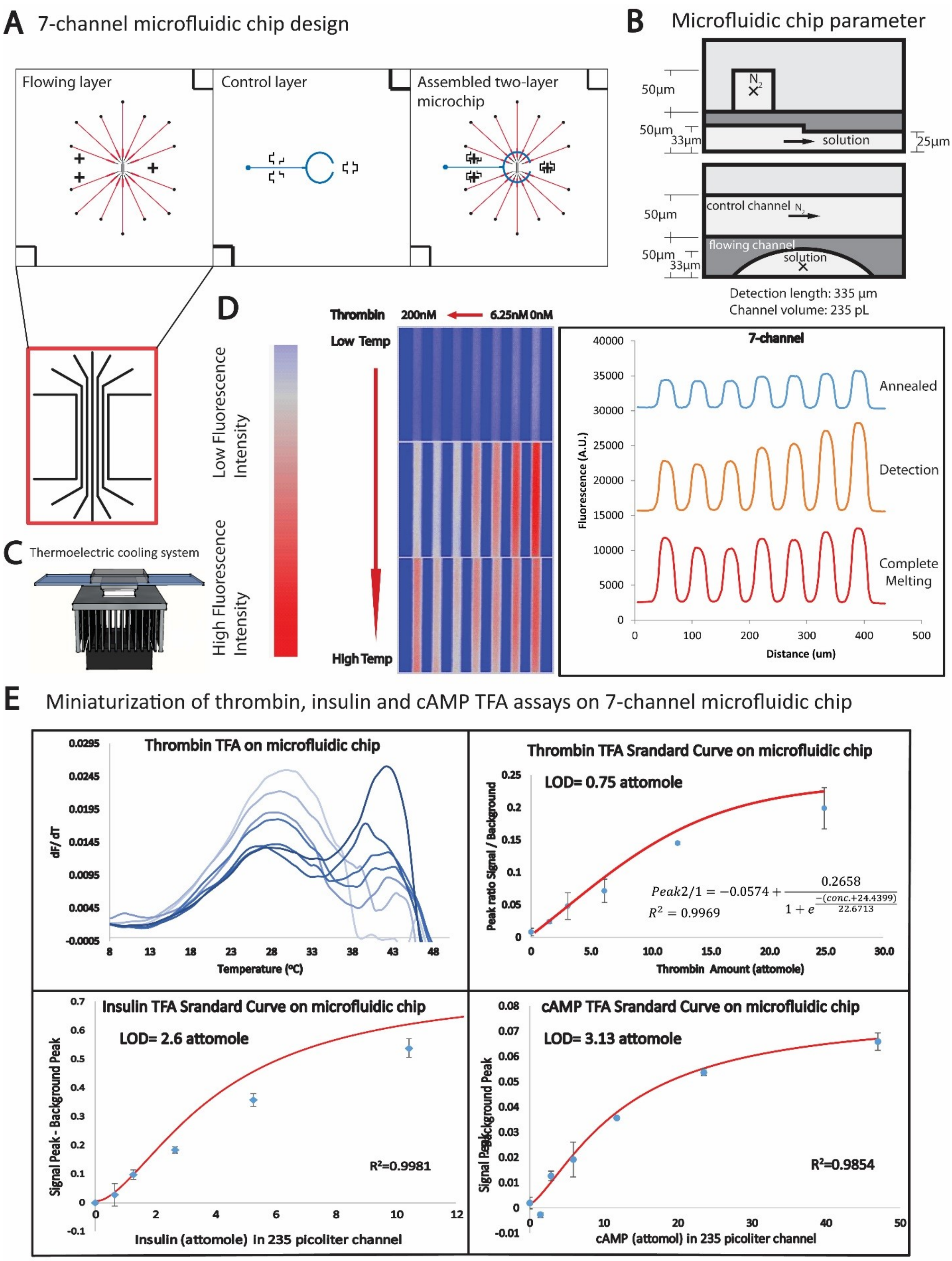

Figure 2.11: Caption next page.

Figure 2.11: (Previous page.)(A) Two-layer soft-lithographic device design with 7-channel flowing layer (bottom layer) and control layer (top layer) as a push-down pneumatic valve under control of solenoid switches to seal the flowing channel during the temperature scanning. The device fabrication protocol same as the one described in chapter4. In the flowing channel, the imaging window (in the red box) are fabricated by SU-8 photoresist, while other parts are manufactured by AZ positive photoresist and reflowed to form round-shape channel for facilitating the complete close of flowing channel by control layer. The control layer is patterned by SU-8 photoresist. (B) the channel dimensions of microfluidic device. (C) Peltier- thermoelectric cooling system for temperature control of microfluidic chip, driven by in-house written LabVIEW programming. (D) Thrombin TFA assay on the 7-channel microfluidic device with 100 nM Thr1_BHQ, 100 nM Thr2_TAMRA and 140 nM pFRET_C21(9-12) were in the assay solution. Thrombin concentrations in the channels were 200 nM, 100 nM, 50 nM, 25 nM, 12.5 nM, 6.25 nM, 0 nM from right to left channel. The temperature scanning range is 5.0 to 55.0 °C with 0.5 °C increment and 20 seconds delay at every temperature point. The red channel TRITC was used in the photo taking and the capture time is 10 seconds. All of probes are annealed at low temperature to give low fluorescence (the upper image); and the background complexes melt at around 37 °C, where the lower fluorescence represents more signal complexes in the solution (the middle image); when the temperature over 48 °C, hybridized DNA tails are separate to reach the highest fluorescence readout and little differences among seven channels (the lower image). (E) Calibration curves of hrombin, insulin and cAMP TFA assay in the 7-channel microfluidic system. LOD: limit of detection, calculated by 3σ. Insulin and cAMP probes concentration are same as the assays in tubes, with temperature scanning from 5.0 to 55.0 °C with 0.5 °C increment and 7 seconds delay at every temperature point for insulin, from 5.0 to 40.0 °C with 0.5 °C increment and 3 seconds delay at every temperature point for cAMP.

to upper nanomolar detection ranges demonstrated herein compare favorably with other non-amplified, direct-readout methods in the literature. TFA has been validated as a promising approach for studies on cell signalling with high calibration repeatability, small sample volume requirement, and the repurposing of a widely-adopted nucleic acid analysis instrument for both hormone and second messenger quantification.

Considering the importance of incretin effects in diabetes, obesity, and metabolic syndrome [147, 148, 149, 12, 150], TFA represents a robust, new tool that could immediately impact studies on incretin-amplified insulin secretion from islets or β-cells. In the future, it should be straightforward to adapt the antibody-oligonucleotide version of TFA to any protein or target with two antibodies (or aptamers), and the development of additional DNA-driven assays for small molecules and second messengers would expand the catalogue of TFA analytes. Multiplexing through spectrally resolved fluorophores and/or thermally resolved melting

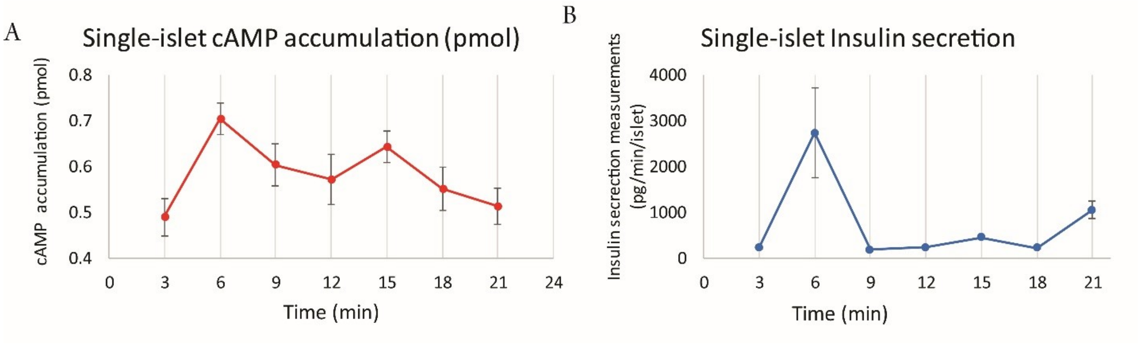

Figure 2.12: (A) One islet, in each reservoir connected to one of seven channels on chip, was incubated in 8 μL 16.8 mM glucose with 250 nM GIP for 3, 6, 9, 12, 15, 18, 21 min at 37 ºC in 7-channel chip. After secretion, 4 μL secretion solution is pipetted out for insulin quantification by insulin TFA assay and 4 μL all-in-one cAMP assay solution was added into the reservoirs, incubated at R.T. for 1h. Then the solutions were vacuumed into the detection channels and the temperature scanning was done on chip for cAMP detection. Error bars are from duplicate scanning from one chip. (B) Insulin quantification in tube via insulin TFA assay.

transitions has already been shown feasible [135], thus further work in this area should permit small-volume, mix-and-read assays on a variety of analytes to be carried out in a single tube. Finally, due to its non-amplified, direct-readout nature, adaptation of TFA to the microfluidic platform is proved practical and can be an obvious yet important field to explore in the future.

Chapter 3

Quantifying Aptamer-Protein Binding via Thermofluorimetric Analysis

This chapter is recovered from publications: Juan Hu, Joonyul Kim and Christopher J. Easley. Quantifying Aptamer-Protein Binding via Thermofluorimetric Analysis. *Anal. Methods*. 2015, 7, 7358-7362.

3.1 Introduction

Realizing the enormous analytical potential of aptamers for quantifying proteins, researchers have devised a variety of methods over the years for quantitative readout of aptamer-protein binding [125, 157, 158, 159, 160, 130, 161, 162, 128, 129, 163, 164, 165]. Homogeneous quantification DNA ligation and amplification [125], real-time detection with quantum-dot aptamer beacons [157], direct micromagnetic [166] or electrochemical sensing [166, 128, 164] and the use of chemiluminescence resonance energy transfer [165] are but a few of many examples. Most of these methods include some exploitation of controlled DNA hybridization. DNA hybridization is sequence-specific, making it flexible and controllable, and downstream enzymatic amplification of the sequences [125, 165] can provide exquisite assay sensitivities. However, method development can be hampered by the lack of generalizability of each approach, often requiring customized method development for each aptamer-protein couple. Although dual probe proximity assays hold promise for improved generalizability [125, 128, 163, 127, 141, 124], this strategy requires aptamer pairs, of which only a few are available to date [161]. As mentioned in previous chapter, simplification of an assays workflow is always an important goal in analysis, and this is particularly true in bioanalysis, where mere sampling of a biological system can be complex. As such, homogeneous protein assays [125, 127, 118] have great potential, and aptamer-based homogeneous assaysreviewed recently by Sassolas et al.[167]could be argued as the most promising toward the bioanalytical ideal of arbitrary protein detection in real time [161]. In terms of readout, fluorescence-based optical detection provides high sensitivity and specificity, yet autofluorescence in biological samples results in high background and usually implores specialized instrumental workarounds such as time-resolved detection or chemiluminescence [118].

In second chapter, a novel approach was introduced for homogeneous protein quantification in biological matrices that exploits a pair of probeseither aptamers or antibody-oligonucleotide conjugatesand a homogeneous fluorescence readout enabled by thermal scanning [135]. This approach provides a method for robust mix-and-read fluorescence detection of proteins, and the thermal scanning allows subtraction of autofluorescence in human serum samples. However, dual proximity probes such as aptamer pairs [161] are still required for this method. Inspired by the benefits of DNA melting approach [135], here we introduce a more generalizable thermal scanning method that only requires a single aptamer for readout and does not require covalent labelling of the aptamers. By staining aptamers with a DNA intercalating dye, we demonstrate that the unbound aptamer and the protein-bound aptamer can be thermally resolved using a standard qPCR instrument that exploits thermofluorimetric analysis (TFA). Platelet-derived growth factor (PDGF) can be quantified in buffer at sub-nanomolar levels using TFA, and the methodology is functional with multiple intercalating dyes and other proteins. Importantly, the ability to negate autofluorescence in human serum [135] is preserved with our single probe TFA, since background can be analytically separated from signal. Due to its simplicity and potential for generalizable protein quantification, this approach provides an important addition to the bioanalytical toolbox.

3.2 Experimental settings

3.2.1 Reagents and Materials

Reagents included deionized ultra-filtered water (Fisher Scientific), bovine serum albumin (BSA), SYBR Green (10,000 concentrate in DMSO; Lonza), and recombinant human PDGF-BB (R&D Systems), which is a homodimer of the beta polypeptide of PDGF (referred to simply as“PDGF” herein). All oligonucleotides were purchased from Integrated DNA Technologies (IDT) and purified by standard desalting or HPLC. Pathogen-screened, normal human serum samples were purchased from BioreclamationIVT.

3.2.2 Aptamer preparation

The parent sequence of the DNA aptamer with affinity to PDGF was obtained from Green et al. 28. For purposes not related to the current work, additional nucleotides were added to this aptamer, which minimally affected protein binding. The PDGF aptamer sequence (parent sequence underlined) was as follows (5’ to 3’): GGC GCA CCC AAC TCA AAA <u>AAA TAC TCA GGG CAC TGC AAG CAA TTG TGG TCC CAA TGG GCT GAG TAT</u>. 10 μM of the aptamer in buffer (10 mM Tris-HCl, pH = 8.0, 50 mM KCl, 3.3 mM $MgCl_2$) was folded by heating for 10 min at 95 °C then cooling on ice prior to experiments.

3.2.3 Thermofluorimetric analysis (TFA)

20 μL assay mixtures were prepared in buffer with final concentrations of 100 nM aptamer, 1 SYBR Green or 500 nM SYTOX Orange, and varying concentrations of PDGF. Specifically, 5 μL of 400 nM aptamer in assay buffer (10 mM Tris-HCl, pH = 8.0, 50 mM KCl, 3.3 mM $MgCl_2$, 0.1% BSA) was mixed with 5 μL of 4 SYBR Green or 2 μM SYTOX Orange in the same buffer. 10 μL volumes of varying concentrations of PDGF were prepared in protein buffer (1 PBS buffer, 10.1 mM Na_2HPO_4, 137 mM NaCl, 2.7 mM KCl, 1.8 mM KH_2PO_4, 1.0 mM $MgCl_2$, and 1% BSA). The workflow was slightly different for human serum samples, as follows: 2.5 μL of 800 nM aptamer in assay buffer was mixed with 2.5 μL of 8 SYBR Green; 5 μL of varying concentrations of PDGF in protein buffer were added to 10 μL aliquots of diluted serum; all solutions were mixed to give final serum ratios of 1:3 (25%) or 1:7 (12.5%). All final 20 μL mixtures of aptamer and protein (with or without serum) were then incubated at 37 °C for 15 min, and the temperature was scanned from 4 °C to 90 °C at 0.5 °C min^{-1}. At each set temperature, fluorescence was measured after a 10 s delay with 470 ± 20 nm excitation and 520 ± 10 nm emission filters for SYBR Green staining and 575 ± 15 nm excitation and 630 ±

20 nm emission filters for SYTOX Orange staining (Bio-Rad CFX96$^{\text{TM}}$ qPCR system). Assays were carried out in triplicate, with standard deviations presented in figures.

3.2.4 Microchip electrophoresis

Using an Experion microchip electrophoresis system (Bio-Rad) along with DNA 1K Chip and Reagents Kits (Bio-Rad), mobility shift assays were carried out as described by Hu and Easley [168]. 5 μL of 7.2 μM aptamer was mixed with 5 μL of 7.2 μM DNA adaptor to facilitate increased intercalator binding. The adaptor sequence was as follows: /55-TAMK/GAG GAG AGG AAC ACC <u>CGA TTA AAT GTT GAT</u>, with the underlined portion complementary to the arm of the aptamer; the TAMRA label on this adaptor was not relevant to the current study. The mixture was incubated for 15 min at room temperature. 1.5 μL of the mixture was then added into 1.5 μL of either 3.6 μM or 1.8 μM PDGF or into 1.5 μL buffer for a control experiment. The final mixture was incubated for 15 min at 37 $^{\text{o}}$C, 1 μL was added to 5 μL loading buffer, and microchip electrophoresis with electrokinetic injection was carried out as described by the manufacturer.

3.3 Results and Discussion

3.3.1 Protein-stabilized DNA melting transitions

It is known that the thermal stability of proteins can be increased in the ligand-bound state. Based on this principle, Pantoliano et al. developed a thermal shift assay capable of measuring protein-ligand binding constants, facilitating applications in screening and drug discovery [169]. Their approach utilized protein staining dyes, which exhibit low quantum yields in aqueous solution but high quantum yields in low dielectric solvents, thus increasing fluorescence in the presence of denatured, or melted, proteins. The method was proven as generalizable to determine ligand binding constants with >100 protein targets, and the direct optical readout facilitated high-throughput analysis. A similar method was developed by Niesen et al., who showed that a standard qPCR instrument could be used to determine protein-ligand binding constants due to its thermal scanning capability [170]. However, these approaches were not

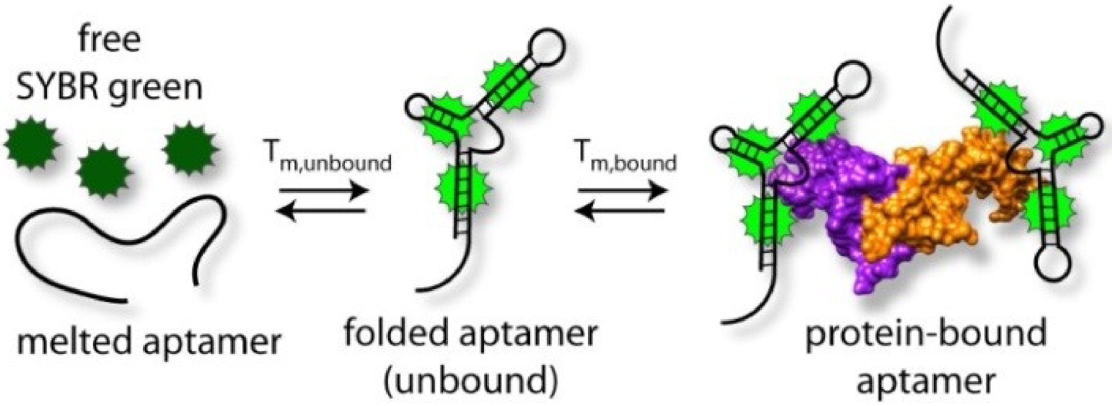

Figure 3.1: Schematic of thermofluorimetric analysis (TFA) of aptamer-protein binding. Intercalator fluorescence is low in the melted, free state (left) and high in the folded aptamer or protein-bound state (middle & right). Protein binding adds stability, increasing aptamer melting temperature, i.e. $T_{m,bound} > T_{m,unbound}$.

used for quantitative measurement of a given protein in a biological matrix, presumably due to the inherent complexity and high signal from background proteins. Since others have shown DNA intercalating dyes capable of isothermal quantification of aptamer-protein interactions [171, 172], we reasoned that significant advantages could be gained by thermally resolving these complexes. Specifically, differential melting analysis of protein-stabilized DNA melt peaks should permit removal of fluorescence interference such as background autofluorescence [135].

In this chapter, we demonstrate that thermofluorimetric analysis (TFA), when coupled with DNA-intercalating dyes, can be used to quantitatively report aptamer-protein interactions in biological fluids. Unlike the methods using differential protein melting [169, 170], TFA monitors aptamer melting, leveraging the increased thermodynamic stability afforded by protein binding. Differential melting of dye-intercalated aptamers allows quantitative delineation of protein-bound aptamers from unbound aptamers, even in the presence of significant autofluorescence in human serum. In contrast to the previous method [135], which utilized thermal scanning to measure binding of fluorescently labelled aptamers or antibody-oligonucleotide pairs and a connecting strand, this approach is simplified further through direct interrogation of the protein-aptamer stability. As shown by the schematic in **figure 3.1**, a DNA-intercalating dye such as SYBR Green is used to quantify folded aptamers. Upon melting of the aptamer, fluorescence decreases to baseline levels (equilibrium shifted left in figure). Since protein-bound aptamers are inherently more thermodynamically stable, their melting temperature ($T_{m,bound}$) should be measurably higher than that of the unbound aptamer ($T_{m,unbound}$). This should allow quantitative discrimination between bound and unbound aptamers, yet without physical separation. If so, background fluorescence could be easily subtracted, since such a well-defined thermal transition should not be present in this interfering fluorescence background [135].

3.3.2 Thermofluorimetric analysis (TFA) of PDGF-aptamer interactions

As a proof-of-concept, TFA was applied as an assay of interactions of a single aptamer with its protein target. Platelet-derived growth factor B-chain (PDGF) is a homodimer that plays an important role in embryogenesis, connective tissue formation, and in cancer proliferation [173]. A high-affinity aptamer for PDGF exists [174], with the Kd value reported to be $\sim$100 pM [125], making this an excellent target for preliminary studies. First, to verify the functionality of our slightly modified PDGF aptamer sequence, we carried out a microchip electrophoresis mobility shift assay [168]. As shown in **figure 3.2A**, the free aptamer migrated past the detector at around 47 s, while the aptamer-protein complex migrated significantly slower and passed the detector around 65 s. The decrease in free aptamer peak area at 47 s was observed to be PDGF concentration dependent, consistent with earlier work [168]. The two peaks observed around 65 s could be attributed to the 1:1 and 2:1 aptamer:protein complexes, although this was not explicitly proven. These peak areas were not significantly different at 150 and 300 nM PDGF, but saturation at 150 nM was expected with 300 nM aptamer and 2:1 complex formation.

Next, TFA was carried out using a standard qPCR instrument in the presence and absence of protein. It is clear from the derivative data (-dF/dT) in **figure 3.2B** that a more thermally stable species was present in solution, having a melting temperature of approximately 63 °C compared to the free aptamer peak at 57 °C. Even at a PDGF concentration of 10 nM, the new peak was easily distinguished from the free aptamer peak. Furthermore, the methodology is functional with other DNA intercalating dyes, as shown in **figure 3.2C** with SYTOX Orange and in **figure 3.3** using Thiazole Orange. **figure 3.3** also shows that other proteins can be assayed using TFA. Thiazole Orange was chosen considering the effective DNA secondary

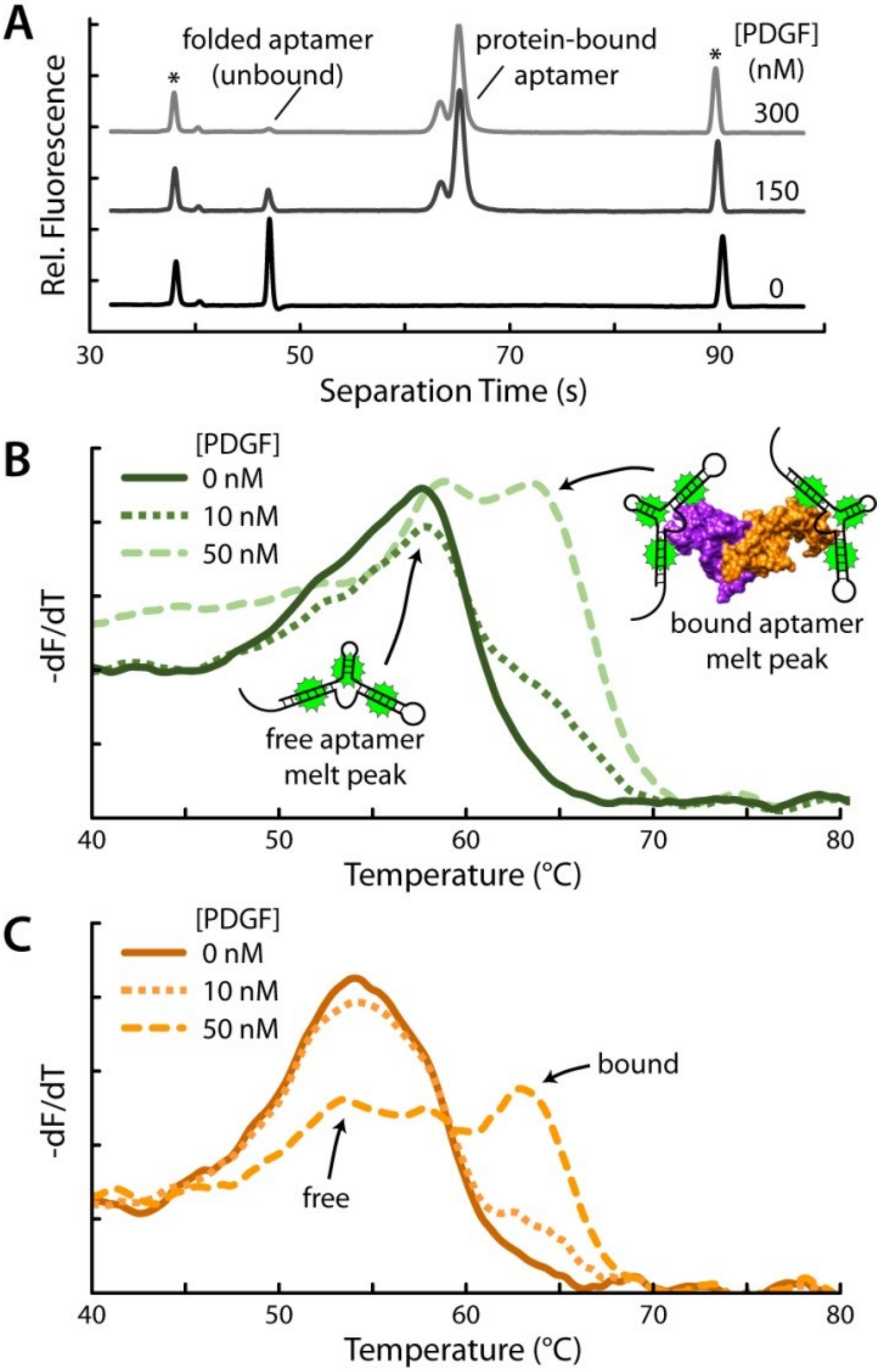

Figure 3.2: Aptamer-protein binding studies. (A) Binding of aptamers to the PDGF target was confirmed using a microchip electrophoresis mobility shift assay. Size markers (15 and 1500 bp) are labelled with stars. Thermofluorimetric analyses (TFA) using (B) SYBR green or (C) SYTOX Orange intercalating dyes were then validated as a readout mechanism for aptamer-protein binding.

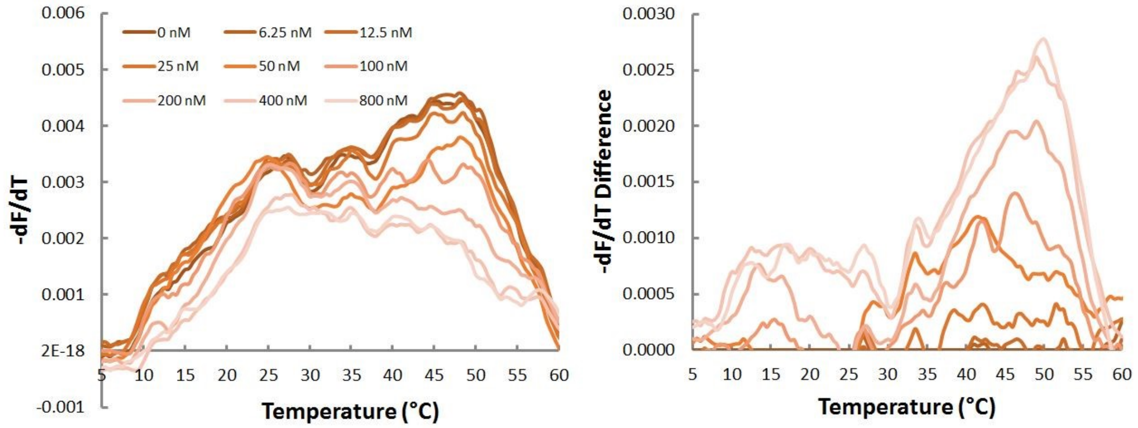

Figure 3.3: Validation of thrombing TFA using thiazole orange (TO) staining dye. Although other tested dyes (SYBR Green, SYPRO Orange) were ineffective for TFA with thrombin aptamers, the G-quartet binding dye, TO, shows promise for detection of additional proteins. As noted in the text, these types of issues highlight that binding mechanism remains important, such that TFA must first be evaluated for each protein target of interest.

structure in thrombin aptamer is G-quadruplex and thiazole orange is the dye can stain the G-quadruplex [175, 143, 176]. Together, these data suggested that protein concentration could be measured without physical separation using TFA. From the results of PDGF and thrombin, there are two possible reasons of the fluorescence change. One is the change of aptamer thermal stability with protein bound; another is that aptamer-protein binding interferes the staining of aptamer by intercalating dye, where the total fluorescence can be changed but the aptamer stability changes are undetectable.

3.3.3 TFA for homogeneous protein quantification

Figure 3.4A-B proved that the fluorescence emission is only due to the intercalating dye bound with aptamer (**figure 3.4A**) and protein with intercalating dye is no fluorescence contribution (**figure 3.4B**). The data analysis is demonstrated in **figure 3.4C-E**. From the results in **figure 3.4 A**, 100 nM PDGF aptamer shows strong fluorescence intensity and high sensitivity at same time because in the linear regression (**figure 3.4 F**), the slope of calibration curve from 100nM aptamer same as 50 nM but 100nM aptamer possesses higher fluorescence intensity in total. By varying the PDGF concentration and holding aptamer levels at 100 nM, we demonstrate that TFA can be used as a quantitative readout of protein levels. In **figure 3.5A**, the PDGF-bound aptamer melt peak is highlighted further by using -dF/dT difference plots, where the -dF/dT trace from the blank measurement ([PDGF] = 0) is subtracted from each protein-dependent -dF/dT trace. The figure depicts a typical set of runs with varying [PDGF]. The inset image shows the same -dF/dT difference plots presented as images, where grayscale colour density is used to depict the concentration dependence of the bound aptamer melt peak (darker pixels = more intense -dF/dT peak). As shown in **figure 3.5B**, triplicate TFA gave a linear response through at least 25 nM PDGF and maximal response at 50 nM. Plotted in the figure are peak heights of the protein-bound aptamer melt peaks in the -dF/dT difference plots. Assay saturation at 50 nM is expected with 100 nM aptamer probes, since there are two aptamer binding sites on each PDGF molecule. With homogeneous fluorescence readout, this system afforded a sub-nanomolar limit of detection (LOD), at 0.74 nM PDGF.

3.3.4 TFA permits subtraction of serum autofluorescence

Finally, a major advantage of TFA is the ability to subtract background fluorescence that does not exhibit clearly defined melting transitions. We demonstrate this advantage using homogeneous, optical protein quantification in human serum. **Figure 3.6A** depicts the -dF/dT difference plot images (grayscale colour density) of PDGF spiked into minimally diluted (1:7 and 1:3) human serum samples. Shown in **figure 3.6B** are the peak heights as a function of protein concentration. As expected, general matrix effects from serum partially degrade assay performance, with sensitivity decreasing with increasing serum fraction. However, the assays in serum retained 61% and 42% of the sensitivity in buffer (for 1:7 and 1:3 dilutions, respectively), while isothermal versions of the assay (25 °C) were essentially nonresponsive to protein (**figure 3.6C**). These results confirm that autofluorescence can be largely subtracted using TFA, allowing robust quantitative analysis of protein levels using a simple, mix-and-read, optical technique in human serum, even at a mere 1:3 dilution. LODs were 1.8 nM and 10.7 nM in the final 20 μL serum samples diluted 1:7 and 1:3, respectively. If correcting to the whole serum LOD, the 1:7 dilution (12.5% serum) provides a more favourable result, allowing direct quantification of as low as 14 nM PDGF in a serum sample. The whole serum LOD was not optimized in this work, since we analysed only spiked samples.

3.3.5 Application of single aptamer TFA in aptamer SELEX

In our understanding, as long as the aptamer bound with protein can induce the aptamer structure change, TFA of single aptamer assay can be established. But not only as assay for protein quantification, this method is potentially applied in aptamer SELEX. One reason for the

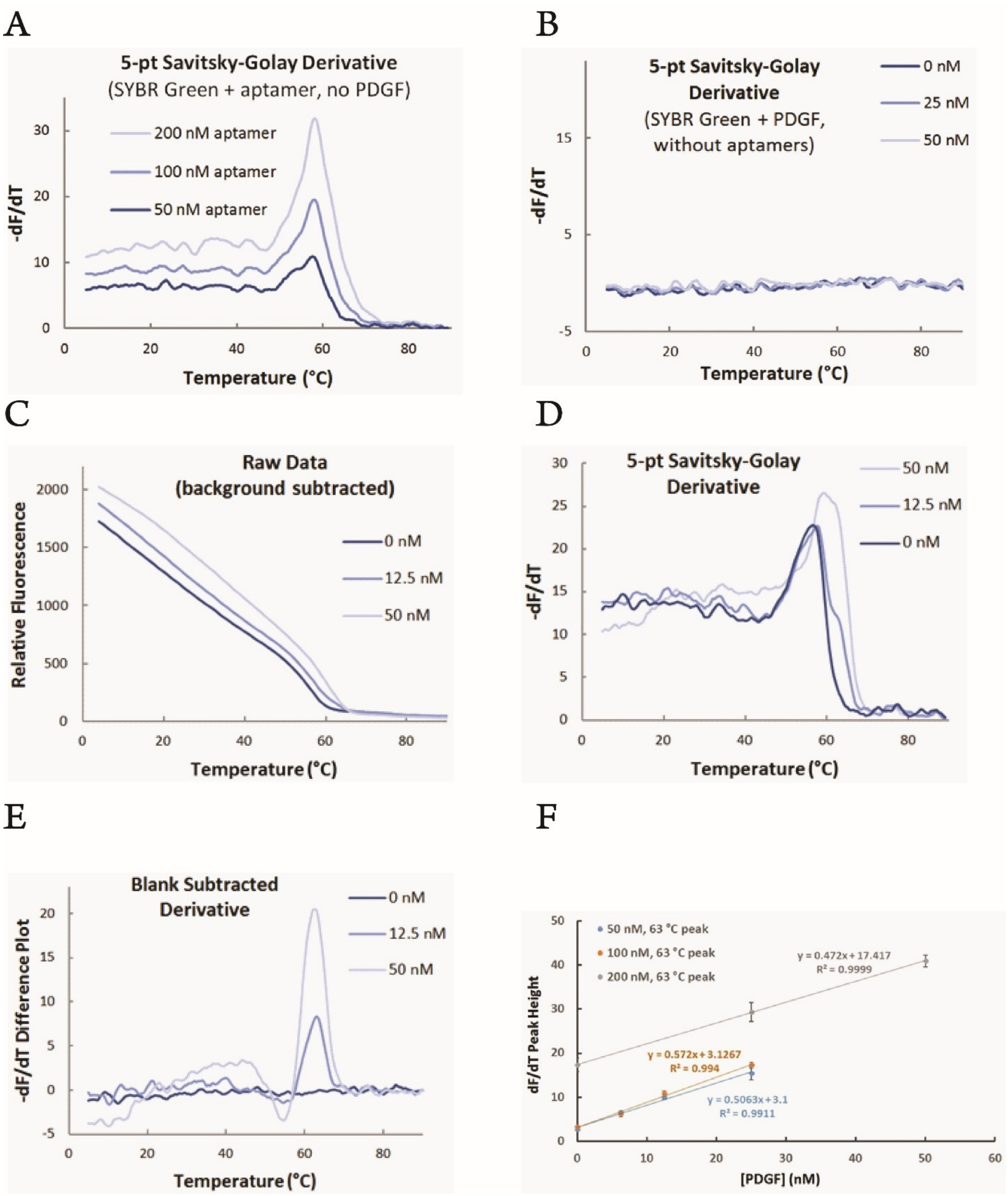

Figure 3.4: Caption next page.

Figure 3.4: (Previous page.)Data analysis. (A) Control experiments to test SYBR Green binding to varying concentrations of aptamers in the absence of PDGF confirmed that aptamer quantities could be determined using SYBR Green and TFA. -dF/dT signal was shown to be directly proportional to aptamer quantity. (B) Control experiments to test SYBR Green binding to varying concentrations of PDGF in the absence of aptamers suggested that there was no appreciable binding. This data confirms negligible protein-SYBR Green interactions, allowing confidence in aptamer-related peak assignments. (C-E) Data processing workflow for -dF/dT difference plots. The background trace (SYBR Green in buffer; no aptamer or protein) was first subtracted from raw thermofluorimetric data to give the plots in C. A 5-point Savitsky-Golay derivative was calculated for DNA melting peak analysis in D, and -dF/dT difference plots in E were calculated by subtraction of the average 0 nM derivative plot (blank). (F) TFA for PDGF quantification was evaluated with different probe concentrations (50, 100, and 200 nM). The highest sensitivity and lowest background was obtained with 100 nM probe, thus most measurements shown in this manuscript were carried out with 100 nM probe concentration. 50 nM probe showed similarly low background but slightly lower sensitivity, while 200 nM probe concentration exhibited much higher background and lower sensitivity toward protein.

low-yield and time- and cost-consuming aptamer SELEX is the unmet demand of methodologies to track the SELEX progress, the binding affinity changing during the evolution. TFA for aptamer-protein complex quantification can discriminate and measure the bound aptamer from unbound ones, which can be used to calculate the dissociation equilibrium constant to monitor the aptamer enrichment. **Figure 3.7** shows that the sixth run of aptamer pool can bind to target more tightly than the library pool based on the target concentration for 50% fluorescence quench.

3.4 Conclusions

We have demonstrated homogeneous, aptamer-based protein quantification using direct fluorescence and thermal scanning, i.e. by using thermofluorimetric analysis (TFA). Results show that TFA permits delineation of unbound and protein-bound aptamers without physical separation. As shown in previous chapter with affinity probe pair [135], a unique capability of TFA is the effective subtraction of autofluorescence in biological samples such as serum, permitting optical protein quantification in serum with low nanomolar detection limits using a simple, mix-and-read workflow and a standard qPCR instrument.

Since many aptamer-protein binding interactions could feasibly be interrogated in this manner, it is expected that a major advantage of TFA should be the generality of the readout.

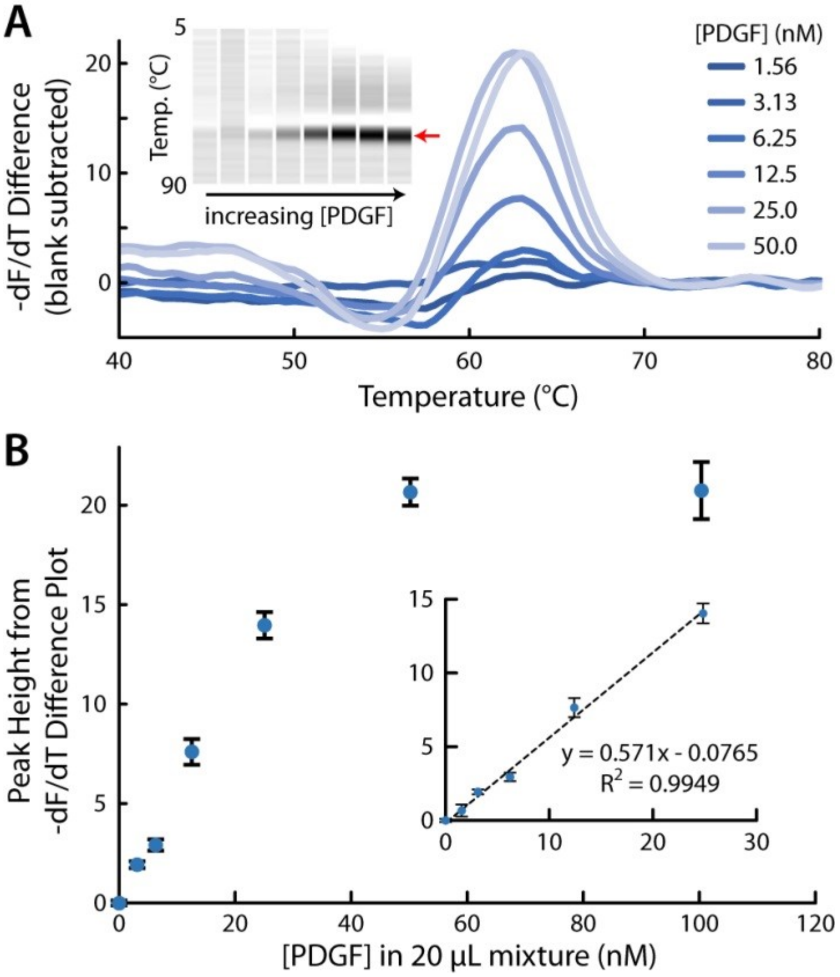

Figure 3.5: Quantitative protein detection with TFA. (A) Blank-subtracted -dF/dT difference plots highlight the protein-bound aptamer melt peaks at 63 °C. Grayscale colour density plots of the same data are inset (peaks labelled with red arrow). (B) Peak heights from -dF/dT difference plots showed a linear assay response through at least 25 nM PDGF, with maximal response at 50 nM as expected. The assay LOD was 0.74 nM PDGF in buffer.

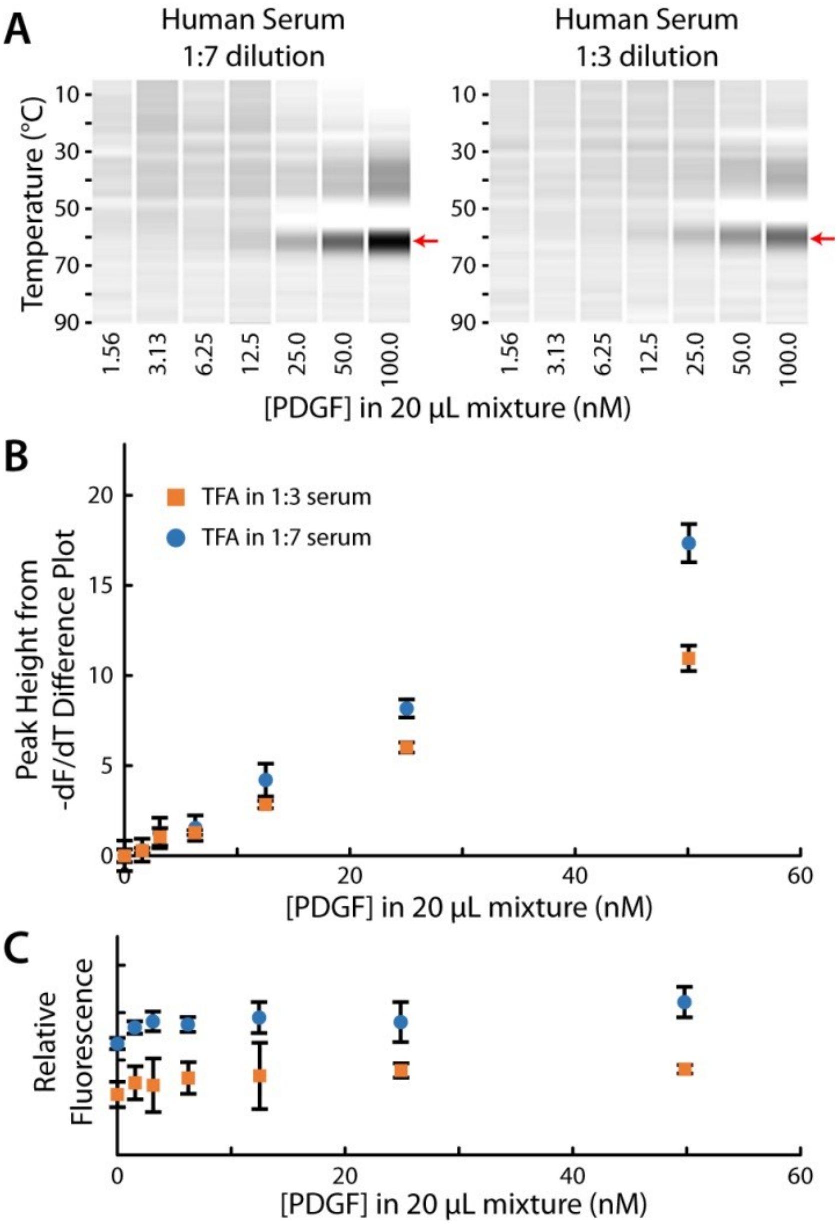

Figure 3.6: Homogeneous quantification of proteins in human serum via TFA. (A) Grayscale colour density images of -dF/dT difference data in 1:7 and 1:3 diluted serum. Protein-bound aptamer peaks (red arrows) show assay sensitivity decreasing with increasing serum fraction. (B) Homogeneous protein assays in serum using direct optical readout were enabled by TFA, (C) while corresponding isothermal protein assays were non-functional due to high background in serum.

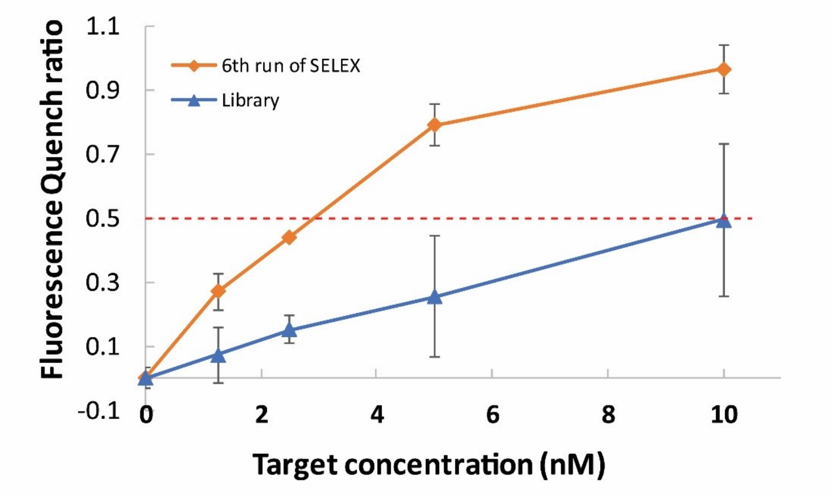

Figure 3.7: TFA of single aptamer assay for aptamer SELEX monitoring. 25 nM of aptamer from the 6th run of SELEX and library were used to quantify targets by 2X SYBR Green. Fluorescence quench is due to the aptamer-protein binding, so the quench ratio represents the bound aptamer. The target is a adipokine secreted from white adipose tissue.

Judging from our prior work using microchip electrophoresis mobility shift assays [168] and from the results, it is likely that TFA could be successfully applied to various other aptamer-protein complexes or even to aptamer-small molecule complexes. However, it is yet to be determined whether differences in aptamer structure could preclude the use of TFA for certain aptamer/target combinations, and the data suggests that various intercalating dyes and aptamer/target combinations should be explored. In the future, based on the simplicity of TFA and its unique capability to overcome fluorescence interferences, studies should be directed toward evaluating responses to various analyte classes in complex matrices. Also, TFA can be exploited as a simple but effective method to facilitate the aptamer SELEX.

Chapter 4

Active microfluidic droplet system to quantify adipose tissue glycerol secretion at high temporal resolution

4.1 Introduction

From the discussion in the introduction chapter, the dynamic studies of hormone and metabolite secretion from cells and tissues such as pancreatic islets and adipose tissue is critical to understand their biochemical and physiological functions and develop therapeutics for related diseases. Traditionally, secretion sampling of metabolites and hormones from cells or tissues is done in tubes and typical temporal resolution of sampling is around one to five minutes for metabolites, and ten minutes to hours for hormones, depending on the abundance of targets and restricted by manual handling [177, 178, 179, 180]. In tube secretion sampling, not only a large amount of tissue or cells are required and the temporal resolution is limited, but also the sampling from steady culture system is highly different from the true, *in vivo* response [181, 182, 183, 184].

With the increasing biological applications of microfluidic devices recently, the state-of-the-art in cell culture systems and its temporal limitations have begun to change. Microfluidics became a powerful tool in studies of cell biology such as cell proliferation, growth, mobility, response for chemical stimuli [185, 62, 186]. One suitable application of microfluidic chips is the investigation of dynamics in ions, genomics and proteomics of cells or tissues under the different treatment due to the automatic and tight control of chemical and mechanical microenvironments by microfabricated systems, which mimics the *in vivo* situation [186, 187]. In dynamic studies, proteomics is more difficult than gene expression, due to the low amount and no direct amplification methods. Off-line quantification by assays such as ELISA is expensive and inefficient and can restrict the temporal resolution of dynamic studies. Besides proteins, we are also interested in metabolites such as glucose, fatty acids, and glycerol from adipose tissue because the dynamics in their metabolism are tightly related to cytokine secretion and cell function in the pancreas, liver, and adipose tissue. However, they remain to be investigated due to lack of adequate tools available to others. Therefore, the integration of sampling and detection on-chip is desperately needed. The Kennedy group has reported a continuous flowing system for glycerol and non-esterized fatty acids quantification from 3T3-L1 adipocytes [188, 189, 190, 191]. But due to the low mixing in continuous flowing microfluidics, a long incubation channel is required, and this will come with high dispersion of the analytes in the solution [99, 89, 192]. As a result, temporal resolution will be diminished during the long incubation process before it reaches the detection window. In such systems, including our own devices, the surface chemistry of the channels (PDMS in our work) should be carefully dealt with to reduce the adsorption of hydrophobic molecules to the surfaces. These above-mentioned problems of high dispersion, slow mixing, and surface chemistry can be solved through our droplet-based analytical system.

A microfluidic droplet system has been recently developed in our laboratory to generate droplets actively and detect insulin secretion from single pancreatic islets by homogeneous immunoassays without the need of a continuous flow perfusion system and PDMS coating [88]. However, homogeneous immunoassays for small molecule quantification, such as one for glycerol, are rarely available. Instead, coupled enzyme assays are well developed for these small molecules. Meanwhile, microfluidic droplets have been proved extraordinarily useful for kinetic studying of enzyme reactions [99, 89]. Thus, our goal in the work reported in this chapter is to apply coupled enzyme reactions in the droplet microfluidic system for small molecule quantification at high temporal resolution.

Here, using this improved and extended droplet system, we sampled and detected glycerol secretion from both 3T3-L1 adipocytes and primary adipose tissue at high temporal resolution. Such high resolution has revealed, for the first time, a pulsatile secretion pattern of glycerol in tissue that is not present in cell clusters. These results suggest the presence of cell-to-cell communication in adipose tissue that is similar to that of pancreatic endocrine tissue.

4.2 Experimental settings

4.2.1 Materials and Reagents

Deionized water was produced by BarnsteadTM MicroPureTM Wter Purification system (ThermoFisher Scientific, serial No. 42034239) with the resistance value as 18.2 MΩ·cm at 23.5 °C and particles less than 0.2 μm. All of buffers in the experiments were prepared with the deionized water. The SYLGARD® 184 silicone elastomer kit (Dow Corning, Midland, MD) was used to make PDMS (Polydimethylsiloxane), containing elastomer base and its curing agent. The silicon wafers were from the Polishing Corporation of America (Santa Clara, CA). The negative photoresist SU-8 2015 and SU-8 2050 was from the Michrochem (Westborough, MA) and the positive photoresist, AZ 40XT-11D, was bought from the AZ Electronic Materials USA (Somerville, NJ). Heat inactivated HyClone™ Fetal Bovine Serum (FBS) was from Gel Healthcare Life Sciences. Hanks' Balanced Salt Solution (HBSS) was purchased from Lonza. D-glucose, HEPES (4-2-hydroxyethyl-1-piperazineethanesulfonicacid), penicillin-streptomycin, NaCl, $CaCl_2 \cdot 2H_2O$, KCl, $MgCl_2 \cdot 6H_2O$, resorufin sodium salt, cholortrimethylsilane, agarose (ultra-low gelling temperarue, molecular biology grade), human insulin solution, 3-Isobutyl-1-methylxanthine, dexamethasone, and Glycerol Assay Kit (cat. MAK 117-1KT) were purchased from Sigma-Aldrich (St. Louis, Missouri). Isoproterenol hydrochloride (>98%, purity), Bovine serum albumin (BSA), Accutase cell detachment solution were from VWR (West Chester, PA). DMEM (Dulbecco's Modified Eagle Medium, low glucose, L-glutamine, sodium pyruvate and phenol red, cat. 11885084), DMEM (no glucose, no glutamine, no phenol red, cat. A11430-01), MEM Non-Essential Amino Acids Solution (100X) (cat. 111400502), Sodium Pyruvate (100 mM) (cat. 11360070), Fetal Bovine Serum (qualified, USDA-approved regions, cat. 10437010), Penicillin-Streptomycin (10,000 U/mL) (cat. 15140122), Dulbecco's Phosphate Buffered Saline (DPBS), and HCS LipidTox Green Phospholipidosis detection reagent (1000X) for cellular imaging from ThermoFisher Scientific (Grand Island, New York). Pico-Surf 2% in Novec 7500 was purchased from Dolomite Microfluidics

(Norwell, MA). NovecTM 7500 Engineered Fluid (HFE 7500) was from 3M. The human insulin concentration was confirmed by protein absorbance at 280 nm (A_{280}) using a NanoDrop 1000 spectrophotometer (ThermoFisher).

4.2.2 Masters fabrication

The microdevice photomasks were designed in Adobe Illustrator and printed by Fineline Imaging (Colorado Spring, CO) at 50,800 DPI resolution. The silicon wafers were ready to use after shaken in diluted sulfuric acid (1M) at 220 rpm speed for 30 min, washed and shaken in D.I. water for 30 min and dried by air. The microchip includes two-layer: the valve channel is on the top and the flowing channel in the bottom. The master wafers were fabricated by commonly used photolithography. For the control layer, the negative photoresist (SU-8 2015) was spin-coated on the wafer at 2000 rpm for 45 seconds, following soft bake on hotplate for 5 min at 95 ^{o}C, then cool down slowly, UV exposure for 2 min ($\sim$200 mJ/cm^2) by an in-house built ultraviolet lithography light source [193], and hard bake for 5 min at 95 ^{o}C, developed in SU-8 developer for 7 min. The photomask is with about 20-μm photoresist in thickness.

For the master of the flow layer, both of negative and positive photoresists were used. In the **figure 4.2A**, the part of chip across with control layer was fabricated by AZ40XT-11D and the long incubation channel was made by SU-8 2050. The negative photoresist layer was done at first. The SU-8 2050 was spin-coated on the pretreated wafer at 3000 rpm for 45 seconds, following soft bake on hotplate for 5 min at 95 ^{o}C, then cool down slowly, UV exposure for 2 min ($\sim$204 mJ/cm^2), and hard bake for 5 min at 95 ^{o}C, and developed in SU-8 developer for 7 min. The photomask is with 50-μm photoresist in thickness. After the pattern was developed, the wafer was put in oven for 30 min at 60 ^{o}C. Then the AZ was used for the next step. The AZ40XT-11D was warmed to room temperature and spincoated on the wafer at 2000 rpm for 45 seconds, soft bake on the hotplate for 5 min at 65 ^{o}C, 5 min at 95 ^{o}C and 5 min at 115 ^{o}C. Then it was cooled down to room temperature very slowly. The photomask was aligned on the AZ photoresist coated wafer and exposed under UV for 90 seconds ($\sim$153 mJ/cm^2), then the post exposure bake was on the hotplate for 5 min at 65 ^{o}C, 5 min at 95 ^{o}C and 90 seconds at 105 ^{o}C. It was also cooled down to room temperature very slowly. The wafer was developed in AZ developer for 6 min. The last step was reflowing, processed on the hotplate for 10 min at 120 °C under the cover of petri dish partially. The negative photoresist layer is 50 μm in thickness, and the positive photoresist layer is 40 μm. After the photolithography was done, two wafer masters were ready to use.

4.2.3 Molds fabrication

The silicon molds were exposed to chlorotrimethylsilane(TMCS) vapor for 30 min before the soft lithography of PDMS. The PDMS precursor and curing agent was mixed at the ratio of 20:1, 10.5 g in total, and degassed and then spin coating on the valve channel master in the speed of 2400 rpm for 45 seconds. At the same time, the PDMS precursor and curing agent was mixed at the ratio of 5:1, 36 g in total, and degassed and poured on the flowing channel master. Both were baked at 60 °C for 30 min in the oven and the flow channel bulk chip were cut and aligned to the valve channel under 3X microscopy. The PDMS was continued to bake for another 4 hours in the oven. After PDMS stamps were peeled off, inlets and outlets punched by Miltex disposable biopsy punches, washed by methanol, air dry, and irreversibly bound to the cover slide (24 mm x 40 mm with 0.13-0.16 mm thickness) by plasma oxidization. The two-layer microchip is ready to use after thermally aged in the 60 °C overnight to avoid the uncured PDMS monomer leakage.

4.2.4 3D-printed template for the fabrication of cell culture reservoir

The 3D-printed templates and insert used in the device fabrication and experiments were designed in the 3D modelling computer program, SketchUp 2017, and printed by MakerBot Replicator 2 with PLA (polylactic acid) filament (HatchBox PLA, 1.75 mm diameter). The design of 3D mold for the fabrication of cell culture reservoir is shown in **figure 4.2B**. The microchip fabrication is as shown as above, except the 3D template was aligned on the wafer mold for the flow channel after pouring PDMS on. After the bulk PDMS was peeled off from the 3D template and wafer, the cell culture reservoir is formed with around 1-mm thick PDMS in the bottom. The 0.75-mm ID punch (69039-07, electron Microscopy Sciences, Hatfield, PA) was used for the tissue trapping reservoir connected to the inlet channel.

4.2.5 Automated flow control system of microchip

The 18 pneumatic control valves in the microfluidic chip were driven by solenoid switches (LHDA 0533115H, the Lee Company, Westbrook, CT) assembled on the metal manifold and under the control of a data acquisition device (PCI-6259, National Instrument, Austin, TX), which is driven by LabVIEW programming software. A valve driver circuit was used as the buffer and current amplifier between the PCI and solenoid switches. A house nitrogen gas source was used to actuate these pneumatic solenoid valves by 26-psi pressure adjusted by a pressure regulator. The control valves on microchip were connected to the corresponding solenoid valve with 90-degree angled 22-gauge blunt 304 stainless steel needles (Jensen Global JG22-0.5HPX-90, Santa Barbara, CA) through Tygon microbore tubing (0.02" I.D. X 0.06" O.D., Cole-Parmer, Vernon Hills, IL). The valve inlet interfaced with the control system were punched by 0.75-mm ID punch (69039-07, electron Microscopy Sciences, Hatfield, PA). An in-house written LabVIEW application was used to control the open/close of the valves. When the valve is set in close status, the solenoid switch will be activated to pressure the nitrogen gas into the dead-end channel of the control layer, filled with deionized water to avoid the air permitting into the channels, to deflect the PDMS membrane up to close the flow channel in the upper layer, which are push-up valve. The schematic of droplet formation by active control is displayed in **figure 4.2**.

4.2.6 Extraction of murine epididymal adipose tissue (eWAT)

C57BL/6J male mice were used in the project. All animal experiments were done in compliance with relevant laws, institutional guidelines and the protocols of 2017-3101 were approved by the institutional animal care and use committee (IACUC) of Auburn University. 12-week male mice, 20-week wild-type mouse and 20-week diet-induced obese (DIO) mouse were used in the experiments. Epidydimal white adipose tissue pads were extracted from mice described in previous papers [194, 195]. After extracted from the mice, they were transferred into 10 mL phosphate-HEPES buffer (10 mM HEPES, 135.3 mM NaCl, 2.2 mM $CaCl_2 \cdot 2H_2O$, 1.2 mM $MgSO_4 \cdot 7H_2O$, 0.4 mM KH_2PO_4, 2.2 mM Na_2HPO_4, 0.4 mM D-glucose, 2% BSA, pH

7.4). Fat pads were placed in the 60 mm Petri dish with phosphate-HEPES buffer and extra vasculature was removed by Iris micro dissecting scissor. 2 mm explants were punched from the fat pads by 2 mm sterile disposable biopsy punch and collected into glass tube with 4 mL phosphate-HEPES buffer. The explants were washed by the buffer for 3 times by centrifuging at 1000 rpm for 3 min. 3 mL buffer was removed by the syringe after centrifuge and 3 mL fresh buffer was added to next step of wash. Then the phosphate-HEPES buffer was changed to fat serum media (DMEM + low glucose and phenol red with 12% fetal bovine serum, 120 units/mL Nystatin, 120 units/mL Penicillin-Streptomycin and 1.2X MEM NEAA), and the explants were washed in the media for another 2 times. After washed, the explants were placed in the sterile 96-well plate with 200 μL fat serum media and 3D-printed anchor to avoid the buoyance of fat tissue, each piece of explant in one well. The explants were cultured in the 37 °C incubator with 5% CO_2, which can be maintained up to 7-10 days if the serum media was refreshed twice per day. The explant for each experiment was pretreated in the high glucose (25 mM) and high insulin (2 nM) DMEM media without serum for 30 min before loaded on the microchip.

4.2.7 3T3-L1 cell culture, differentiation and encapsulation

3T3-L1 fibroblasts (CL-173) were from American Type Culture Collection (ATCC, Manassas, VA) and cultured in DMEM media with 10% BS to 100% confluent in 25 cm^2 cell culture flask. Following it, the adipogenic cocktail (DMEM +10% FBS with 0.5 mM 3-isobutyl-1-methylxanthine, 250 nM dexamethasone and 8.9 μg/mL insulin) was used to culture the cells for 4 days and then the differentiation media was removed and changed to insulin media (DMEM +10% FBS with 8.9 μg/mL insulin) to culture the cells for another 3 days. The 3T3-L1 adipocytes were used in the sixth day after differentiation. Adipogenesis of cells was validated by visualization of lipid droplet accumulation and staining of lipid droplets (**figure 4.1**).

For the encapsulation, the culture media was removed and the cell was washed by 4 mL DPBS for three times. 2 mL 1X LipidTox Green in DPBS was added into the flask and incubated at 37 °C for 30 minutes, cellular imaging was collected in FITC channel in Nikon Eclipse Ti-E fluorescence microscope. The staining solution was removed and cells were washed by 4 mL DPBS for three times. The cell detachment from the cell culture flask by incubating cells

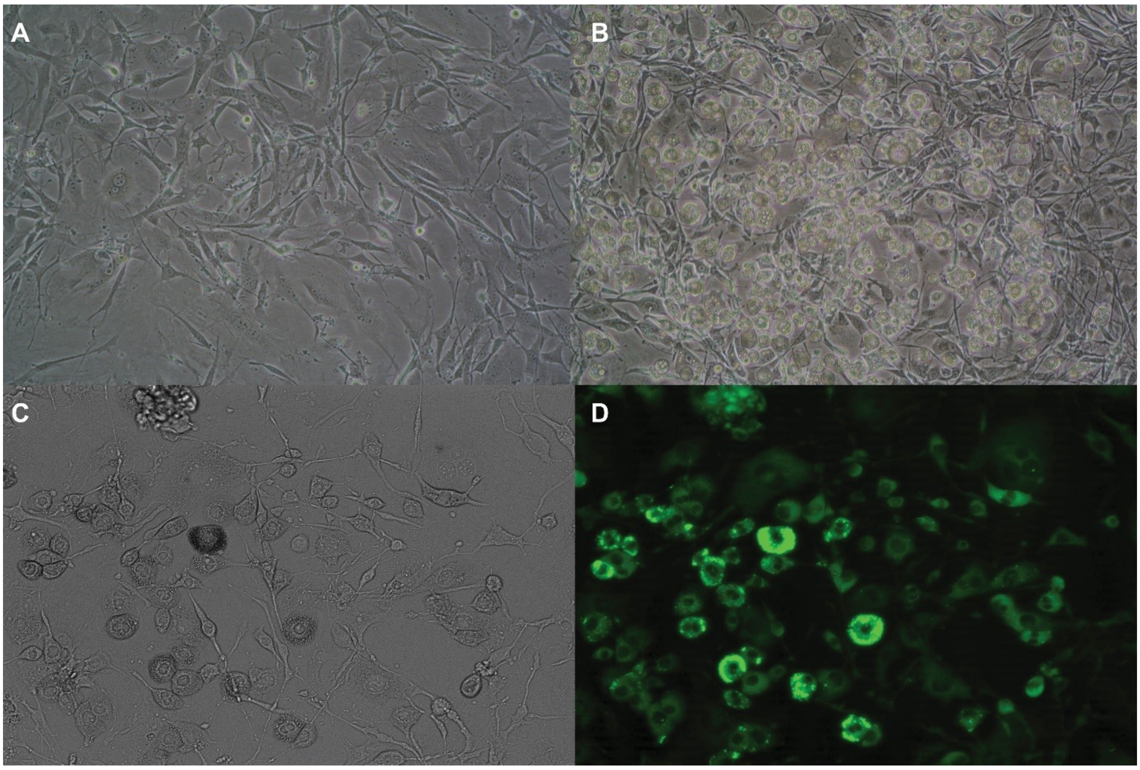

Figure 4.1: The culture and differentiation of 3T3-L1 cell line. (A) The fibroblasts of 3T3-L1 at around 90% confluence. (B) Differentiated 3T3-L1 adipocytes. The cell morphology is changed from the fibroblast-like to circular shaped with visible lipid droplets formed in the cells. (A) and (B) were captured by a digital camera (Nikon J1) under 10X magnification of Nikon TS100F inverted microscope. (C) DIC image and fluorescence image of 3T3-L1 adipocytes by the objective with 10X magnification. The lipid droplets in the adipocytes were stained by LipidTox Green and detected in the FITC channel of the fluorescence microscope.

with 2 mL Accutase cell detachment solution at 37 °C for 10 minutes. The cell suspension was transferred from the flask to 15 mL sterile conical tube and centrifugated at 1000 rpm for 3 min, then the upper layer of solution was aspirated and the cell pellet was resuspended in 200 μL cell culture media. Around 10 μL of cell suspension was loaded in the second inlet on the microfluidic device. 0.125 g agarose (ultra-low gelling temperature) was dissolved in 10 mL DPBS by heating in microwave for 15 seconds. The agarose gel solution was loaded in the first and third inlets on the device. HFE7500 with 0.5% Pico-Surf was utilized as oil phase and loaded in the oil inlet. The celldrop program was running with 350 ms of sample pump time and 20 of sample pump cycle, and 450 ms of oil pump time and 2 of oil pump cycle. The cell encapsulated droplets were collected in the reference inlet which was set as outlet in the specific application. The droplets suspension was chilled on ice for 5 min to gel formation, then the droplet layer (upper layer) was transferred to adipocyte insulin media in the 3 mL Petri dish and conserved in the 37 °C incubator with 5% CO_2 until using.

4.2.8 Glycerol release measurement, image acquisition and analysis

The microfluidic chip was set up on the stage of the fluorescence microscope mounted with a Tokai Hit microscope stage top incubator, with D.I. water back-filled into the microchip valve inlets. All experiments were operated at 37 °C in the incubator. For the standard curve of glycerol assay on the microfluidic device, 1 μL of dye reagent and 1 μL of ATP from the glycerol assay kit were mixed with 135 μL glycerol assay buffer from the glycerol assay kit with 0.25% BSA and 20 μL of the solution was added into the substrates inlet (**figure 4.2A**). 1 μL of enzyme mix reagent from the glycerol assay kit was mixed with 99 μL glycerol assay buffer with 0.25% BSA and 20 μL of the solution was loaded into the enzyme inlet (**figure 4.2A**). 85 μM resorufin was prepared in DMEM (no glucose, no glutamine, no phenol red) with 1% BSA and added into the reference inlet (**figure 4.2A**). And HFE7500 with 0.5% Pico-Surf was used as oil phase and loaded in the oil inlet (**figure 4.2A**). The glycerol standards (0 μM, 18.75 μM, 37.5 μM, 75 μM, 150 μM, 300 μM) were diluted from 0.1M glycerol stock by DMEM (no glucose, no glutamine, no phenol red) with 0.25% BSA and 30 μL of the solution added into the cell culture inlet (**figure 4.2A**) one by one. The"droplet generation" program was run to form droplet with 350 ms sample pumping time and 2 sample pump cycles, 400 ms of oil pumping time with 2 cycles, and 250 ms of reference pumping time with 3 cycles. Each of the standards was run for 8 minutes to form droplets and then changed to another concentration of standard by pipetting. The fluorescence imaging in the detection window (**figure 4.2A**) were operated continuously in 150 ms interval in TRITC filter cube (λ_{ex}=540/25 nm, λ_{em}=605/55 nm) by CCD camera (CoolSnap HQ2; Photometrics Scientific) interfaced with Nikon inverted T*i*-E fluorescence microscope (40X, 0.75 NA). The incubation time for enzyme assay in the long channel was around 10 minutes after the droplet was formed.

For the glycerol secretion from eWAT and encapsulated 3T3-L1 adipocytes, the experiment settings were similar as above, except the cell culture inlet was loaded with tissue explants or encapsulated cells. The pretreated tissue explant or encapsulated cells was added into the 0.75-mm reservoir in the cell culture inlet (**figure 4.2C**). For the eWAT explant, a 3D-printed insert was used to help trap the tissue. The treatments of HGHI [25mM glucose and 2nM insulin in DMEM (no glucose, no glutamine, no phenol red) with 0.25% BSA] and LGLIS [3mM glucose, 50 pM insulin with 20 μM isoproterenol in DMEM (no glucose, no glutamine, no phenol red) with 0.25% BSA] were administrated to the cell culture inlet alternatively to test the glycerol secretion response from the samples. Fluorescence images were captured similarly as above. The fluorescence intensity data from the images were analyzed by ImageJ and data analysis was processed in Excel.

4.3 Results and Discussion

4.3.1 Microchip design

We have shown the development of our microfluidic droplet system and its application for homogeneous immunoassays in recent work [88], which is the first generation of the droplet-based microfluidic device including a Y-shape channel for probe loading and secretion sampling, T-junction for droplet formation by using fluorinated oil as continuous phase, a reference inlet to introduce the lock-in method in quantification [114, 113, 115], and long incubation channel for the equilibrium of assay solution. However, the application of this first generation

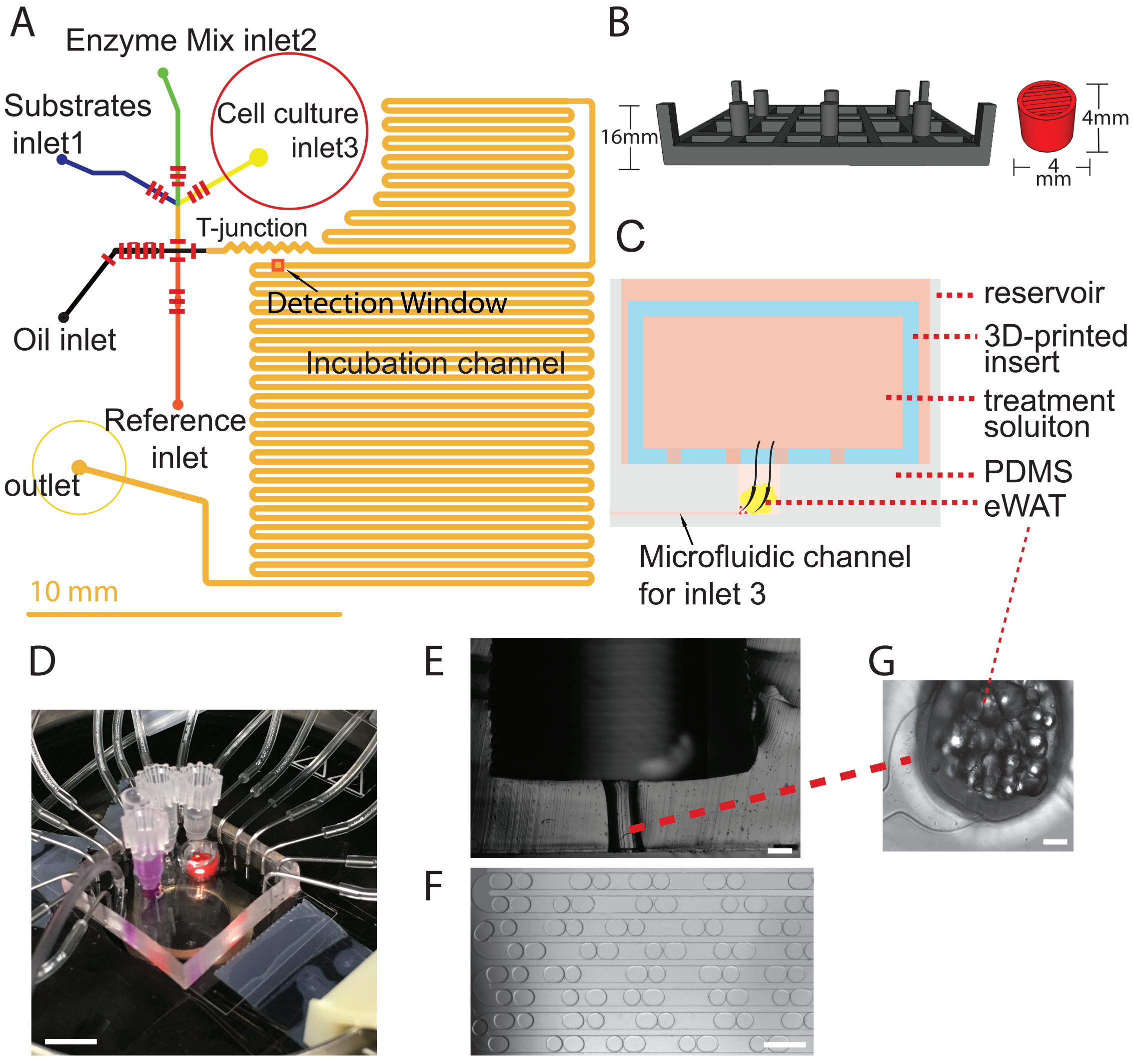

Figure 4.2: Microchip design and experimental setting. (A) Two-layer microfluidic chip design: the short red lines, representing the microvalves, is the bottom layer for controlling; the inlets and incubation channel are in the top layer for fluid flow. (B) 3D-printed template (dark gray) for cell culture reservoir fabrication, and the 3D-printed insert (red) used in eWAT tissue sampling to trap the tissue in the reservoir during solution exchange. (C) Schematic figure of the cross-section of cell/tissue culture reservoir. (D) Experimental setting on the stage of fluorescence microscope, connected to solenoid switches. Scale bar, 10 mm. (E) Sliced cross section of reservoir for cell/tissue culture reservoir: upper open part for bulk solution, narrow lower part for trapping tissue or cell spheroid close to microchannel. Scale bar, 500 μm. (F) Formed droplets in the long-incubation channel, with small-sized droplets as references and large sample droplets (see also supplementary video 1). Scale bar, 500 μm. (G) eWAT tissue in the narrow part of the reservoir in E, connected to the microchannel for sample droplet formation. Scale bar, 150 μm.

For video 1 about droplet formation, visit the website as below. `http://www.auburn.edu/cosam/faculty/chemistry/easley/research/hujuan/video001.htm` of device was limited for mix-and-read assays such as homogeneous immunoassays, where the probes can be pre-mixed before loading into the inlet. Low cost, simple workflows and sensitivity are the benefits of homogeneous immunoassay [135, 136], but it requires the antibody pair or the pair of other affinity probes like aptamers, and currently only a small number of target molecules secreted from tissues or cells can be detected by affinity probe pairs in homogeneous assay format, especially for primary adipose tissue. Adipose tissue is a critical organ for energy homeostasis by regulating the glucose and fat metabolism, as well as a endocrine organ [22, 196]. A variety of small molecules are taken up into and released from the adipose tissue under the regulation of a variety of hormones [197]. It is important to quantify the uptake and secretion of these molecules and monitor the dynamics of these processes for better understanding the physiological and pathological functions of the tissue. The choices of homogeneous assay for small molecules is much narrower, but a number of enzymatic assays are well developed, e.g. assays for glucose, glycerol and non-esterized fatty acids. Therefore, the second generation of our microfluidic droplet system was designed for sampling, reaction of secretome with enzymatic assay reagents, on-chip incubation, and on-chip readout. For the coupled-enzyme assay, the substrate and enzymes should be separated before mixing with the samples, so one extra inlet is included in the second chip design, ending with three inlets for sample droplet formation: one inlet for substrate, another for enzymes mixture, and a third one for cell/ tissue culture similar to the first design (**figure 4.2A**). Most other components in the microchip are the same as in the first design [88], except the microvalves for oil pumping were altered. A serpentine-shaped microvalve with five crossing points was exploited in the this device to increase the contact area, effectively increasing the oil pumping volume by about 8-fold for each pump cycle, with the volumetric oil flow rate of 9.3 μL·h^{-1} (**figure 4.4**).Incidentally, this means that the new design can replace the first chip for homogeneous immunoassays with faster droplet generation and higher temporal resolution, thus the device is now suitable for immunoassays and coupled enzyme assays.

Another important component of the chip is the cell-culture reservoir (**figure 4.2E**), which is fabricated by 3D-printed template (**figure 4.2B**, black one) [88, 194]. As the schematic in **figure 4.2C** demonstrates, the treatment solution was continuously flowing through the tissue,

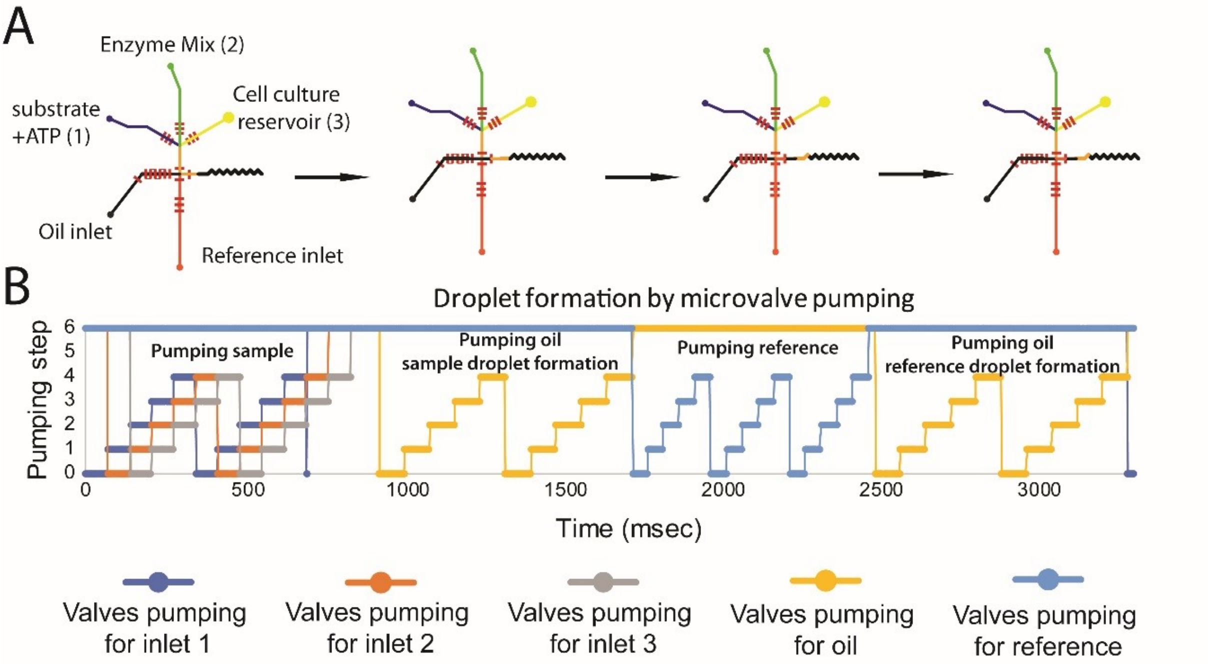

Figure 4.3: In-house written LabVIEW application was run to control the formation of a pair of sample and reference droplets. (A) Schematic figure shows the open/close states of microvalves in control layer for droplet formation. (B) 5-step pumping was used to control the solution flowing into the channel sequentially to generate a pair of droplets. Each micropump includes three valves, and the pumping steps for each group of microvalves are labelled from 0 to 4, representing the 001,101, 100,110,111, (1 = close and 0 = open; 5 is 000 and 6 means 111).

carrying secreted analytes into the microchannel to be trapped into droplets thereafter. The continuous flow brings fresh media to tissue or cells and takes the metabolic molecules away to reduce auto-inhibition of biochemical reaction in the cell–arguably more akin to the *in vivo* situation. We previously showed this samplinge design capable of complete capture of analytes from the tissue with high temporal resolution [88].

4.3.2 Microchip function

An in-house written LabVIEW application was used to control the microvalve pumping in a 5-step pumping cycle, shown in the **figure 4.3** and supplementary video 1. A pair of sample and reference droplets were formed by doing sample pumping, oil pumping, reference pumping and oil pumping sequentially. The droplet size was controlled by the number of pumping cycles and was chosen with consideration for the width of incubation channel, since a widened pancake-shape of droplet in the incubation channel facilitates microscopic imaging

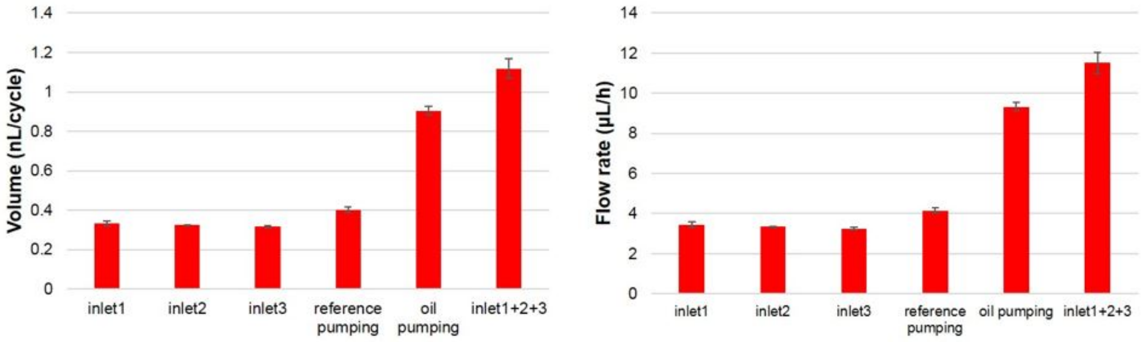

Figure 4.4: Measurement of the valve pumping volumes. (A) Volume for each pumping cycle from the various inlets. 3 tests were done for each group of valves, and the pumping frequency is 2.86 Hz. (B) Flow rate measurement by pumping each group of valves.

by achieving a consistent optical path length. The droplets with smaller size than the channel width will flow through the channel in different rates and the order of droplets could also be undesirably altered with small droplets. Since the volume for each pumping cycle of the micropumping is highly consistent, droplets could be generated at precise volumes. As shown in **figure 4.5**, droplet sizes during a 50 minutes testing experiment were stable, changing less than 1.5%. For all experiments reported in the chapter, 2 cycles of sample pumping at 2.86 Hz, 3 cycles of reference pumping at 4 Hz, and 2 cycles of oil pumping at 2.5 Hz were set in the programming to produce droplets with average volumes of 2.58 ± 0.04 nL (%CV= 1.5%) for the sample droplets and 2.18 ± 0.04 nL for the reference droplets (**figure 4.5**).

4.3.3 Calibration of glycerol enzymatic assay in microfluidic droplets

For every experiment, the microchip was calibrated with glycerol standards before sample measurements. The substrate and ATP were mixed and loaded in the left reservoir, the enzyme mix was added into the middle reservoir, and different concentrations of glycerol were added into the right reservoir in sequence. Each concentration of glycerol was loaded to form droplets for 8 minutes, and then the input (right reservoir) was changed to another concentration of glycerol by pipette. 85 μM of resorufin was utilized as the reference to correct the fluctuation of fluorescence measurement by imaging. Other than the tissue/cell culture reservoir, the reagents in the other three reservoirs were sealed by mineral oil to avoid the evaporation during the experiments (see in **figure 4.2D**). Generated droplets travelled in the long incubation channel

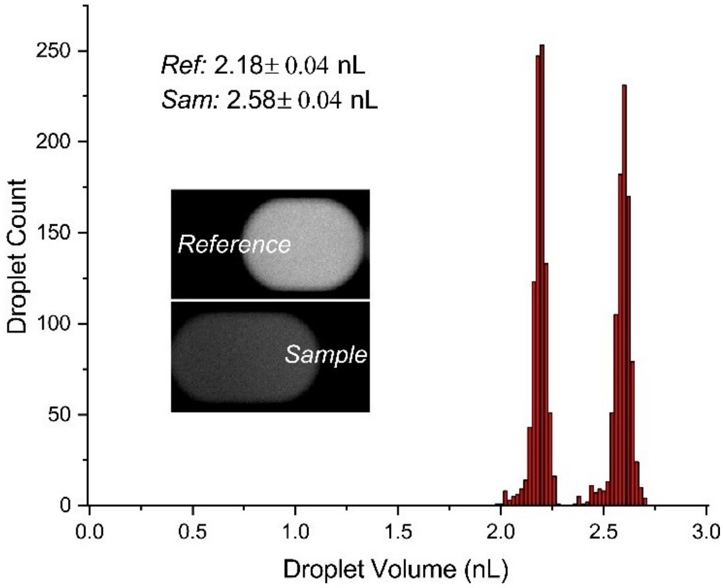

Figure 4.5: Droplet volume measurement shows high precision control with our device, using 914 droplets for each type. The volumes of droplets were calculated by $V = Ah + \frac{\pi h^2 P}{8}$ (h is the channel depth, A is the droplet area from top-view images, P is the perimeter of the droplet).

for ∼8 minutes to reach the plateau of enzyme reaction before the fluorescence images were taken. The BSA in the assay buffers was shown to obviate through- oil, diffusional cross-talk of resorufin between droplets compared to the test without BSA (data not shown). Besides, BSA is also required for cell secretion experiments, since these proteins help carry out the lipolysis products such as fatty acids through solution and thereby reduce the auto-inhibition effects. The data indicates that the enzyme reaction in droplets can reach equilibrium within about one minute in static droplets (**figure 4.6**), and the reaction rate should be faster in moving droplet due to the mixing by formation of counterrotating vortices18. After images were collected, the fluorescence intensity data of sample and reference droplets were obtained by image analysis in ImageJ (**figure 4.7**) and the fluorescence intensity ratio between the sample droplet and reference droplet was taken as response to concentration changing of glycerol, shown in **figure 4.8A**. In the calibration curve of glycerol (see in **figure 4.8B**), the limit of detection was determined to be 0.74 μM in the droplet, which equals 1.92 fmol in amount, based on a volume of 2.58 nL of one sample droplet. The average percent coefficient of variance (%CV) of the glycerol assay in droplets was about 1.7%.It can be observed that the fluctuations shown in raw data from reference droplets, due to optical perturbations during changing of glycerol solutions,

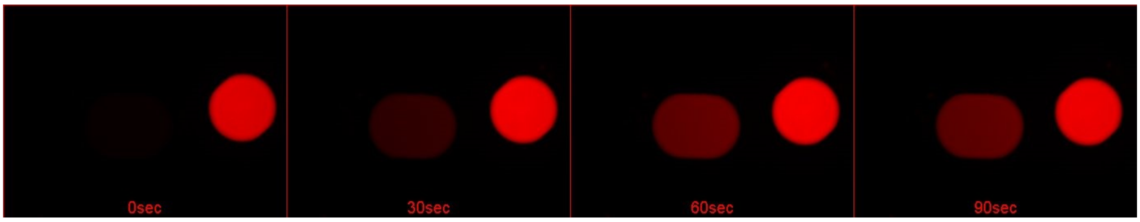

Figure 4.6: The progress of the detection kit's enzyme reaction was monitored in static droplets. The smaller droplet was reference droplet with 85 μM resorufin, and the larger was the sample droplet containing 100 μM glycerol, enzymes, substrate, and ATP. Imaging started as soon as the droplets were formed. The produced fluorogenic molecule, resorufin, in the static sample droplet reached its highest concentration within about one minute

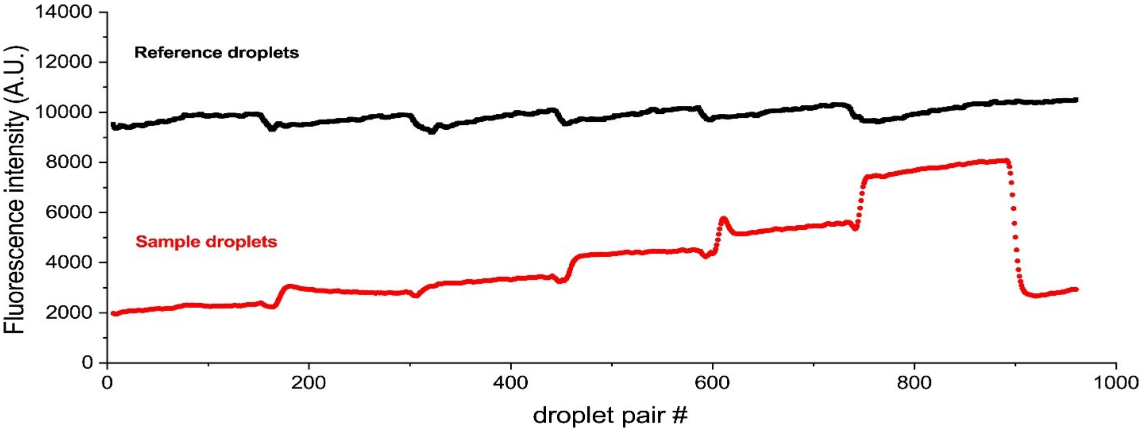

Figure 4.7: Raw data of fluorescence intensity for each droplet during continuous, on-chip calibration. The fluorescence images were analyzed by ImageJ. Based on the droplet size and sequence, reference droplets could be separated from the sample droplets. The number of each droplet pair is shown on, the x-axis, corresponding to about 55 minute total for ~1000 droplets.

could be corrected through our lock-in droplet analysis methodology [113, 114, 115]; **figure 4.8** shows the corrected data.

4.3.4 Encapsulation of adipose cell line into spheroids using microfluidics

To apply our device to glycerol secretion required adipocytes to be interfaced to the microfluidic reservoir; however, it is very difficult to manipulate single cells or small numbers of cells in this way. For this reason, we developed a method–using the same microfluidic device–to encapsulate adipocyte cells (3T3-L1 adipocytes) into agarose droplets. Differentiated from 3T3-L1 fibroblasts, 3T3-L1 adipocytes are typically characterized as white adipocytes in the basal bioenergetics and gene expression profile, and they respond sensitively to catecholamines and insulin; the cells widely used as an *in vitro* model of white adipocytes [198]. To fit the cells

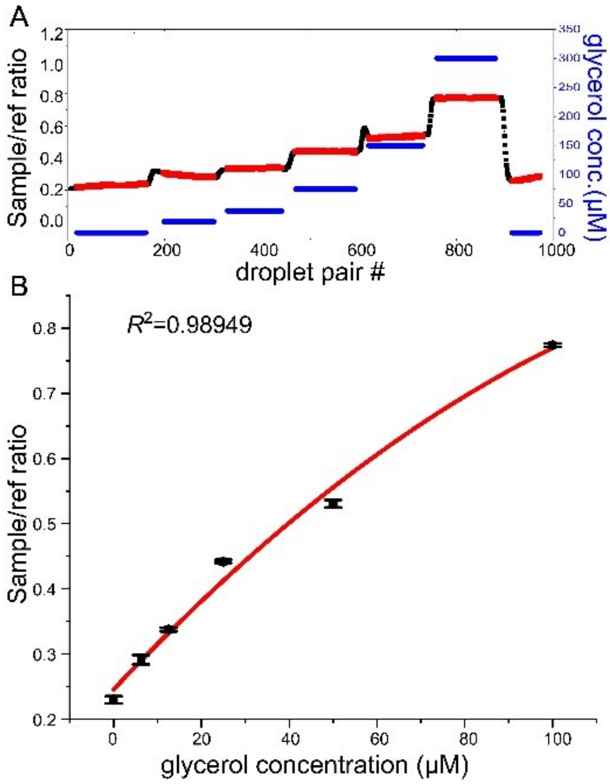

Figure 4.8: Calibration of glycerol enzyme assay in droplets. (A) The sample-to-reference ratio (from raw data in **figure 4.7**) for each droplet pair responded to the different concentrations of glycerol loaded into the cell culture inlet. Red labeled data were used in the standard curve calculation. (B) Corresponding calibration curve, which was fitted to a quadratic polynomial model with *R*-square 0.98949.

into our cell culture system, we used the same device to encapsulate mature 3T3-L1 adipocytes into agarose gel droplets to form 3-D spheroids of cells with around 200 μm diameter. Once gelled, these spheroids could then be easily loaded into and removed from the cell culture reservoir by pipetting–akin to manipulating pancreatic islets [88].To form the spheroids, the cell suspension was added into the middle aqueous inlet, and the other two inlets were filled with 1.25% agarose with ultra-low gelling temperature (in DPBS buffer). In this case, the reference channel (normally an inlet) was used as an outlet for droplet collection (see **figure 4.9** and supplementary video 2). The collected droplets were then gelled into 3D spheroids by reducing the temperature on ice for 3 minutes. We found that adipocytes could be cultured within the gel for up to one week and that cell viability was usually reduced by about 15% after passing through the microvalves (data not shown).

It should also be noted that the calculated flow rate of media (see below) was about 92 ± 4 μL/min for per gram of cells or tissue in our system, which is close to the experimental measurement of blood flow rate through the epididymal adipose tissue in the morning, 0.10 ± 0.1 mL/min per gram tissue in un-anesthetized rats [199]. The author also showed the blood flow rate is 0.17 ± 0.1 mL/min per gram tissue in the evening. From the secretion plots below and from calculated flow rates in our previous tests [88], we can concludeclaim that thise flow rate of sampling was high enough to carry out secreted targets without accumulation in the reservoir. This represents a major difference between our the continuous flowing sampling system and more standard, static sampling methods in tubes.

4.3.5 Real-time quantification of glycerol release from 3T3-L1 adipocytes

To validate that glycerol secretion could be quantified in real time via the microfluidic droplet system, glycerol secretion from these encapsulated adipocyte cells was quantified under different treatments. As seen in **figure 4.10** , the lipid droplets in the adipocytes were stained by LipidTox Green to visualize the trapped adipocytes and confirm that they were present in the agarose spheroids. After changing the treatment from high glucose with high insulin (HGHI) to low glucose with low insulin (LGLI) and 20 μM isoproterenol, the glycerol release from these adipocyte spheroidss was sampled using our microfluidic device, mixed with enzyme

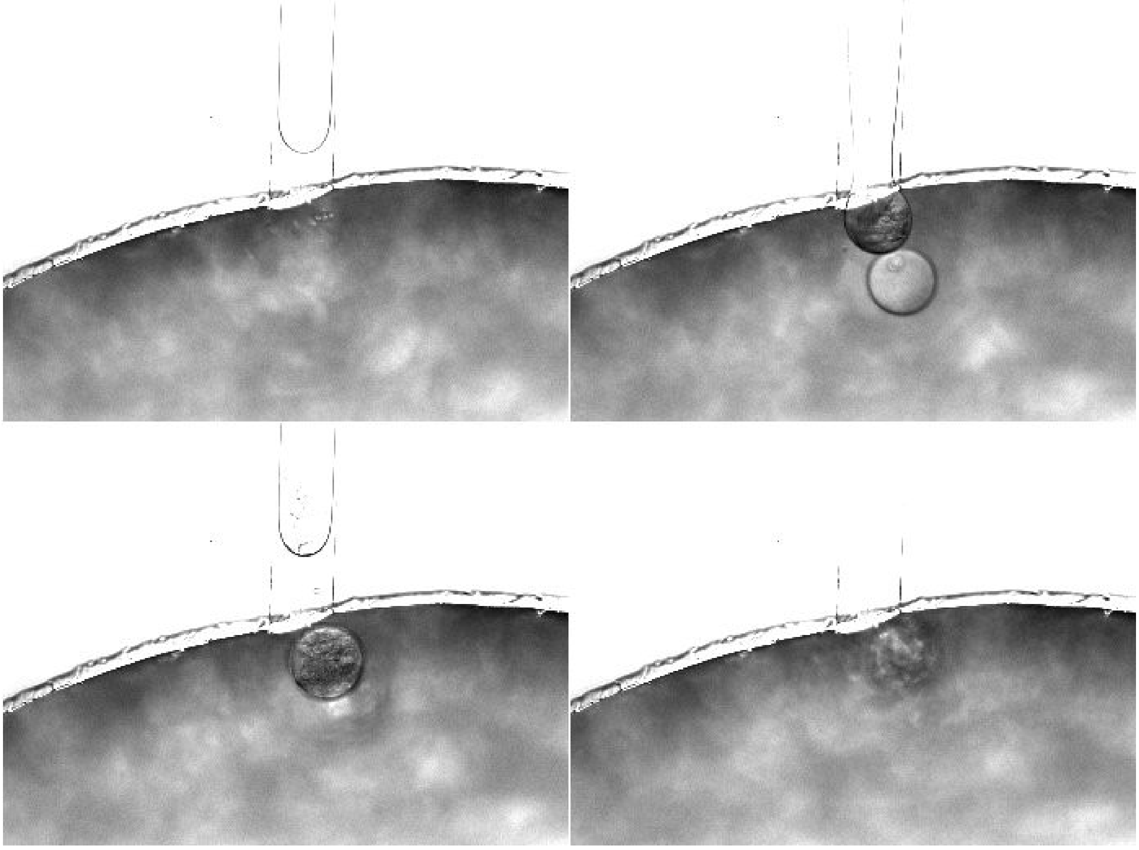

Figure 4.9: 3T3-L1 adipocytes spheroid generation in the microfluidic droplet chip (see also supplementary video 2).

For video 2 about cell encapsulation, visit the website as below. `http://www.auburn.edu/cosam/faculty/chemistry/easley/research/hujuan/video002.htm`

assay reagents, then detected by fluorescence imaging in the downstream channel. The processed and calibrated data (see section 4.3.3) is shown in **figure 4.10A**.Glycerol release from the adipocyte spheroids was observed to increased almost immediately (**figure 4.10A**), and the secreted amount was increased by by 2.5 to 5.5 fold compared to baseline, depending on the cell number in the gel (**figure 4.10E**). Previous results from others by using continuous flowing microfluidics have reported a similar fold changes [188]. Also noteworthy is the relatively constant secretion rate that was observed both before and after stimulation, an important point for comparison to tissue results below. Thus, our high-resolution microfluidic sampling system with integrated enzyme assay was proven functional for assaying cellular secretions.

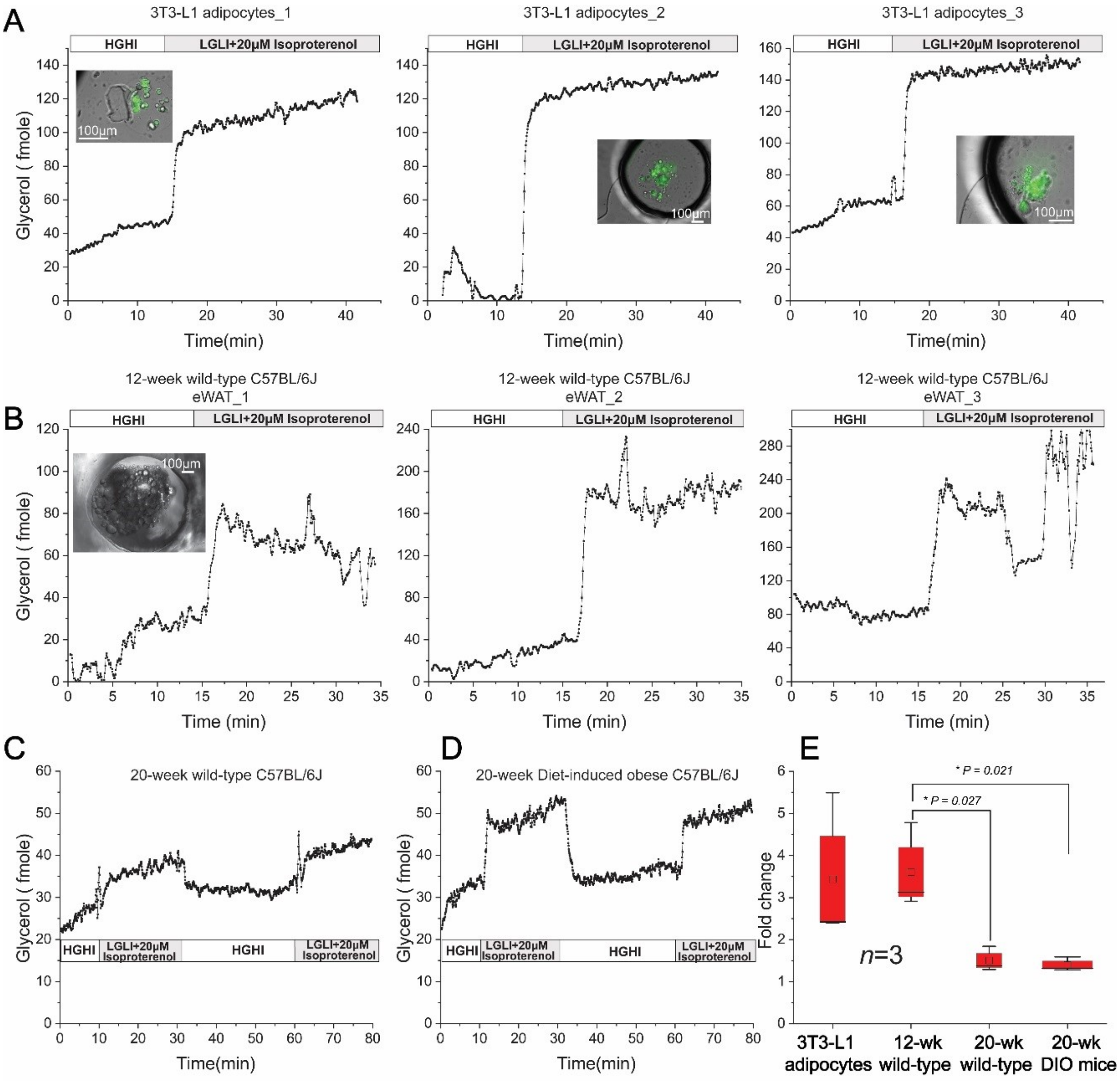

Figure 4.10: (A) Glycerol release from three 3T3-L1 adipocytes spheroids was observed to respond quickly to treatment changes, with sustained release rates before and after, using our high temporal resolution microfluidic droplet sampling and analysis system. Inset images show merged DIC and fluorescence images of stained adipocytes in the spheroids. (B) By contrast, glycerol release from three primary murine eWAT explants (12-week old mice) was observed to oscillate. (C) Glycerol release from eWAT explants from 20-week old mice was less pronounced, as was the release from 3T3-L1 cell spheroids. (D) Explants from 20-week old diet-induced obese (DIO) mice. (E) Compiled fold changes of glycerol release from the four different types of eWAT explants after changing the treatment from the HGHI to LGLI+20 μM isoproterenol.

4.3.6 Real-time quantification of glycerol release from eWAT

Primary cells are considered as ideal models for drug discovery and toxicity tests because they are representative of phenotypic gene expression and behavior of organs [200]. However, even short periods of culturing can reduce their specificities if the cells are isolated from surrounding tissue by digestion. Therefore, when available, undigested primary tissue should be a better *in vitro* model and should present more organotypic secretomes. For this reason, we have used our device here to sample glycerol secretion from primary murine eWAT explants taken directly from mouse tissue. Appropriate sizes of eWAT explants were loaded into the cell culture reservoir and glycerol secretion under different treatments was quantified. As shown in **figure 4.10B**, fast and dramatic changes were observed within one minute after changing the treatment from HGHI to LGLI with isoproterenol, and obvious dynamic changes were superimposed upon these responses to treatments. Note that these changes would not be observable with other analytical systems. It is through our droplet-based, quantitative secretion sampling at 3.3-second temporal resolution that these effects are observable. In **figure 4.10E**, the glycerol secretion from adipose tissue of a 12-week old mouse increased 3-5 fold upon treatment, which was similar to the response from 3T3-L1 adipocytes used in the sixth day after differentiation.

Surprisingly, glycerol release from eWAT explants exhibited an oscillatory pattern (**figure 4.10B**), which was not observed in encapsulated 3T3-L1 adipocytes (**figure 4.10A**). Four pieces of adipose tissues from two 12-week wild-type mice were applied in the glycerol secretion test, and all four experiments showed similar oscillations with periods of 1-2 minutes (three data sets shown).

Since our micro-analytical system sampled at such high temporal resolution, it was possible to delve deeper into the analysis and carry out fast Fourier transforms (FFTs) on the data. **Figure 4.11** shows the comparisons of oscillatory patterns between encapsulated cells lines and eWAT explants. A low-pass filter with 1.0 Hz cutoff was applied to the time-domain data (shown in top plots) to aid in visualizing oscillations, and the frequency domain data from 0 to 2 min^{-1} are also shown (bottom plots). Little to no glycerol secretion oscillations were observable from the cell spheroids, while strong oscillations were observed from the tissue from

12-week old mice. Rich patterns can be observed in the frequency domain data of these tissues, in contrast to the flat and featureless frequency domain data from cell spheroids. Interestingly, fewer oscillations were observed from tissue of the 20-week old mice. These results suggest a possible role for tissue connectivity in the adipose tissue's dynamic secretory function.

As described in the introduction chapter, these types of patterns can be a result of small molecule transfer between the cell population in the tissue through gap junctions, channels on cell membranes that permit intercellular communication by facilitating exchange of small molecules such as ions and metabolites. Such gap junctional tissue coupling can transfer signals between cells and induce the synchronization of electrical and metabolic activities in the connective tissue [46]. Notably, the synchronization and oscillation of insulin secretion from pancreatic islets have been shown to result from gap junctional electrical coupling of beta-cells, which results in oscillations of Ca^{2+} , followed by downstream insulin oscillations [4, 5, 6].Since previous reports have shown that similar gap junctions also exist in the epidydimal white adipose tissue (eWAT) [50, 51],and since we did not observe oscillations from cell spheroids, we hypothesize that our observed glycerol secretion oscillations from eWAT tissue explants were also related to gap-junctional coupling within the tissue sampled in our microfluidic system. We expect that gap junctions in 3T3-L1 adipocytes could have been lost during the cell detachment and encapsulation process, which would result in the observed oscillation deficiency. On the other hand, several publications (using lower-resolution sampling) have reported that plasma glycerol and free fatty acid concentrations oscillated by the regulation of adrenergic signaling in periods of 6±1 min [201],and one group suggested that lipogenic oscillations with ~5-min pulses were driven by glycolysis in adipocytes and might have impact on the delivery of FFA and glycerol to liver [177]. In our investigations, we note that whole adipose tissue explants were analyzed which can conserve phenotypic characteristics and the local microenvironments within the adipose tissue compared to isolated adipocytes.Further studies are needed to confirm or deny the role of gap junctional coupling in adipose tissue to oscillatory glycerol secretion. Nonetheless, that our results provide evidence for cell-to-cell communication and lipogenic synchronization and oscillation that exists naturally in the adipose tissue. To our knowledge, these results are the first to show such oscillations, and the collection of these data was uniquely enabled by our novel, droplet-based microfluidic sampling and analysis system. Another result we observed was that the fold-increases in glycerol release in response to isoproterenol became lower, and the oscillations got smaller and less pronounced in the old mice and obese mice (**figure 4.10C**, **4.10D** and **4.10E**, **figure 4.11D** and **4.11E**). The lack of a difference in glycerol release from eWAT of the 20-week wild-type mouse and the DIO mouse may be because the mouse became more overweight at 20 weeks compared to 12 weeks, with or without high-fat feeding, which can be proved by simply comparing the total weight of eWAT extracted from the three types of mice.However, further investigations are in need for a better understanding of this intercellular communication and its changes related to age and obesity.

Another result we observed is that the glycerol release increase responding to isoproterenol becomes lower and the oscillation gets smaller and less in the old mouse and obese mouse (**figure 4.10C**, **4.10D** and **4.10E**, **figure 4.11D** and **4.11E**). The indifference of glycerol release of eWAT between 20-wk wild-type mouse and DIO mouse may be because the mouse got more obese in 20 weeks than 12 weeks with or without high-fat feeding, which can be proved by simply comparing the total weight of eWAT extracted from the three types of mouse. Further investigations are in need for better understanding of the intercellular communication and its changes related to age and obesity.

4.4 Conclusions

Our automated microfluidic droplet system was improved to allow on-chip coupled enzyme assays following droplet-based sampling at high temporal resolution from cells or tissue. Droplets with highly consistent volume were generated without connecting to macroscopic plumbing such as syringe pumps to control the flow rate of solutions for droplet formation and cell perfusion. Homogeneous immunoassays and enzyme-coupled assays are now able to be applied in this system to enable unique dynamic studies of small moleculess and low-abundance proteins secreted from either primary tissue or cell spheroids. Only small number of cells or tiny sections of primary tissues are needed for investigation in our droplet system, and different treatment solutions are easily changed and delivered to pass through the sample freshly. This

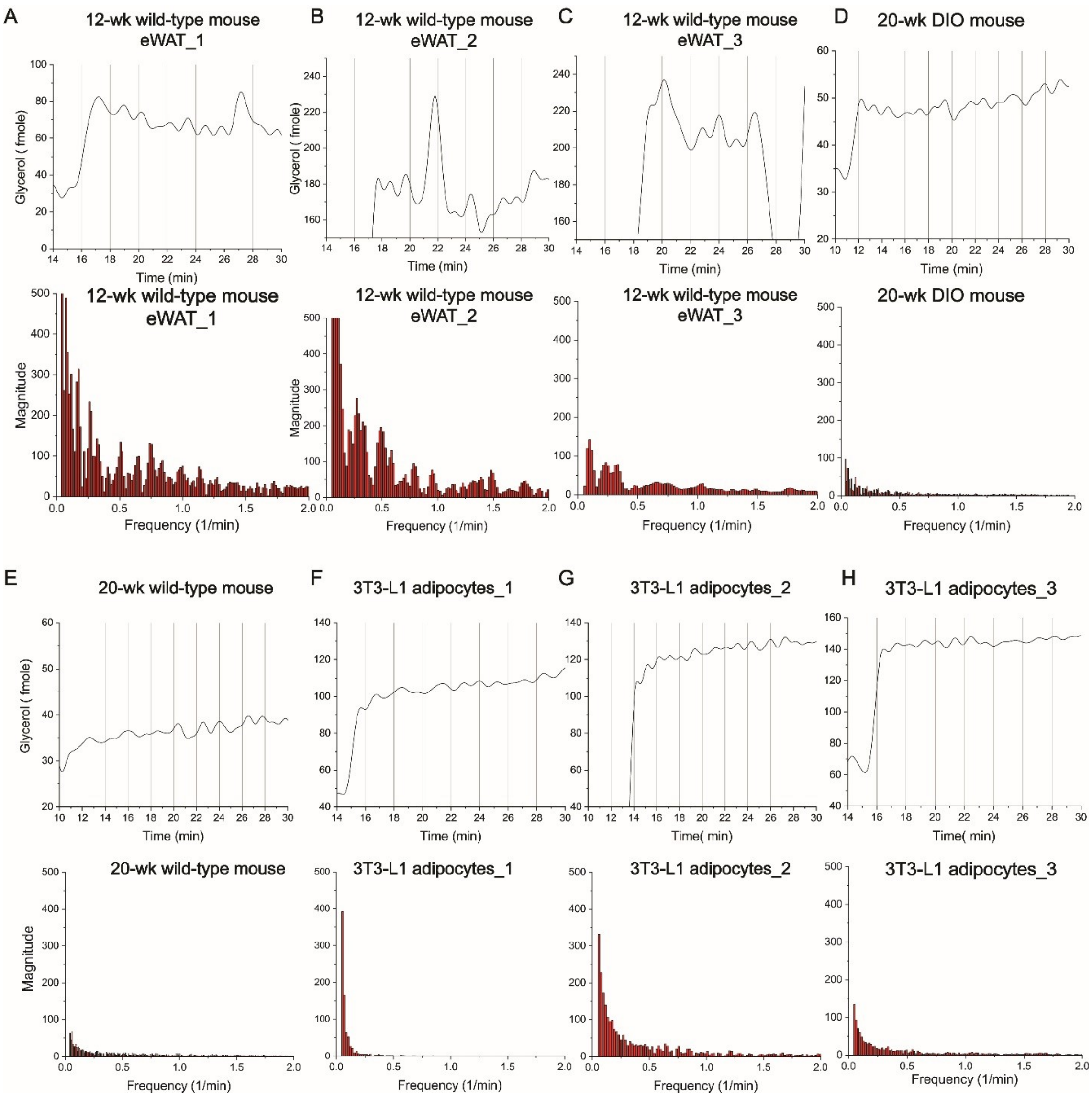

Figure 4.11: Oscillation analysis of glycerol release from primary white adipose tissues and 3T3-L1 adipocytes. In each group of figures, the upper plot shows that data in **figure 4.10** were analyzed by low-pass filter with 1 Hz frequency cutoff to demonstrate the oscillation of glycerol release in the eWAT from C57BL/6J mouse. The lower plot displays that data in **figure 4.10** were analyzed by fast fourier transform to show the less oscillation in 3T3-L1 adipocytes than eWAT.

droplet system can conserve temporal resolution of sampling with minimal diffusion and dispersion, and it should be possible to achieve higher temporal resolution by improving the chip design.

The investigations of primary tissue using our microfluidic droplet system shows different glycerol secretion pattern from the encapsulated cell, which may be the results of cell-to-cell communications. But more studies are required to get more solid conclusions about intercellular connections and our device provides the platform for this type of dynamic secretion studies.

Chapter 5

Asprosin secretion studies

5.1 Introduction

Cells can adapt to variations in their microenvironment very fast by responding to a wide range of signals, which requires a negative feedback in signalling [202]. Feedback will drive oscillations in biological processes and synchronous oscillations can amplify and transmit the signal more efficiently. The dynamics of oscillatory secretion is supposed to exist in many cell types, but few have been well investigated, with the exception of pancreatic β-cells. The reason is simply due to the shortage of bioanalytical tools to directly detect cellular secretions at high temporal resolution. Insulin secretion is regulated by calcium waves, and calcium oscillations in the cytoplasm can be studied simply by imaging [203]. To study insulin secretion oscillation in pancreatic function directly, other groups have developed electrophoresis-based microfluidic systems [204, 205]. But due to the dispersion of continuous flowing microfluidics compromising the temporal resolution to some extent, and the complexity of the methodology itself requiring high voltage and fluorophore labelled targets for competitive assays, these systems have not yet been widely utilized for other cells and targets. In Chapter 4, we discussed our microfluidic droplet system that was successfully applied to detect insulin secretion dynamics from single islets [88] and glycerol release from adipose tissue. In this chapter, we will further explore the applications of our microfluidic droplet system for other targets through the development of novel homogeneous immunoassays for the target and adaptation to our microanalytical device. The target we are focused on in this chapter is a very recently discovered adipokine, asprosin.

As we learned in Chapter 1, adipose tissue is now recognized as a vital endocrine organ that secretes hormones and responds dynamically to stimuli, not simply as an energy storage depot. A new hormone, asprosin, was recently discovered to be secreted by white adipose tissue (WAT) and was shown to strongly regulate hepatic glucose production by Chopra and coworkers in 2016 [33]. The following year, asprosin was shown to be an orexigenic hormone that stimulates appetite through the activation of Agouti-related protein (AgRP) [206]. While its importance as a potential therapeutic target for obesity, diabetes, or metabolic syndrome is clear, currently asprosin measurements must be conducted using the laborious and expensive enzyme-linked immunosorbent assays (ELISA) from only a few commercial sources, and there has been essentially no information collected on the dynamics of asprosin secretion.

In the work reported in this chapter, we first designed customized antibody-oligonucleotide conjugates for human asprosin detection and applied our thermofluorimetric analysis (TFA) methodology as described in Chapter 2. This approach provided the first demonstration of homogeneous, mix-and-read quantification in $<$ 1 hour in human serum samples and with high selectivity for human asprosin. Also shown is the development of an aptamer pair based TFA for mouse asprosin. TFA has thus provided a significantly simplified workflow and should promote expedited studies on this newly discovered hormone. Based on the assay performance in TFA, an isothermal proximity assay (IPA) was developed for mouse asprosin and successfully interfaced with the microfluidic droplet system (from Chapter 4) for investigating asprosin secretion dynamics from primary murine white adipose tissue for the first time.

5.2 Experimental

5.2.1 Human asprosin TFA assay by antibody-oligonucleotide probes

Materials and Reagents.

The asprosin antibody pair was chosen from fibrillin 1 commercially available antibodies to recognize different amino acid sequences of asprosin. Anti-fibrillin 1 (FBN1) monoclonal antibody (aa2772-2872) was obtained from antibodies-online (product: ABIN396145), and FBN1 polyclonal antibody (catalog: PAB17824) was purchased from Abnova. These two antibodies were conjugated to single-stranded DNA oligonucleotides and purified by Mediomics (St. Louis, MO).“Oligo MANT” was linked to the monoclonal antibody and the sequence is

5’-/5AmMC6/TAGG TGC TCG ACG CTG AC. “Oligo MAGS” was covalently bound to the polyclonal antibody and the sequence is 5’-/5AmMC6/TAG GAG AGA GAG AGA GGA. The labeled DNA oligo complementary to oligo MANT is “rev-MANT-TAMRA” with sequence as 5’-GCT CAT XGT CAG CGT CGA GCA CCTA (X= dT-TAMRA); an oligo complementary to oligo MAGS is “rev-MAGS-FAM” with sequence as 5’-/6-FAM/ATG AGC TTC CTC TCT CTC TCT CCTA. The conjugated DNA strands and labeled DNA oligonucleotides were obtained from Integrated DNA Technologies (IDT) and were purified by HPLC. 200 μg/mL recombinant human asprosin (carrier-free) and recombinant mouse asprosin (carrier-free) were purchased from Biolegend (San Diego, CA). Recombinant mouse fibrillin-1/asprosin (N-8His) was obtained from Novoprotein (Summit, NJ). Bovine serum albumin(BSA), HEPES (4-2-hydroxyethyl-1-piperazineethane sulfonicacid), sodium chloride, calcium chloride dihydrate, potassium chloride, and magnesium chloride hexahydrate were purchased from Sigma-Aldrich (St. Louis, Missouri). Human serum samples were collected and sold by BioreclamationIVT, where they were prescreened for viral and bacterial pathogens.

Probe preparation.

After purified oligo-conjugated antibodies were obtained from Mediomics, the probe “Asprosin -MANT-TAMRA” (Probe A) was prepared by mixing the 2.90 μM oligo MANT conjugated polyclonal antibody and 9.00 μM rev-MANT-TAMRA oligo at equivalent volumes and incubating for 30 min at room temperature. Similarly, 4.70 μM oligo MAGS conjugated monoclonal antibody and 4.81 μM rev-MAGS-FAM oligo were mixed at equivalent volumes and incubated for 30 min at room temperature to generate the probe “Asprosin-MAGS-FAM” (Probe B).

Thermofluorimetric analysis (TFA) for a human asprosin assay.

Probe A and B were diluted to 60 or 80 nM for probe premix, 4x higher than the probe concentration in the final assay solution from the respective stock solution by BMHH buffer with 0.1% BSA, containing 10 mM HEPES, 125 mM NaCl, 5.7 mM KCl, 2.5 mM $CaCl_2$, and 1.2 mM $MgCl_2$. Based on the probes concentration, eight or nine different concentrations of recombinant human asprosin were prepared for the standard curve from the stock asprosin solution which is diluted in BMHH buffer 0.1% BSA. Probe A and B were mixed each other to make the probe premix. Then 10 μL assay probe solution and 10 μL asprosin standard were mixed and incubated at room temperature for 30 min. The final assay solution was loaded into a 96-well qPCR plate for measurement. A real-time quantitative PCR (qPCR) instrument, Bio-Rad CFX96, was used for all of these asprosin TFA experiments. The protocol was set to incubate assay mixtures incubated at 4 ^{o}C for 10 min, and then the tubes were scanned thermally from 4 ^{o}C to 90 ^{o}C with a 0.5 ^{o}C increment and a 2-second delay before each fluorescence emission was measured. During thermal scanning, the FAM channel (λ_{ex}= 470 ± 20 nm, λ_{em}= 522 ± 8 nm) was chosen for fluorescence detection for each solution. The solution with maximum fluorescence was prepared by mixing the 4X probe B and 15 μL BMHH buffer with 0.1% BSA, which was used for the normalization in data analysis. The solution of minimum fluorescence was 20 μL BMHH buffer with 0.1% BSA used to exclude the background fluorescence from the assay buffer. Triplicate experiments were done for the standard curves of asprosin detection.

Asprosin measurement in human serum.

In the experiments of asprosin detection in human serum, , different dilutions were applied to give a total of 10 μL of sample.5 μL human serum and 5 μL BMHH buffer with 0.1% BSA were mixed to prepare the samples solution for the human serum from the non-fasted and type II diabetic donors, while 6 μL serum and 4 μL BMHH buffer with 0.1% BSA were mixed for obese donors. For the human serum from fasted donors, 3 μL human serum and 7 μL BMHH buffer with 0.1% BSA were mixed to prepare the samples solution. Then 10 μL assay probe solution and 10 μL sample were then mixed and incubated on ice for 30 min, after which thermal scanning was done using the qPCR instrument as in the protocol above. The solutions with maximum fluorescence (for normalization) was prepared by mixing the 5 μL 4X probe B,the appropriate volume of human serum (5, 6, or 3 μL for non-fasted, diabetic, or fasted, respectively), and enough BMHH buffer with 0.1% BSA to reach a total of 20 μL per sample.

Solutions with minimal fluorescence were made without probe using serum (5, 6, or 3 μL) and buffer volumes (15, 14, or 17 μL) required for the sample type (non-fasted, diabetic, or fasted).

Statistical analysis.

For statistical analysis, data was processed using the unpaired Student's *t*-test with heterogeneous variance in asprosin measurements of human serum.

5.2.2 Mouse asprosin TFA assay by aptamer pair probes

Materials and Reagents.

Collaborating with Proximity Biosciences LLC, two mouse asprosin aptamer pairs "PbA_Asp" and "PbB_Asp"; "PbFA_Asp" and "PbFB_Asp") were selected *in vitro* using recombinant mouse asprosin (Biolegend, San Diego, CA) as the target using a customized aptamer selection procedure (modified SELEX) and sequenced by next-generation sequencing (NGS). The below oligos were purchsed from IDT and used for probe preparation, described in next section. "Rev_ LibA _FAM_2": 5'- /6-FAM/TGA CAT GAG CTG CAG TCC TAC TTG CTC AC, hybridized to PbA_Asp and PbFA_Asp; "Rev_ LibB_TAMRA": 5'- CCT ATT CTG CTG CTT TCT CCA CTT TAC TCA CTT CAC CTT T / 36-TAMSp /, hybridized to PbB; "Connector_libAB_8-10": 5'- TCA TGT CAA AAG GTG AAG, hybridized to "Rev_ LibA_FAM_2" and "Rev_ LibB_TAMRA"; "Connector_libAB_10-10": 5'- GCT CAT GTC AAA AGG TGA AG, same function as "Connector_libAB_8-10"; "Rev_ 007_LibB_TAMRA": 5'-TCA TGT CAX CCT CTT TCG TCG TCT TAT CCT (X: T/i6-TAMN/), hybridized to "PbFB_Asp". BufferA: 40 mM HEPES, 120 mM NaCl; 5 mM KCl; 5 mM $MgCl_2$; 0.05% Tween 20. DMEM (no glucose, no glutamine, no phenol red, cat. A11430-01) and Dulbecco's Phosphate Buffered Saline (DPBS) from ThermoFisher Scientific (Grand Island, New York).

Probe preparation.

"PbA_FAM" was prepared by mixing the 1 μM aptamer"PbA_Asp" and 1 μM "Rev_ LibA_FAM _2" adaptor at equivalent volumes and incubating for 30 min at room temperature.

Similarly, we combined 1 μM “PbB_Asp” with 1 μM “Rev_ LibB_TAMRA” in equal volumes to get ”PbB_TAMRA”, “PbFA_Asp” with “Rev_LibA_FAM_2 to produce “PbFA_FAM”, and “PbFB_ Asp” with “Rev_ 007_ LibB_TAMRA” to obtain “PbFB_TAMRA”.

Thermofluorimetric analysis (TFA) for mouse asprosin assay.

80 nM of “PbFA_FAM” and 96 nM of “PbFB_Asp” in bufferA were mixed in 1:1 volume to prepare the probe mixture and 10 μL of the mixture was added into 10 μL recombinant mouse asprosin solution with different concentration in DMEM (no glucose, glutamine and phenol red) with 1%BSA. The final assay solution is composed of 20 nM “PbFA_FAM”, 24 nM “PbFB_Asp” and mouse asprosin (0,80, 140, 200, 300 nM), which was incubated at room temperature for 30 minutes. 19 μL of the solution was loaded into 96-well PCR microplate, and duplicate experiments were set for each concentration of standards. Temperature scanning was proceeded from 4 to 95 ^{o}C with 0.5 ^{o}C increment and a 2 s delay for each increment. The FAM channel in the qPCR instrument was used for fluorescence quantification. The fluorescence raw data were analyzed as above for the human asprosin TFA assay, but in this case only the reduction of background peak was used as the target-dependent response due to its peak shift and higher temperature. The background solution was an equal volume mixture of bufferA and DMEM (no glucose, glutamine or phenol red) with 1%BSA, and the maximum of fluorescence solution was 20 nM “PbFA_FAM” in the final assay solution without “PbFB_Asp” or target. For asprosin quantification in the secretion samples obtained from the simplified 8-channel microchip, the assay solutions preparation were the same, except the standards were replaced by the collected samples.

5.2.3 Mouse asprosin secretion dynamics

Materials and Reagents.

Sylgard® 184 Silicone Elastomer Clear was obtained from Dow Chemical. DMEM (Dulbecco’s Modified Eagle Medium, low glucose, L-glutamine, sodium pyruvate and phenol red, cat. 11885084, only use in tissue culture), DMEM (no glucose, no glutamine, no phenol red, cat. A11430-01, used in treatment solution and asprosin assay), MEM Non-Essential Amino Acids Solution (100X) (cat. 111400502), Sodium Pyruvate (100 mM) (cat. 11360070), Fetal Bovine Serum (qualified, USDA-approved regions, cat. 10437010), Penicillin-Streptomycin (10,000 U/mL) (cat. 15140122), Dulbecco's Phosphate Buffered Saline (DPBS) from ThermoFisher Scientific (Grand Island, New York). Pico-Surf 2% in Novec 7500 was purchased from Dolomite Microfluidics (Norwell, MA). Novec^{TM} 7500 Engineered Fluid (HFE 7500) was from 3M. HBSS buffer without glucose (0.14M NaCl, 5mM KCl, 0.4mM $MgSO_4 \cdot 7H_2O$, 0.5mM $MgCl_2 \cdot 7H_2O$, 0.3mM $NaHPO_4$, 0.4mM KH_2PO_4, 4mM $NaHCO_3$, 1mM $CaCl_2$, Forskolin (CAS 66575-29-9), TH Antibody (F-11) (cat.: sc-25269), 6-Hydroxydopamine hydrobromide (CAS 636-00-0), Rp-8-Br-cAMPS (CAS 129735-00-8) and DAPI (CAS 28718-90-3) were from Santa Cruz Biotechnology (Dallas, TX). 3-isobutyl-1-methylxanthine (IBMX) was obtained from Sigma-Aldrich (St. Louis, Missouri). Connexin 43 Monoclonal Antibody (CX-1B1) labeled by Alexa Fluor 488 (cat.: 138388),Image-IT Fixative solution (4%formaldehyde in PBS, methanol-free), proteinase K solution (20 mg/mL), 5-CFDA AM (5-carboxyfluorescein diacetate, acetoxymethyl Easter) were from ThermoFisher (Waltham, MA).

Isothermal proximity assay (IPA) of mouse asprosin.

In tube assays, 64 nM "PbA_FAM", 76.8 nM "PbB_Asp", 96 nM "Connector_libAB_ 8-10" were mixed in 1:1:2 volume ratio in bufferA. 10 μL of the mixture was added into 10 μL of the different concentration of recombinant mouse asprosin in DMEM (no glucose, glutamine and phenol red) media with 0.25% BSA. The finale mixture, including 8 nM "PbA_ FAM", 9.6 nM "PbB_ Asp", 24 nM "Connector_ libAB_ 8-10" and specific concentration of asprosin, was incubated at room temperature for 30 min. Thrombin was used as the negative control of target. 19 μL of the final assay solution was loaded into 384-well solid black microplates with flat bottom, and fluorescence was measured in microplate reader (Beckman Coulter, FilterMaxTM F5 Multi-mode microplate reader) at 37 °C with excitation wavelength 485 nm, emission wavelength at 535 nm and 1000 ms integration time. 10 μL bufferA plus 10 μL DMEM (no glucose, glutamine or phenol red) with 0.25% BSA was used for the background fluorescence correction. For the standard curve, duplicate experiments were run for each concentration. The fluorescence quench ratio was calculated by the following equation: quench ratio= 1- (F-F_0)/(F_{max}-F_0), where F_0 is background fluorescence, F_{max} is the maximum of fluorescence signal (blank, no target and only probes in assay solution), and F is raw fluorescence readout of the sample.

Microchip fabrication.

8-channel microchip fabrication. A passively operated, 8-channel microchip for tissue sampling has been reported previously by the Easley laboratory [194]. The photomask was designed in Adobe Illustrator and printed by Fineline imaging (Colorado Springs, CO). The master wafer was patterned using SU-8 photoresist (Microchem, Newton, MA), as stated in the traditional photolithography. The PDMS mold was produced from the master wafer by Sylgard® 184 Silicone Elastomer Clear (Dow Chemical): mixing the base and curing reagents in 10:1 ratio, poured on the master, degassed, setting the 3D-printed template on the appropriate position of the master, and curing at 60 °C overnight. The PDMS devices were peeled off and cut to suitable sizes.A biopsy punch was utilized to create 2-mm hole at the cross point of the 8 channels. The PDMS stamp was plasma bound to the glass slide. A 3D-printed template for cell culture reservoirs was designed in the SketchUp and printed by a MakerBot Replicator 2 (0.2 mm layer height), using polylactic acid filament (PLA, 1.75 mm).

Droplet microchip fabrication. Droplet microfluidic chip fabrication and control were done following the protocols discussed in the Chapter 4.

Murine epididymal white adipose tissue extraction.

Primary adipose tissue was prepared according to the previously published protocol [194, 207]. Epididymal adipose tissue pads were separated from C57BL/6J mice. Right after removal from mice, tissues were placed in 37 °C phosphate-HEPES buffer (10 mM HEPES, 135.3 mM NaCl, 2.2 mM $CaCl_2 \cdot 2H_2O$, 1.2 mM $MgSO_4 \cdot 7H_2O$, 0.4 mM KH_2PO_4, 2.2 mM Na_2HPO_4, 0.4 mM D-glucose, 2% BSA, pH 7.4) until used. The extra vascular tissues were removed, and the fat tissue pads were punched into 2-mm sections. The explants were washed by 4 mL warm phosphate-HEPES buffer twice by centrifugation for 3 min at 1000 rpm. Then they were further cleaned using 4 mL warm fat tissue culture media three times by centrifugation for 3 min at 1000 rpm. The explants were transferred to 96-well microplate for culture. For each well, a 3D-printed anchor was used to overcome the buoyancy of fat tissue [194, 207]. The fat culture serum media (DMEM with low glucose and phenol red with 12% fetal bovine serum, 120 units/mL nystatin, 120 units/mL penicillin-streptomycin and 1.2X MEM NEAA) needed to be refreshed twice per day. Under these culture condition, fat explants could live up to 7-10 days.

Mouse asprosin secretion dynamics from eWAT

Dynamic study in 8-channel sampling microdevice. 2-mm eWAT explants were pre-treated in 25mM glucose in DMEM or HBSS (without glucose) with 1% BSA and loaded into the 2-mm reservoir of 8-channel chip. The 3D-printed insert was used to push the explant down and keep it in the reservoir. Different treatment solutions were then added into the large reservoir. In the experiments, the high glucose solution (HG, 25 mM glucose) and low glucose solution with 20 μM isoproterenol (LGiso, 3 mM glucose) were applied to stimulate the tissue function. 8 channels connected with Tygon microbore tubing (0.020"x0.060"OD, Cole-Parmer, Vermon Hills, IL) were used for sample collection at 20-min intervals under vacuum produced by 60-mL syringe. The flow rate for sampling was 245 μL/h. The bulk solution reservoir remained full during experiments. The asprosin concentrations in the collected samples were measured by TFA using the mouse asprosin assay as described above.

Dynamic study in droplet microchip. As mentioned, the eWAT explant was pre-treated in 25 mM glucose of DMEM with 1% BSA and loaded into the 0.75-mm reservoir of droplet chip, and the 3D-printed insert was used to trap the tissue in the place for experiment. Different treatment solutions were then added into the large reservoir. In these experiments, the high glucose solution (HG, 25 mM glucose,2 nM insulin), the low glucose solution (LG, 3mM glucose, 50 pM insulin) and low glucose solution with 20 μM isoproterenol (LGiso, 3 mM glucose, 50 pM insulin) were used to study asprosin secretion dynamics from the eWAT explants. In the droplet-based microfluidic device, the upper left inlet was filled with the probe mixture for IPA mouse asprosin assay, the middle inlet was filled with bufferA, and the right inlet was the cell culture reservoir for the tissue. Sampling and measurement followed the protocol mentioned previously in Chapter 4. The probe mixture was mixed with an equal volume of DMEM with 0.25%BSA to generate the reference solution and added into the lower reference reservoir. The "Celldrop" LabVIEW application was run with 350 ms of sample pumping time at 2 cycles, 400 ms of oil pumping time at 2 cycles, 250 ms of reference pumping time at 3 cycles, and with a 10 ms oil delay and 20 ms pump delay. These parameter settings determined the droplet formation at 0.602 Hz, meaning that droplet-based sampling resolution was 3.3 second.

5.3 Results and Discussion

5.3.1 Human asprosin TFA assay

Data analysis and standard curve of asprosin TFA assay.

The assay design is based on the molecular pincer assay develpoed by the Heyduck group [127, 134], which is a homogeneous immunoassay. The tails of probe A and B are able to hybridize with each other and the fluorescence of FAM in probe B will be quenched by TAMRA in probe A, based on the Föster resonance energy transfer (FRET). During temperature scanning, the assembled DNA will denature, and the fluorescence will increase as the separation of fluorophore and quencher occurs. The raw fluorescence data was measured by the qPCR instrument, and the steps of data analysis for the asprosin TFA assay is shown in **figure 5.1**. In the figure, 20 nM of probe A and B were used to detect asprosin. The raw fluorescence data were plotted in panel **A** of **figure 5.1** against the concentration of recombinant human asprosin. Due to the background fluorescence from the detection system and buffers used in the assay, the minimum fluorescence from the buffer (Mini, lower blue curve) was used to exclude the background fluorescence by subtracting it from the raw data at each temperature. The background-subtracted data is shown in panel **B** of **figure 5.1**. Also, because the fluorescence of the fluorophore ("FAM") decreased as the temperature increased (as expected), the maximum fluorescence curve (red) from 20 nM of probe B was used to correct the data from panel B by normalizing; the resultant data is shown in panel **C** of **figure 5.1**. After background correction and normalization, it is clearly demonstrated that the fluorescence changes during the melting shifted to high temperatures as a function of asprosin concentration. Two different melting transitions were observed, similar to the insulin and cyclic AMP TFA assays described in Chapter 2. This result is attributed to the proximity effect, in tat the target binding will bring the DNA tails close to each other and help stabilize the assembled DNA helix at the probe tails, thus the melting of the DNA helix will shift to the higher temperatures to give a new melting transition.

When first derivative of the data from panel C was taken (dF/dT), the melting temperatures could be obtained for the two different complexes with or without target binding, exhibited in **D** of **figure 5.1**. In **figure 5.1D**, two different melting peaks are given: the peak in lower temperature is from dissociation of the complex without target binding, and the peak in higher temperature from the dissociation of complexes with target binding to the antibodies in two probes. The acmes of two peaks slightly shift with the asprosin concentration rising. To achieve the better separation of two melting peaks, the blank was subtracted from the data, shown in **E** of **figure 5.1**. The peak 1 represents the complexes melting of probes unbound to targets and the peak2 is from the the complexes melting of probes bound with targets. The difference sum of peak 1 and peak2 were used as the response in the asprosin detection, and the standard curve is plotted in **E** of **figure 5.1**. The data was regressed by applying 3-parameter sigmoidal equation as below and the standard curve is fitted as the red line in **F** of **figure 5.1**, with R^2 0.9967. In the equation, the value of a is 0.5805, b 3.123 and x_0 11.1641. The 3σ limit of detection (LOD) of asprosin TFA assay is 4.1 nM. The dynamic range of detection is from 4 to 20 nM. It should be noted that the dynamic range can typically be tuned by manipulating the probe concentrations.

$$y = \frac{a}{1 + e^{(\frac{x_0 - x}{b})}} \tag{5.1}$$

Standard curves of asprosin TFA with different probes concentration.

To lower the probes concentration and reduce the assay cost as much as possible, different concentration of probes were tested for the assay performance to lower the cost of assay and

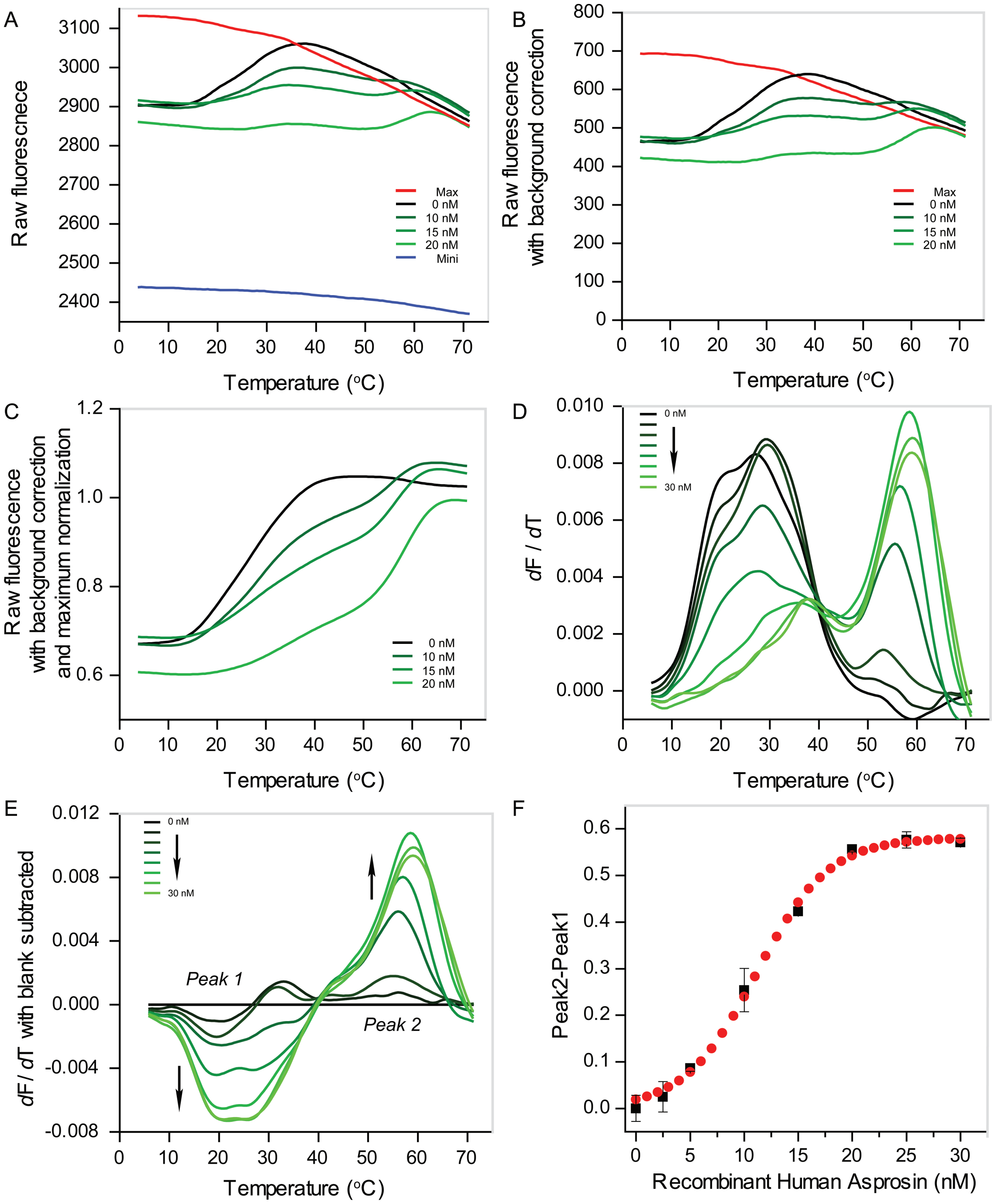

Figure 5.1: Data analysis for human asprosin TFA assay. (A) Raw fluorescence data from qPCR instrument with different recombinant human asprosin concentrations. Max represents the maximum of fluorescence of 20 nM probe B without quencher in the solution. Mini represents the minimum of fluorescence from the assay buffer. (B) The minimum was subtracted from the raw fluorescence data to exclude the detector background arising from the buffer. (C) The data from B were normalized to the maximum fluorescence curve. (D) The first derivative of the data from C. The asprosin concentration was varied from 0 nM to 30 nM. (E) The blank curve without asprosin was subtracted from each first derivative curve. (F) The standard curve with sigmoidal fit, where the y = peak2 - peak1 from E. The standard data were fitted to a 3-parameter sigmoidal equation.

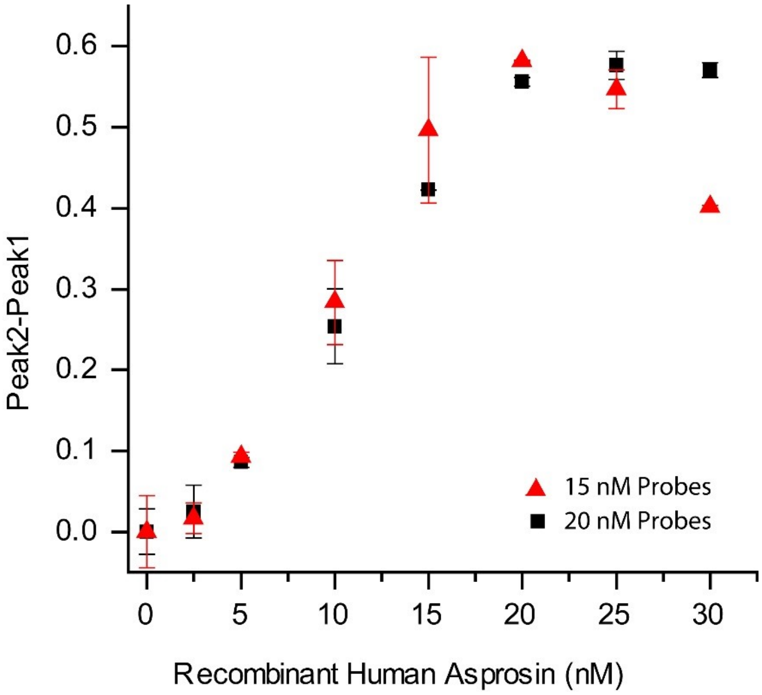

Figure 5.2: Standard curves for human asprosin TFA assay with two different concentration of probes, 15 nM and 20 nM. Triplicate experiments were run for each data point.

results are shown in **figure 5.2**. The data was also regressed by applying 3-parameter sigmoidal equation with R^2 0.9956. Parameter values were: a = 0.5693, b = 2.5898, and x_0 = 9.9267. For 15 nM probes, the limit of detection (LOD) of asprosin was around 5.6 nM and the detection range was up to 20 nM. The better assay performance was given by 20 nM of probes compared to the 15 nM of probes, when standard deviation for each data point was taken into consideration; yet the LOD and the detection range were similar. Thus, 15 nM of probes was chosen for later experiments. The LOD is dependent on the standard deviation in the blank without asprosin in the assay solution, and recent data showed that the LOD of asprosin TFA assay can be down to 0.6 nM (data not shown here).

Specificity test of asprosin TFA.

The asprosin assay showed good specificity when recombinant mouse asprosin and recombinant mouse asprosin with 8-His tag were utilized to perform the same experiments (seen in **figure 5.3**). The three-dimension structures of human and mouse asprosin are unknown until now, but the mouse asprosin has 91% identity as human asprosin in amino acid sequence, which were compared by Protein BLAST online software. The data proved that our asprosin

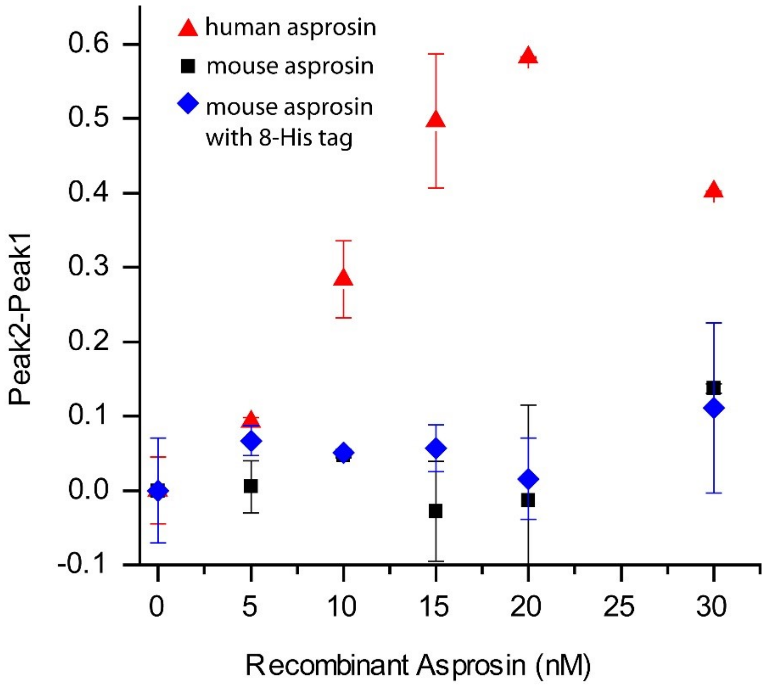

Figure 5.3: Specificity test for human asprosin TFA assay with two similar proteins, recombinant mouse asprosin and recombinant mouse asprosin with 8-His at the N-terminal. Data of recombinant human asprosin were same as **figure 5.2**. Duplicate experiments were run for the other two.

TFA assay was characterized by high specificity toward human asprosin by using antibody-oligo conjugated probes.

Detection of asprosin in human serum using TFA.

The newly developed asprosin TFA assay was next exploited to detect asprosin in human serum. Human serum samples were collected by BioreclamationIVT and 4 different groups of patients were sampled, including fasting, non-fasting, obese (Body Mass Index (BMI) > 30), and Type II diabetic donors. 4-5 different patients' serum samples were collected for each group. In our previous publications [135], TFA was proven to perform in human serum and human plasma, since the differential analysis could eliminate autofluorescence influences from complex matrix. From the results in **figure 5.4**, the thermofluorimetric assay was successfully applied to detect asprosin directly in human serum. The asprosin concentration in the serum

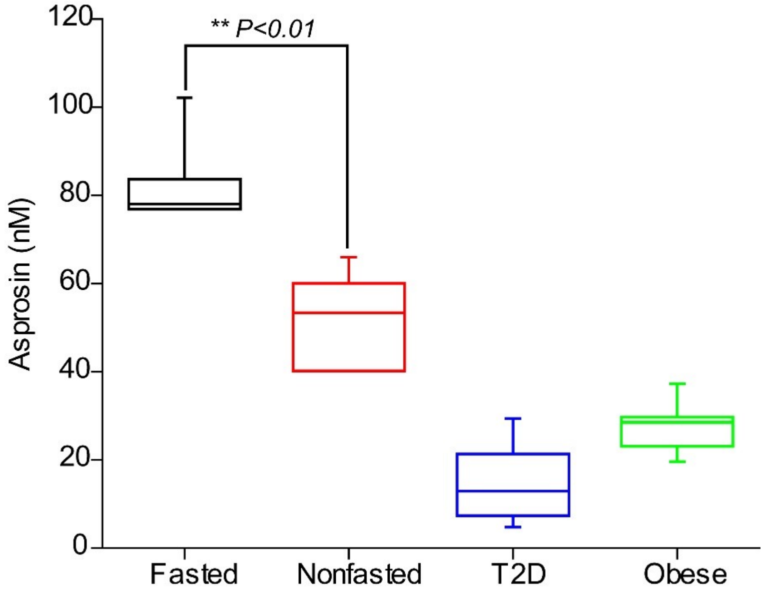

Figure 5.4: Biological application of human asprosin TFA assay. Serum samples were collected from four different groups of patients: fasted, nonfasted, Type II diabetic and obese (with Body Mass Index > 30). 4-5 different patient serum samples were tested for each group. Duplicate experiments were run for each sample with different dilution factors.

from fasted donors were significantly higher than those in non-fasted donors, as expected. According to the seminal publication [33], asprosin was characterized as a fasting-induced hormone, so the fasting status will boost the asprosin concentration in human serum. The data from the obese and T2D group were difficult to interpret due to the unknown information about the fasting status of the donors. However, the obese and diabetic donors showed significantly lower asprosin levels than the other donors, and the data represent some of the first clinical measurements of asprosin in these patient groups, to our knowledge. In fact, asprosin levels within each donor group (n = 4 or 5) were clustered near a similar mean value for the group. Overall, these results suggest that our asprosin TFA methodology could be a valuable addition to the toolbox of physician seeking to evaluate the health of their patients, particularly those showing compromised glucose homeostasis.

It is noteworthy that a human asprosin ELISA kit was purchased in our attempts to detect recombinant human asprosin and asprosin in human serum, with the intention to validate our TFA methods. However, the ELISA kit was found to be inadequate for unknown reasons. Perhaps this problem is due to the fact that asprosin was only recently discovered, and the kits are still being developed. To further validate our TFA method's performance, human preadipocytes were cultured and differentiated according to the manufacturer protocol and used for asprosin secretion tests. The results showed that asprosin secretion increased by 2-3 folds in DMEM media without glucose compared to in the media with 4.5 g/L glucose. Therefore, our TFA method was successfully proven with recombinant asprosin standards, human serum samples, and cell secretion.

To sum this part up, the molecular pincer assay format was chosen to design antibody-oligo probes for human asprosin, and thermofluorimetric analysis (TFA) approach was successfully applied as an asprosin assay. From the results, the assay can be applied to asprosin detection in human serum. Considering that asprosin is a newly discovered adipokine and with nanomolar concentration in human circulation system, this homogeneous assay should be extraordinarily useful in the characterization of asprosin in regulating glucose homeostasis. With these results, we also proved that our assay format can be easily translated to quantify other proteins with the benefits of rapidity, low cost, and simple manipulation. At the same time, from the derivative data, the background and signal from the asprosin assay can be clearly separated at room temperature, which underlies that the assay will also function for direct readout at room temperature without thermal scanning (albeit without the ability for differential background correction). In this way, the asprosin assay can be readily miniaturized onto our microfluidic device to be used for dynamic research of asprosin secretion from WAT, similar to the glycerol results described in Chapter 4. In the remainder of this chapter, I discuss our application of such asprosin assay with passive and active microfluidic devices to uncover unique information on WAT secretion dynamics.

5.3.2 Mouse asprosin TFA assay and mouse asprosin secretion study in 8-channel chip

As discussed in Chapter 4, primary tissue is an ideal model for dynamic studies of hormone secretion, which is characteristic of organotypic features compared to cell lines. And the mouse, especially the C57BL/6J strain, is a well-developed animal model for diet-induced obesity, type II diabetes and other related diseases. Since asprosin is an orexigenic hormone, studying its dynamic function in primary murine WAT should be considered high priority. Our laboratory is well-poised to undertake these studies using microfluidics and droplet-based sampling, as long as there is an applicable homogeneous assay available. Therefore, a TFA assay for *mouse* asprosin is in demand, particularly since our human asprosin TFA did not respond to mouse asprosin. Considering the successful development of human asprosin assay using antibody-oligo conjugated probes and the better TFA assay performance with an aptamer pair compared to antibody pair shown in Chapter2, we decided to establish a homogeneous assay for mouse asprosin using an aptamer pair. Aptamer pair SELEX was successfully conducted, using recombinant mouse asprosin as the target, by collaborating with an Auburn-based startup company, Proximity Biosciences LLC. The binding affinity of each aptamer was in the picomolar to few nanomolar range, measured by the AGILE R100 (Nanomedical Diagnostics), which is a sensitive biosensor for label-free analysis of small molecules and proteins based on the graphene field-effect transistor (FET). A quick test of aptamer pair performance for target detection can be accomplished using an isothermal proximity assay (IPA), described in later section of 5.3.3.

The molecular pincer assay format was adapted to the aptamer pair by hybridizing the aptamer to a fluorophore/ quencher labelled DNA oligonucleotide, shown in the inset figure of **figure 5.5A**. Same principles of TFA were followed in the assay to analytically separate background from signal. Experimental setting and fluorescence measurement were similar to the TFA of human asprosin assay, and the dF/dT with blank subtraction results are demonstrated in **figure 5.5A**. Likened to the results of human asprosin TFA assay (**figure 5.1E**), the background and signal peaks were well differentiated, but the background melting peak was narrower and the separation of two peaks was even better, without any overlapping; this is likely due to the well-defined 1:1 ratio of aptamer:adaptor. However, taking the higher melting temperature and melting peak shift of signal complexes into account, only the peak area under "Peak 1" (**figure 5.5A**) was calculated as the response in the calibration curve (**figure 5.5B**), where the asprosin concentration was linearly correlated to the peak area representing the amount of background complex. After the performance of TFA mouse asprosin assay was proven, epididymal WAT explants were extracted from a C57BL/6J mouse (< 20 weeks in age), and tube secretion samples of asprosin were collected under the treatment of high glucose, with varied stimulation on each piece of fat explant. The fold change of asprosin secretion was obtained by dividing the asprosin secretion stimulated by each treatment by the amounts secretec at high glucose. Three treatments were applied: low glucose, low glucose + isoproterenol or low glucose + IBMX + forskolin. The fold changes of asprosin secretion under different stimuli are shown in **figure 5.5C**. Asprosin secretion increased under low glucose + isoproterenol treatment was significantly higher than that with the low glucose treatment. However, the secretion results from low glucose + IBMX + forskolin were not statistically different, yet the data variance was much higher; one explanation could be the large phenotypic variation of the explants, and another cause may be the inconsistent secretion of asprosin in static tube secretion by comparing with the results from a microfluidic system. It has been reported that the lipolytic products like glycerol or non-esterized fatty acids can inhibit lipolysis by negative feedback [177], and we considered that the same feedback inhibition effect could feasibly occur with asprosin secretion.

Therefore, our simple, passively operated 8-channel microfluidic chip was exploited for asprosin secretion sampling, with results displayed in the inset figure of **figure 5.5D**. In the chip, 8 channels were used for collection of 8 samples at 8 different but continuous time points under different treatments. The results in **figure 5.5D** are from two different pieces of explants. From the plot, changing the treatment solution from the high glucose to low glucose with isoproterenol, the asprosin secretion was increased two to five folds and secretion was reduced when the treatment was switched back to high glucose. More consistent results were thus shown in the flowing system but more experiments need to be conducted to give solid arguments about the negative feedback control of lipolytic products or asprosin itself on asprosin secretion.

5.3.3 Dynamic mouse asprosin secretion studied in a droplet microfluidic system

In Chapter4, it has been shown that glycerol release from the primary epididymal WAT occured in an oscillatory pattern, different from encapsulated 3T3-L1 differentiated adipocytes. We hypothesized that gap junctional coupling is required for these oscillation to occur. It has been proven that gap junctions exist in WAT through electrophysiological methods and immunostaining [50, 51, 26], and gap junctions exhibit well-known importance for cell coupling to propagate nervous or other stimulating signals by exchanging of metabolites, ions, and other second signalling molecules like cAMP [44]. Gap junctions can also regulate the synthesis, storage, and secretion of secretory products in endocrine cells to optimize the delivery of secreted molecules to function organs [208]. Therefore, we expect that asprosin, a secreted hormone from adipose tissue, will demonstrate an oscillatory secretion pattern if sampled and

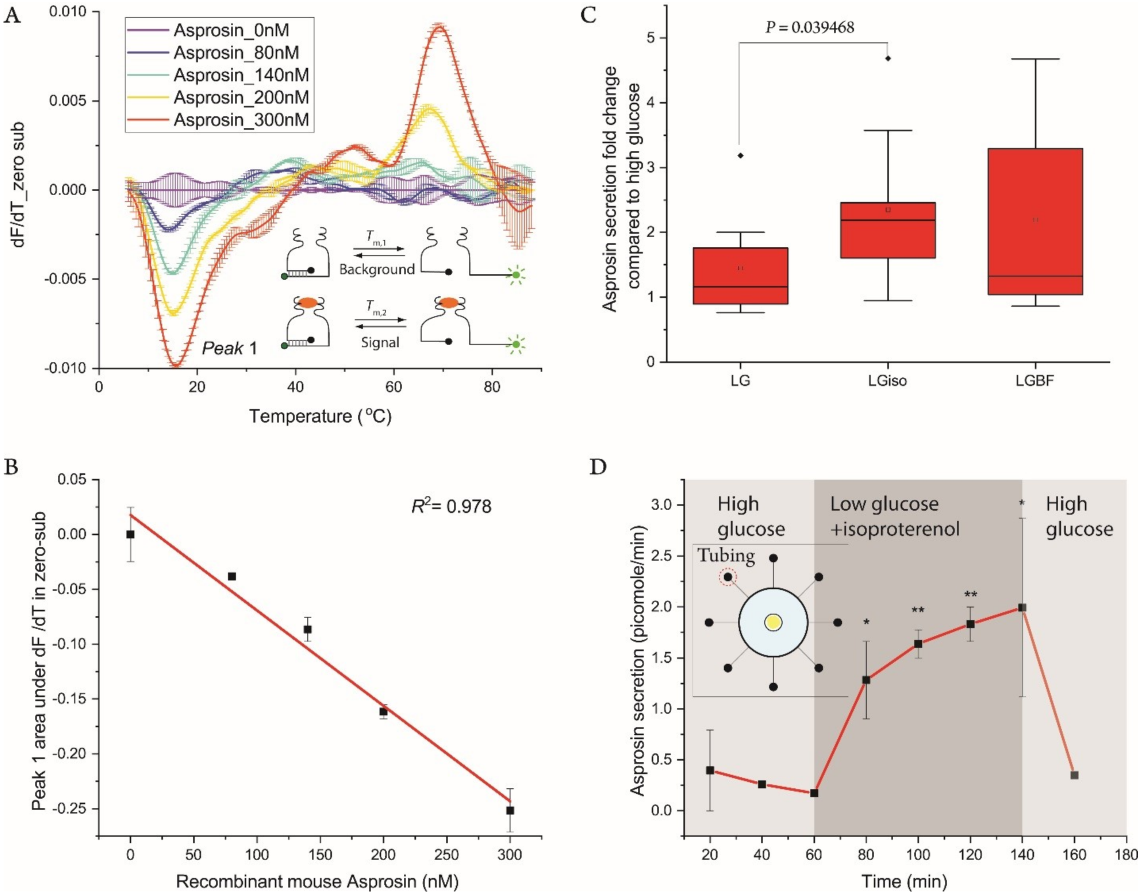

Figure 5.5: TFA of mouse asprosin assay for asprosin secretion dynamics. (A) TFA of mouse asprosin assay by probes 20 nM “PbFA_ FAM”and 24 nM “PbFB_ TAMRA”. The plot is dF/dT data subtracted from the blank, zero targets. The error bar was calculated from duplicate experiments. The inset figure shows TFA of asprosin assay design and principle. Same as human asprosin, the molecular pincer format was chosen for assay design, except mouse asprosin aptamer pair was used instead of antibody pair. TFA was applied to discriminate the background complexes from the signal complexes. (B) Standard curve of mouse asprosin TFA assay. Same data shown in A, and the peak area under Peak 1 in A was calculated and plotted as y-axis. Linear regression model was fitted to the data with *R*-square 0.978.

Figure 5.5: (C) Asprosin secretion fold changes under different conditions compared to the secretion amount when the murine eWAT explants was treated by high glucose (25 mM) media. LG: low glucose (3mM); LGiso: low glucose (3 mM) + 20 M isoproterenol; LGBF: low glucose (3 mM) + 200 μM IBMX + 10 μM Forskolin. The asprosin secretion was operated in PCR tube from one 2-mm fat explant in each tube and secretion was stimulated by 12 μL different treatments for 1 hour at 37 °C. The fold change was calculated by dividing the asprosin concentration from the stimulated secretion samples by asprosin concentration of secretion sample from the same explant treated in high glucose solution. One-tail of Student *t*-test was applied to compare the differences among three treatments. (n= 8, 9, 7 for each group, respectively). (D) Asprosin secretion dynamic study. Asprosin secretion samples were collected through 8-channel microfluidic chip from 3-mm primary murine eWAT under treatment changing from high glucose to low glucose with isoproterenol and then back to high glucose. Asprosin was quantified by mouse asprosin TFA assay was exploited to quantify. ($*$: $P < 0.05$, $**$: $P < 0.01$, compared to the asprosin secretion amount between 40-60 minutes.) The inset figure is the 8-channel microfluidic chip setting (yellow is fat explant, light blue the bulk treatment solution, and 8 channels are connected to tygon tubing for secretion solution collecting.).

quantified at high temporal resolution. In this section, similar experiments were set as in Chapter4, except that an isothermal proximity assay (IPA) of mouse asprosin–developed in our lab (see above) was applied within the microfluidic droplet system for asprosin quantification.

The mouse asprosin IPA assay format was based on the aptamer pair screened in collaboration with Proximity Biosciences, as described above. A more general assay format was designed as the in the inset figure of **figure 5.6A**, where adaptors introduced the fluorophore and quencher to aptamers, and a connector was hybridized with both tails of the probe pair to bring the fluorophore and quencher into proximity for FRET. The format can be readily extended to other aptamer pairs produced in the future and can be used as an assay to test aptamer pair performance. Interestingly, this assay does not function as well in TFA, likely due to the complexity of the five separate oligos in in the complex. Before miniaturizing on the microfluidic chip, this mouse asprosin IPA was tested in a microplate reader, where 8 nM of probes were used for these experiments. The fluorescence quenching ratio was calculated by using zero target as the maximum of fluorescence signal and buffer as the baseline of fluorescence measurement. The results of the calibration curve can be seen in the **figure 5.6A**. Thrombin was chosen to be the negative control to prove the probe specificity, which had little signal change in the aptamer-based IPA for asprosin.

After the assay performance was proven in a standard microplate reader, it was applied as a homogeneous assay within microfluidic droplets to quantify asprosin secretion dynamics from eWAT. The IPA probe mixture was loaded into the left upper inlet, buffer was loaded into the upper middle, and the tissue was cultured and sampled (or calibration standards added) in the upper right inlet. The probe mixture was mixed with buffer in equal volume to prepare the reference solution and loaded into the reference inlet (seen in the inset figure of **figure 5.6B**). Other settings were same as the ones in Chapter4. The droplets were formed at 3.3-second temporal resolution, which defines the resolution of sampling. Before starting asprosin secretion tests from eWAT, the system was calibrated by recombinant mouse asprosin and results are exhibited in **figure 5.6B**. The calibrated system was used to study the asprosin secretion dynamics from eWAT explants extracted from a 20-week diet-induced obese mouse (**figure 5.6C** and **D**) and a 20-week wild-type mouse (**figure 5.6E** and **F**, **G** and **H**). From the overall secretion pattern of three groups of data, the asprosin secretion was observed to increase right after changing the media to no glucose solution from high glucose and high insulin media and asprosin levels reached their maximum within 10 min.

As we had hypothesized, under the high temporal resolution of sampling with our microfluidic system, the asprosin secretion manifested an oscillatory pattern. Additionally, the high temporal resolution enabled detailed frequeny-domain analysis with fast Fourier transform (FFT) processing. From the FFT analysis and the zoomed-in fine temporal structure analysis (seen in the inset plots in **figure 5.6D**, **F** and **H**) of the diagrams in **figure 5.6C**, **E** and **G**, we observed oscillation periods in the range of 30 seconds to 2 minutes, with most oscillations centered around a period of $\sim$1 min.These results represent the first report of oscillatory asprosin secretion, to our knowledge.

The observed oscillations may be a result of calcium oscillation waves in the gap junctionally coupled adipose tissue. Gap junctions couple adipocytes and optimize the bioactive molecules secretion by synchronizing endocrine cells. Calcium is an ion in the cells (Ca^{2+}), well-understood in other tissues to transfer between the cytoplasm of cells freely through gap junctions and closely related to the regulation of hormone granule exocytosis, a common pathway for hormone secretion. As shown in pancreatic islets the gap junction can modulate the insulin biphasic secretion dynamics [5]. On the other hand, cytoplasmic calcium concentration has been reported to oscillate in a constant amplitude and frequency at 1/min stimulated by acetylcholine [209]. Other secondary messengers like cAMP can also travel across the gap junctions to drive secretion oscillations. The gap junction and its function and mechanism in adipokines secretion remains to be understood. Taking previous publications and our observations into consideration, our microfluidic droplet system can be a powerful tool to help study the hormone secretion dynamics directly.

5.4 Conclusions

Biomolecule secretion and delivery through the circulatory system are dynamic processes. The oscillatory concentration change is also a signal delivered to the target organs. As shown in the second and third chapters, our TFA methodoly provides a unique tool because it can detect proteins in complex matrices like serum. In this chapter, TFA method was developed for human asprosin and proven to work in human serum. By screening an aptamer pair and matching the format, TFA assay and isothermal proximity assay (IPA) for mouse asprosin were also developed and the IPA assay was successfully miniaturized into our microfluidic droplet-based sampling system for dynamic asprosin secretion quantification from primary adipose tissue. The high temporal resolution of sampling allowed the oscillatory secretion patterns of asprosin from the tissue to be detected for the first time. Taking the previous results of glycerol release from the tissue different from the encapsulated adipocytes into account, we propose that the oscillations may be due to the gap-junctional coupling in primary tissue.

Gap junctions play a significant role in cell-to-cell communication. Remodelling of coupled adipose tissue is associated with the changed physiological and pathological functions of tissue such as Chagas disease, which results in the upregulation of Cx43 in WAT to facilitate lipolysis [51]. Also, the upregulation of Cx43 in cardiomyocytes is related to Duchenne muscular dystrophy (DMD) and the reduction of full channel formation using Cx43 peptide mimetics (Gap26/ Gap19) can reduce the isoproterenol-induced arrhythmias [45]. To study the gap junction influences in hormone or other bioactive molecule secretion from tissues, the microfluidic system with compatible isothermal mix-and-read assays developed in this chapter should prove to be powerful tools. The system shown here is a two-layer microfluidic chip with multiple microvalves, a little more fabrication process is needed compared to the single-layer

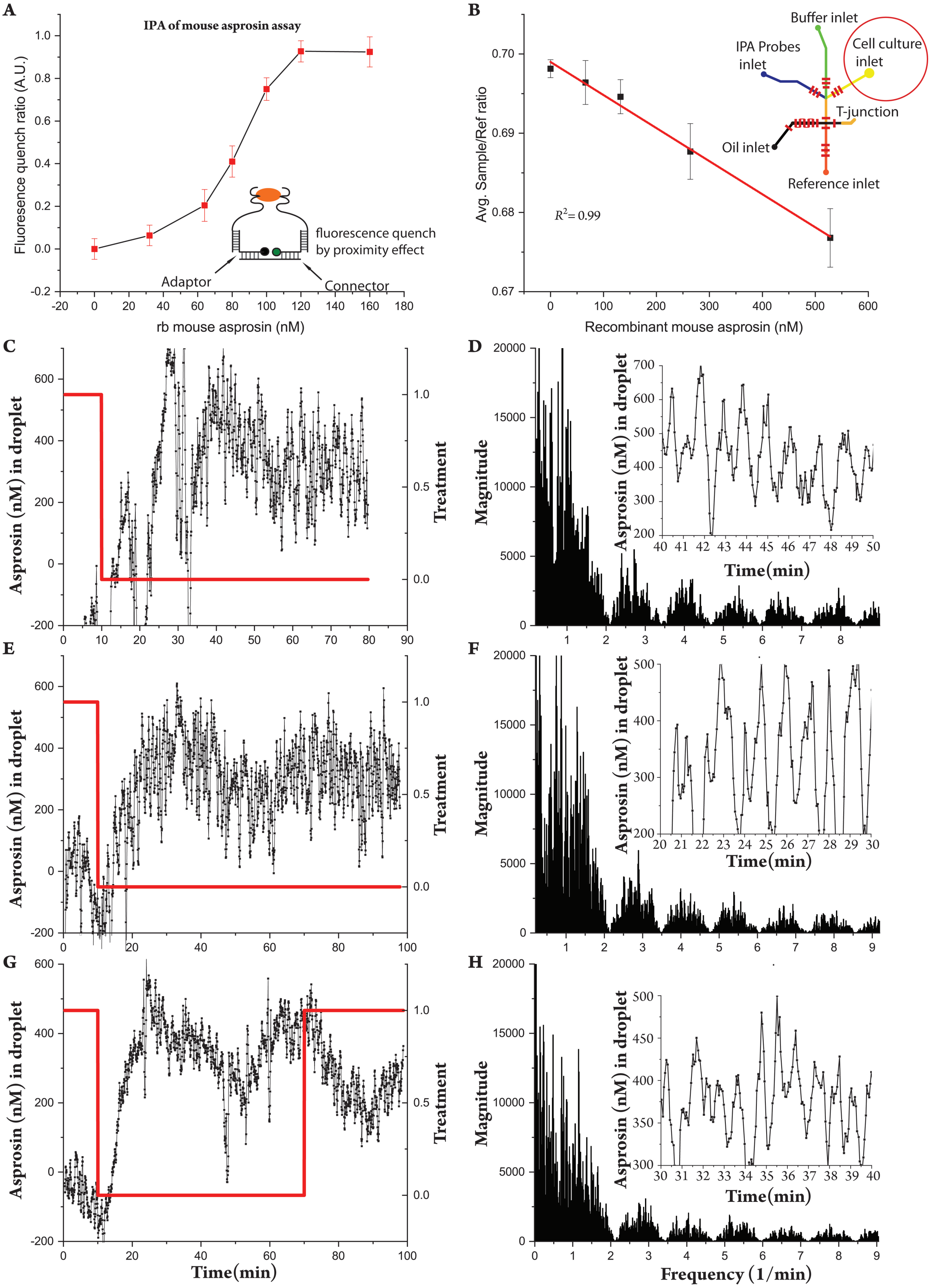

Figure 5.6: Caption next page.

Figure 5.6: (A) Isothermal proximity assay (IPA) of mouse asprosin. Aptamer pair probes (8 nM "PbA_ FAM", 9.6 nM "PbB_ Asp" and 24 nM "Connector_ libAB_ 8-10" were used for the assay and the fluorescence was detected in microplate reader at 37 °C. Zero target solution provided the maximum of fluorescence (F_{max}) and buffer solution gave the baseline of fluorescence detection (F_0). As the target concentration increased, the fluorescence (F) got reduced due to the more signal complex (**figure 5.5B**) formed. The fluorescence quench ratio was calculated by 1- (F-F_0)/(F_{max}-F_0) and plotted as y-axis. (B) Standard curve of IPA mouse asprosin assay in droplet microfluidic system with 33 nM "PbA_ FAM", 39.6 nM "PbB_ Asp" and 99 nM "Connector_ libAB_ 8-10" in each droplet, calculation details shown in chapter4. Linear regression model was fitted to the data with *R*-square 0.984. The inset figure demonstrates the microdevice setting. (C) Asprosin secretion dynamic from mouse eWAT explant extracted from the 20-week diet-induced obese C57BL/6J mouse. Treatment: 1 represents the high glucose high insulin (HGHI, 25mM glucose and 2 nM insulin in DMEM with 0.25% BSA); 0 means the no glucose in DMEM with 0.25% BSA. (D) Fast Fourier Tranform (FFT) analysis of data in C. The inset figure is a zoomed C to the 10-min zone. E and F from mouse eWAT explant extracted from the 20-week wild-type C57BL/6J mouse. G and H from another piece of explant of 20-week wild-type C57BL/6J mouse.

chip. However, this process can, in turn, save time to set up sophisticated perfusion systems and complicated tissue macro-to micro interfacing. In the future, we will focus on the improvement of automatic switching of treatment solution and application of our systems in studying the phenotype and functions of primary tissues.

Chapter 6

Conclusion and future work

The research projects in this dissertation were aimed at developing microfluidic tools and compatible, small-volume assay formats to enable high-resolution temporal secretion studies of biomolecules from pancreatic and adipose tissues.For the assays, homogeneous immunoassays based on thermofluorimetric analysis (TFA) were developed, miniaturized, and integrated into the microfluidic system, which sampled secretions into nanoliter-scale aqueous-in-oil droplets for downstream fluorescence readout.

Specific assays for homogeneous, thermofluorimetric analysis (TFA) of thrombin, insulin, asprosin and cAMP homogeneous assays were developed and applied to quantify molecules from primary tissues. Generally, TFA has been validated in the dissertation work as a promising approach for studies on cell signaling. The merits of TFA include its simple mix-and-read workflow, high calibration repeatability, small sample volume requirement, and the repurposing of a widely-adopted nucleic acid analysis instrument for both hormone and second messenger quantification. These qualities distinguish TFA from previously reported methods and enable a number of biological experiments to be conducted with ease. In the short term–considering the importance of incretin effects in diabetes, obesity, and metabolic syndrome–TFA represents a robust, new tool that could immediately impact studies on incretin-amplified insulin secretion from islets or β-cells. It will also help study asprosin related functions, which is identified as an important hunger hormone functioning on the liver as well as the brain. In the future, it should be straightforward to adapt the presented antibody-oligonucleotide versions of TFA to any protein or target with two antibodies (or aptamers), and the development of additional DNA-driven assays for small molecules and second messengers would expand the catalog of TFA analytes. Multiplexing through spectrally resolved fluorophores and/or thermally resolved melting transitions has already been shown feasible [135], thus further work in this area should permit small-volume, mix-and-read assays on a variety of analytes to be carried out in a single tube. The miniaturization of TFA in microfluidic system by two temperature zones is another future direction, which will save the time for temperature scanning but keep the advantages of TFA to differentiate the signal from the background.

In terms of the microfluidic developments presented herein, an improved microfluidic droplet system with faster sampling speed could be readily generalized to other targets (with further assay development), which will facilitate various dynamic secretion studies of biomolecules from primary tissues. The microfluidic system was shown to combines high-resolution sampling with integrated optical detection, and expansion to other targets would certainly improve its scientific impact. In the future, droplet merging by electric fields and/or picoinjection should be also introduced into the system to improve its flexibility for droplet manipulations such as reagents dilution and addition. With more types of assays interfaced to the system, our laboratorys continuous calibration lock-in detection approach for each sample could be included [114, 115]. Another direction is to combine our fluidic multiplexer system [195] with the droplet system to control the treatment solutions switching more easily and precisely.

To develop simple but reliable techniques for fast sampling and accurate detection of analytes is every analytical chemist's research goal. Such advancement of bioanalytical methods can hasten the research progress in the related biological and biomedical areas. As shown in this dissertation work, the ability of our system to study and observe novel dynamics of biomolecule secretion directly on-chip at high temporal resolution has given us a unique look at the real-time function of these hormones and metabolites secreted from endocrine tissues.

References

[1] L Guariguata, D R Whiting, I Hambleton, J Beagley, U Linnenkamp, and J E Shaw. Global estimates of diabetes prevalence for 2013 and projections for 2035. *Diabetes research and clinical practice*, 103(2):137–49, feb 2014.

[2] Ralph A. DeFronzo, Ele Ferrannini, Leif Groop, Robert R. Henry, William H. Herman, Jens Juul Holst, Frank B. Hu, C. Ronald Kahn, Itamar Raz, Gerald I. Shulman, Donald C. Simonson, Marcia A. Testa, and Ram Weiss. Type 2 diabetes mellitus. *Nature Reviews Disease Primers*, 1:15019, jul 2015.

[3] Over Cabrera, Dora M Berman, Norma S Kenyon, Camillo Ricordi, Per-Olof Berggren, and Alejandro Caicedo. The unique cytoarchitecture of human pancreatic islets has implications for islet cell function. *Proceedings of the National Academy of Sciences of the United States of America*, 103(7):2334–9, feb 2006.

[4] Richard K.P. Benninger, Min Zhang, W. Steven Head, Leslie S. Satin, and David W. Piston. Gap Junction Coupling and Calcium Waves in the Pancreatic Islet. *Biophysical Journal*, 95(11):5048–5061, dec 2008.

[5] W Steven Head, Meredith L Orseth, Craig S Nunemaker, Leslie S Satin, David W Piston, and Richard K P Benninger. Connexin-36 gap junctions regulate in vivo first- and second-phase insulin secretion dynamics and glucose tolerance in the conscious mouse. *Diabetes*, 61(7):1700–7, jul 2012.

[6] Richard K P Benninger, Troy Hutchens, W Steven Head, Michael J McCaughey, Min Zhang, Sylvain J Le Marchand, Leslie S Satin, and David W Piston. Intrinsic islet

heterogeneity and gap junction coupling determine spatiotemporal Ca wave dynamics. *Biophysical journal*, 107(11):2723–33, dec 2014.

[7] B. Thorens. Neural regulation of pancreatic islet cell mass and function. *Diabetes, Obesity and Metabolism*, 16(S1):87–95, sep 2014.

[8] Helena Edlund. Organogenesis: Pancreatic organogenesis developmental mechanisms and implications for therapy. *Nature Reviews Genetics*, 3(7):524–532, jul 2002.

[9] Susumu Seino, Tadao Shibasaki, and Kohtaro Minami. Dynamics of insulin secretion and the clinical implications for obesity and diabetes. *The Journal of clinical investigation*, 121(6):2118–25, jun 2011.

[10] June Chunqiu Hou, Le Min, and Jeffrey E. Pessin. Chapter 16 Insulin Granule Biogenesis, Trafficking and Exocytosis. In *Vitamins and hormones*, volume 80, pages 473–506. 2009.

[11] A. R. Meloni, M. B. DeYoung, C. Lowe, and D. G. Parkes. GLP-1 receptor activated insulin secretion from pancreatic β-cells: mechanism and glucose dependence. *Diabetes, Obesity and Metabolism*, 15(1):15–27, jan 2013.

[12] Daisuke Yabe and Yutaka Seino. Two incretin hormones GLP-1 and GIP: Comparison of their actions in insulin secretion and β cell preservation. *Progress in Biophysics and Molecular Biology*, 107(2):248–256, nov 2011.

[13] Josephine M. Egan, Angela Bulotta, Hongxiang Hui, and Riccardo Perfetti. GLP-1 receptor agonists are growth and differentiation factors for pancreatic islet beta cells. *Diabetes/Metabolism Research and Reviews*, 19(2):115–123, mar 2003.

[14] Wook Kim and Josephine M Egan. The role of incretins in glucose homeostasis and diabetes treatment. *Pharmacological reviews*, 60(4):470–512, dec 2008.

[15] Deborah M. Muoio and Christopher B. Newgard. Molecular and metabolic mechanisms of insulin resistance and β-cell failure in type 2 diabetes. *Nature Reviews Molecular Cell Biology*, 9(3):193–205, mar 2008.

[16] Pedro González-Muniesa, Miguel-Angel Mártinez-González, Frank B. Hu, Jean-Pierre Després, Yuji Matsuzawa, Ruth J. F. Loos, Luis A. Moreno, George A. Bray, and J. Alfredo Martinez. Obesity. *Nature Reviews Disease Primers*, 3:17034, jun 2017.

[17] Richard Dobbs, James Manyika, Jonathan Woetzel Michael Chui, and Susan Lund. Overcoming obesity: An initial economic analysis The McKinsey Global Institute. *McKinsey & Company*, 2014.

[18] Katja Rabe, Michael Lehrke, Klaus G Parhofer, and Uli C Broedl. Adipokines and insulin resistance. *Molecular medicine (Cambridge, Mass.)*, 14(11-12):741–51, 2008.

[19] Neil M Iyengar, Clifford A Hudis, and Andrew J Dannenberg. Obesity and inflammation: new insights into breast cancer development and progression. *American Society of Clinical Oncology educational book. American Society of Clinical Oncology. Meeting*, 33:46–51, 2013.

[20] Daniel F Argolo, Clifford A Hudis, and Neil M Iyengar. The Impact of Obesity on Breast Cancer. *Current oncology reports*, 20(6):47, apr 2018.

[21] Katharine S. Steinbeck, Natalie B. Lister, Megan L. Gow, and Louise A. Baur. Treatment of adolescent obesity. *Nature Reviews Endocrinology*, 14(6):331–344, jun 2018.

[22] Xiangpeng Li and Christopher J. Easley. Microfluidic systems for studying dynamic function of adipocytes and adipose tissue. *Analytical and Bioanalytical Chemistry*, 410(3):791–800, jan 2018.

[23] J L Halaas, K S Gajiwala, M Maffei, S L Cohen, B T Chait, D Rabinowitz, R L Lallone, S K Burley, and J M Friedman. Weight-reducing effects of the plasma protein encoded by the obese gene. *Science (New York, N.Y.)*, 269(5223):543–6, jul 1995.

[24] Erin E. Kershaw and Jeffrey S. Flier. Adipose Tissue as an Endocrine Organ. *The Journal of Clinical Endocrinology & Metabolism*, 89(6):2548–2556, jun 2004.

[25] Cristina Contreras, Rubén Nogueiras, Carlos Diéguez, Gema Medina-Gómez, and Miguel López. Hypothalamus and thermogenesis: Heating the BAT, browning the WAT. *Molecular and Cellular Endocrinology*, 438:107–115, dec 2016.

[26] Yi Zhu, Yong Gao, Caroline Tao, Mengle Shao, Shangang Zhao, Wei Huang, Ting Yao, Joshua A. Johnson, Tiemin Liu, Aaron M. Cypess, Olga Gupta, William L. Holland, Rana K. Gupta, David C. Spray, Herbert B. Tanowitz, Lei Cao, Matthew D. Lynes, Yu-Hua Tseng, Joel K. Elmquist, Kevin W. Williams, Hua V. Lin, and Philipp E. Scherer. Connexin 43 Mediates White Adipose Tissue Beiging by Facilitating the Propagation of Sympathetic Neuronal Signals. *Cell Metabolism*, 24(3):420–433, sep 2016.

[27] You-Ying Chau, Roberto Bandiera, Alan Serrels, Ofelia M. Martínez-Estrada, Wei Qing, Martin Lee, Joan Slight, Anna Thornburn, Rachel Berry, Sophie McHaffie, Roland H. Stimson, Brian R. Walker, Ramon Muñoz Chapuli, Andreas Schedl, and Nick Hastie. Visceral and subcutaneous fat have different origins and evidence supports a mesothelial source. *Nature Cell Biology*, 16(4):367–375, apr 2014.

[28] Robert I. Gregerman. Aging and Hormone-Sensitive Lipolysis: Reconciling the Literature. *The Journals of Gerontology*, 49(4), jul 1994.

[29] Bodil Bjørndal, Lena Burri, Vidar Staalesen, Jon Skorve, and Rolf K Berge. Different adipose depots: their role in the development of metabolic syndrome and mitochondrial response to hypolipidemic agents. *Journal of obesity*, 2011:490650, feb 2011.

[30] Marilia Sanches Santos Rizzo Zuttion, Cristiane Valverde Wenceslau, Pedro A. Lemos, Celso Takimura, and Irina Kerkis. Adipose Tissue-Derived Stem Cells and the Importance of Animal Model Standardization for Pre-Clinical Trials. *Revista Brasileira de Cardiologia Invasiva (English Edition)*, 21(3):281–287, jan 2013.

[31] E Shrago and T Spennetta. The carbon pathway for lipogenesis in isolated adipocytes from rat, guinea pig, and human adipose tissue. *The American Journal of Clinical Nutrition*, 29(5):540–545, may 1976.

[32] Pauline Morigny, Marianne Houssier, Etienne Mouisel, and Dominique Langin. Adipocyte lipolysis and insulin resistance. *Biochimie*, 125:259–266, jun 2016.

[33] Chase Romere, Clemens Duerrschmid, Juan Bournat, Petra Constable, Mahim Jain, Fan Xia, Pradip K. Saha, Maria Del Solar, Bokai Zhu, Brian York, Poonam Sarkar, David A. Rendon, M. Waleed Gaber, Scott A. LeMaire, Joseph S. Coselli, Dianna M. Milewicz, V. Reid Sutton, Nancy F. Butte, David D. Moore, and Atul R. Chopra. Asprosin, a Fasting-Induced Glucogenic Protein Hormone. *Cell*, 165(3):566–579, apr 2016.

[34] D O Allen and J T Quesenberry. Quantitative differences in the cyclic AMP-lipolysis relationships for isoproterenol and forskolin. *Journal of Pharmacology and Experimental Therapeutics*, 244(3), 1988.

[35] Li Kang and Laura E. Nagy. Chronic Ethanol Feeding Suppresses β-Adrenergic Receptor-Stimulated Lipolysis in Adipocytes Isolated from Epididymal Fat. *Endocrinology*, 147(9):4330–4338, sep 2006.

[36] Kevin J Acheson, Gérard Gremaud, Isabelle Meirim, Franck Montigon, Yves Krebs, Laurent B Fay, Louis-Jean Gay, Philippe Schneiter, Charles Schindler, and Luc Tappy. Metabolic effects of caffeine in humans: lipid oxidation or futile cycling? *The American Journal of Clinical Nutrition*, 79(1):40–46, jan 2004.

[37] Dara Leto and Alan R. Saltiel. Regulation of glucose transport by insulin: traffic control of GLUT4. *Nature Reviews Molecular Cell Biology*, 13(6):383–396, jun 2012.

[38] B. A. Henry and I. J. Clarke. Adipose Tissue Hormones and the Regulation of Food Intake. *Journal of Neuroendocrinology*, 20(6):842–849, jun 2008.

[39] Hong Ruan and Lily Q. Dong. Adiponectin signaling and function in insulin target tissues. *Journal of Molecular Cell Biology*, 8(2):101–109, apr 2016.

[40] T. Romacho, M. Elsen, D. Röhrborn, and J. Eckel. Adipose tissue and its role in organ crosstalk. *Acta Physiologica*, 210(4):733–753, apr 2014.

[41] Adilson Guilherme, Joseph V. Virbasius, Vishwajeet Puri, and Michael P. Czech. Adipocyte dysfunctions linking obesity to insulin resistance and type 2 diabetes. *Nature Reviews Molecular Cell Biology*, 9(5):367–377, may 2008.

[42] Robin E. Duncan, Maryam Ahmadian, Kathy Jaworski, Eszter Sarkadi-Nagy, and Hei Sook Sul. Regulation of Lipolysis in Adipocytes. *Annual Review of Nutrition*, 27(1):79–101, aug 2007.

[43] Muriel Abbaci, Muriel Barberi-Heyob, Walter Blondel, François Guillemin, and Jacques Didelon. Advantages and limitations of commonly used methods to assay the molecular permeability of gap junctional intercellular communication. *BioTechniques*, 45(1):33–62, jul 2008.

[44] Reiner Eckert. Gap-junctional single-channel permeability for fluorescent tracers in mammalian cell cultures. *Biophysical journal*, 91(2):565–79, jul 2006.

[45] J. Patrick Gonzalez, Jayalakshmi Ramachandran, Lai-Hua Xie, Jorge E. Contreras, and Diego Fraidenraich. Selective Connexin43 Inhibition Prevents Isoproterenol-Induced Arrhythmias and Lethality in Muscular Dystrophy Mice. *Scientific Reports*, 5(1):13490, oct 2015.

[46] Cedric Bathany, Derek Beahm, James D. Felske, Frederick Sachs, and Susan Z. Hua. High Throughput Assay of Diffusion through Cx43 Gap Junction Channels with a Microfluidic Chip. *Analytical Chemistry*, 83(3):933–939, feb 2011.

[47] Jia-hui Xia., Chun-yu Liu, Bei-sha Tang, Qian Pan, Lei Huang, He-ping Dai, Bao-rong Zhang, Wei Xie, Dong-xu Hu, Duo Zheng, Xiao-liu Shi, De-an Wang, Kun Xia, Kuan-ping Yu, Xiao-dong Liao, Yong Feng, Yi-feng Yang, Jian-yun Xiao, Ding-hua Xie, and Jian-zheng Huang. Erratum: Mutations in the gene encoding gap junction protein β-3 associated with autosomal dominant hearing impairment. *Nature Genetics*, 20(4):370–373, dec 1998.

[48] D. P. Kelsell, J. Dunlop, H. P. Stevens, N. J. Lench, J. N. Liang, G. Parry, R. F. Mueller, and I. M. Leigh. Connexin 26 mutations in hereditary non-syndromic sensorineural deafness. *Nature*, 387(6628):80–83, may 1997.

[49] J P Revel, A G Yee, and A J Hudspeth. Gap junctions between electrotonically coupled cells in tissue culture and in brown fat. *Proceedings of the National Academy of Sciences of the United States of America*, 68(12):2924–7, dec 1971.

[50] J D Sheridan. Electrical coupling between fat cells in newt fat body and mouse brown fat. *The Journal of cell biology*, 50(3):795–803, sep 1971.

[51] Shoshana Burke, Fnu Nagajyothi, Mia M. Thi, Menachem Hanani, Philipp E. Scherer, Herbert B. Tanowitz, and David C. Spray. Adipocytes in both brown and white adipose tissue of adult mice are functionally connected via gap junctions: implications for Chagas disease. *Microbes and Infection*, 16(11):893–901, nov 2014.

[52] Magalie A Ravier, Martin Gü, Anne Charollais, Asllan Gjinovci, Dorothé E Caille, Goran Sö, Claes B Wollheim, Klaus Willecke, Jean-Claude Henquin, and Paolo Meda. Loss of Connexin36 Channels Alters -Cell Coupling, Islet Synchronization of Glucose-Induced Ca 2 and Insulin Oscillations, and Basal Insulin Release. *Diabete*, 54(6):1798–1807, 2005.

[53] T G Youngstrom and T J Bartness. Catecholaminergic innervation of white adipose tissue in Siberian hamsters. *The American journal of physiology*, 268(3 Pt 2):R744–51, mar 1995.

[54] M Bamshad, V T Aoki, M G Adkison, W S Warren, and T J Bartness. Central nervous system origins of the sympathetic nervous system outflow to white adipose tissue. *The American journal of physiology*, 275(1 Pt 2):R291–9, jul 1998.

[55] Bernard G. Slavin and Kathryn W. Ballard. Morphological studies on the adrenergic innervation of white adipose tissue. *The Anatomical Record*, 191(3):377–389, jul 1978.

[56] Haochen Jiang, Xiaofan Ding, Ying Cao, Huanhuan Wang, and Wenwen Zeng. Dense Intra-adipose Sympathetic Arborizations Are Essential for Cold-Induced Beiging of Mouse White Adipose Tissue. *Cell metabolism*, 26(4):686–692.e3, oct 2017.

[57] Wenwen Zeng, Roksana M. M Pirzgalska, Mafalda M.A. M A Pereira, Nadiya Kubasova, Andreia Barateiro, Elsa Seixas, Yi-Hsueh Lu, Albina Kozlova, Henning Voss, Gabriel G. G Martins, Jeffrey M. M Friedman, and Ana I. I Domingos. Sympathetic Neuro-adipose Connections Mediate Leptin-Driven Lipolysis. *Cell*, 163(1):84–94, sep 2015.

[58] Akira Takahashi and Takashi Shimazu. Hypothalamic regulation of lipid metabolism in the rat: effect of hypothalamic stimulation on lipogenesis. *Journal of the Autonomic Nervous System*, 6(2):225–235, sep 1982.

[59] Felix Kreier, Eric Fliers, Peter J Voshol, Corbert G Van Eden, Louis M Havekes, Andries Kalsbeek, Caroline L Van Heijningen, Arja A Sluiter, Thomas C Mettenleiter, Johannes A Romijn, Hans P Sauerwein, and Ruud M Buijs. Selective parasympathetic innervation of subcutaneous and intra-abdominal fat–functional implications. *The Journal of clinical investigation*, 110(9):1243–50, nov 2002.

[60] L. Pénicaud. Relationships between adipose tissues and brain: what do we learn from animal studies? *Diabetes & Metabolism*, 36:S39–S44, oct 2010.

[61] Johan Ruud and Jens C. Brüning. Light on leptin link to lipolysis. *Nature*, 527(7576):43–44, nov 2015.

[62] Todd A. Duncombe, Augusto M. Tentori, and Amy E. Herr. Microfluidics : reframing biological enquiry. *Nature Reviews. Molecular Cell Biology*, 16(9):554–567, sep 2015.

[63] Ron Milo, Rob Phillips, and Nigel Orme. *Cell Biology by the Numbers*. Garland Science, 1st editio edition, 2015.

[64] George M. Whitesides. The origins and the future of microfluidics. *Nature*, 442(7101):368–373, jul 2006.

[65] Elisabetta Primiceri, Maria Serena Chiriacò, Ross Rinaldi, and Giuseppe Maruccio. Cell chips as new tools for cell biology results, perspectives and opportunities. *Lab on a Chip*, 13(19):3789, aug 2013.

[66] Michael Junkin, Alicia J Kaestli, Zhang Cheng, Christian Jordi, Cem Albayrak, Alexander Hoffmann, and Sava Tay. High-Content Quantification of Single-Cell Immune Dynamics. *Cell reports*, 15(2):411–22, apr 2016.

[67] Douglas B. Weibel, Maarten Kruithof, Scott Potenta, Samuel K. Sia, Andrew Lee, , and George M. Whitesides*. Torque-Actuated Valves for Microfluidics. *analytical chemistry*, 77(15):4726–4733, 2005.

[68] Jungkyu Kim, Amanda M. Stockton, Erik C. Jensen, and Richard A. Mathies. Pneumatically actuated microvalve circuits for programmable automation of chemical and biochemical analysis. *Lab on a Chip*, 16(5):812–819, feb 2016.

[69] Anthony K Au, Hoyin Lai, Ben R Utela, and Albert Folch. Microvalves and Micropumps for BioMEMS . *Micromachines*, 2:179–220, 2011.

[70] Bingqian Lin, Zhichao Guan, Yanling Song, Eunyeong Song, Zifei Lu, Dan Liu, Yuan An, Zhi Zhu, Leiji Zhou, and Chaoyong Yang. Lateral flow assay with pressure meter readout for rapid point-of-care detection of disease-associated protein. *Lab on a Chip*, 18(6):965–970, mar 2018.

[71] Yuanyuan Yang, Eka Noviana, Michael P. Nguyen, Brian J. Geiss, David S. Dandy, and Charles S. Henry. Paper-Based Microfluidic Devices: Emerging Themes and Applications. *Analytical Chemistry*, 89(1):71–91, jan 2017.

[72] Todd Thorsen, Richard W. Roberts, Frances H. Arnold, and Stephen R. Quake. Dynamic Pattern Formation in a Vesicle-Generating Microfluidic Device. *Physical Review Letters*, 86(18):4163–4166, apr 2001.

[73] L. D. van Vliet, P.-Y. Colin, and F. Hollfelder. Bioinspired genotype-phenotype linkages: mimicking cellular compartmentalization for the engineering of functional proteins. *Interface Focus*, 5(4):20150035–20150035, may 2015.

[74] Alexander K. Price and Brian M. Paegel. Discovery in Droplets. *Analytical Chemistry*, 88(1):339–353, jan 2016.

[75] Cheryl J. DeJournette, Joonyul Kim, Haley Medlen, Xiangpeng Li, Luke J. Vincent, and Christopher J. Easley. Creating Biocompatible OilWater Interfaces without Synthesis: Direct Interactions between Primary Amines and Carboxylated Perfluorocarbon Surfactants. *Analytical Chemistry*, 85(21):10556–10564, nov 2013.

[76] Jan-Willi Janiesch, Marian Weiss, Gerri Kannenberg, Jonathon Hannabuss, Thomas Surrey, Ilia Platzman, and Joachim P. Spatz. Key Factors for Stable Retention of Fluorophores and Labeled Biomolecules in Droplet-Based Microfluidics. *Analytical Chemistry*, 87(4):2063–2067, feb 2015.

[77] K C Lowe, M R Davey, and J B Power. Perfluorochemicals: their applications and benefits to cell culture. *Trends in biotechnology*, 16(6):272–7, jun 1998.

[78] C. Holtze, A. C. Rowat, J. J. Agresti, J. B. Hutchison, F. E. Angilè, C. H. J. Schmitz, S. Köster, H. Duan, K. J. Humphry, R. A. Scanga, J. S. Johnson, D. Pisignano, and D. A. Weitz. Biocompatible surfactants for water-in-fluorocarbon emulsions. *Lab on a Chip*, 8(10):1632, sep 2008.

[79] Fabienne Courtois, Luis F. Olguin, Graeme Whyte, Ashleigh B. Theberge, Wilhelm T. S. Huck, Florian Hollfelder, and Chris Abell. Controlling the Retention of Small Molecules in Emulsion Microdroplets for Use in Cell-Based Assays. *Analytical Chemistry*, 81(8):3008–3016, apr 2009.

[80] Philipp Gruner, Birte Riechers, Benoît Semin, Jiseok Lim, Abigail Johnston, Kathleen Short, and Jean-Christophe Baret. Controlling molecular transport in minimal emulsions. *Nature Communications*, 7:10392, jan 2016.

[81] Patrick A. Sandoz, Aram J. Chung, Westbrook M. Weaver, and Dino Di Carlo. Sugar Additives Improve Signal Fidelity for Implementing Two-Phase Resorufin-Based Enzyme Immunoassays. *Langmuir*, 30(23):6637–6643, jun 2014.

[82] Yousr Skhiri, Philipp Gruner, Benoît Semin, Quentin Brosseau, Deniz Pekin, Linas Mazutis, Victoire Goust, Felix Kleinschmidt, Abdeslam El Harrak, J. Brian Hutchison, Estelle Mayot, Jean-François Bartolo, Andrew D. Griffiths, Valérie Taly, and Jean-Christophe Baret. Dynamics of molecular transport by surfactants in emulsions. *Soft Matter*, 8(41):10618, oct 2012.

[83] Adam R. Abate and David A. Weitz. Air-bubble-triggered drop formation in microfluidics. *Lab on a Chip*, 11(10):1713, may 2011.

[84] J. H. Xu, S. W. Li, J. Tan, Y. J. Wang, and G. S. Luo. Preparation of highly monodisperse droplet in a T-junction microfluidic device. *AIChE Journal*, 52(9):3005–3010, sep 2006.

[85] Pingan Zhu and Liqiu Wang. Passive and active droplet generation with microfluidics: a review. *Lab on a Chip*, 17(1):34–75, dec 2017.

[86] Adrian M. Nightingale, Gareth W. H. Evans, Peixiang Xu, Byung Jae Kim, Sammer-ul Hassan, and Xize Niu. Phased peristaltic micropumping for continuous sampling and hardcoded droplet generation. *Lab on a Chip*, 17(6):1149–1157, mar 2017.

[87] Yong Zeng, Mimi Shin, and Tanyu Wang. Programmable active droplet generation enabled by integrated pneumatic micropumps. *Lab Chip*, 13(2):267–273, dec 2013.

[88] Christopher J. Easley Xiangpeng Li, Juan Hu. No Title. *In preparation*, 2018.

[89] Helen Song, Joshua D. Tice, and Rustem F. Ismagilov. A Microfluidic System for Controlling Reaction Networks in Time. *Angewandte Chemie International Edition*, 42(7):768–772, feb 2003.

[90] Adam Sciambi and Adam R. Abate. Generating electric fields in PDMS microfluidic devices with salt water electrodes. *Lab Chip*, 14(15):2605–2609, jul 2014.

[91] Jean-Christophe Baret. Surfactants in droplet-based microfluidics. *Lab Chip*, 12(3):422–433, jan 2012.

[92] Andrew B. MacConnell, Alexander K. Price, and Brian M. Paegel. An Integrated Microfluidic Processor for DNA-Encoded Combinatorial Library Functional Screening. *ACS Combinatorial Science*, 19(3):181–192, mar 2017.

[93] Heng-Dong Xi, Hao Zheng, Wei Guo, Alfonso M. Gañán-Calvo, Ye Ai, Chia-Wen Tsao, Jun Zhou, Weihua Li, Yanyi Huang, Nam-Trung Nguyen, and Say Hwa Tan. Active droplet sorting in microfluidics: a review. *Lab on a Chip*, 17(5):751–771, feb 2017.

[94] Jean-Christophe Baret, Oliver J. Miller, Valerie Taly, Michaël Ryckelynck, Abdeslam El-Harrak, Lucas Frenz, Christian Rick, Michael L. Samuels, J. Brian Hutchison, Jeremy J. Agresti, Darren R. Link, David A. Weitz, and Andrew D. Griffiths. Fluorescence-activated droplet sorting (FADS): efficient microfluidic cell sorting based on enzymatic activity. *Lab on a Chip*, 9(13):1850, jul 2009.

[95] Sathyakumar S. Kuntaegowdanahalli, Ali Asgar S. Bhagat, Girish Kumar, and Ian Papautsky. Inertial microfluidics for continuous particle separation in spiral microchannels. *Lab on a Chip*, 9(20):2973, oct 2009.

[96] Wesley G. Cochrane, Amber L. Hackler, Valerie J. Cavett, Alexander K. Price, and Brian M. Paegel. Integrated, Continuous Emulsion Creamer. *Analytical Chemistry*, 89(24):13227–13234, dec 2017.

[97] Balint Kintses, Liisa D van Vliet, Sean RA Devenish, and Florian Hollfelder. Microfluidic droplets: new integrated workflows for biological experiments. *Current Opinion in Chemical Biology*, 14(5):548–555, oct 2010.

[98] Marian Weiss, Johannes Patrick Frohnmayer, Lucia Theresa Benk, Barbara Haller, Jan-Willi Janiesch, Thomas Heitkamp, Michael Börsch, Rafael B. Lira, Rumiana Dimova, Reinhard Lipowsky, Eberhard Bodenschatz, Jean-Christophe Baret, Tanja Vidakovic-Koch, Kai Sundmacher, Ilia Platzman, and Joachim P. Spatz. Sequential bottom-up

assembly of mechanically stabilized synthetic cells by microfluidics. *Nature Materials*, 17(1):89–96, oct 2017.

[99] Helen Song and Rustem F. Ismagilov*. Millisecond Kinetics on a Microfluidic Chip Using Nanoliters of Reagents. *J. AM. CHEM. SOC.*, 125:14613–14619, 2003.

[100] Monpichar Srisa-art, Andrew J DeMello, and Joshua B Edel. High-Throughput DNA Droplet Assays Using Picoliter Reactor Volumes. *Anal. Chem.*, 79(17):6682–6689, 2007.

[101] Palani Kumaresan, Chaoyong James Yang, Samantha A. Cronier, Robert G. Blazej, and Richard A. Mathies. High-Throughput Single Copy DNA Amplification and Cell Analysis in Engineered Nanoliter Droplets. *Analytical Chemistry*, 80(10):3522–3529, may 2008.

[102] Duc T Tran, Valerie J Cavett, Vuong Q Dang, Héctor L Torres, and Brian M Paegel. Evolution of a mass spectrometry-grade protease with PTM-directed specificity. *Proceedings of the National Academy of Sciences of the United States of America*, 113(51):14686–14691, dec 2016.

[103] Philip Mair, Fabrice Gielen, and Florian Hollfelder. Exploring sequence space in search of functional enzymes using microfluidic droplets. *Current Opinion in Chemical Biology*, 37:137–144, apr 2017.

[104] Chawaree Chaipan, Anna Pryszlak, Hansi Dean, Pascal Poignard, Vladimir Benes, Andrew D. Griffiths, and Christoph A. Merten. Single-Virus Droplet Microfluidics for High-Throughput Screening of Neutralizing Epitopes on HIV Particles. *Cell Chemical Biology*, 24(6):751–757.e3, jun 2017.

[105] Nachiket Shembekar, Hongxing Hu, David Eustace, and Christoph A Merten. Single-Cell Droplet Microfluidic Screening for Antibodies Specifically Binding to Target Cells. *Cell reports*, 22(8):2206–2215, feb 2018.

[106] Yu Fen Samantha Seah, Hongxing Hu, and Christoph A. Merten. Microfluidic single-cell technology in immunology and antibody screening. *Molecular Aspects of Medicine*, 59:47–61, feb 2018.

[107] Joseph Abatemarco, Maen F. Sarhan, James M. Wagner, Jyun-Liang Lin, Leqian Liu, Wafa Hassouneh, Shuo-Fu Yuan, Hal S. Alper, and Adam R. Abate. RNA-aptamers-in-droplets (RAPID) high-throughput screening for secretory phenotypes. *Nature Communications*, 8(1):332, dec 2017.

[108] Aniruddha M. Kaushik, Kuangwen Hsieh, Liben Chen, Dong Jin Shin, Joseph C. Liao, and Tza-Huei Wang. Accelerating bacterial growth detection and antimicrobial susceptibility assessment in integrated picoliter droplet platform. *Biosensors and Bioelectronics*, 97:260–266, nov 2017.

[109] Allon M Klein, Linas Mazutis, Ilke Akartuna, Naren Tallapragada, Adrian Veres, Victor Li, Leonid Peshkin, David A Weitz, and Marc W Kirschner. Droplet barcoding for single-cell transcriptomics applied to embryonic stem cells. *Cell*, 161(5):1187–1201, may 2015.

[110] Evan Z. Macosko, Anindita Basu, Rahul Satija, James Nemesh, Karthik Shekhar, Melissa Goldman, Itay Tirosh, Allison R. Bialas, Nolan Kamitaki, Emily M. Martersteck, John J. Trombetta, David A. Weitz, Joshua R. Sanes, Alex K. Shalek, Aviv Regev, and Steven A. McCarroll. Highly Parallel Genome-wide Expression Profiling of Individual Cells Using Nanoliter Droplets. *Cell*, 161(5):1202–1214, may 2015.

[111] Atray Dixit, Oren Parnas, Biyu Li, Jenny Chen, Charles P. Fulco, Livnat Jerby-Arnon, Nemanja D. Marjanovic, Danielle Dionne, Tyler Burks, Raktima Raychowdhury, Britt Adamson, Thomas M. Norman, Eric S. Lander, Jonathan S. Weissman, Nir Friedman, and Aviv Regev. Perturb-Seq: Dissecting Molecular Circuits with Scalable Single-Cell RNA Profiling of Pooled Genetic Screens. *Cell*, 167(7):1853–1866.e17, dec 2016.

[112] Britt Adamson, Thomas M. Norman, Marco Jost, Min Y. Cho, James K. Nuñez, Yuwen Chen, Jacqueline E. Villalta, Luke A. Gilbert, Max A. Horlbeck, Marco Y. Hein, Ryan A.

Pak, Andrew N. Gray, Carol A. Gross, Atray Dixit, Oren Parnas, Aviv Regev, and Jonathan S. Weissman. A Multiplexed Single-Cell CRISPR Screening Platform Enables Systematic Dissection of the Unfolded Protein Response. *Cell*, 167(7):1867–1882.e21, dec 2016.

[113] Kennon S. Deal and Christopher J. Easley. Self-Regulated, Droplet-Based Sample Chopper for Microfluidic Absorbance Detection. *Analytical Chemistry*, 84(3):1510–1516, feb 2012.

[114] Jean T. Negou, L. Adriana Avila, Xiangpeng Li, Tesfagebriel M. Hagos, and Christopher J. Easley. Automated Microfluidic Droplet-Based Sample Chopper for Detection of Small Fluorescence Differences Using Lock-In Analysis. *Analytical Chemistry*, 89(11):6153–6159, jun 2017.

[115] Jean T. Negou, Juan Hu, Xiangpeng Li, and Christopher J. Easley. Advancement of analytical modes in a multichannel, microfluidic droplet-based sample chopper employing phase-locked detection. *Analytical Methods*, 2018.

[116] David M Rissin, Cheuk W Kan, Todd G Campbell, Stuart C Howes, David R Fournier, Linan Song, Tomasz Piech, Purvish P Patel, Lei Chang, Andrew J Rivnak, Evan P Ferrell, Jeffrey D Randall, Gail K Provuncher, David R Walt, and David C Duffy. Single-molecule enzyme-linked immunosorbent assay detects serum proteins at subfemtomolar concentrations. *Nature Biotechnology*, 28(6):595–599, jun 2010.

[117] Limor Cohen and David R. Walt. Single-Molecule Arrays for Protein and Nucleic Acid Analysis. *Annual Review of Analytical Chemistry*, 10(1):345–363, jun 2017.

[118] E F Ullman, H Kirakossian, S Singh, Z P Wu, B R Irvin, J S Pease, A C Switchenko, J D Irvine, A Dafforn, and C N Skold. Luminescent oxygen channeling immunoassay: measurement of particle binding kinetics by chemiluminescence. *Proceedings of the National Academy of Sciences of the United States of America*, 91(12):5426–30, jun 1994.

[119] E F Ullman, H Kirakossian, A C Switchenko, J Ishkanian, M Ericson, C A Wartchow, M Pirio, J Pease, B R Irvin, S Singh, R Singh, R Patel, A Dafforn, D Davalian, C Skold, N Kurn, and D B Wagner. Luminescent oxygen channeling assay (LOCI): sensitive, broadly applicable homogeneous immunoassay method. *Clinical Chemistry*, 42(9), 1996.

[120] Hui Zhao, Guanfeng Lin, Tiancai Liu, Junyu Liang, Zhiqi Ren, Rongliang Liang, Baihong Chen, Wenhua Huang, and Yingsong Wu. Rapid quantitation of human epididymis protein 4 in human serum by amplified luminescent proximity homogeneous immunoassay (AlphaLISA). *Journal of Immunological Methods*, 437:64–69, oct 2016.

[121] François Degorce, Amy Card, Sharon Soh, Eric Trinquet, Glenn P Knapik, and Bing Xie. HTRF: A technology tailored for drug discovery - a review of theoretical aspects and recent applications. *Current chemical genomics*, 3:22–32, may 2009.

[122] Michaela Adamcova and Fedor Šimko. Multiplex biomarker approach to cardiovascular diseases. *Acta Pharmacologica Sinica*, pages 1–5, apr 2018.

[123] Karl-Johan Leuchowius, Malin Jarvius, Malin Wickström, Linda Rickardson, Ulf Landegren, Rolf Larsson, Ola Söderberg, Mårten Fryknäs, and Jonas Jarvius. High content screening for inhibitors of protein interactions and post-translational modifications in primary cells by proximity ligation. *Molecular & cellular proteomics : MCP*, 9(1):178–83, jan 2010.

[124] Hongquan Zhang, Feng Li, Brittany Dever, Chuan Wang, Xing-Fang Li, and X. Chris Le. Assembling DNA through Affinity Binding to Achieve Ultrasensitive Protein Detection. *Angewandte Chemie International Edition*, 52(41):10698–10705, oct 2013.

[125] Simon Fredriksson, Mats Gullberg, Jonas Jarvius, Charlotta Olsson, Kristian Pietras, Sigrún Margrét Gústafsdóttir, Arne Östman, and Ulf Landegren. Protein detection using proximity-dependent DNA ligation assays. *Nature Biotechnology*, 20(5):473–477, may 2002.

[126] Fredrik Dahl, Mats Gullberg, Johan Stenberg, Ulf Landegren, and Mats Nilsson. Multiplex amplification enabled by selective circularization of large sets of genomic DNA fragments. *Nucleic acids research*, 33(8):e71, apr 2005.

[127] Ewa Heyduk, Benjamin Dummit, Yie-Hwa Chang, and Tomasz Heyduk. Molecular Pincers: Antibody-Based Homogeneous Protein Sensors. *Analytical Chemistry*, 80(13):5152–5159, jul 2008.

[128] Jiaming Hu, Tanyu Wang, Joonyul Kim, Curtis Shannon, and Christopher J. Easley. Quantitation of Femtomolar Protein Levels via Direct Readout with the Electrochemical Proximity Assay. *Journal of the American Chemical Society*, 134(16):7066–7072, apr 2012.

[129] Jiaming Hu, Yajiao Yu, Jessica C. Brooks, Leah A. Godwin, Subramaniam Somasundaram, Ferdous Torabinejad, Joonyul Kim, Curtis Shannon, and Christopher J. Easley. A Reusable Electrochemical Proximity Assay for Highly Selective, Real-Time Protein Quantitation in Biological Matrices. *Journal of the American Chemical Society*, 136(23):8467–8474, jun 2014.

[130] Martin Lundberg, Anna Eriksson, Bonnie Tran, Erika Assarsson, and Simon Fredriksson. Homogeneous antibody-based proximity extension assays provide sensitive and specific detection of low-abundant proteins in human blood. *Nucleic Acids Research*, 39(15):e102–e102, aug 2011.

[131] Andrew D. Ellington and Jack W. Szostak. In vitro selection of RNA molecules that bind specific ligands. *Nature*, 346(6287):818–822, aug 1990.

[132] C Tuerk and L Gold. Systematic evolution of ligands by exponential enrichment: RNA ligands to bacteriophage T4 DNA polymerase. *Science (New York, N.Y.)*, 249(4968):505–510, 1990.

[133] Gerard Mathis. Rare Earth Cryptates and Homogeneous Fluoroimmunoassays with Human Sera. *CUNICAL.CHEMISTRY*, 39(9):1953–1959, 1993.

[134] Ewa Heyduk, Michael M Moxley, Alison Salvatori, John A Corbett, and Tomasz Heyduk. Homogeneous insulin and C-Peptide sensors for rapid assessment of insulin and C-peptide secretion by the islets. *Diabetes*, 59(10):2360–5, oct 2010.

[135] Joonyul Kim, Juan Hu, Andresa B. Bezerra, Mark D. Holtan, Jessica C. Brooks, and Christopher J. Easley. Protein Quantification Using Controlled DNA Melting Transitions in Bivalent Probe Assemblies. *Analytical Chemistry*, 87(19):9576–9579, oct 2015.

[136] Juan Hu, Joonyul Kim, and Christopher J Easley. Quantifying Aptamer-Protein Binding via Thermofluorimetric Analysis. *Analytical methods : advancing methods and applications*, 7(17):7358–7362, sep 2015.

[137] Tomasz Heyduk and Ewa Heyduk. Molecular beacons for detecting DNA binding proteins. *Nature Biotechnology*, 20(2):171–176, feb 2002.

[138] Ewa Heyduk, Ying Fei, and Tomasz Heyduk. Homogeneous Fluorescence Assay for Cyclic AMP. *Combinatorial Chemistry & High Throughput Screening*, 6(4):347–354, jun 2003.

[139] Y Stefan, P Meda, M Neufeld, and L Orci. Stimulation of insulin secretion reveals heterogeneity of pancreatic B cells in vivo. *The Journal of clinical investigation*, 80(1):175–83, jul 1987.

[140] Leah A. Godwin, Meagan E. Pilkerton, Kennon S. Deal, Desiree Wanders, Robert L. Judd, and Christopher J. Easley. Passively Operated Microfluidic Device for Stimulation and Secretion Sampling of Single Pancreatic Islets. *Analytical Chemistry*, 83(18):7166–7172, sep 2011.

[141] Joonyul Kim, Jiaming Hu, Rebecca S. Sollie, and Christopher J. Easley. Improvement of Sensitivity and Dynamic Range in Proximity Ligation Assays by Asymmetric Connector Hybridization. *Analytical Chemistry*, 82(16):6976–6982, aug 2010.

[142] Louis C. Bock, Linda C. Griffin, John A. Latham, Eric H. Vermaas, and John J. Toole. Selection of single-stranded DNA molecules that bind and inhibit human thrombin. *Nature*, 355(6360):564–566, feb 1992.

[143] Diane M Tasset, Mark F Kubik, and Walter Steiner. Oligonucleotide inhibitors of human thrombin that bind distinct epitopes. *Journal of Molecular Biology*, 272(5):688–698, oct 1997.

[144] Juan Hu and Christopher J. Easley. Homogeneous Assays of Second Messenger Signaling and Hormone Secretion Using Thermofluorimetric Methods That Minimize Calibration Burden. *Analytical Chemistry*, 89(16):8517–8523, aug 2017.

[145] Susumu Seino, Tadao Shibasaki, and Kohtaro Minami. Pancreatic β–cell signaling: toward better understanding of diabetes and its treatment. *roc. Jpn. Acad., Ser. B*, 86:563–577, 2010.

[146] Eduardo Alegría Ezquerra, José M Castellano Vázquez, Ana Alegría Barrero, and E Alegría. Obesity, Metabolic Syndrome, and Diabetes: Cardiovascular Implications and Therapy. *Rev Esp Cardiol*, 61(7):752–64, 2008.

[147] E G Siegel and W Creutzfeldt. Stimulation of insulin release in isolated rat islets by GIP in physiological concentrations and its relation to islet cyclic AMP content. *Diabetologia*, 28(11):857–61, nov 1985.

[148] Daniel J. Drucker. The biology of incretin hormones. *Cell Metabolism*, 3(3):153–165, mar 2006.

[149] Sameer Mohammad, Lavoisier S Ramos, Jochen Buck, Lonny R Levin, Francesco Rubino, and Timothy E McGraw. Gastric inhibitory peptide controls adipose insulin sensitivity via activation of cAMP-response element-binding protein and p110β isoform of phosphatidylinositol 3-kinase. *The Journal of biological chemistry*, 286(50):43062–70, dec 2011.

[150] J. Dupre, S.A. Ross, D. Watson, and J.C. Brown. STIMULATION OF INSULIN SECRETION BY GASTRIC INHIBITORY POLYPEPTIDE IN MAN. *The Journal of Clinical Endocrinology & Metabolism*, 37(5):826–828, nov 1973.

[151] Catherine L Lawson, David Swigon, Katsuhiko S Murakami, Seth A Darst, Helen M Berman, and Richard H Ebright. Catabolite activator protein: DNA binding and transcription activation. *Current Opinion in Structural Biology*, 14(1):10–20, feb 2004.

[152] W G Ding and J Gromada. Protein kinase A-dependent stimulation of exocytosis in mouse pancreatic beta-cells by glucose-dependent insulinotropic polypeptide. *Diabetes*, 46(4):615–21, apr 1997.

[153] M Prentki and F M Matschinsky. Ca2+, cAMP, and phospholipid-derived messengers in coupling mechanisms of insulin secretion. *Physiological reviews*, 67(4):1185–248, oct 1987.

[154] Ghupurjan Gheni, Masahito Ogura, Masahiro Iwasaki, Norihide Yokoi, Kohtaro Minami, Yasumune Nakayama, Kazuo Harada, Benoit Hastoy, Xichen Wu, Harumi Takahashi, Kazushi Kimura, Toshiya Matsubara, Ritsuko Hoshikawa, Naoya Hatano, Kenji Sugawara, Tadao Shibasaki, Nobuya Inagaki, Takeshi Bamba, Akira Mizoguchi, Eiichiro Fukusaki, Patrik Rorsman, and Susumu Seino. Glutamate Acts as a Key Signal Linking Glucose Metabolism to Incretin/cAMP Action to Amplify Insulin Secretion. *Cell Reports*, 9(2):661–673, oct 2014.

[155] R H Alasbahi and M F Melzig. Forskolin and derivatives as tools for studying the role of cAMP. *Die Pharmazie*, 67(1):5–13, jan 2012.

[156] A Björklund and V E Grill. Relief from glucose-induced over-stimulation sensitizes the adenylate cyclase-cAMP system of rat pancreatic islets. *The Journal of endocrinology*, 166(3):537–44, sep 2000.

[157] Matthew Levy, Sean F Cater, and Andrew D Ellington. Quantum-dot aptamer beacons for the detection of proteins. *Chembiochem : a European journal of chemical biology*, 6(12):2163–6, dec 2005.

[158] Yi Xiao, Takanori Uzawa, Ryan J White, Daniel Demartini, and Kevin W Plaxco. On the Signaling of Electrochemical Aptamer-Based Sensors: Collision- and Folding-Based Mechanisms. *Electroanalysis*, 21(11):1267–1271, jun 2009.

[159] Andrew Csordas, Aren E Gerdon, Jonathan D Adams, Jiangrong Qian, Seung Soo Oh, Yi Xiao, and H Tom Soh. Detection of proteins in serum by micromagnetic aptamer PCR (MAP) technology. *Angewandte Chemie (International ed. in English)*, 49(2):355–8, jan 2010.

[160] Daniel C Leslie, Afshin Sohrabi, Pranvera Ikonomi, Marian L McKee, and James P Landers. Size-based separations as an important discriminator in development of proximity ligation assays for protein or organism detection. *Electrophoresis*, 31(10):1615–22, may 2010.

[161] Minseon Cho, Seung Soo Oh, Jeff Nie, Ron Stewart, Monte J. Radeke, Michael Eisenstein, Peter J. Coffey, James A. Thomson, and H. Tom Soh. Array-based Discovery of Aptamer Pairs. *Analytical Chemistry*, 87(1):821–828, jan 2015.

[162] Ian R. Olmsted, Yi Xiao, Minseon Cho, Andrew T. Csordas, Jonathan H. Sheehan, Jens Meiler, H. Tom Soh, and Darryl J. Bornhop. Measurement of AptamerProtein Interactions with Back-Scattering Interferometry. *Analytical Chemistry*, 83(23):8867–8870, dec 2011.

[163] Jishan Li, Yuhua Jia, Jing Zheng, Wenwan Zhong, Guoli Shen, Ronghua Yang, and Weihong Tan. Aptamer degradation inhibition combined with DNAzyme cascade-based signal amplification for colorimetric detection of proteins. *Chemical Communications*, 49(55):6137, jun 2013.

[164] Kewei Ren, Jie Wu, Feng Yan, and Huangxian Ju. Ratiometric electrochemical proximity assay for sensitive one-step protein detection. *Scientific reports*, 4(1):4360, mar 2014.

[165] Hyoyoung Mun, Eun-Jung Jo, Taihua Li, Hyou-Arm Joung, Dong-Gu Hong, Won-Bo Shim, Cheulhee Jung, and Min-Gon Kim. Homogeneous assay of target molecules based on chemiluminescence resonance energy transfer (CRET) using DNAzyme-linked aptamers. *Biosensors and Bioelectronics*, 58:308–313, aug 2014.

[166] Kevin W. Plaxco and H. Tom Soh. Switch-based biosensors: a new approach towards real-time, in vivo molecular detection. *Trends in Biotechnology*, 29(1):1–5, jan 2011.

[167] Audrey Sassolas, Loïc J. Blum, and Béatrice D. Leca-Bouvier. Homogeneous assays using aptamers. *The Analyst*, 136(2):257–274, dec 2011.

[168] Jiaming Hu and Christopher J. Easley. A simple and rapid approach for measurement of dissociation constants of DNA aptamers against proteins and small molecules via automated microchip electrophoresis. *The Analyst*, 136(17):3461, aug 2011.

[169] M W Pantoliano, E C Petrella, J D Kwasnoski, V S Lobanov, J Myslik, E Graf, T Carver, E Asel, B A Springer, P Lane, and F R Salemme. High-density miniaturized thermal shift assays as a general strategy for drug discovery. *Journal of biomolecular screening*, 6(6):429–40, dec 2001.

[170] Frank H Niesen, Helena Berglund, and Masoud Vedadi. The use of differential scanning fluorimetry to detect ligand interactions that promote protein stability. *Nature Protocols*, 2(9):2212–2221, sep 2007.

[171] Cuisong Zhou, Yaxin Jiang, Shuang Hou, Baocheng Ma, Xiaohong Fang, and Menglong Li. Detection of oncoprotein platelet-derived growth factor using a fluorescent signaling complex of an aptamer and TOTO. *Analytical and Bioanalytical Chemistry*, 384(5):1175–1180, feb 2006.

[172] Chun-Wei Chi, Yeh-Hsing Lao, Yi-Shan Li, and Lin-Chi Chen. A quantum dot-aptamer beacon using a DNA intercalating dye as the FRET reporter: Application to label-free thrombin detection. *Biosensors and Bioelectronics*, 26(7):3346–3352, mar 2011.

[173] Carl-Henrik Heldin and Bengt Westermark. Mechanism of Action and In Vivo Role of Platelet-Derived Growth Factor. *Physiological Reviews*, 79(4):1283–1316, jan 1999.

[174] Louis S. Green, Derek Jellinek, Robert Jenison, Arne Östman, Carl-Henrik Heldin, and Nebojsa Janjic. Inhibitory DNA Ligands to Platelet-Derived Growth Factor B-Chain. *Biochemistry*, 35(45):14413–14424, 1996.

[175] R F Macaya, J A Waldron, B A Beutel, H Gao, M E Joesten, M Yang, R Patel, A H Bertelsen, and A F Cook. Structural and functional characterization of potent antithrombotic oligonucleotides possessing both quadruplex and duplex motifs. *Biochemistry*, 34(13):4478–92, apr 1995.

[176] Hijiri Hasegawa, Ken-Ichi Taira, Koji Sode, and Kazunori Ikebukuro. Improvement of Aptamer Affinity by Dimerization. *Sensors (Basel, Switzerland)*, 8(2):1090–1098, feb 2008.

[177] Lisa Getty-Kaushik, Ann-Marie T. Richard, and Barbara E. Corkey. Glucose-dependent Insulin Modulation of Oscillatory Lipolysis in Perifused Rat Adipocytes. *Obesity Research*, 13(12):2058–2065, dec 2005.

[178] Cristina Alarcon, Brandon B Boland, Yuji Uchizono, Patrick C Moore, Bryan Peterson, Suryalekha Rajan, Olivia S Rhodes, Andrew B Noske, Leena Haataja, Peter Arvan, Bradly J Marsh, Jotham Austin, and Christopher J Rhodes. Pancreatic β-Cell Adaptive Plasticity in Obesity Increases Insulin Production but Adversely Affects Secretory Function. *Diabetes*, 65(2):438–50, feb 2016.

[179] Mickaël F. El Hachmane, Ali M. Komai, and Charlotta S. Olofsson. Cooling Reduces cAMP-Stimulated Exocytosis and Adiponectin Secretion at a Ca2+-Dependent Step in 3T3-L1 Adipocytes. *PLOS ONE*, 10(3):e0119530, mar 2015.

[180] Tomomi Tsubai, Yukihiro Noda, Kazuma Ito, Makoto Nakao, Yusuke Seino, Yutaka Oiso, and Yoji Hamada. Insulin elevates leptin secretion and mRNA levels via cyclic AMP in 3T3-L1 adipocytes deprived of glucose. *Heliyon*, 2(11):e00194, nov 2016.

[181] Allan Guan, Parisa Hamilton, Yi Wang, Maud Gorbet, Zhenyu Li, and K. Scott Phillips. Medical devices on chips. *Nature Biomedical Engineering*, 1(3):1–10, 2017.

[182] Eric K Sackmann, Anna L Fulton, and David J Beebe. The present and future role of microfluidics in biomedical research. *Nature*, 507(7491):181–189, 2014.

[183] Chun-Ting Kuo, Alison M. Thompson, Maria Elena Gallina, Fangmao Ye, Eleanor S. Johnson, Wei Sun, Mengxia Zhao, Jiangbo Yu, I-Che Wu, Bryant Fujimoto, Christopher C. DuFort, Markus A. Carlson, Sunil R. Hingorani, Amy L. Paguirigan, Jerald P. Radich, and Daniel T. Chiu. Optical painting and fluorescence activated sorting of single adherent cells labelled with photoswitchable Pdots. *Nature Communications*, 7:11468, apr 2016.

[184] Yi-Chin Toh, Chi Zhang, Jing Zhang, Yuet Mei Khong, Shi Chang, Victor D. Samper, Danny van Noort, Dietmar W. Hutmacher, and Hanry Yu. A novel 3D mammalian cell perfusion-culture system in microfluidic channels. *Lab on a Chip*, 7(3):302, mar 2007.

[185] Jamil El-Ali, Peter K. Sorger, and Klavs F. Jensen. Cells on chips. *Nature*, 442(7101):403–411, jul 2006.

[186] Matthias Mehling. Microfluidic cell culture. *Current Opinion in Biotechnology*, 25:95–102, feb 2014.

[187] Ryan A Kellogg, Rafael Gómez-Sjöberg, Anne A Leyrat, and Sava Tay. High-throughput microfluidic single-cell analysis pipeline for studies of signaling dynamics. *Nature Protocols*, 9(7):1713–1726, jun 2014.

[188] Colleen E. Dugan and Robert T. Kennedy. Measurement of Lipolysis Products Secreted by 3T3-L1 Adipocytes Using Microfluidics. *Methods in Enzymology*, 538:195–209, jan 2014.

[189] Colleen E Dugan, William P Cawthorn, Ormond A MacDougald, and Robert T Kennedy. Multiplexed microfluidic enzyme assays for simultaneous detection of lipolysis products from adipocytes. *Analytical and bioanalytical chemistry*, 406(20):4851–9, aug 2014.

[190] Shusheng Lu, Colleen E. Dugan, and Robert T. Kennedy. Microfluidic Chip with Integrated Electrophoretic Immunoassay for Investigating CellCell Interactions. *Analytical Chemistry*, 90(8):5171–5178, apr 2018.

[191] Colleen E. Dugan, James P. Grinias, Sebastian D. Parlee, Mahmoud El-Azzouny, Charles R. Evans, and Robert T. Kennedy. Monitoring cell secretions on microfluidic chips using solid-phase extraction with mass spectrometry. *Analytical and Bioanalytical Chemistry*, 409(1):169–178, jan 2017.

[192] Paul J A Kenis, Rustem F Ismagilov, Shuichi Takayama, George M Whitesides, Shulong Li, and Henry S White. Fabrication inside Microchannels Using Fluid Flow. *Acc. Chem. Res. 2*, 33:841–847, 2000.

[193] M. Erickstad, E. Gutierrez, and A. Groisman. A low-cost low-maintenance ultraviolet lithography light source based on light-emitting diodes. *Lab on a Chip*, 15(1):57–61, dec 2015.

[194] Jessica C. Brooks, Katarena I. Ford, Dylan H. Holder, Mark D. Holtan, and Christopher J. Easley. Macro-to-micro interfacing to microfluidic channels using 3D-printed templates: application to time-resolved secretion sampling of endocrine tissue. *The Analyst*, 141(20):5714–5721, oct 2016.

[195] Xiangpeng Li, Jessica C. Brooks, Juan Hu, Katarena I. Ford, and Christopher J. Easley. 3D-templated, fully automated microfluidic input/output multiplexer for endocrine tissue culture and secretion sampling. *Lab on a Chip*, 17(2):341–349, jan 2017.

[196] Maria Eugenia Frigolet Vázquez-Vela, Nimbe Torres, and Armando R. Tovar. White Adipose Tissue as Endocrine Organ and Its Role in Obesity. *Archives of Medical Research*, 39(8):715–728, nov 2008.

[197] M Lafontan. Advances in adipose tissue metabolism. *International Journal of Obesity*, 32(S7):S39–S51, dec 2008.

[198] Shona Morrison and Sean L McGee. 3T3-L1 adipocytes display phenotypic characteristics of multiple adipocyte lineages. *Adipocyte*, 3945(July):295–302, 2015.

[199] J Alan, H Maurice, and A Grose. Blood flow rates through adipose tissues of unanesthetized rats '. *AMERICAN JOURNAL OF PHYSIOLOGY*, 214(2):263–268, 1968.

[200] Pavel Neužil, Stefan Giselbrecht, Kerstin Länge, Tony Jun Huang, and Andreas Manz. Revisiting lab-on-a-chip technology for drug discovery. *Nature Reviews Drug Discovery*, 11(8):620–632, 2012.

[201] L Getty, A E Panteleon, S D Mittelman, M K Dea, and R N Bergman. Rapid oscillations in omental lipolysis are independent of changing insulin levels in vivo. *The Journal of clinical investigation*, 106(3):421–30, aug 2000.

[202] Raymond Cheong and Andre Levchenko. Oscillatory signaling processes: the how, the why and the where. *Current Opinion in Genetics & Development*, 20(6):665–669, dec 2010.

[203] Rohit N Kulkarni, Michael G Roper, Gabriella Dahlgren, David Q Shih, Lisa M Kauri, Jennifer L Peters, Markus Stoffel, and Robert T Kennedy. Islet secretory defect in insulin receptor substrate 1 null mice is linked with reduced calcium signaling and expression of sarco(endo)plasmic reticulum Ca2+-ATPase (SERCA)-2b and -3. *Diabetes*, 53(6):1517–25, jun 2004.

[204] John F Dishinger, Kendra R Reid, and Robert T Kennedy. Quantitative monitoring of insulin secretion from single islets of Langerhans in parallel on a microfluidic chip. *Analytical chemistry*, 81(8):3119–27, apr 2009.

[205] Lian Yi, Xue Wang, Raghuram Dhumpa, Adrian M. Schrell, Nikita Mukhitov, and Michael G. Roper. Integrated perfusion and separation systems for entrainment of insulin secretion from islets of Langerhans. *Lab on a Chip*, 15(3):823–832, jan 2015.

[206] Clemens Duerrschmid, Yanlin He, Chunmei Wang, Chia Li, Juan C. Bournat, Chase Romere, Pradip K. Saha, Mark E. Lee, Kevin J. Phillips, Mahim Jain, Peilin Jia, Zhongming Zhao, Monica Farias, Qi Wu, Dianna M. Milewicz, V. Reid Sutton, David D. Moore, Nancy F. Butte, Michael J. Krashes, Yong Xu, and Atul R. Chopra. Asprosin is a centrally acting orexigenic hormone. *Nature medicine*, 23(12):1444–1453, 2017.

[207] Jessica C. Brooks, Robert L. Judd, and Christopher J. Easley. Culture and Sampling of Primary Adipose Tissue in Practical Microfluidic Systems. In *Thermogenic Fat*, pages 185–201. Humana Press, New York, NY, 2017.

[208] Laetitia Michon, Rachel Nlend Nlend, Sabine Bavamian, Lorraine Bischoff, Nathalie Boucard, Dorothée Caille, José Cancela, Anne Charollais, Eric Charpantier, Philippe Klee, Manon Peyrou, Céline Populaire, Laurence Zulianello, and Paolo Meda. Involvement of gap junctional communication in secretion. *Biochimica et Biophysica Acta (BBA) - Biomembranes*, 1719(1-2):82–101, dec 2005.

[209] E. A. Turovsky, N. P. Kaimachnikov, M. V. Turovskaya, A. V. Berezhnov, V. V. Dynnik, and V. P. Zinchenko. Two mechanisms of calcium oscillations in adipocytes. *Biochemistry (Moscow) Supplement Series A: Membrane and Cell Biology*, 6(1):26–34, mar 2012.

Appendices

Appendix A

LabVIEW Codes

A.1 LabVIEW application for temperature control on Peltier

A.2 LabVIEW application for microfluidic droplet system

Total time (s) 20.0000

Time (s) 20.0000

Tset 20.0000

Tstart (deg C) 20

Tend (deg C) 30

time delay (s) 20

Tstep (deg C) 1

Current (Amp) 28.09

Figure A.1: Front panel of LabVIEW application for Peltier temperature control.

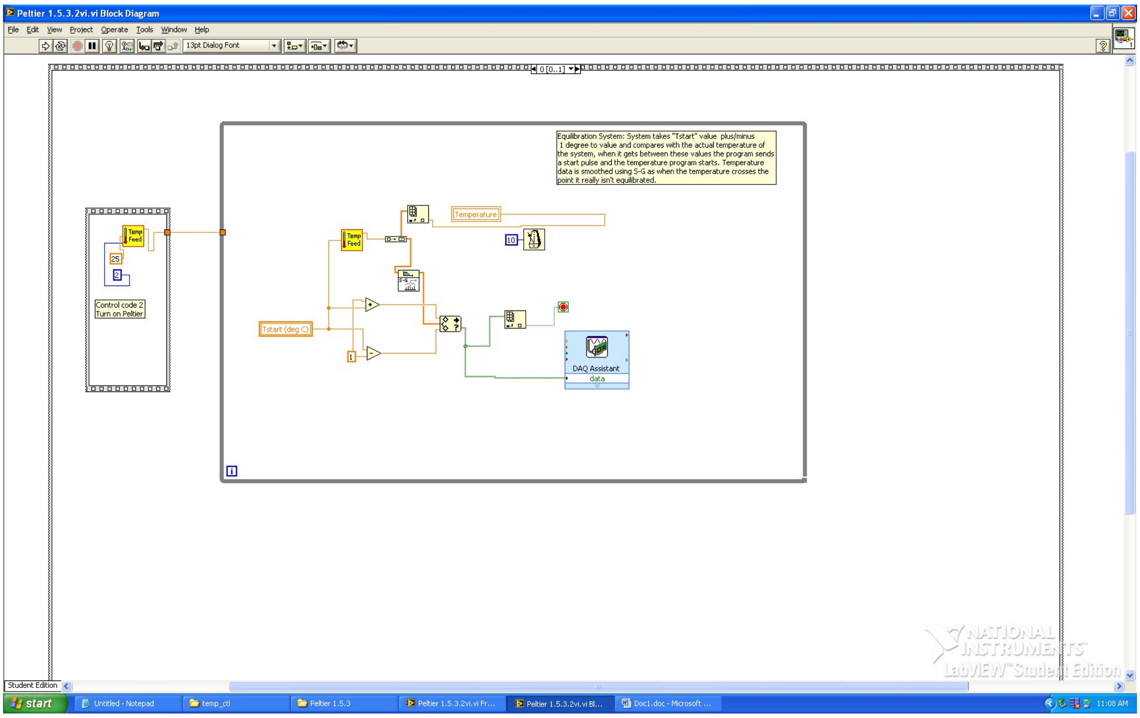

Equilibration System: System takes "Tstart" value plus/minus 1 degree to value and compares with the actual temperature of the system, when it gets between these values the program sends a start pulse and the temperature program starts. Temperature data is smoothed using S-G as when the temperature crosses the point it really isn't equilibrated.

Figure A.2: Block diagram 1 of LabVIEW application for Peltier temperature control.

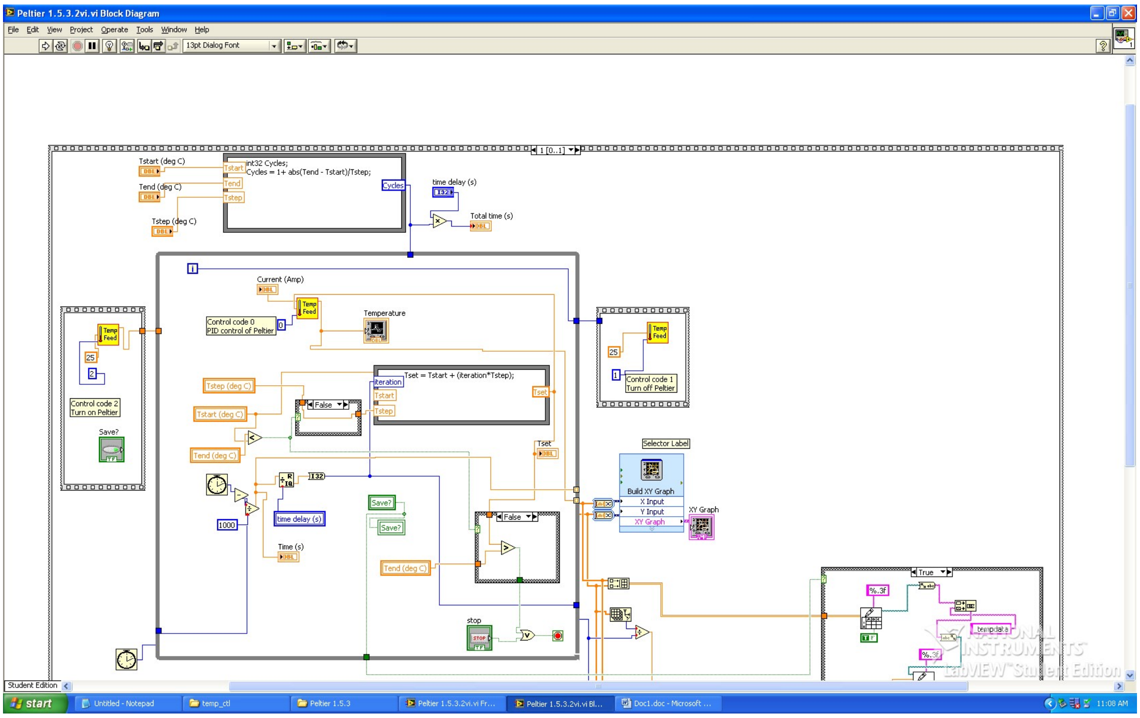

```
int32 Cycles;
Cycles = 1+ abs(Tend - Tstart)/Tstep;
```

```
Tset = Tstart + (iteration*Tstep);
```

Figure A.3: Block diagram 2 of LabVIEW application for Peltier temperature control.

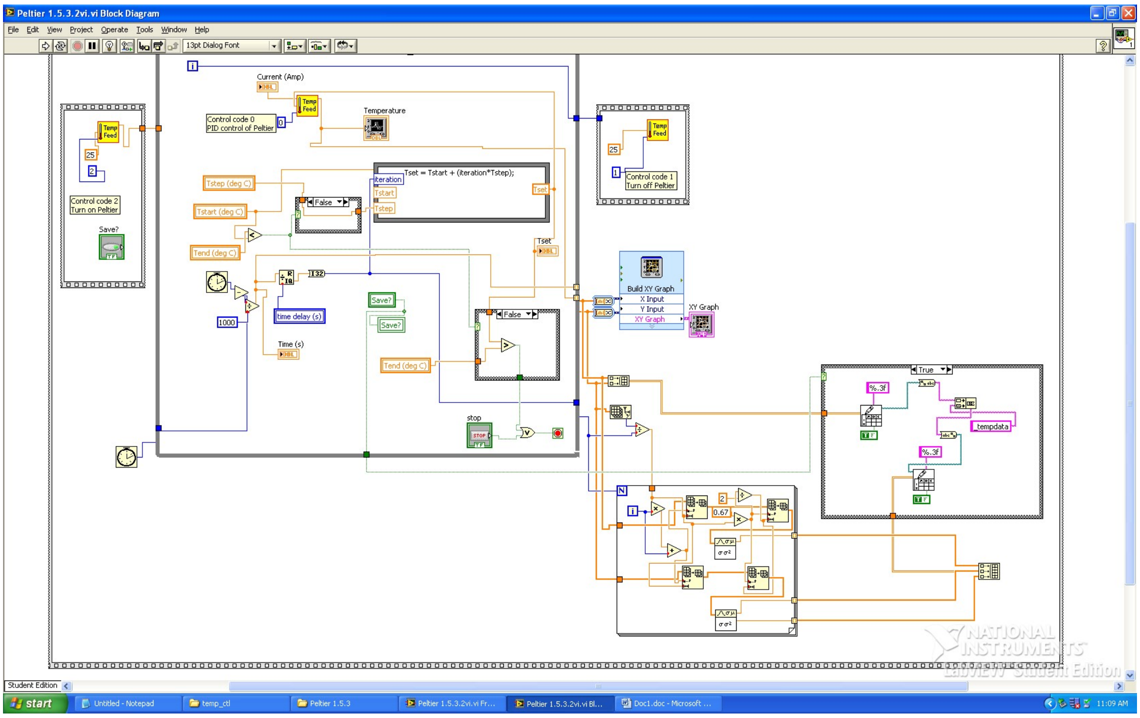

```
Tset = Tstart + (iteration*Tstep);
```

Figure A.4: Continued block diagram 2 of LabVIEW application for Peltier temperature control.

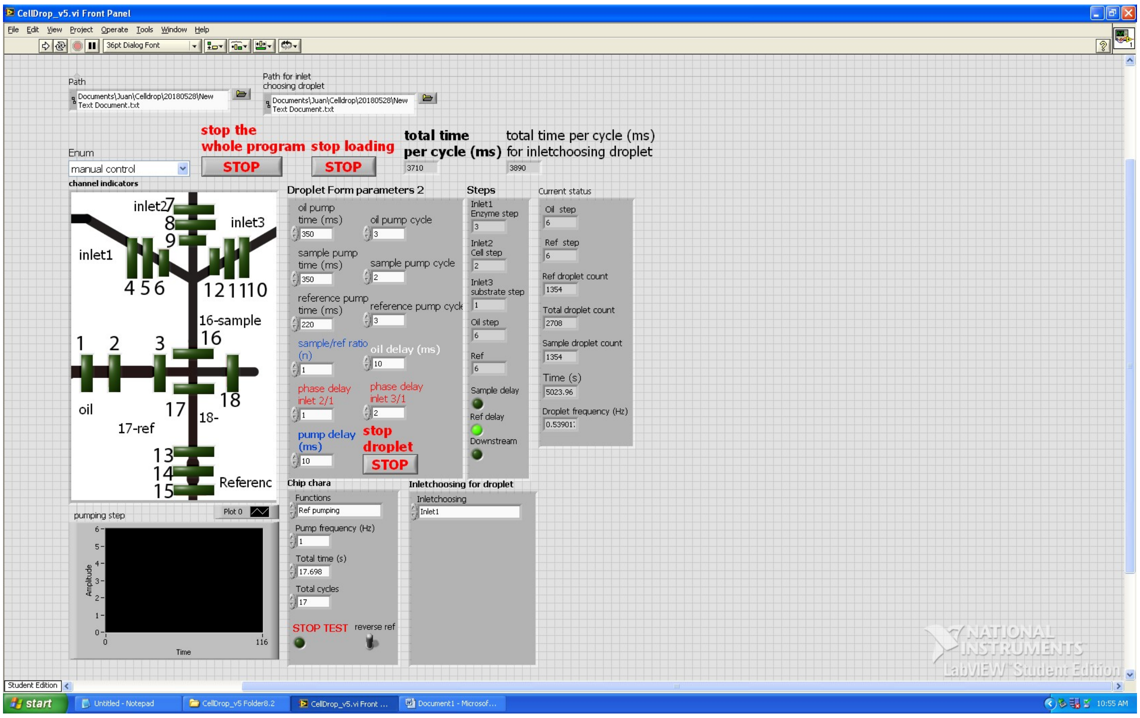

Path: Documents\Juan\Celldrop\20180528\New Text Document.txt

Path for inlet choosing droplet: Documents\Juan\Celldrop\20180528\New Text Document.txt

Enum: manual control

total time per cycle (ms): 3710

total time per cycle (ms) for inletchoosing droplet: 3890

oil pump time (ms): 350
oil pump cycle: 3
sample pump time (ms): 350
sample pump cycle: 2
reference pump time (ms): 220
reference pump cycle: 3
sample/ref ratio (n): 1
oil delay (ms): 10
phase delay inlet 2/1: 1
phase delay inlet 3/1: 2
pump delay (ms): 10

Inlet1 Enzyme step: 3
Inlet2 Cell step: 2
Inlet3 substrate step: 1
Oil step: 6
Ref: 6

Oil step: 6
Ref step: 6
Ref droplet count: 1354
Total droplet count: 2708
Sample droplet count: 1354
Time (s): 5023.96
Droplet frequency (Hz): 0.53901

Functions: Ref pumping
Pump frequency (Hz): 1
Total time (s): 17.698
Total cycles: 17

Inletchoosing: Inlet1

Figure A.5: Block diagram of main program of LabVIEW application for microfluidic droplet system.

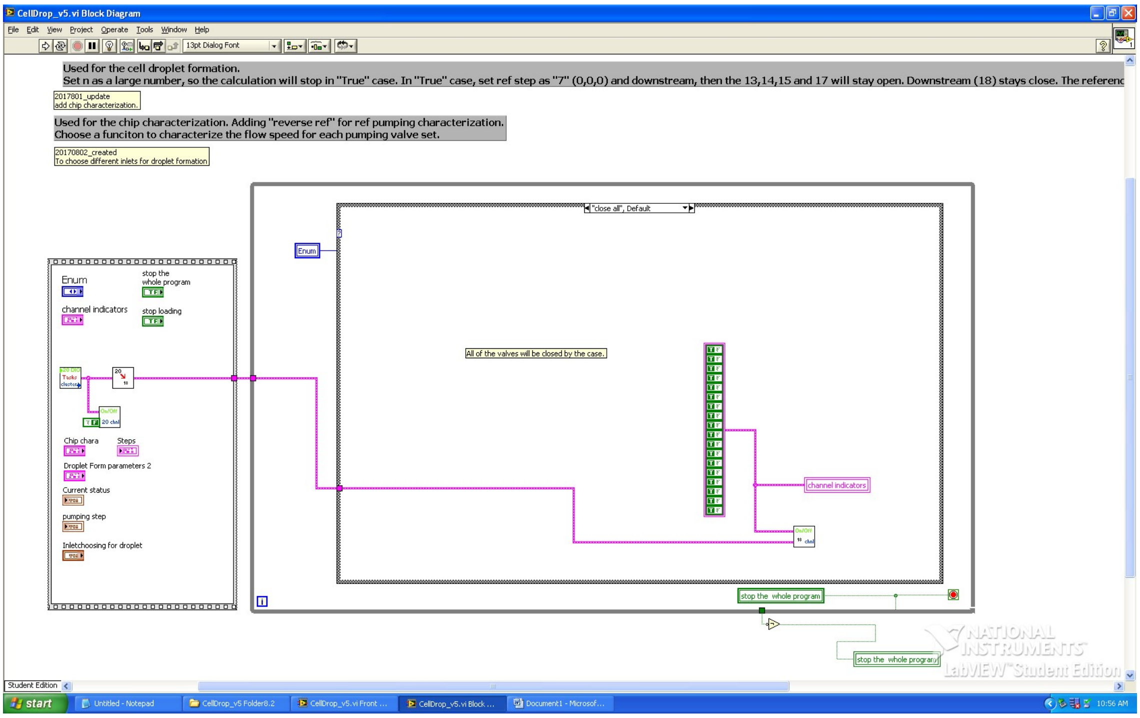

Used for the cell droplet formation.
Set n as a large number, so the calculation will stop in "True" case. In "True" case, set ref step as "7" (0,0,0) and downstream, then the 13,14,15 and 17 will stay open. Downstream (18) stays close. The referenc

2017801_update
add chip characterization.

Used for the chip characterization. Adding "reverse ref" for ref pumping characterization.
Choose a funciton to characterize the flow speed for each pumping valve set.

20170802_created
To choose different inlets for droplet formation

All of the valves will be closed by the case.

Figure A.6: Block diagram of main program of LabVIEW application for microfluidic droplet system–to close all valves.

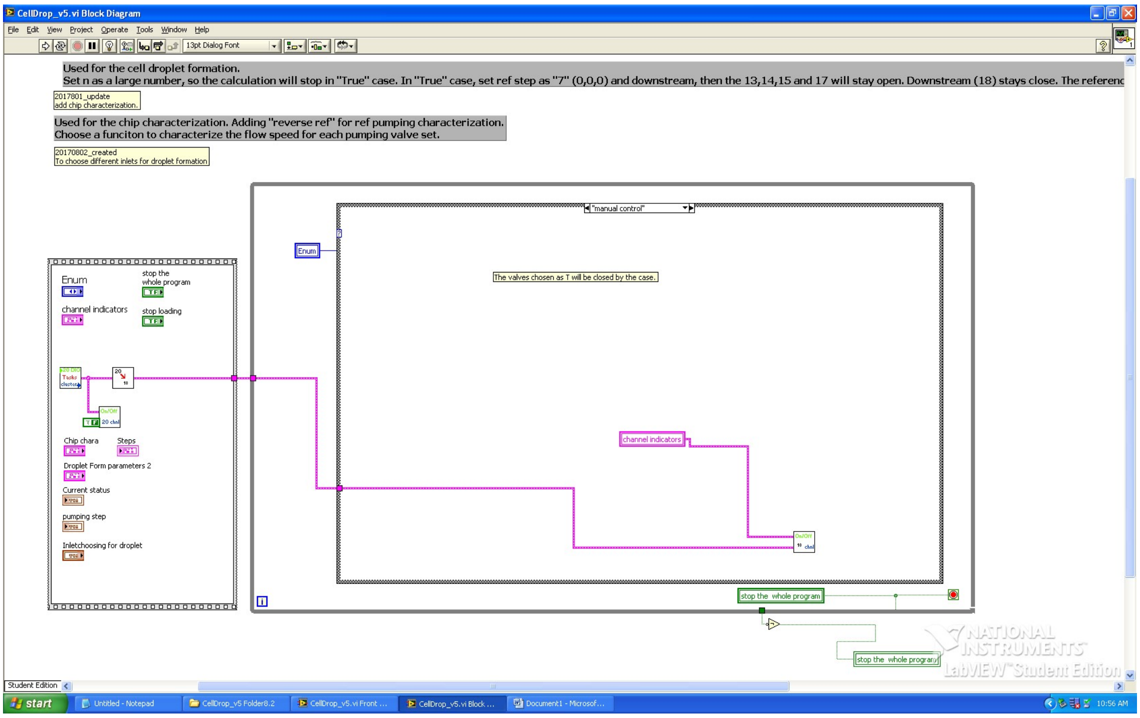

Used for the cell droplet formation.
Set n as a large number, so the calculation will stop in "True" case. In "True" case, set ref step as "7" (0,0,0) and downstream, then the 13,14,15 and 17 will stay open. Downstream (18) stays close. The referenc

2017801_update
add chip characterization.

Used for the chip characterization. Adding "reverse ref" for ref pumping characterization.
Choose a funciton to characterize the flow speed for each pumping valve set.

20170802_created
To choose different inlets for droplet formation

The valves chosen as T will be closed by the case.

Figure A.7: Block diagram of main program of LabVIEW application for microfluidic droplet system–manual control on/of of each valve.

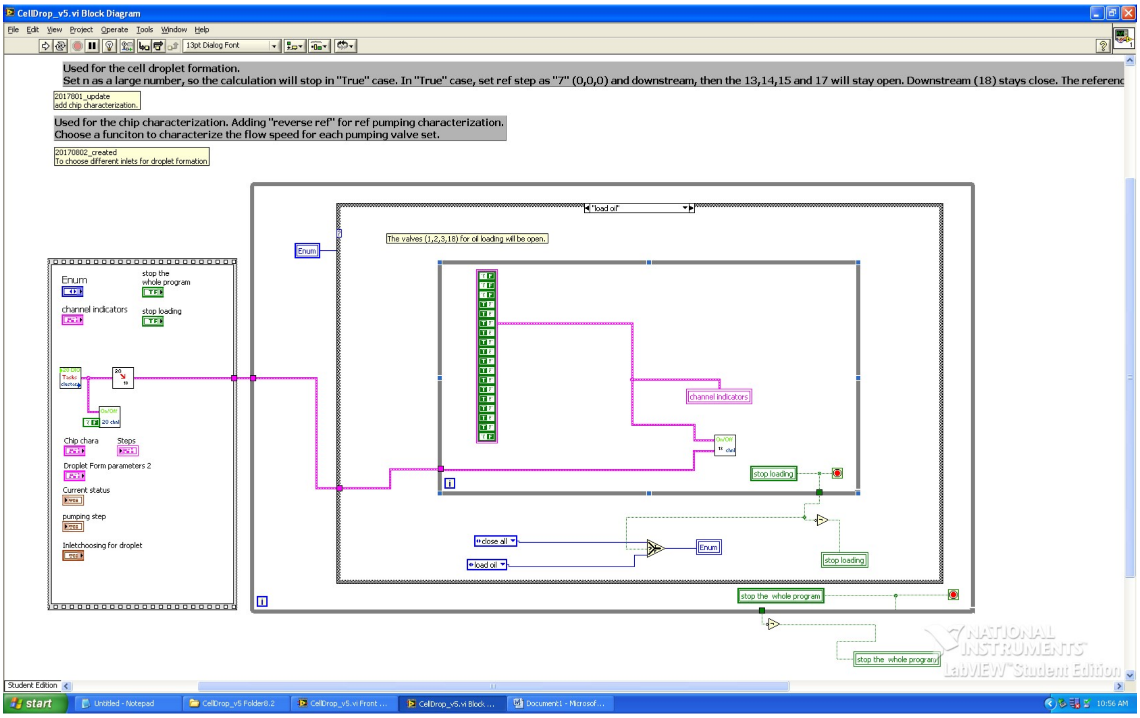

Used for the cell droplet formation.
Set n as a large number, so the calculation will stop in "True" case. In "True" case, set ref step as "7" (0,0,0) and downstream, then the 13,14,15 and 17 will stay open. Downstream (18) stays close. The referenc

2017801_update
add chip characterization.

Used for the chip characterization. Adding "reverse ref" for ref pumping characterization.
Choose a funciton to characterize the flow speed for each pumping valve set.

20170802_created
To choose different inlets for droplet formation

The valves (1,2,3,18) for oil loading will be open.

Figure A.8: Block diagram of main program of LabVIEW application for microfluidic droplet system–“load oil”.

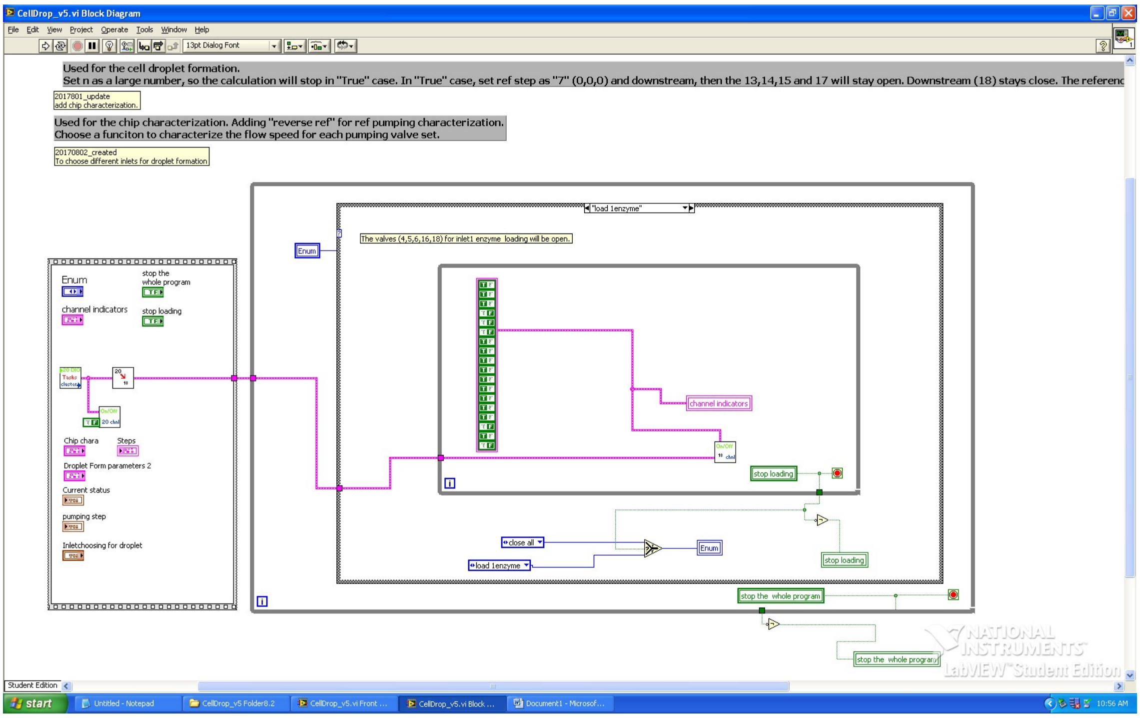
Used for the cell droplet formation.
Set n as a large number, so the calculation will stop in "True" case. In "True" case, set ref step as "7" (0,0,0) and downstream, then the 13,14,15 and 17 will stay open. Downstream (18) stays close. The referenc

2017801_update
add chip characterization.

Used for the chip characterization. Adding "reverse ref" for ref pumping characterization.
Choose a funciton to characterize the flow speed for each pumping valve set.

20170802_created
To choose different inlets for droplet formation

The valves (4,5,6,16,18) for inlet1 enzyme loading will be open.

Figure A.9: Block diagram of main program of LabVIEW application for microfluidic droplet system–"load enzyme".

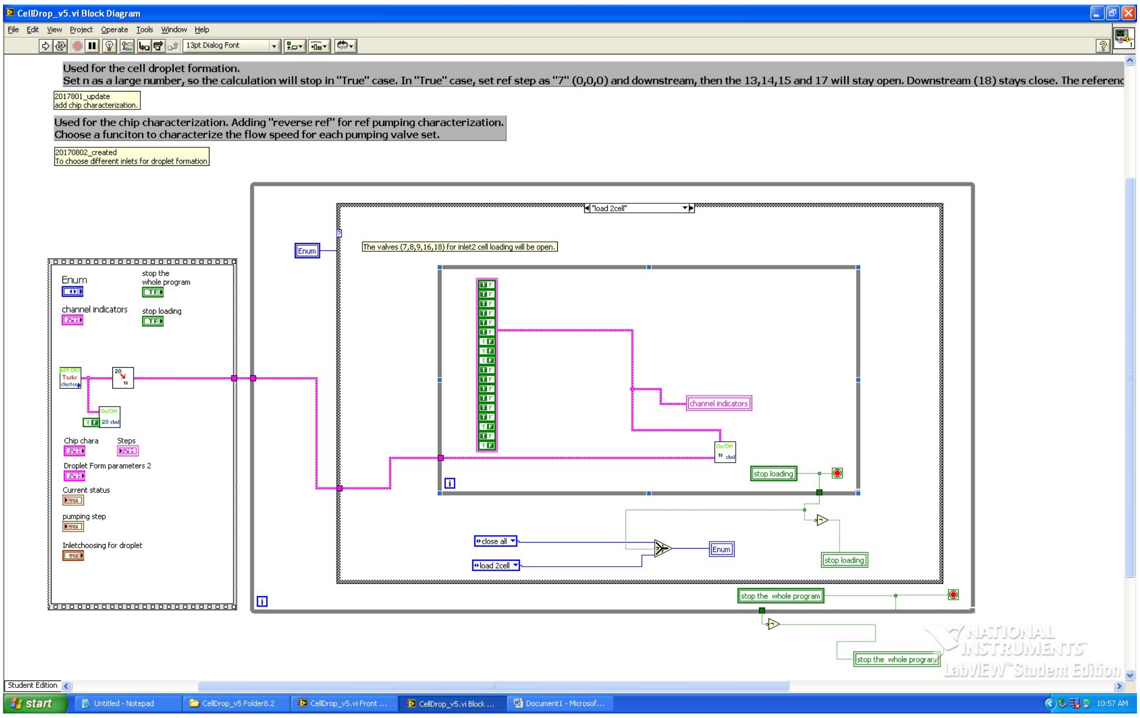
Used for the cell droplet formation.
Set n as a large number, so the calculation will stop in "True" case. In "True" case, set ref step as "7" (0,0,0) and downstream, then the 13,14,15 and 17 will stay open. Downstream (18) stays close. The referenc

2017801_update
add chip characterization.

Used for the chip characterization. Adding "reverse ref" for ref pumping characterization.
Choose a funciton to characterize the flow speed for each pumping valve set.

20170802_created
To choose different inlets for droplet formation

The valves (7,8,9,16,18) for inlet2 cell loading will be open.

Figure A.10: Block diagram of main program of LabVIEW application for microfluidic droplet system–"load 2 cell".

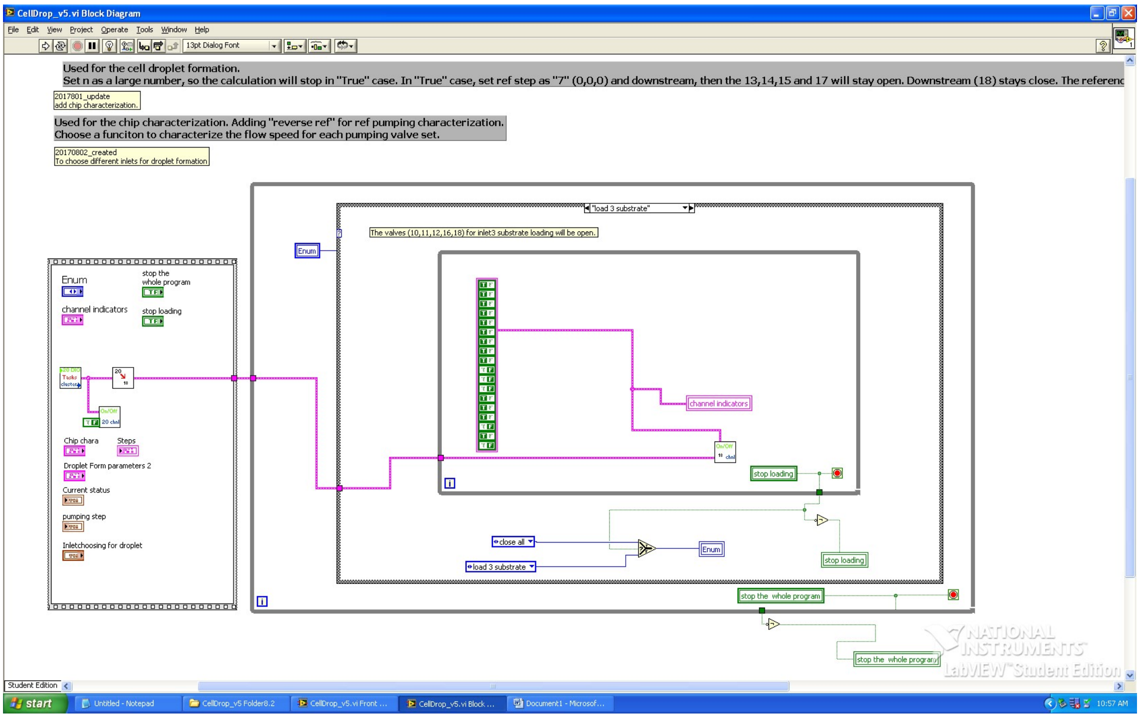

CellDrop_v5.vi Block Diagram

Used for the cell droplet formation.
Set n as a large number, so the calculation will stop in "True" case. In "True" case, set ref step as "7" (0,0,0) and downstream, then the 13,14,15 and 17 will stay open. Downstream (18) stays close. The referenc

2017801_update
add chip characterization.

Used for the chip characterization. Adding "reverse ref" for ref pumping characterization.
Choose a funciton to characterize the flow speed for each pumping valve set.

20170802_created
To choose different inlets for droplet formation

"load 3 substrate"

The valves (10,11,12,16,18) for inlet3 substrate loading will be open.

Figure A.11: Block diagram of main program of LabVIEW application for microfluidic droplet system–“load 3 substrate”.

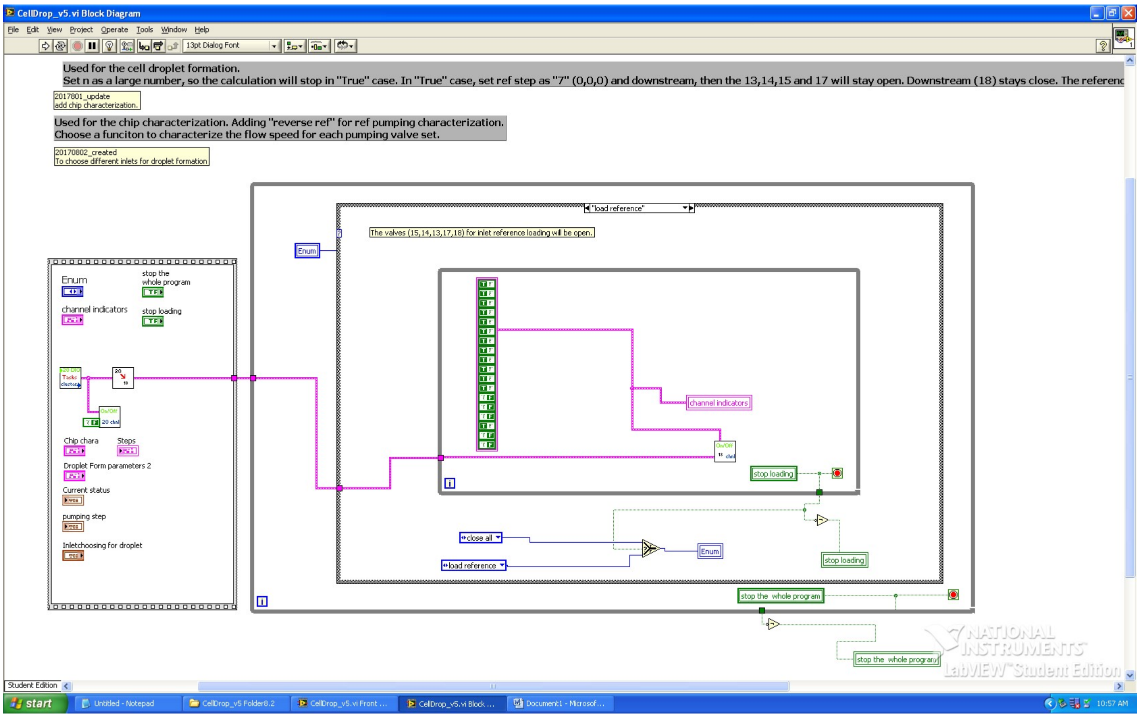

CellDrop_v5.vi Block Diagram

Used for the cell droplet formation.
Set n as a large number, so the calculation will stop in "True" case. In "True" case, set ref step as "7" (0,0,0) and downstream, then the 13,14,15 and 17 will stay open. Downstream (18) stays close. The referenc

2017801_update
add chip characterization.

Used for the chip characterization. Adding "reverse ref" for ref pumping characterization.
Choose a funciton to characterize the flow speed for each pumping valve set.

20170802_created
To choose different inlets for droplet formation

"load reference"

The valves (15,14,13,17,18) for inlet reference loading will be open.

Figure A.12: Block diagram of main program of LabVIEW application for microfluidic droplet system–“load reference”.

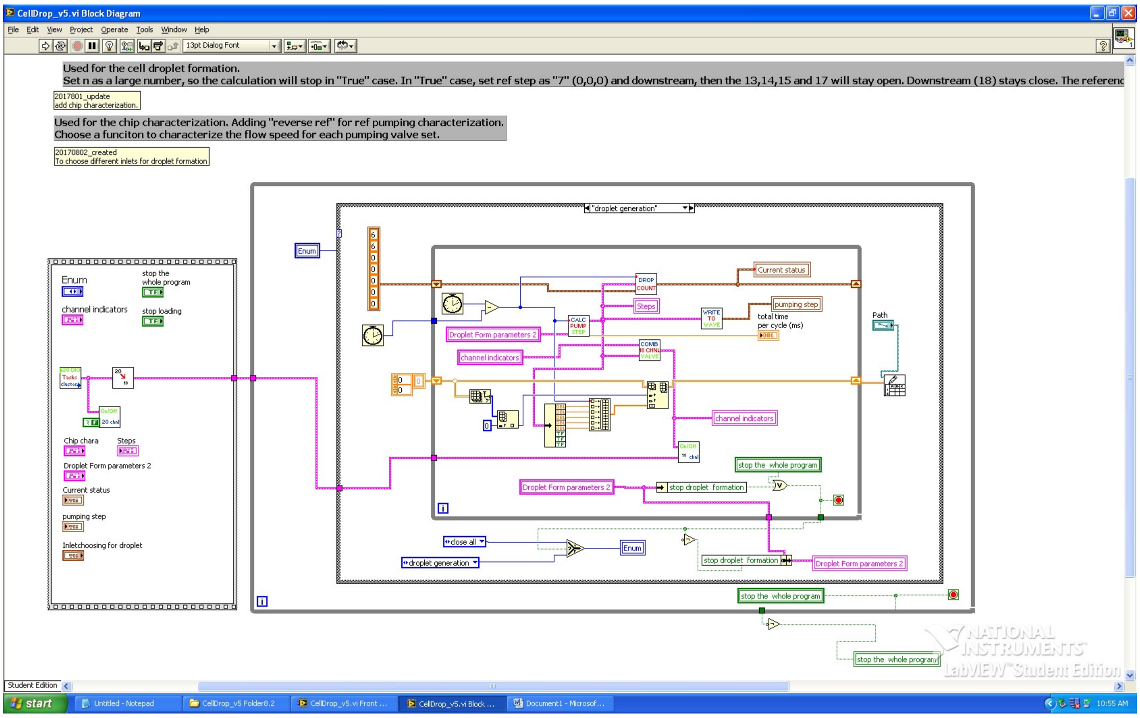

CellDrop_v5.vi Block Diagram

Used for the cell droplet formation.
Set n as a large number, so the calculation will stop in "True" case. In "True" case, set ref step as "7" (0,0,0) and downstream, then the 13,14,15 and 17 will stay open. Downstream (18) stays close. The referenc

2017801_update
add chip characterization.

Used for the chip characterization. Adding "reverse ref" for ref pumping characterization.
Choose a funciton to characterize the flow speed for each pumping valve set.

20170802_created
To choose different inlets for droplet formation

Figure A.13: Block diagram of main program of LabVIEW application for microfluidic droplet system–“droplet generation”.

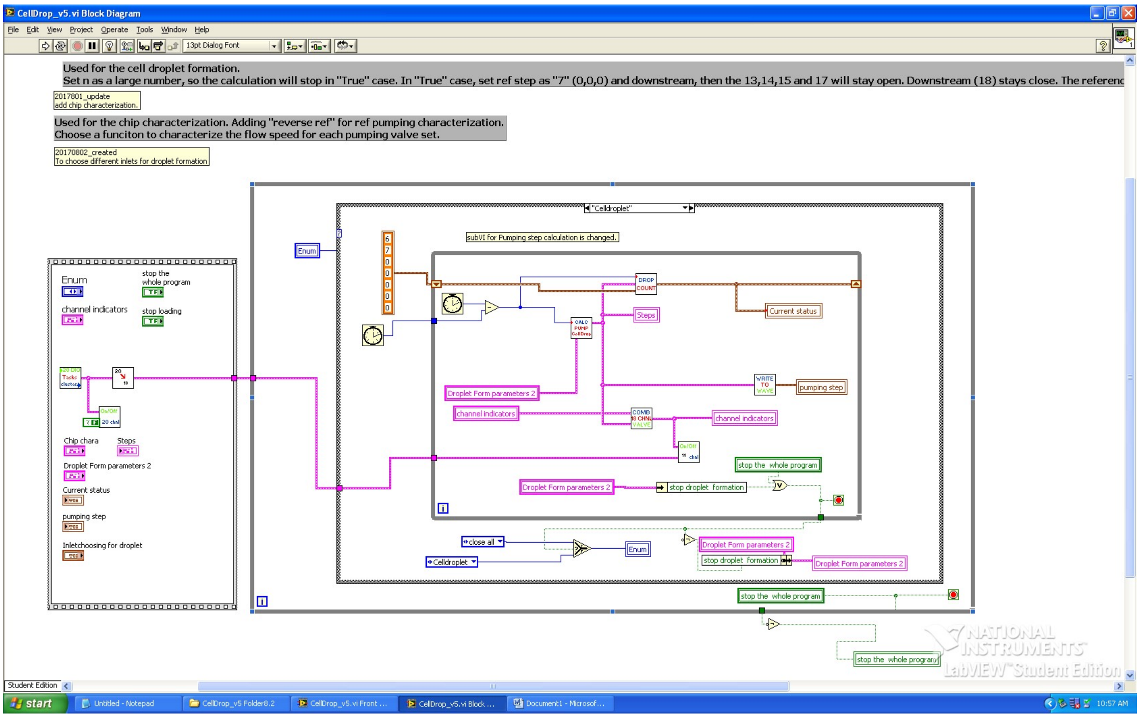

CellDrop_v5.vi Block Diagram

Used for the cell droplet formation.
Set n as a large number, so the calculation will stop in "True" case. In "True" case, set ref step as "7" (0,0,0) and downstream, then the 13,14,15 and 17 will stay open. Downstream (18) stays close. The referenc

2017801_update
add chip characterization.

Used for the chip characterization. Adding "reverse ref" for ref pumping characterization.
Choose a funciton to characterize the flow speed for each pumping valve set.

20170802_created
To choose different inlets for droplet formation

subVI for Pumping step calculation is changed.

Figure A.14: Block diagram of main program of LabVIEW application for microfluidic droplet system–“Celldroplet for cell encapsulation”.

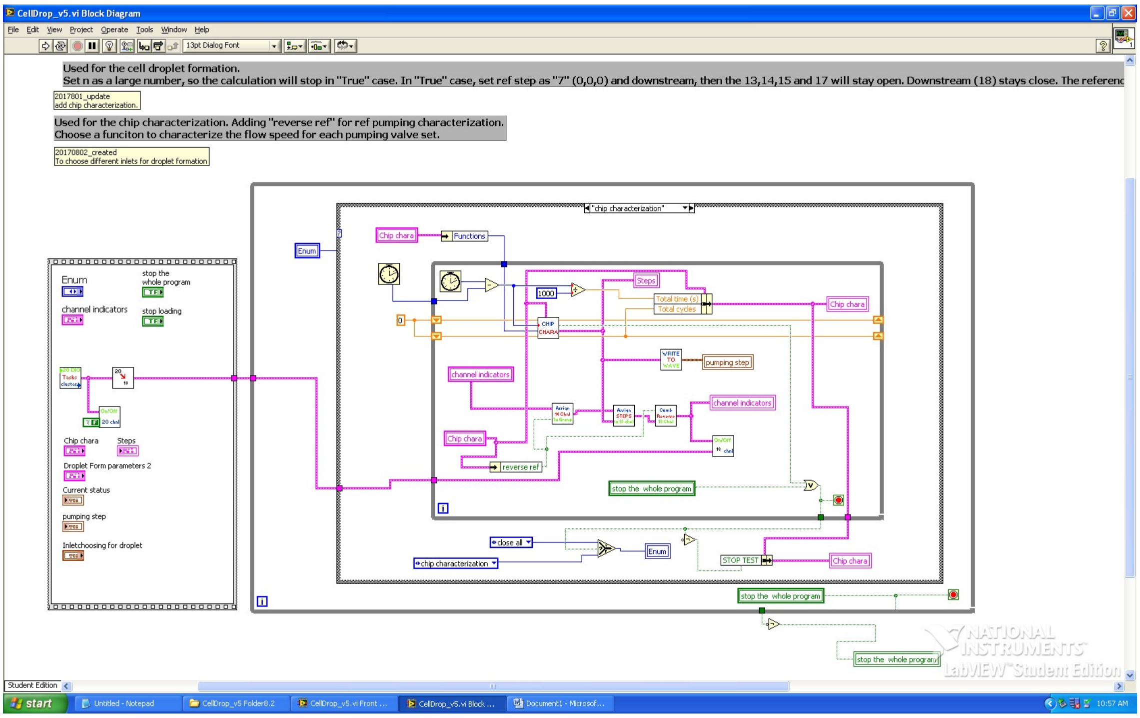

Used for the cell droplet formation.
Set n as a large number, so the calculation will stop in "True" case. In "True" case, set ref step as "7" (0,0,0) and downstream, then the 13,14,15 and 17 will stay open. Downstream (18) stays close. The referenc

2017801_update
add chip characterization.

Used for the chip characterization. Adding "reverse ref" for ref pumping characterization.
Choose a funciton to characterize the flow speed for each pumping valve set.

20170802_created
To choose different inlets for droplet formation

Figure A.15: Block diagram of main program of LabVIEW application for microfluidic droplet system–"chip characterization".

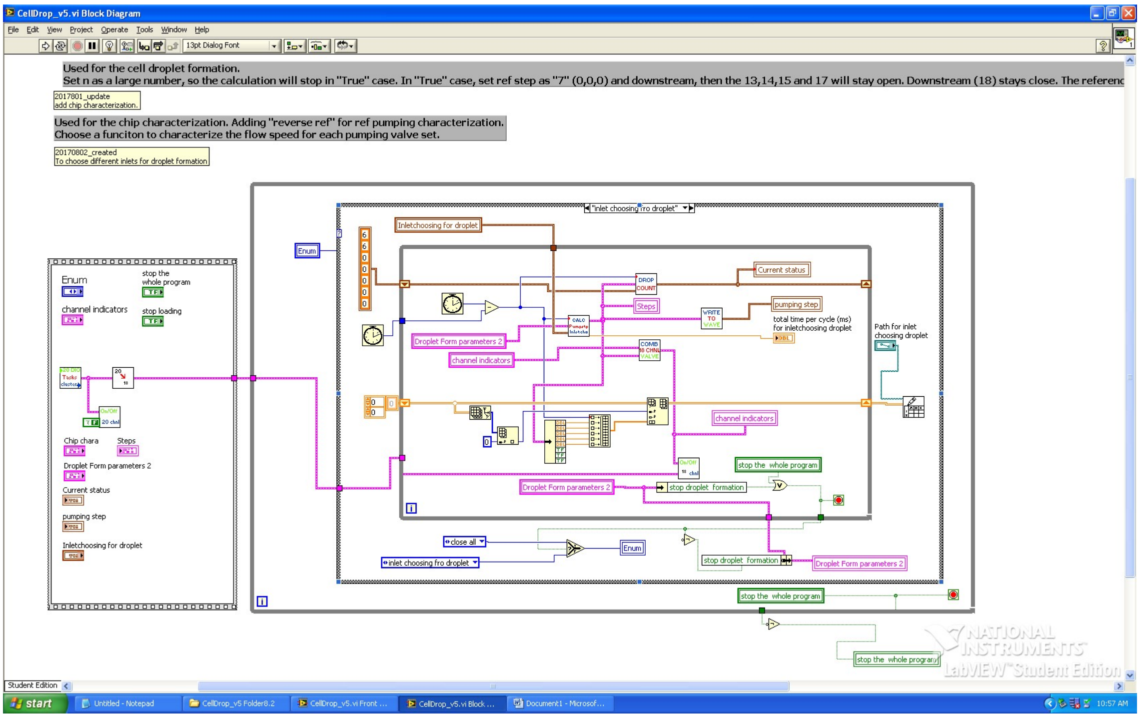

Used for the cell droplet formation.
Set n as a large number, so the calculation will stop in "True" case. In "True" case, set ref step as "7" (0,0,0) and downstream, then the 13,14,15 and 17 will stay open. Downstream (18) stays close. The referenc

2017801_update
add chip characterization.

Used for the chip characterization. Adding "reverse ref" for ref pumping characterization.
Choose a funciton to characterize the flow speed for each pumping valve set.

20170802_created
To choose different inlets for droplet formation

Figure A.16: Block diagram of main program of LabVIEW application for microfluidic droplet system–"inlet choosing for droplet".

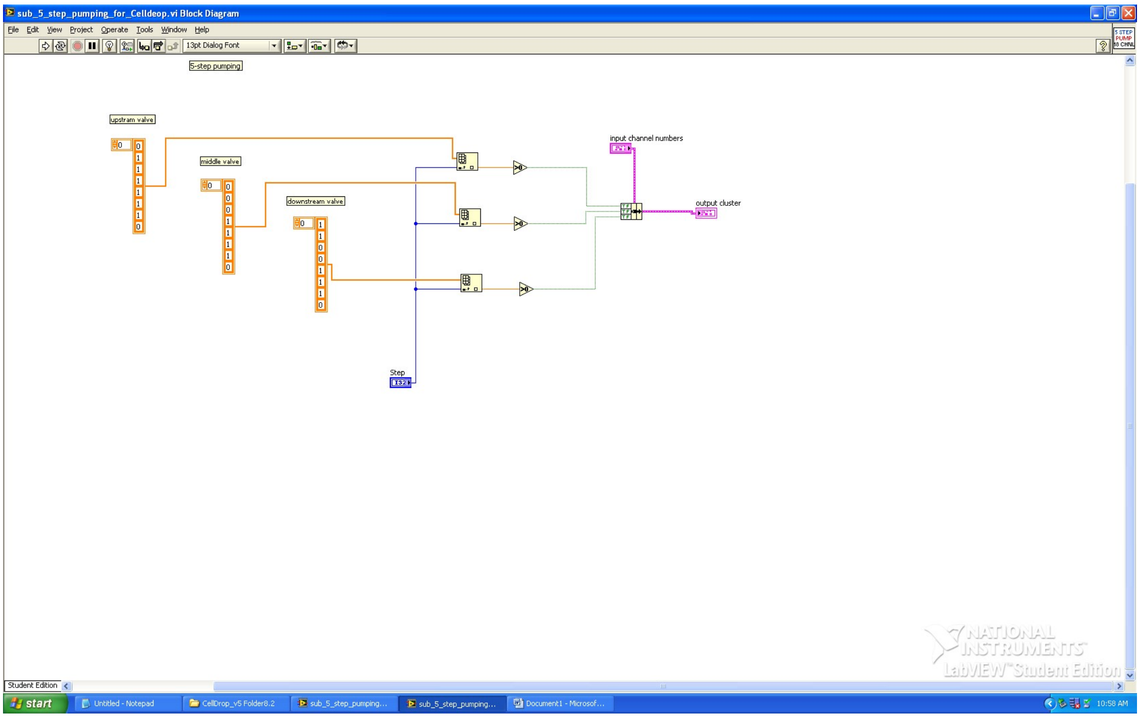

Figure A.17: Block diagram of LabVIEW application subprogram for 5-step pumping.

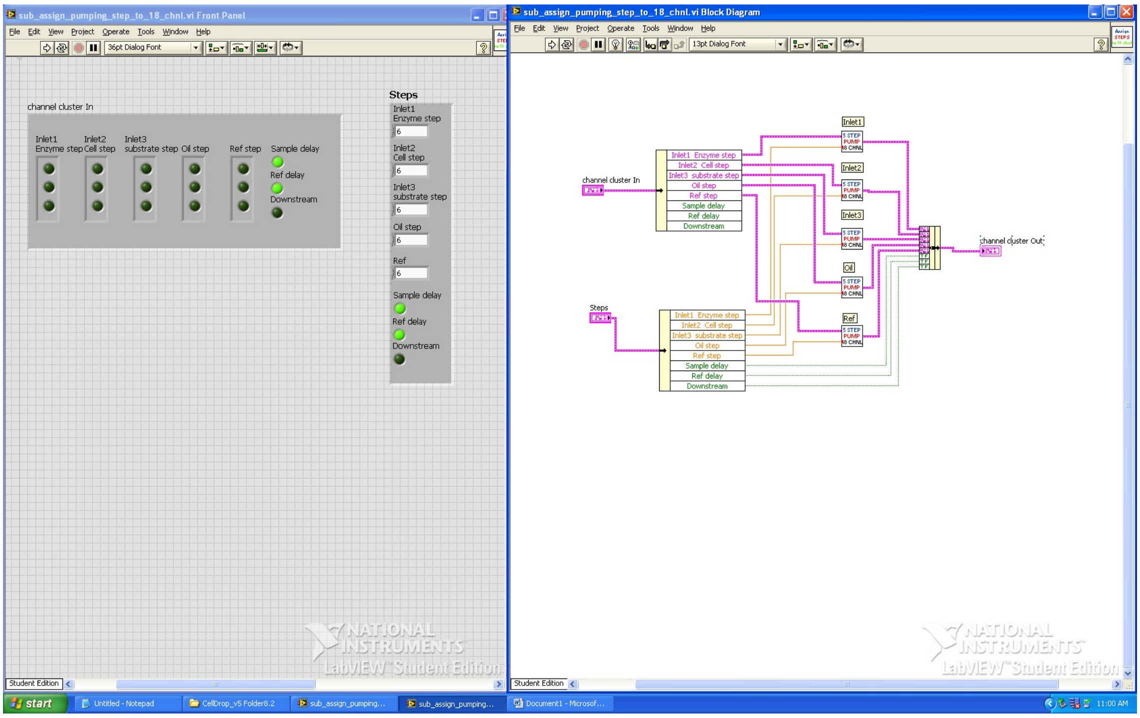

Figure A.18: Front panel and block diagram of LabVIEW application subprogram for valves pumping assignment.

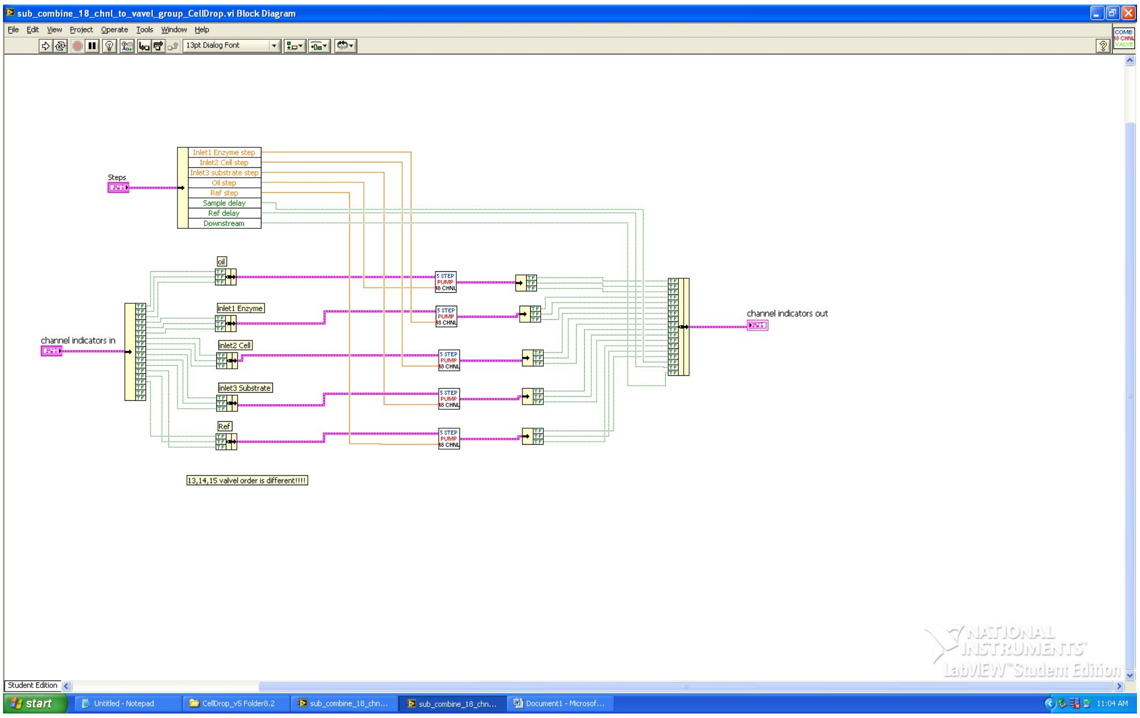

Figure A.19: Block diagram of LabVIEW application subprogram for valve grouping.

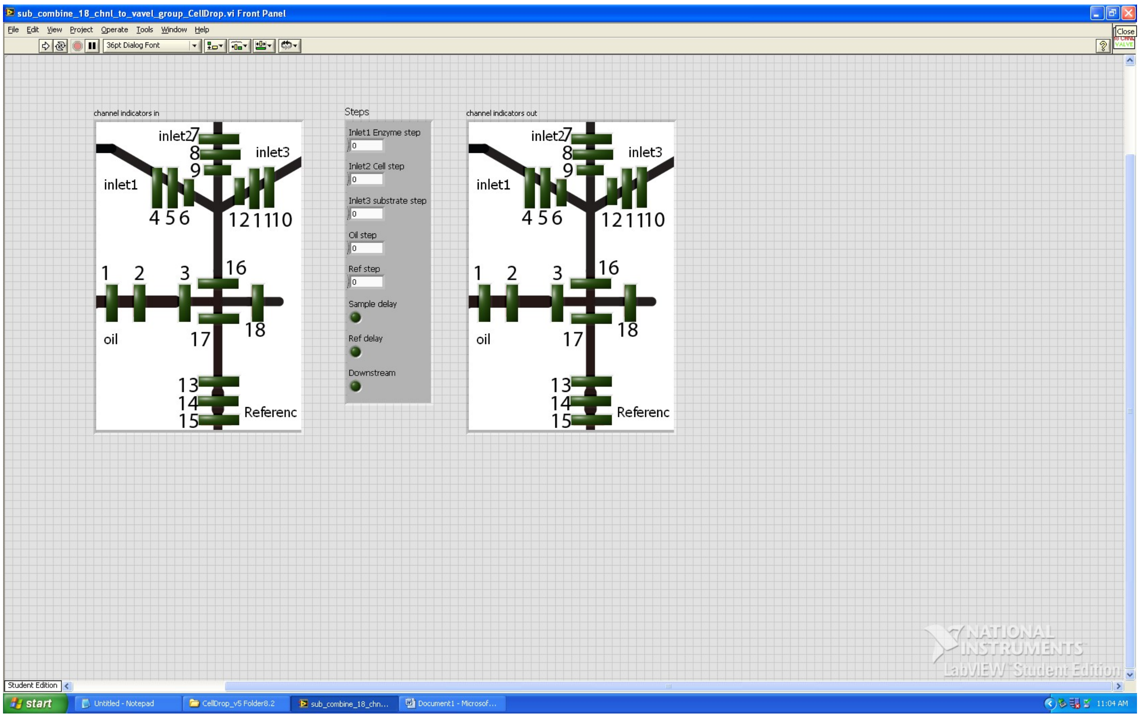

Figure A.20: Front Panel of LabVIEW application subprogram for valve grouping.

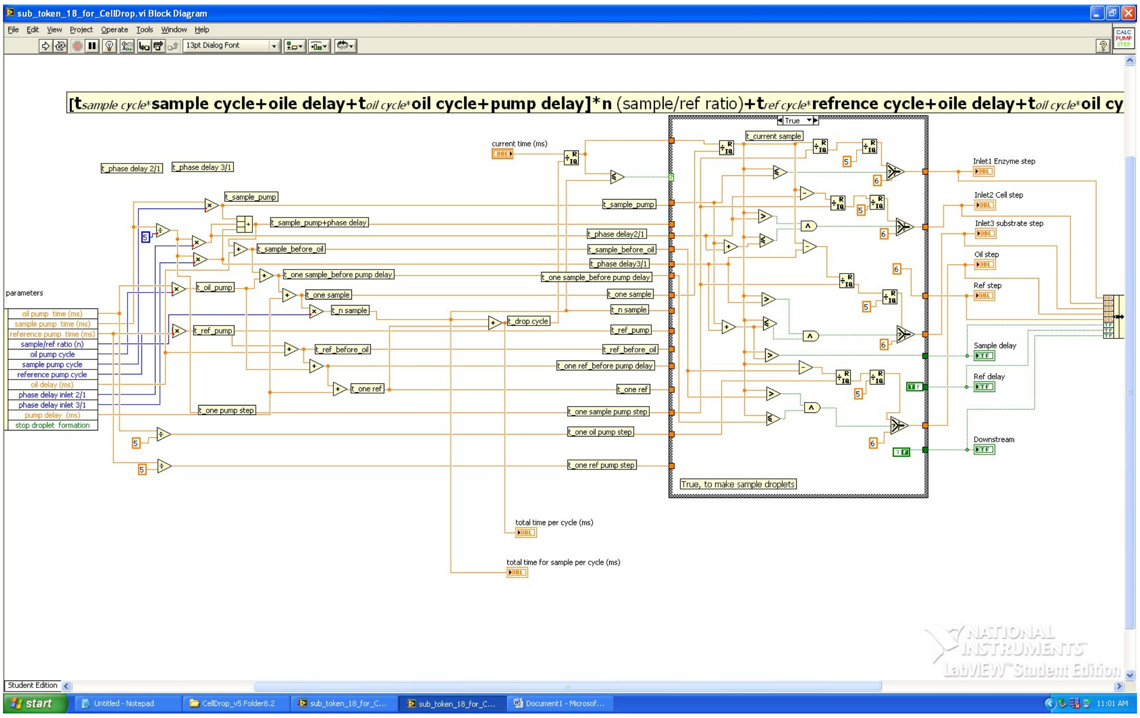

[tsample cycle*sample cycle+oile delay+t oil cycle*oil cycle+pump delay]*n (sample/ref ratio)+t ref cycle*refrence cycle+oile delay+t oil cycle*oil cy

Figure A.21: Block diagram of LabVIEW application subprogram for pumping time calculation in “droplet generation”.

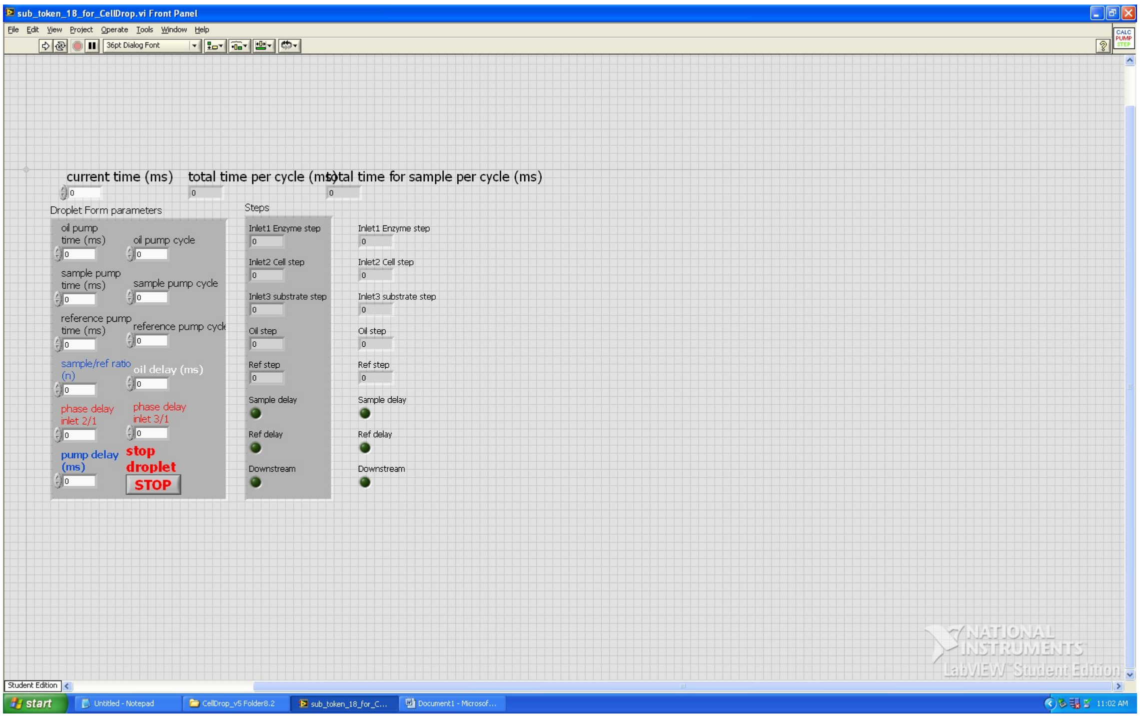

current time (ms) 0
total time per cycle (ms) 0
total time for sample per cycle (ms) 0

Droplet Form parameters

oil pump time (ms) 0
oil pump cycle 0
sample pump time (ms) 0
sample pump cycle 0
reference pump time (ms) 0
reference pump cycle 0
sample/ref ratio (n) 0
oil delay (ms) 0
phase delay inlet 2/1 0
phase delay inlet 3/1 0
pump delay (ms) 0
stop droplet STOP

Steps

Inlet1 Enzyme step 0
Inlet2 Cell step 0
Inlet3 substrate step 0
Oil step 0
Ref step 0
Sample delay ●
Ref delay ●
Downstream ●

Inlet1 Enzyme step 0
Inlet2 Cell step 0
Inlet3 substrate step 0
Oil step 0
Ref step 0
Sample delay ●
Ref delay ●
Downstream ●

Figure A.22: Front panel of LabVIEW application subprogram for pumping time calculation in “droplet generation”.

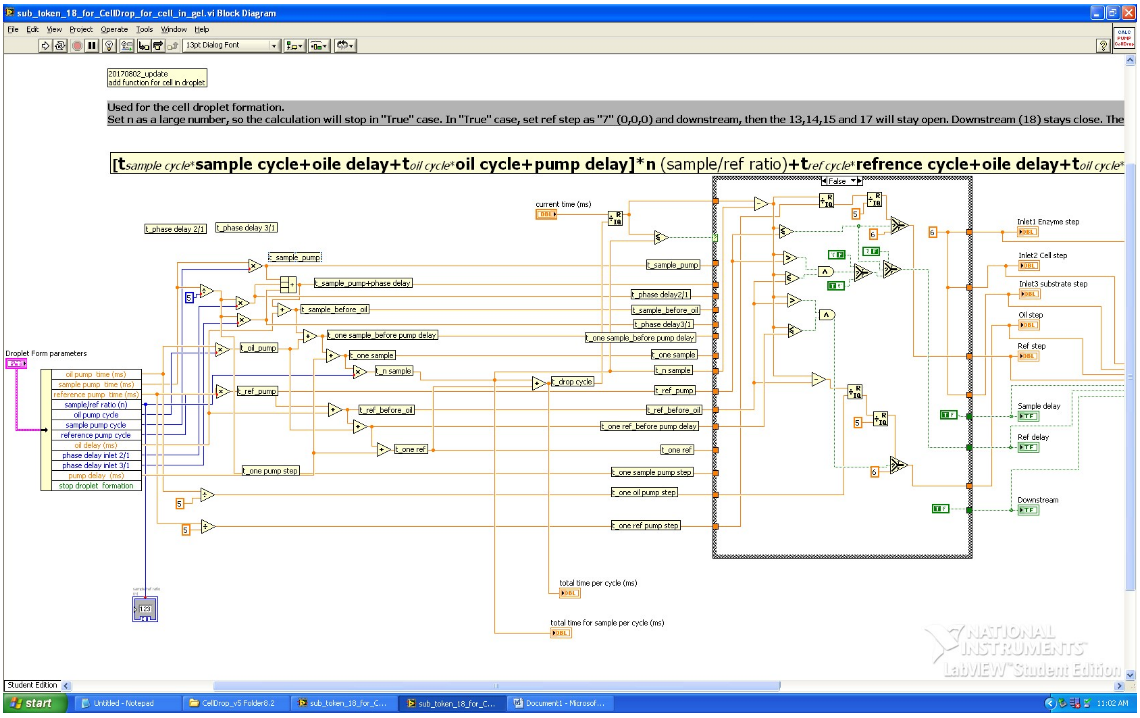

sub_token_18_for_CellDrop_for_cell_in_gel.vi Block Diagram

20170802_update
add function for cell in droplet

Used for the cell droplet formation.
Set n as a large number, so the calculation will stop in "True" case. In "True" case, set ref step as "7" (0,0,0) and downstream, then the 13,14,15 and 17 will stay open. Downstream (18) stays close. The

[tsample cycle*sample cycle+oile delay+toil cycle*oil cycle+pump delay]*n (sample/ref ratio)+tref cycle*refrence cycle+oile delay+toil cycle*

Figure A.23: Block diagram of LabVIEW application subprogram for pumping time calculation in "Celldroplet".

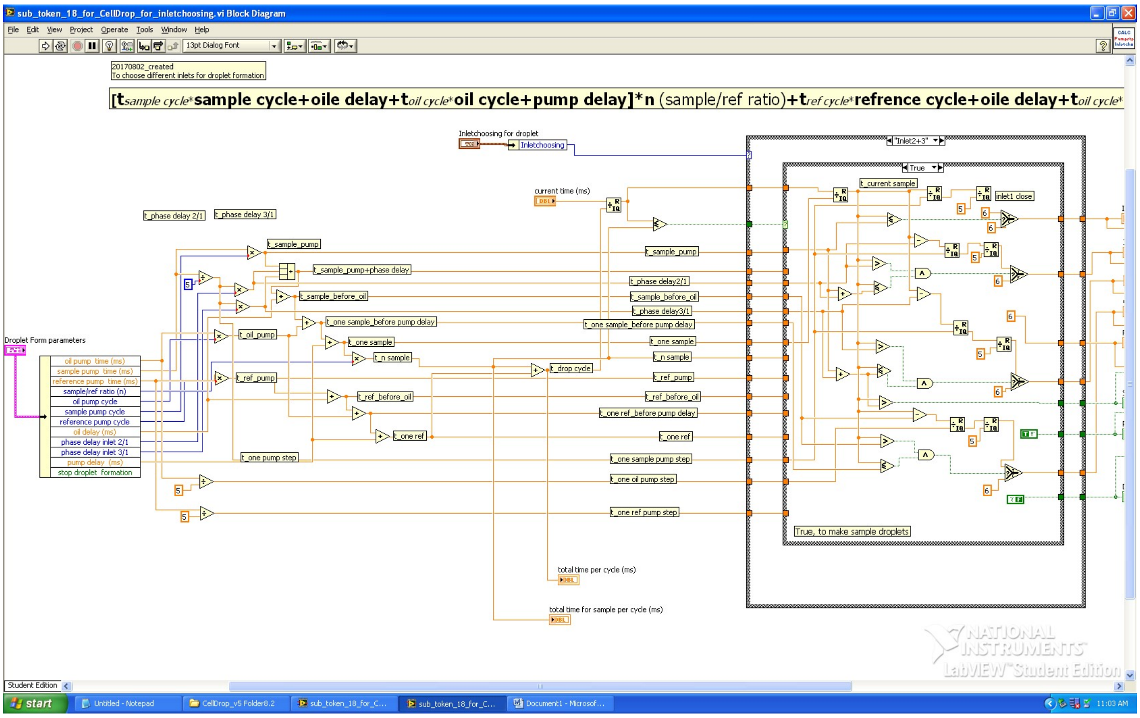

sub_token_18_for_CellDrop_for_inletchoosing.vi Block Diagram

20170802_created
To choose different inlets for droplet formation

[tsample cycle*sample cycle+oile delay+toil cycle*oil cycle+pump delay]*n (sample/ref ratio)+tref cycle*refrence cycle+oile delay+toil cycle*

True, to make sample droplets

Figure A.24: Block diagram of LabVIEW application subprogram for pumping time calculation in "inlet choosing for droplet".